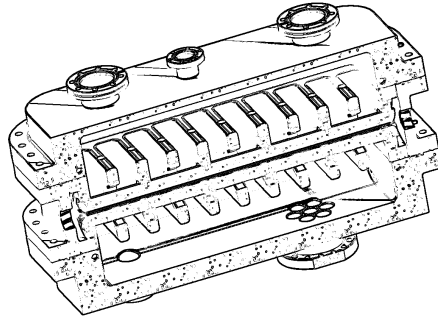# Design and Development of a 325 MHz Ladder RFQ

DISSERTATION

zur Erlangung des Doktorgrades
der Naturwissenschaften

vorgelegt beim Fachbereich Physik
der Johann Wolfgang Goethe-Universität
in Frankfurt am Main

von
Maximilian Schütt
aus Aschaffenburg

Frankfurt am Main, 2017
(D30)

vom Fachbereich Physik der
Johann Wolfgang Goethe-Universität als Dissertation angenommen.

Dekan: Prof. Dr. Owe Phillipsen
Gutachter: Prof. Dr. Ulrich Ratzinger
              Prof. Dr. Holger Podlech

Datum der Disputation: 01.02.2018

Contents

List of Tables

List of Figures

Kapitel 1

Zusammenfassung

Zur effizienten Beschleunigung von Ionen wird meist nach deren Erzeugung in einer Ionenquelle und vor den Driftröhrenbeschleunigern ein **R**adio **F**requenz **Q**uadrupol verwendet. Die vorliegende Dissertation befasst sich mit Entwicklung, Bau und Messung des Prototyps eines neuartigen Leiter-RFQs, der bei 325 MHz betrieben wird (s. Abb. 1.1). Der Leiter-RFQ verfügt über ein neuartiges mechanisches Design und versucht die Vorteile der beiden vorrangig im Betrieb befindlichen RFQ Typen, des 4-Rod und 4-Vane RFQs, zu verbinden. Die physikalischen Parameter sind der Spezifikation des RFQs für den geplanten Protonenlinac (p-Linac) am FAIR[1]-Projekt an der GSI Darmstadt entnommen. Darüber hinaus wird der aktuelle Planungs- und Simulationsstand eines modulierten Prototyps mit der vollen Länge von ca. 3,5 m zur Durchführung von Strahltests dargestellt.

Ein RFQ erfüllt im Wesentlichen drei Aufgaben. Zum Einen wird der Teilchenstrahl gebuncht. Das bedeutet, dass der aus der Ionenquelle extrahierte kontinuierliche Strahl adiabatisch, d.h. ohne Teilchenverluste und unter stetiger Änderung der Strahldynamikparameter, in Teilchenpakete (Bunche) zerteilt wird. Durch eine variable Anpassung der Phase wird eine Akzeptanz im gesamten Phasenraum über $\pm 180°$ ermöglicht. Des Weiteren wird der Strahl vorbeschleunigt, um von nachfolgenden Driftröhrenbeschleunigern angenommen werden zu können. Darüber hinaus wird der Teilchenstrahl fokussiert. Den abstoßenden Raumladungskräften der gleichartig geladenen Ionen wirken die fokussierenden Kräfte im RFQ entgegen, so dass der Strahl im Aperturbereich bleibt und möglichst wenig Emittanzwachstum erfährt. RFQs stellen

---

[1]**F**acility for **A**ntiproton and **I**on **R**esearch.
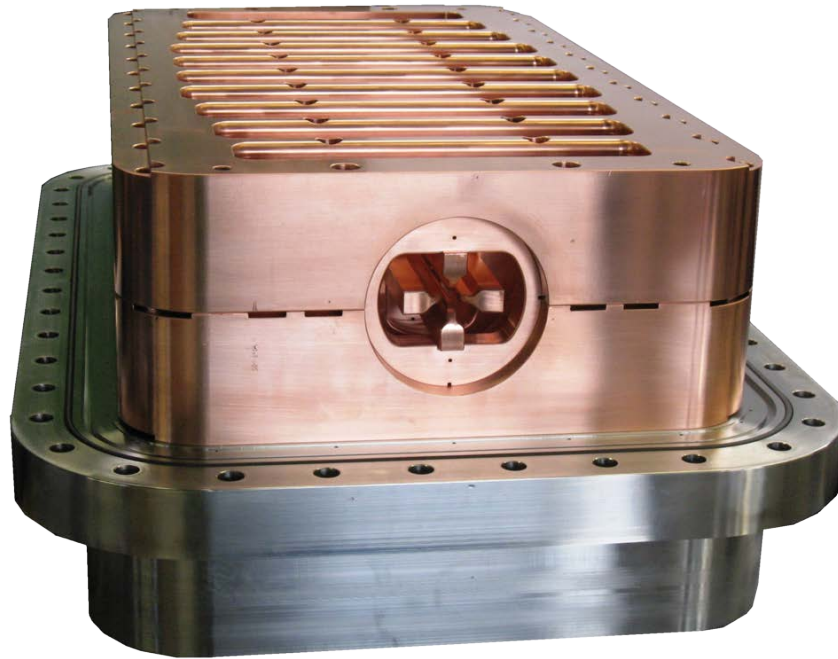
Abbildung 1.1: Isometrische Ansicht des unmodulierten Leiter-RFQ Prototyps mit einer Elektrodenlänge von 630 mm bei geöffnetem Tank.

damit das Bindeglied zwischen der Ionenquelle und den Driftröhrenbeschleunigern dar und ersetzen die früher eingesetzen Van-de-Graff Gleichstrombeschleuniger.

Das FAIR Projekt (s. Kap. 2.1) startete 2007 als eine internationale Zusammenarbeit zur Erforschung von Antiprotonen und Ionen. Es umfasst die Erweiterung der bestehenden GSI Anlage um ein Synchrotron SIS100, sowie weitere Speicherringe. Um die benötigte Anzahl an Antiprotonen zu erzeugen, kann der sich zur Zeit im Betrieb befindliche Linearbeschleuniger UNILAC nicht ausreichend Protonen zur Verfügung stellen. In Folge ist ein dedizierter Linearbeschleuniger zur Beschleunigung von Protonen im Aufbau. Der p-Linac mit einer Länge von ca. 30 m soll Protonen bei einem Strom von bis zu 70 mA auf 68 MeV bei einem Tastverhältnis von 0.08% beschleunigen und in das Synchrotron SIS18 injizieren. Aufgrund der Wahl der Klystren, welche die Leistung für die Beschleunigerstrukturen bereitstellen (jeweils bis zu 2,5 MW), ist die Frequenz auf 325,224 MHz festgelegt. Der RFQ soll bei einer Elektrodenlänge von ca. 3.2 m den Strahl von 95 keV auf 3 MeV beschleunigen.

Die wichtigsten Schritte und Erkenntnisse dieser Arbeit können folgendermaßen zusammengefasst werden:

- Einführung über die Funktionsweise von RFQs im Allgemeinen hinsichtlich des Hochfrequenzverhaltens der Kavität als auch der Strahldynamik, Einführung der am häufigsten verwendeten Bauarten, sowie die Einführung wichtiger physikalischer Begriffe zur Beschreibung von RFQs (s. Kap. 3),

- Vorstellung von bisher realisierten Ansätzen von Leiter RFQs und Herleitung eines theoretischen Modells zur Auslegung der grundlegenden Parameter und Dimensionen eines Leiter-RFQs (s. Kap. 4),

- Simulationen zu Hochfrequenzfeldern, insbesondere zum longitudinalen Verlauf der Elektrodenspannung, Bestimmung von Dipolfeldern, Hochfrequenz-Einkopplung, Frequenztuning und Temperaturverteilungen (s. Kap. 5),

- Vorstellung des mechanischen Designs des unmodulierten Leiter-RFQ Prototyps (s. Kap. 6),

- Messung der grundlegenden HF-Parameter inkl. Konditionierung und Hochleistungstests des unmodulierten Prototyps (s. Kap. 7), sowie

- Simulationen, Auslegung und Design eines modulierten Leiter-RFQs bei voller Länge, der für Strahltests zur Beschleunigung von Protonen auf 3 MeV verwendet werden kann (s. Kap. 8).

Zuerst werden die Dimensionen der Leiterstruktur und der Elektroden in einem analytischen Model abgeschätzt, um eine Grundlage für die Simulationen zu erhalten. Darüber hinaus gibt das Model Auskunft über das Verhalten der Frequenz bei Änderung einzelner geometrischen Größen.

Im nächsten Schritt werden die physikalischen Parameter in 3-dimensionalen EM-Simulationen untersucht. Zunächst müssen die Dimensionen der Leiterstrukutur aus dem analytischen Modell, insbesondere die Höhe und Breite der Leitersprossen, validiert und an die exakte Frequenz angepasst werden. Anschließend wird der longitudinale Feldverlauf entlang der Strahlachse untersucht. Für eine möglichst verlustfreie und effiziente Beschleunigung sollte der transversale Feldverlauf entlang

der Strahlachse und damit auch die Spannungsdifferenz zwischen den Elektroden möglichst konstant sein. Durch eine Anpassung der Länge des Strompfads, respektive der Leiterhöhen, kann die Spannungsverteilung lokal verändert werden. Im Gegensatz zu herkömmlichen RFQs ist bei dem Leiter-RFQ, der aus einem massiven Kupferteil gefräst wird, eine nachträgliche Anpassung durch variabel verstellbare Tuningplatten nicht möglich. Es benötigt daher möglichst präzise und realistische Simulationen, um die optimale Konfiguration bestimmen zu können. Durch die hohe Symmetrie des Leiter-RFQs wird in den Simulation gezeigt, dass eine Anpassung der ersten und letzten drei Zellhöhen genügt, um eine flache Feldverteilung zu erhalten.

Aufgrund der endlichen transversalen Abmessungen der Elektroden kann der RFQ keine ideale Quadrupolkonfiguration darstellen. Somit ist die Untersuchung von störenden Dipolkomponenten nötig. Der Leiter-RFQ enthält aufgrund seiner symmetrischen Bauart jedoch von Grund auf einen sehr geringen Dipolanteil.

Während des Betriebs ist die Resonanzfrequenz nicht konstant, da aufgrund der Erwärmung durch Ohmsche Verluste das Material ausgedehnt wird. Die Frequenz muss daher mit mechanischen Kolben korrigiert werden. In den Simulationen können diese hinsichtlich einer möglichst großen Wirkung auf die Frequenz, jedoch einer möglichst kleinen Auswirkung auf den longitudinalen Feldverlauf entlang der Strahlachse, angepasst werden. Darüber hinaus muss die Einkoppelschleife zum Einkoppeln der HF-Leistung für den angepassten Fall dimensioniert werden.

Jegliche Änderung und Optimierung einzelner physikalischer Eigenschaften muss im Hinblick auf alle anderen Eigenschaften bei jeder Simulation kontrolliert werden, da diese nicht unabhängig voneinander sind. Zur Auslegung des Kühlsystems wird die Temperaturentwicklung unter Last untersucht. Letztendlich wird das parametrisierte Modell mit dem realistischeren „as built" CAD Model verglichen, um die Prognose der Simulation vor dem Bau des RFQs zuverlässiger einschätzen zu können.

Mit der Bestimmung aller geometrischen Parameter aus den Simulationen kann das mechanische Design eines unmodulierten Prototyps erstellt werden. Der unmodulierte Prototyp mit einer Elektrodenlänge von 63 cm dient dem Test und der Bestätigung des simulierten HF-Verhaltens, sowie dem Test unter Leistung. Der Prototyp verzichtet auf eine Modulierung der Elektroden, d.h. die Apertur wird konstant bei

einem mittleren Wert gehalten[2]. Der Prototyp ist ausschließlich in der Länge auf zehn Leiterzellen beschränkt, wobei die übrigen Größen einem vollständigen RFQ entsprechen. Der Leiter-RFQ besteht aus zwei Hauptkomponenten, dem Tank und der darin eingebetteten Leiterstruktur aus Kupfer. Der Tank dient vorwiegend der mechanischen Stabilität und der Ausrichtung der Kupferstruktur. Darüber hinaus hält er durch ein implementiertes Dicht- und Vorvakuumsystem das Vakuum von ca. 10^{-8} mbar aufrecht. Die im Tank integrierten Kühlkanäle sorgen für eine konstante Betriebstemperatur bei einem Tastverhältnis von 0,08%. Die Leiterstruktur besteht aus zwei symmetrischen, horizontal geteilten Leiterhälften, zwischen denen das bereits an der GSI erfolgreich im Betrieb befindliche Ring-Elektroden System eingebunden ist. Dieses ermöglicht eine symmetrische, elektrisch leitende und mechanisch stabile Verbindung der Elektroden mit den Leiterhälften. Des Weiteren beinhaltet das mechanische Design die Auslegung allen Zubehörs, wie des Vakuumsystems, der Wasserkühlung, der permanenten und motorgetriebenen Frequenztuner, der Supportflansche, sowie der Einkoppelschleife.

Nach der Herstellung und Montage des Prototyps wurden die HF-Messungen durchgeführt. Zu den wichtigsten Messungen zählten hierbei die Bestimmung der exakten Resonanzfrequenz und der Güte. Mit einem Wert von 5080 erreicht die gemessene Güte 75% des theoretischen Wertes von 6800. Die Frequenzmessung ergab mit ca. +1 MHz eine Abweichung von ca. +0,3% gegenüber der simulierten Frequenz. Das Tuning, d.h. das Erreichen einer möglichst konstanten, longitudinalen Spannungsverteilung, erfolgte in zwei Schritten. Bei der Herstellung wurden zunächst die einzelnen Zellhöhen mit einem Aufmaß von 5 mm pro Seite belassen. In einer ersten Messung wurde die Flatness mit den Simulationen verglichen und in weiteren Simulationen konnten sowohl die Flatness optimiert als auch die Frequenz angepasst werden. Zeitgleich mit der Verkupferung des Tanks wurden die einzelnen Zellhöhen der Leiterhälften entsprechend den Simulationsergebnissen ausgefräst. Die anschließende Messung der Flatness ergab eine relative Abweichung der Elektrodenspannung von maximal ±0,4% entlang der Strahlachse. Ebenso wurden die Frequenztuner vermessen. Sowohl der statische als auch der elektrisch verstellbare Tuner sollten in ihrer

---

[2]Wirtschaftlich gesehen ist dieses Vorgehen sinnvoller, um zunächst die grundlegende Realisierbarkeit und Funktionalität zu bestätigen, bevor ein modulierter Prototyp bei voller Länge geplant und gebaut wird.

Grundposition auf gleicher Höhe möglichst genau die Zielfrequenz von 325,224 MHz treffen. Der maximale Frequenzhub mit zwei Kupferzylindern mit einem Durchmesser von 28 mm beträgt ca. 470 kHz, was für einen Betrieb ausreichend ist. Ebenso wurde die optimale Größe und Form der Einkoppelschleife bestimmt. Um zusätzlich zu den Ohmschen Verlusten die Strahlleistung bedienen zu können, muss der RFQ entsprechend überkoppelt betrieben werden. Nach dem Test des Vakuumsystems und einer Leckprüfung konnte der RFQ am IAP bis zu einer Vorwärtsleistung von ca. 440 W gepulst und bei Dauerstrich konditioniert werden. Anschließend wurde der RFQ im Testbunker der GSI bis zu einer eingekoppelten Leistung von 483 kW getestet. Dies entspricht ca. den 3,6-fachen nominalen Verlusten während des regulären Betriebs. Es ergab sich ein maximaler Kilpatrick Faktor von 3,1. Eine optische Kontrolle zeigte zwar Verfärbungen auf der Oberfläche der Elektroden und des unverkupferten Tankmittelteils, jedoch keine Beschädigungen oder Ablation.

Die erfolgreichen Hochleistungstests des unmodulierten Prototyps gaben Anlass zum Design und Bau eines modulierten Prototyps mit einer Elektrodenlänge von ca. 3328 mm. Die Anzahl der Leiterzellen beträgt hierbei 55. Zunächst wurden die grundlegenden Leiterdimensionen erneut durch Simulationen überprüft, sowie die Möglichkeiten zum Tunen der Flatness. Gemäß den Simulationen wäre es auch bei dieser Länge ausreichend, den longitudinalen Spannungsverlauf des Leiter-RFQs mit einer Variation der ersten und letzten drei Zellhöhen (d.h. in den Zellen 1-3 und 53-55) zu optimieren. Um die Ergebnisse weiter zu verbessern, werden jedoch die ersten und letzten vier Zellhöhen angepasst. Da die Modulation der Elektroden auch Einflüsse auf die Flatness hat, wurden alle Simulationen zusätzlich unter Berücksichtigung dieser durchgeführt. Des Weiteren wurde neben den in den Tank Tiefloch-gebohrten Kühlkanälen eine direkte Kühlung der Kupferstrukutur integriert. Mit dieser erweiterten Kühlung wäre ein Betrieb bis zu einem Tastverhältnis von mindestens 5% möglich.

Der Leiter-RFQ kombiniert Vorteile eines 4-Rod RFQs mit jenen von 4-Vane Strukturen. Die Komponenten werden ausschließlich miteinander verschraubt, wodurch auf Schweißen und Löten verzichtet werden kann[3]. Somit ist die Wartung und

---

[3]Ausgenommen hiervon ist die Einbringung der direkten Kühlung der Leiterstruktur im Falle des modulierten Leiter RFQs (vgl. Kap. 8.5), wobei die Kühlkanäle mit Hilfe von Elektronenstrahlen

Flexibilität für einen potentiellen Elektrodenaustausch jederzeit gegeben. Durch die hohe Symmetrie der Leiterstruktur ist der Anteil an Dipolmoden von Grund auf sehr klein ($< 1\%$), womit sich der Leiter-RFQ vor allem bei Frequenzen oberhalb von $300\,\text{MHz}$ eignet. Mit den positiven Ergebnissen bei den Hochleistungstests bezüglich der Spannungsfestigkeit, sowie der gemessenen Flatness mit einer maximalen, relativen Abweichung von maximal 0.4%, stellt der Leiter-RFQ, insbesondere bei hohen Frequenzen ab $250\,\text{MHz}$ eine vielversprechende Alternative zu bereits existierenden Strukturen dar.

---

zugeschweißt werden, um einen Wärmeeintrag und Verformung der Struktur zu vermeiden. Der Tank und eine Wartung des RFQs ist davon jedoch nicht beeinträchtigt.

Chapter 2

Introduction

> "All human knowledge begins with intuitions, proceeds from thence to concepts, and ends with ideas."
>
> *Immanuel Kant*

What happened at the creation of time? This fundamental question of mankind has been asked for centuries. To the greatest possible extend, the answer was given so far mostly by religion or philosophy. From the start of the groundbreaking research with particle accelerators, a scientific response to this question seems to be within reach. Highly accelerated particles and their energy enable the artificial imitation of hot dense matter - that very state of our universe at a tiny fraction of a second after the Big Bang. The European Organization for Nuclear Research (CERN[1]), for example, takes advantage of large accelerator structures to accelerate protons to high energies. The collision of these particles produces temperatures and densities which predominated our early universe.

Furthermore, there are plenty more scopes of application. For example, the energy of heavy ions can precisely be deposited into tissue according to their velocity. By these means, tumors can be treated, as it is successfully done at the Heidelberg Ionbeam-Therapy Center (HIT) [Bechtold, 2003]. In contrast to laser treatments, healthy circumjacent tissue is being preserved.

One of the topical issues is the investigation of accelerators for transmutation. An

---

[1]**C**onseil **E**uropéen pour la **R**echerche **N**ucléaire

Accelerator Driven System (ADS) is a sub critical reactor producing electricity. At the same time it reduces the half-life period of heavy ions contained in spent fuel from nuclear power plans from several hundred thousand years to a few hundred [Rubbia et al., 2001, Abderrahim et al., 2010, Busch, 2015, Mäder, 2014]. The nuclear waste is hereby irradiated by neutrons causing a nuclear reaction. The neutrons, in turn, are created through spallation, i.e. the irradiation of heavy nuclei by protons accelerated in a particle accelerator. Due to the stress of the impact fragments of the material, respectively neutrons, are being emitted.

Synchrotron radiation, emitted from charged particles that are accelerated radially, is widely used in research and industries. The field of applications includes material sciences like surface treatment, in biology for the determination of the structures of molecules (lithography), non-destructive examinations (e.g. in cultural sciences), free electron lasers, meteorology, medicine and many more.

Considering all broadly based applications and the increasing demand for accelerated particles, the research and further development of particle accelerators should be supported and pushed. Particularly desirable is an increase of their efficiency, i.e. a decrease of the electricity demand and a maximization of the net energy gain per length. At this point one should concern about investment costs as well as operating costs. The latter are crucial factors, e.g. for tumor therapy facilities at hospitals. Furthermore, many application purposes generate a rising demand for higher beam currents, which is not trivial referring to space-charges. Thus, there are still enough reasons for an ongoing R&D.

Basically, accelerator facilities can be divided in two categories: Linear- and circular accelerators. Still, a linear accelerator (Linac) is always needed as an injector feeding circular accelerator rings. Linac's consist of several different parts. In general, linac's consist of three main parts: An ion source creating the particles, an RFQ and afterwards further accelerating structures. The first accelerating unit is an RFQ (**R**adio-**F**requency **Q**uadrupole), before the beam is further accelerated by a variety of different types, mostly drift tube linac's (DTL's). The main purposes and advantages of an RFQ are:

- **Bunching**: The electric field of the extraction in the ion source has to be static. As a consequence, the extracted particle beam is a continuous dc-beam.

DTL's are only capable of accepting and accelerating a bunched beam, i.e. the particles have to be transformed into bunches (packets). The RFQ is able to adiabatically bunch a dc-beam with almost no losses.

- **Focusing**: The particles and ions of a beam are equally charged - either positive or negative. Because of the repulsive electromagnetic forces (also known as space-charge forces) the particles within the beam are moved apart leading to an emittance growth. Those forces have to be compensated. The electric field of an RFQ contains time-dependent transversal as well as longitudinal components. This field provides a spatial stability of the beam propagating through the RFQ. Especially in the low-energy section, which is equal to a low particle velocity, the strong electric focusing is a major advantage compared to drift tube linacs with magnetic quadrupole focusing.

- **Accelerating**: In addition, the RFQ serves as a pre-accelerator between the ion source and the following drift-tube linacs. The minimum distance of the drift-tubes of DTL's, the gap distance, is limited by the manufacturing process, mechanical stability and their electric strength. Furthermore, the gap distance depends on the velocity of the particle beams. The phase of the RF has to correspond with the time of arrival in the center of the gaps. The velocity after the extraction from the source would be too small to fulfill these requirements. The RFQ ensures a perfect matching of the beam into the upcoming drift tube structure.

There are several ways of constructing an RFQ (s. chap. 3.2). In this work the Ladder RFQ is studied and examined with a prototype. The principal idea of a ladder-type RFQ firstly arised in the 1980's by A. Fabris et al. [Fabris et al., 1987] and M. Browman [Browman et al., 1988]. The first realization of a ladder structure used for beam operation was the RFQ for the Lead-Ion Facility at CERN in 1994. Operating at 101,28 MHz, it accelerates heavy ions from 2.5 keV to 250 keV. The mostly used ion is $^{208}\text{Pb}^{27+}$ with a beam current of 80 µA and a repetition rate of 10 Hz [Bezzon et al., 1994]. Another example for a ladder-type structure is the 202.5 MHz RFQ for ASACUSA[2] at CERN. It slows down antiprotons from 5.33 MeV

---

[2]**A**tomic **S**pectroscopy **A**nd **C**ollisions **U**sing **S**low **A**ntiprotons

to variable energies between 10 keV to 120 keV [Bylinsky et al., 2000].

The Ladder RFQ, which is the subject of this study, is designed for protons accelerated from 95 keV to 3 MeV with a beam current of 70 mA and a duty factor of 0.08% (200 µs pulses with a repetition rate of 4 Hz [Brodhage et al., 2013, Schuett et al., 2014, Schuett et al., 2015, Schuett et al., 2016a, Schuett et al., 2016b]. The operating frequency at 325 MHz, for which primarily 4-Vane RFQ's are used so far, is significantly higher than previously built 4-Rod RFQ's. The parameters follow the requirements of the planned Proton Linac (p-linac) at FAIR[3] (s. chap. 2.1). Initially, a prototype with an electrode length of 630 mm was planned, designed and simulated. The RFQ was than manufactured. Subsequently, RF measurements as well as power tests were performed (s. chap. 7). Considering the experience feedback of the prototype, the real RFQ with a length of 3.4 m was conceived, simulated and commissioned (s. chap. 8).

2.1 GSI and the FAIR Project

In 1969, GSI[4] was founded for the research on heavy particle acceleration and nuclear physics. Besides atomic physics, spectroscopy, material science and biophysics, the focus was on the synthesis of heavy elements and tumor therapy. The commissioning of the **Uni**versal **L**inear **Ac**celerator (UNILAC) in 1975, which accelerates particles from hydrogen up to uranium with 11.4 MeV at a total length of 120 m, laid the foundation for the discovery of six new elements until 1996, i.a. Darmstadtium 110 and Roentgenium 111. The first synchrotron SIS18 ("Schwerionen Synchrotron") with a maximum bending power of 18 Tm and the ESR[5] were launched in 1990. By using special techniques like electron- and laser-cooling, the ESR is able to store high brilliance ion beams with an energy up to 560 MeV. In 1997, the first successful tumor treatment of a patient with carbon ions at an energy of $200 - 400$ MeV/u was realized. In 2008, the scope of research areas was enhanced by the PHELIX[6] facility.

---

[3] **F**acility for **A**ntiproton and **I**on **R**esearch
[4] GSI Helmholtzzentrum für Schwerionenforschung, formerly Gesellschaft für Schwerionenforschung mbH
[5] **E**xperimental **S**torage **R**ing
[6] **P**etawatt **H**igh-**E**nergy **L**aser for Heavy **I**on E**X**periments

The versatile Nd:glass laser system delivers intense laser beams for either picosecond pulses at $2 \cdot 10^{21}\,\mathrm{W/cm^2}$ or nanosecond pulses at $10^{16}\,\mathrm{W/cm^2}$.
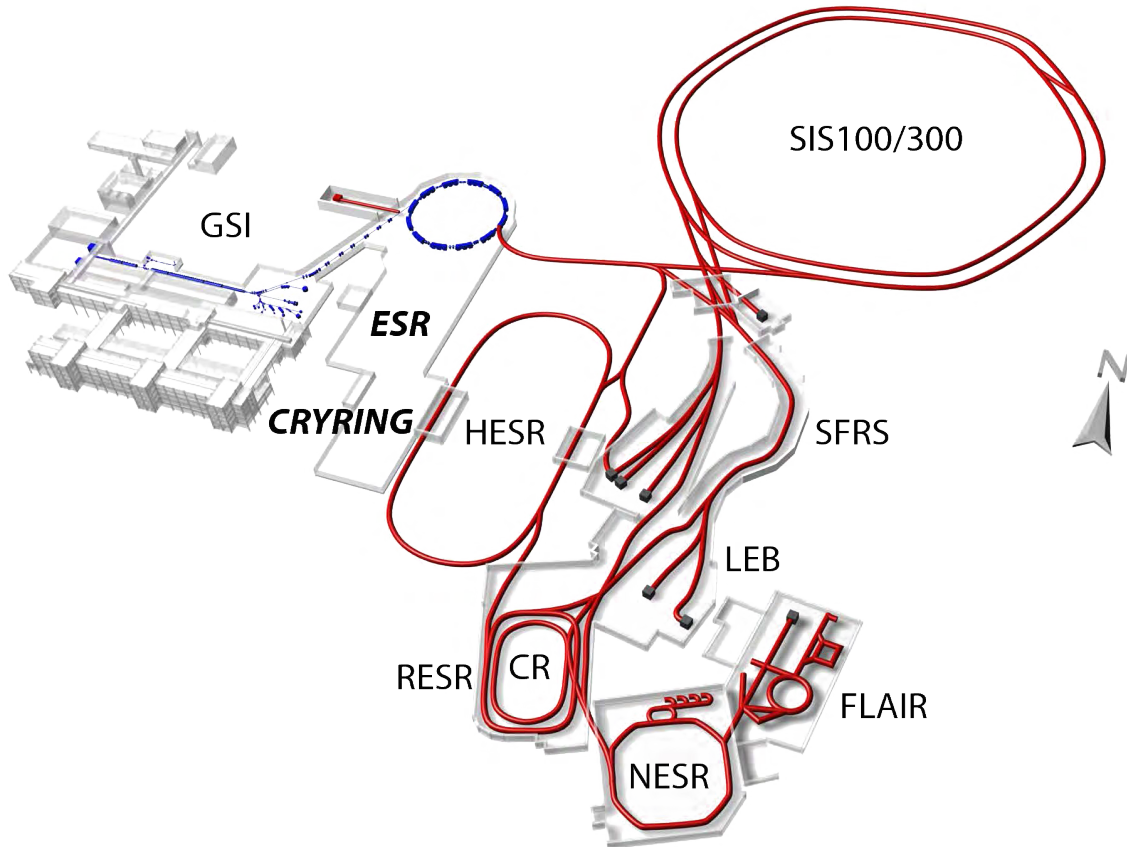
Figure 2.1: Overview of the GSI and FAIR project [Kester et al., 2015]. The existing GSI facilities UNILAC, SIS18, ESR and CRYRING are colored in blue. The planned FAIR facilities are shown in red, respectively.

The FAIR project has officially started in 2007, as an international accelerator facility for antiproton and ion research. The funding is borne by its ten member nations, with Germany and the State of Hesse being the main contributors. Using the available GSI infrastructure as an injector, it extends the existing UNILAC and SIS18 by a synchrotron SIS100. With a circumference of 1100 m, a bending power of 100 Tm and a fast ramping of 4 T/s, it accelerates high intensities of heavy ions with A/q-values as low as 8.5 up to 1 GeV/u at a repetition rate of 1 Hz. The tunnel will be installed 20 m below ground for shielding reasons. As a great side effect it also keeps the environment above the tunnel green. The tunnel is designed for a possible

future upgrade by an additional SIS300 [Kester et al., 2014]. Furthermore, FAIR will contain eight storage rings feeding individual experiments (s. fig. 2.1). A further essential component of the accelerator family will be the superconducting fragment separator (Super-FRS). It is an in-flight separator for relativistic radioactive beams and exotic nuclei. The project also includes several storage rings like the cooling ring (CR) and the high-energy storage ring (HESR). The isochronously operated CR offers stochastic cooling and mass analysis for short-lived radioactive ions and antiprotons. It will be used for the preparation of secondary particle beams. The HESR which is optimized for the storage and cooling of antiprotons up to 14 GeV will include an internal fixed target and the PANDA detector, combining two spectrometers for a full angular coverage around the interaction region as well as forward direction.

In the light of higher beam intensities, power as well as brilliant beam qualities, FAIR will guarantee parallel operation of the four pillars of the experimental program:

- APPA (**A**tomics, **P**lasma **P**hysics and **A**pplications)

- PANDA (Anti**p**roton **An**nihilation at **Da**rmstadt experiment)

- CBM (**C**ompressed **B**aryonic **M**atter)

- NUSTAR (**Nu**clear **St**ructure, **A**strophysics and **R**eactions)

The PANDA experiment as a central part of FAIR will make use of antiprotons for fixed target collisions, to study strong interaction physics by proton-antiproton annihilation. Especially the programs for antiprotons require a high intensity proton driver beam.

2.2 The Proton Linac

The requirement for the antiproton program at FAIR is to provide $7 \cdot 10^{10}$ cooled antiprotons per hour for various experiments. Considering the pbar production and cooling rate (the generation rate for antiprotons is approximately 1:10,000), this number is equivalent to a rate of $2 \cdot 10^{16}$ protons per hour in the primary beam, which have to be provided after the extraction of the synchrotron SIS100 at an energy of 29 GeV. Furthermore, a normalized brilliance of at least $16.5 \, \text{mA/µm}$
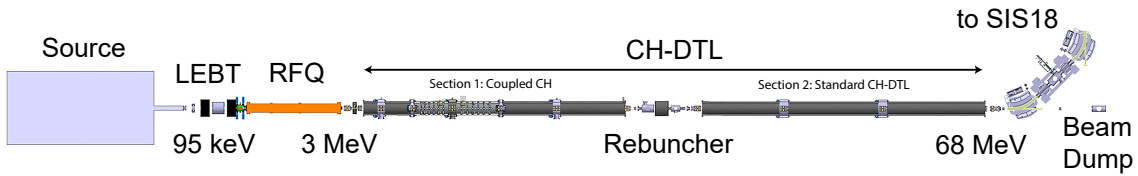
Figure 2.2: Schematic layout of the planned FAIR 68 MeV Proton Linac [Clemente et al., 2010] with a total length of approx. 35 m.

with a momentum spread of less than 0.1% is required to accomplish the transverse acceptance of SIS18 [Kester, 2013]. The UNILAC is able to provide not more than $0.25\,\mathrm{mA} \cdot A/q$, which exactly corresponds to a maximum beam current of $0.25\,\mathrm{mA}$ at 18 MeV for protons. Even with major improvements and efforts like using a hydrocarbon (CH_3), the UNILAC is not able to deliver more than 3 mA [Heilmann et al., 2015]. Otherwise, the primary proton rate is limited by the space charge of SIS18, which is filled by horizontal multi-turn injection. As a consequence, the number of protons within a SIS100 spill correlates with the space charge limit of SIS18. The maximum number of ions depends on their velocity by $\beta^2\gamma^3$ [Ratzinger, 1998]:

$$N_{max,SIS18} \propto \beta^2 \cdot \gamma^3 \cdot \frac{A}{q^2} \tag{2.1}$$

Additionally, the rate of cooled antiprotons is limited by the stochastic cooling capability of the CR. In summary, the economically optimized injection energy into SIS18 is around 70 MeV [Groening et al., 2004]. A smaller energy leads to higher space charge forces and decreases the number of protons per spill, whereas a higher driver energy increases the waiting time of SIS100 as the cooling time for the antiprotons in the CR exceeds the cycle time of the synchrotron. The chosen injector energy is seen as a good compromise between costs and efforts from the linac down to the experimental rings.

Conceptional Design of the Proton Linac

The final decision was to build and employ a dedicated Proton Linac, to deliver at least 35 mA at 68 MeV[7] for direct injection into SIS18 (s. fig. 2.2). Besides the required energy and beam current, an advantage of a dedicated and separated proton driver is the parallel use of SIS100 for the acceleration of ion species, which are different from protons and injected by the UNILAC, during the cooling times of the antiprotons.
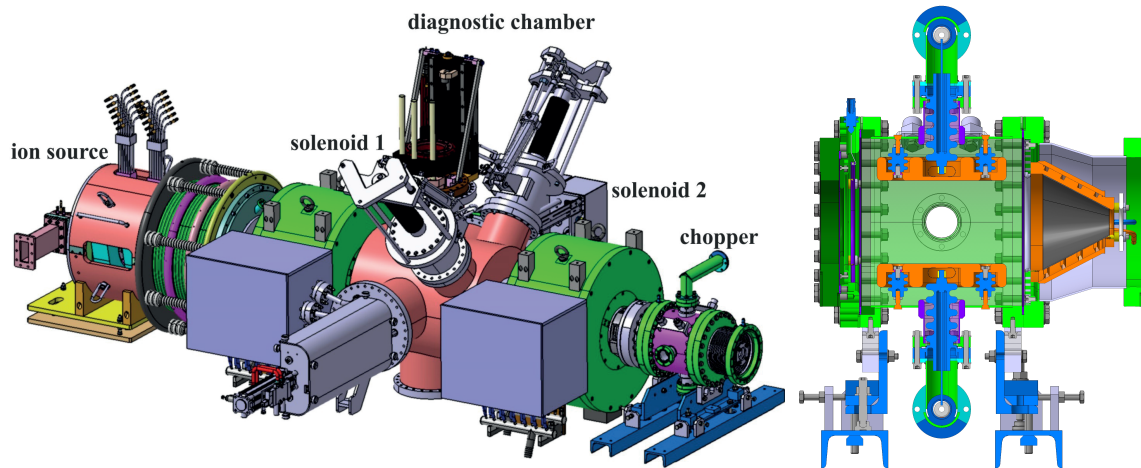
Figure 2.3: Isometric view of the LEBT (left) and cross sectional views of the chopper and injection cone (right) (Designed by CEA/Saclay).

At the beginning, a 2.45 GHz ECR[8] source extracts up to 100 mA of 95 keV protons. The source and LEBT (s. fig. 2.3 left) are an in-kind contribution by CEA/Irfu. It uses a five electrode extraction system with an electric field kept below 96 kV/cm to minimize sparking risks. A LEBT[9] provides two magnetic focusing solenoids which separates H_2^+ and H_3^+ from the proton beam by a Wien filter and a diagnostic chamber. The LEBT diagnostics are contributed by GSI and CEA in joint responsibility. There are plans to integrate an Allison scanner for beam emittance measurements, a beam stopper and two ACCT's[10] for the measurement of beam current and intensity [Bayle et al., 2014]. One ACCT is foreseen to be implemented after the extraction system

---

[7]In early 2017, it was decided to reduce the final energy from 70 MeV to 68 MeV due to the limited klystron power.
[8]**E**lectron **C**yclotron **R**esonance
[9]**L**ow **E**nergy **B**eam **T**ransfer
[10]**AC C**urrent **T**ransformer

and another one after the second solenoid. A chopper (s. fig. 2.3 right) in front of the RFQ cuts the beam into four bunches per second with a length of 50 µs each. The chopped beam is dumped on a water cooled tungsten injection cone. Subsequently, an RFQ further bunches, focuses and accelerates the beam to 3 MeV.
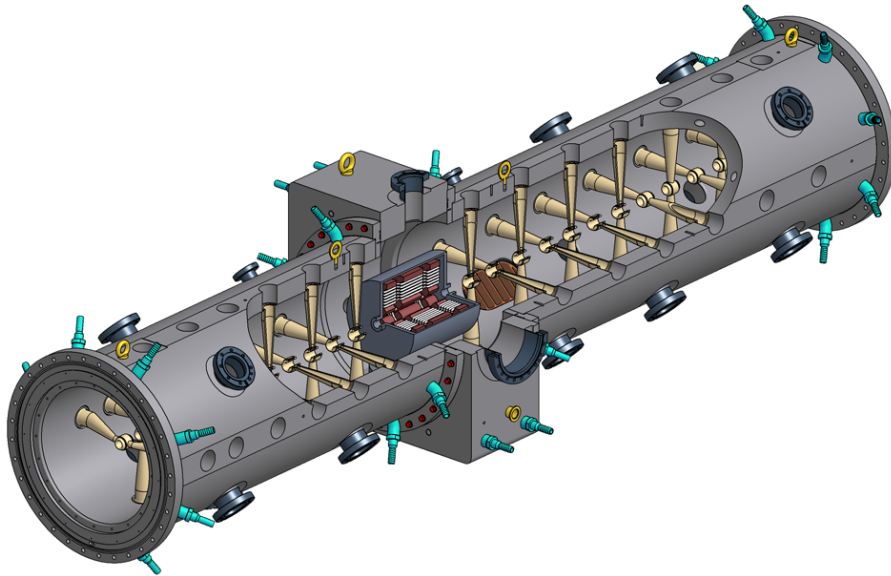
Figure 2.4: Isometric view of the coupled CH prototype for the p-linac [Brodhage et al., 2015]. Both drift tube sections are combined by a coupling cell with a length of $2\beta\lambda$, hosting the quadrupole triplet lense and the coupler flange.

In the following MEBT[11] section a steerer, two quadrupole triplets and a rebuncher will match the beam emittances into the Cross-Bar H-type (CH) drift tube linac. The 33 MeV section consists of three coupled CH-cavities (s. fig. 2.4). Each of them combines two drift tube structures, which are RF-coupled by a single cell resonator oscillating in the Alvarez mode. This cell also houses a quadrupole triplet for transversal focusing. The Cross-Bar cavities use the $H_{21(0)}$-mode for acceleration with neighbored stems oriented perpendicularly to each other. In comparison, IH[12] structures are operated in the $H_{11(0)}$-mode with stems located in one plane. Accordingly, the higher frequency of CH-structures allows similar construction sizes

---

[11]**M**edium **E**nergy **B**eam **T**ransport
[12]**I**nterdigital **H**-mode

compared to IH-cavitites but at nearly twice the RF frequency.

Figure 2.5: Digital mock-up of the p-linac building seen from the south (courtesy of K. Knie, GSI).

A separation at 33 MeV will be used for beam diagnostics including a buncher for longitudinal focusing. Subsequently, three more single CH structures perform the final boost to 68 MeV, before the beam enters the transfer channel for the injection into SIS18. Each cavity as well as the RFQ are powered by a total of seven 3 MW klystron amplifiers. Besides quadrupole triplets for focusing, the Proton Linac will also make use of different beam diagnostic elements. These include, among others, three Faraday cups as a beam dump, nine ACCT's (plus two in the LEBT), four SEM grids for an emittance measurement, an iris for halo scraping, 14 BPM's[13] [Almalki et al., 2014] as well as a Feschenko monitor for the bunch shape. The minimum beam current for operation is 35 mA, whereas the design current is 70 mA. This allows a possible future upgrade. The total number of pbars will be increased by raising the number of protons per spill, if stochastic cooling can be increased. The completion of the p-linac building (s. fig. 2.5) is scheduled for 2019, to be ready

---

[13]**B**eam **P**osition **M**onitor

for the installation and followed by beam tests with the LEBT and the RFQ.

Chapter 3

Theoretical Background

> "Regardless of any deviations, it was
> clear I was supposed to end up in
> math and physics."
>
> *Edward Witten*

Linear accelerators consist of several constituents. At the front end, an ion source contains the atoms or molecules of ions used for acceleration. These particles are ionized within a plasma and subsequently extracted by a static electric field at an energy of $30 - 150\,\text{keV}$. The following part is a **L**ow **E**nergy **B**eam **T**ransport (LEBT). It contains of several elements for beam focusing and - analyzing, such as quadrupole triplets, beam position monitors or Faraday cups. Afterwards, the beam is accelerated mostly by drift tube linac's (DTL). The beam has to have a certain minimum velocity to be completely acceptable by the DTL. This velocity depends on the gap distance. The gap distance gets smaller for slower particles, but is limited by the manufacturing process and its mechanical solidity. In addition, only particle bunches can be accelerated in every gap matched to the RF phase within the gaps.

Historically, the first working ion-accelerator was built by John Cockcroft and Ernest Walton in 1932 [Cockcroft and Walton, 1932a, Cockcroft and Walton, 1932b]. Similar to a Van-de-Graaff accelerator, it uses a static electric field to accelerate the ions. The required voltage was provided by a high-voltage cascade, which is based on works by H. Greinacher [Greinacher, 1921]. The combination of diodes and condensators supply a high voltage potential out of an alternating voltage. Cockcroft and Walton were able to produce the first artificial nuclear reaction by

Accelerating
tube
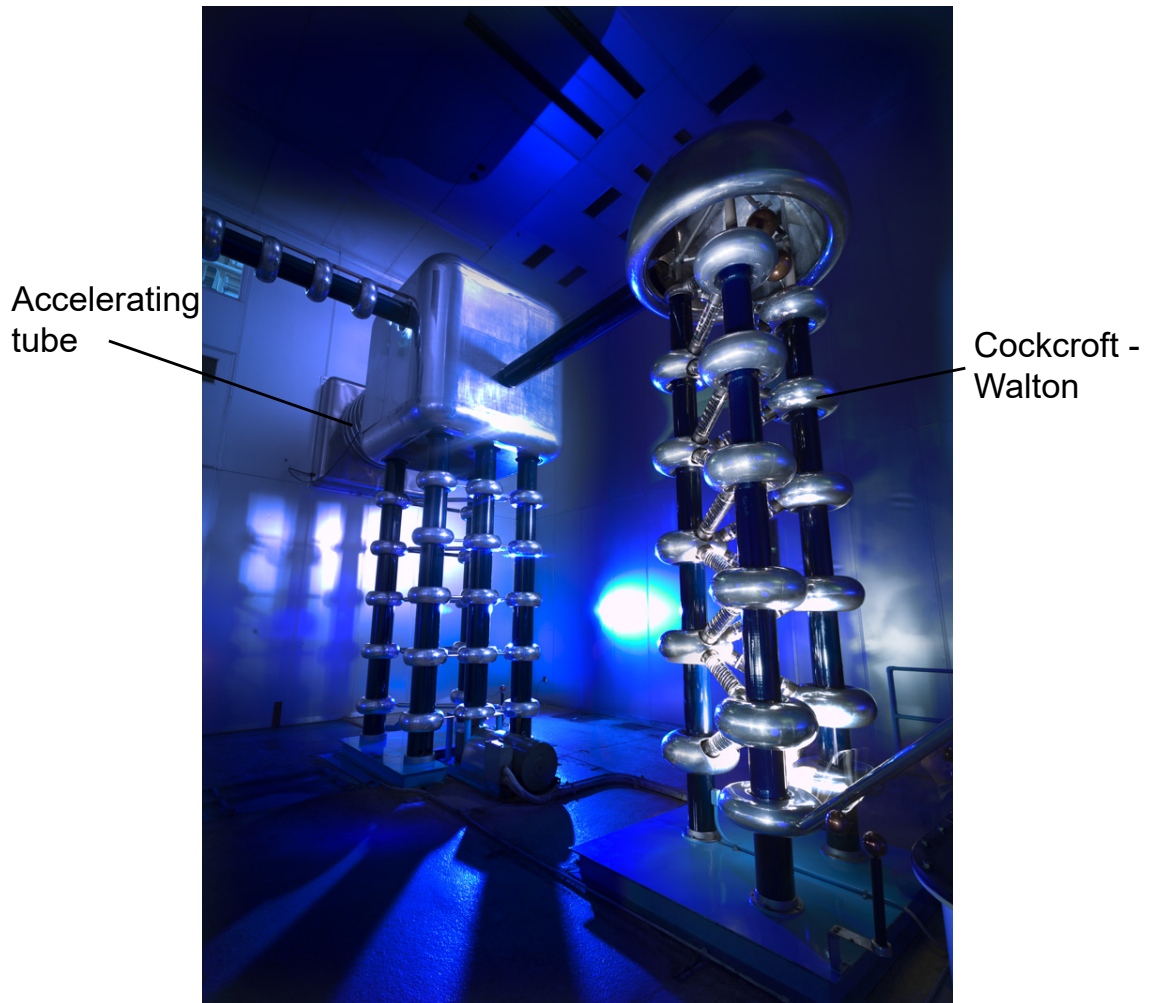
Cockcroft -
Walton

Figure 3.1: Cockcroft-Walton generator at Fermilab. After 40 years of operation, it was replaced by a 4-ROD RFQ in 2012 [Schmidt, 2014, Schmidt et al., 2014]. Photo: Reidar Hahn, Fermilab.

injecting 400 keV protons on the nuclei of a lithium target, creating two helium nuclei. In 1951, they were awarded the Nobel Prize in Physics. Beside the remarkable dimensions of the voltage generators, which fill a whole room (s. fig. 3.1), the static electric field causes further disadvantages. The maximum voltage limited to the electric strength cannot exceed several hundred kV [Hinterberger, 2008]. Furthermore, the high-voltage cascade does not actively bunch the beam. The beam has to be bunched before by the ion source or by a mechanical or electromagnetic chopper. The acceleration tube separated by a ceramic insulator act as a focusing lens.

The solution to eliminate all drawbacks was first proposed by Kapchinskiy and Tepliakov at the Moscow Institute for Theoretical and Experimental Physics (ITEP[1]) in 1969 (Translated 1970) [Kapchinsky and Teplyakov, 1970] and modeled in 1974 at the USSR Institute for High Energy Physics (IHEP[2]) in Protvino. In 1977, the paper was brought into the west for the first time by a Czech refugee and translated into English. The proposal was picked up by the Los Alamos National Laboratory (LANL[3]). In the light of higher beam currents, the RFQ was further improved. In addition, the research resulted in the development of a beam dynamics code, which was later distributed under PARMTEQ-M. In a first principal feasibility beginning in 1979 and successfully tested in February 1980 LANL demonstrated a 4-Vane RFQ with 90% transmission, accelerating 20 mA protons from 100 keV up to 640 keV with a length of 1.1 m operated at 425 MHz [Wangler and Stokes, 1980]. Compared to electrostatic accelerators, it had a considerably higher beam current and the ability to bunch the beam adiabatically without losses.

Based on those principles, different resonant structures were designed and developed in the early 1980s. The most commonly used RFQ's are the 4-Vane and the 4-Rod type. The latter was mainly developed at the Institute of Applied Physics (IAP) in Frankfurt [Schempp et al., 1985, Schempp, 1996]. The principle manner of functioning, described in the following chapter, is basically the same through all types of RFQ's. The main differences concern the RF mode as well as the geometric form of the resonators and of the quadrupole electrodes (s. chap. 3.2).

3.1 RFQ's - an Introduction

This chapter will explain the functional principles of an RFQ. As showed in fig. 3.2, the main concept consists of four electrodes with an opposite potential on adjacent electrodes and the same potential on opposing electrodes generating a quadrupole field. In order to accelerate, bunch and focus particles in an electric field, the surface of the electrodes is modulated (s. fig. 3.6). The modulation adds to the transversal electrical field of a classical quadrupole field a component in the direction of the beam

---

[1]http://www.itep.ru

[2]http://www.ihep.ru

[3]www.lanl.gov
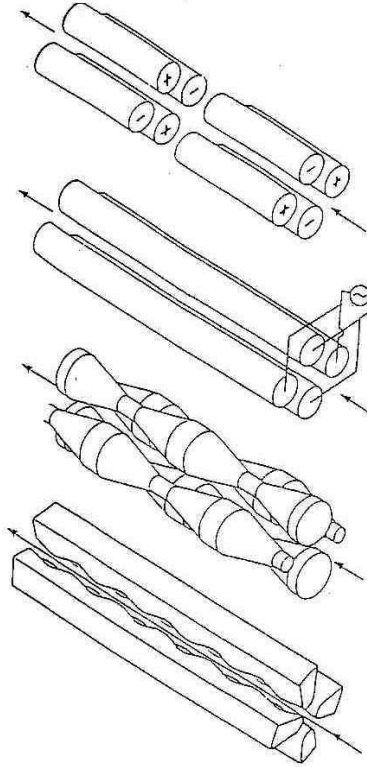
Figure 3.2: Geometric development of the electrodes of an RFQ [Fischer, 2006]. The first design is made of single magnetic or electric quadrupoles in series, used by J. Blewett and L. Tang in 1952 and 1954 [Blewett, 1952, Teng, 1954]. The second approach was realized by an RF-driven Quadrupol [Paul, 1955]. Next up, I. Kapchinski and V. Tepliakov [Kapchinsky and Teplyakov, 1970] used a simple triangular shaped modulation, limited by the process of manufacturing and the lack of simulation methods. The lower picture shows the state of the art electrode modulation, using modern CNC milling machines and powerful 3-D simulations codes regarding multipoles.

axis. The electrode design is construed from the beam dynamics requirements and calculations. The physics behind the details of the functionality of electrodes and the beam dynamics are explained in chapter 3.4. The potential between the electrodes oscillates within every cell and RF-period to accelerate continuously. Therefore, the electrodes are part of a resonator. The oscillating field within the cavity ensures an alternating voltage of the electrodes. The frequency of the resonating structure is hereby fully determined by the capacitance and inductance, which in turn are fixed by the geometries of the resonant structure and the electrode design. The

resonance frequency can be calculated by the Thomson equation for oscillating circuits: $\omega = 1/\sqrt{LC}$ [4]. An analytical model for finding the resonance frequency of the Ladder RFQ is derived in chapter 4.2. There are several possibilities to achieve a resonant structure, which are outlined in the next section.

3.2 Types of RFQ's

The resonant frequency of an RFQ is generally defined by the geometry of the resonator. Basically, the resonators can be divided into two different types. On the one hand, there are transmission-line (or Lecher) type resonators, in which the current mainly flows on the inner structure and defines the RF. The classical 4-Rod RFQ is of that type. On the other hand, the 4-VANE RFQ's applies the relevant cavity mode, which is determined by the current flow on the walls. The beam dynamics of all types of RFQ's is specified by the geometry of the electrodes (cf. chap. 3.4). Hereafter, the most common types of RFQ's – the 4-ROD and 4-VANE – as well as the IH-RFQ, are introduced. The Ladder RFQ profits from advantages and technologies of all of those types. Different realizations and the history of ladder-like structures are shown in chap. 4.1. Further designs of RFQ's can be found in [Teplyakov, 1992, Schempp, 1992b]. The main applications for RFQ's, in general, are listed in [Schempp, 2008, Schempp, 1992a].

3.2.1 IH-RFQ

The IH-RFQ is operated in the $TE_{11(0)}$-Mode. Opposite pairs of electrodes are fixed on carrier rings, which are mounted on stems pointing upwards and downwards in an alternating way. The currents are flowing over the cavity walls from one electrode pair to the other. Consequently, the radius of the tank mainly defines the inductance and the frequency, respectively. The dimensions are suited for low frequencies below $100\,\mathrm{MHz}$. According to the used mode, the diameter of an IH-RFQ is less than half of a 4-Vane if operated at the same frequency. Additionally, losses are primarily and homogeneously distributed on the cavity walls, easing the water-cooling and

---

[4]First derived by William Thomson in 1853 for the oscillating behavior of a Leyden jar [Blanchard, 1941].
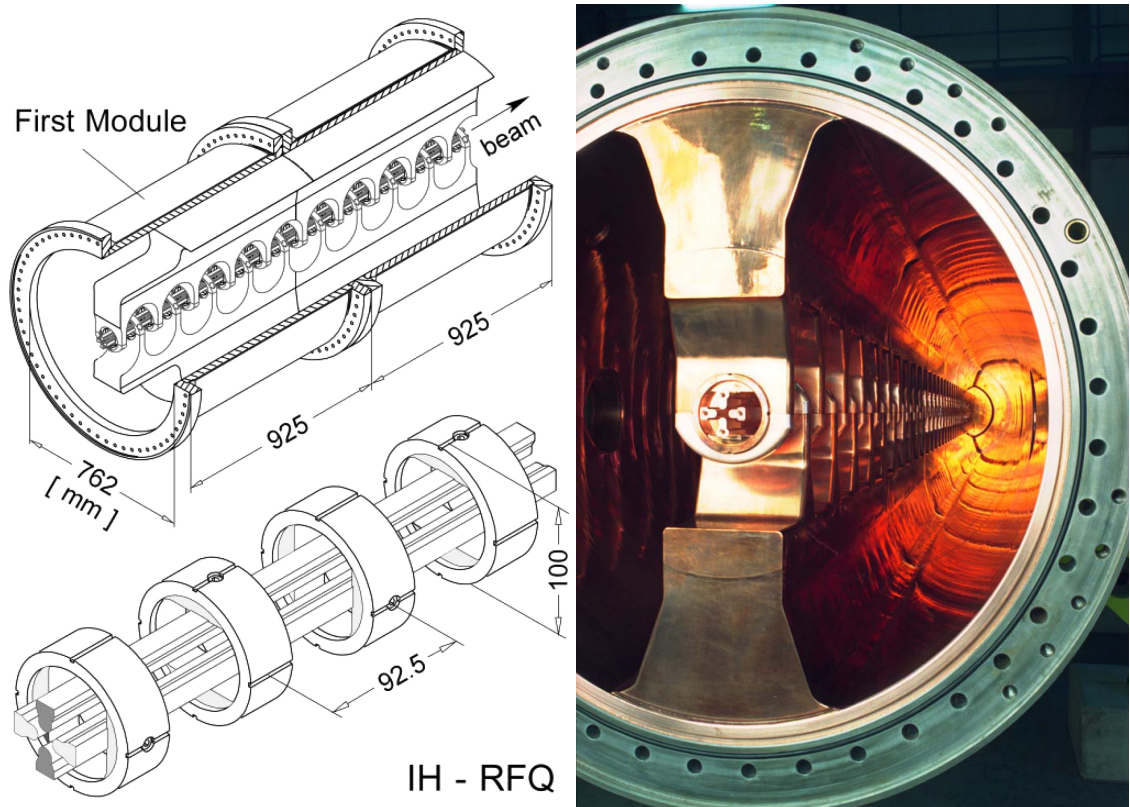
Figure 3.3: Schematic illustration and photo of the 36 MHz IH-RFQ with a total length of 9.2 m at the GSI High-Current Injector Linac [Ratzinger et al., 1998] (left). It accelerates ions with a mass to charge ratio up to 65 from 2.2 to 120 keV/u. The RFQ is in operation since 1999. In the scope of the FAIR upgrade, an electrode upgrade for the HSI is envisaged, which can be performed relatively easy at that type of RFQ [Zhang et al., 2016, Baschke et al., 2016].

improving the shunt impedance. As distances between the carrier stems and electrode mountings can be kept very close, a cooling of the electrodes is not needed at low duty factors. The field-flatness as well as the coarse frequency can be tuned by varying the depth of the end windows (undercut length of the girders). That tuning method requires a constant capacity along the electrodes, which is achieved by individual tip radii and widths as well as corrections of the ring nose width. The frequency is fine-tuned via capacitive plungers. Besides the GSI HSI[5] IH-RFQ (s. fig. 3.3), which is in operation since 1999, the 101.28 MHz MAFF[6] IH-RFQ is a second structure of

---

[5]**H**och **S**trom **I**njektor / High Current Injector
[6]**M**unich **A**ccelerator for **F**ission **F**ragments

this type [Siebert, 2001, Pasini et al., 2004, Bechtold et al., 2006].

3.2.2 4-Vane
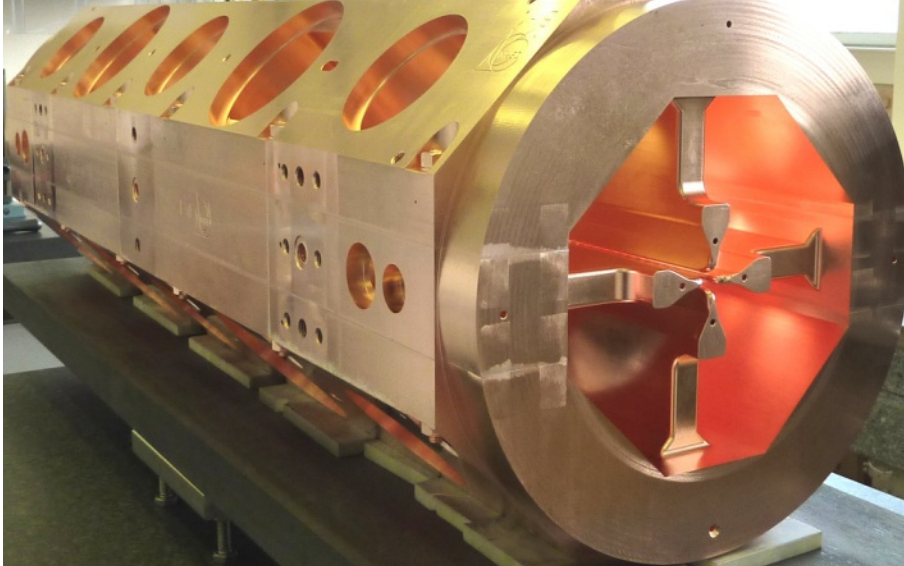
Figure 3.4: One module of the 4-Vane RFQ for Linac4 at CERN
with a length of 3 m (left). It operates at 352.2 MHz
accelerating protons from 45 keV to 3 MeV at a total
length of 3 m [Mathot et al., 2010].

Because of their four-fold geometry 4-Vane RFQ's apply the TE_{211}-Mode
(quadrupole mode) where the longitudinal magnetic field direction is reversed
in adjacent chambers and commutated in opposing chambers. They are suited for a
wide frequency range from about 80 MHz up to 750 MHz [Vretenar et al., 2014]. For
less than 80 MHz the sizes become very large and economically inefficient. The four
vanes are placed symmetrically in the center of the cavity (s. fig. 3.4). The electrodes
may be machined from four equal solid quadrants and afterwards welded together.
4-Vane RFQ's are cavity resonators. The magnetic energy is stored in the field all
over the whole hollow space within the cavity and currents mainly occur on the walls.
Accordingly, they have a high effectivity and low losses. The quadrants are usually
made from solid copper blocks and vacuum brazed to each other, by which current
transitions between different components do not suffer from losses in conductance.
The capacitance is determined by the four electrodes and the inductance by the

cross-sectional area of the quadrants. The reason why the structure reacts very sensitive to geometric deviations of the quadrants is the identical frequency of the quadrupole mode with dipole modes of that cavity. Thus, every quadrant has to be tuned properly. Frequency and field-flatness tuning can be done by several plungers along the beam axis, which also have to be arranged symmetrically in every quadrant [Rossi et al., 2012].

3.2.3 4-Rod
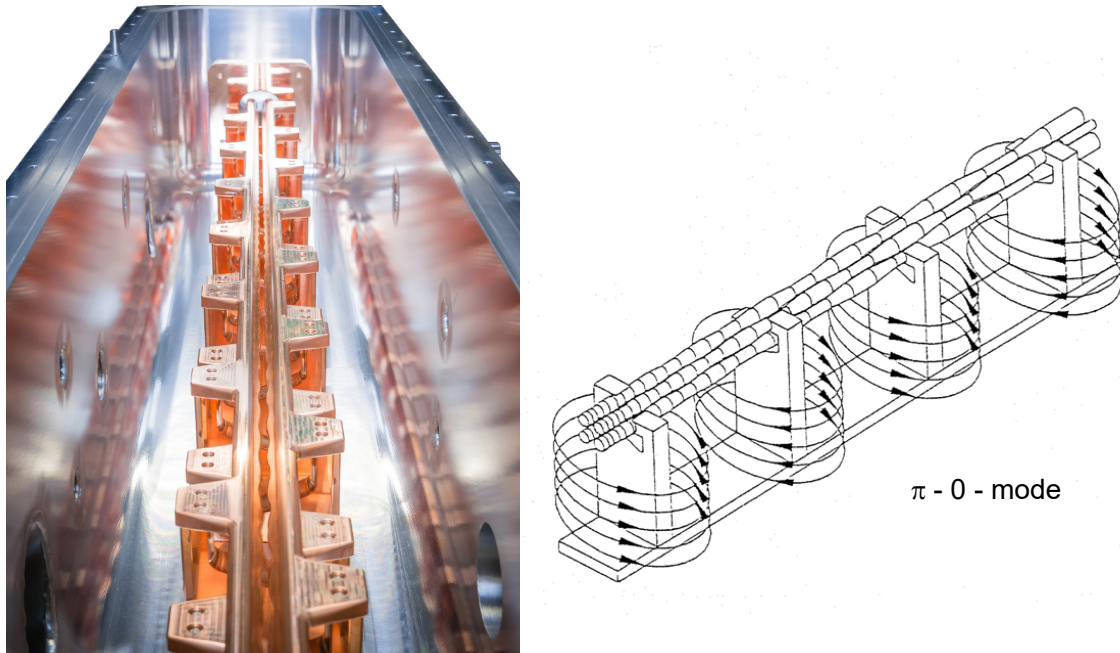
Figure 3.5: Left: Photo of the 175 MHz **Fra**nkfurt **N**eutronsource at the Stern-Gerlach-**Z**entrum (FRANZ) 4-Rod RFQ at IAP Frankfurt. Photo: Malte Schwarz, IAP. Right: Schematic drawing of a 4-Rod RFQ with magnetic field lines [Schmidt, 2014].

The 4-Rod RFQ, which has been mainly developed at IAP, Frankfurt [Schempp et al., 1985], consists as well of 4 electrodes generating the quadrupole field. Due to their small height relative to that of a 4-Vane RFQ the electrodes are called rods (or sometimes mini-vanes). Opposite pairs of rods are alternatingly screwed on stems, which, in turn, are mounted on a base plate (s. fig. 3.5). The stems, whose height is approximately $\lambda/4$, represent a chain of LC-resonators. Since it is a transmission-line resonator, the geometry of the tank does not influence the resonating structure

considerably. The main current flows along one rod pair and over the stems and base plate to the neighbored stems and rod pair. Beyond the resonating structure, the interior of the tank is almost field-free. The frequency is mainly determined by the geometry of the stems, such as width, height and distance. As a consequence, the 4-Rod RFQ does not show a quadrupole symmetry like a 4-Vane. Flanges can be arranged ad libitum. The resonating mode is called $\pi - 0 - \text{mode}$. The nomenclature of modes based on the phase shift between every structure cell is defined by:

$$\pi \cdot \frac{l}{N} \tag{3.1}$$

N is hereby the total number of cells and l the longitudinal number of the electric standing half-waves. The frequency shift among consecutive cells is π. With $l = 0$ in the operating mode, the electric field is constant along the rods. The Field-flatness can be adjusted by varying the height of the stems. Tuning plates are inserted between every two adjacent stems, which leads to a shortening of the current path and a relative decrease of the inductance, respectively. The frequency can be additionally tuned by plungers penetrating the cavity.

3.3 Characteristic Terms and Definitions for Resonators

In order to describe a cavity, there are several physical parameters determining the basic RF behavior. Accelerating structures like RFQ's as well as any other resonator are resonant systems. The energy is stored by electromagnetic alternating fields inside the cavity and the resonance is determined by the field distribution for a given mode. Due to the Ohmic resistance of the material, the resonant system is damped. The most important characteristic parameters are introduced in the following chapters.

3.3.1 Stored Energy of a Resonator

The energy of a resonator W is stored in the alternating, time and spatial dependent, electric field $\vec{E}$ and magnetic field $\vec{B}$:

$$W = \frac{1}{2} \int_V \left(\mu_0 \left| \vec{H}(x,y,z,t) \right|^2 + \varepsilon_0 \left| \vec{E}(x,y,z,t) \right|^2 \right) \mathrm{d}V \tag{3.2}$$

The electric and magnetic vector field can be divided into a time-dependent and a spatial part. The phase shift between both fields is 90°. Every quarter of the RF period, when the phase becomes $\varphi = \omega t = n \cdot \pi/2$, one of both fields is evolved to its maximum while the other field is zero. Therefore, the energy can be divided into two parts:

$$W = \frac{1}{2} \mu_0 \int_V \left| \vec{H}(x,y,z)_{max} \right|^2 \mathrm{d}V = \frac{1}{2} \varepsilon_0 \int_V \left| \vec{E}(x,y,z)_{max} \right|^2 \mathrm{d}V \tag{3.3}$$

The oscillating circuit of an RFQ can alternatively be described by its equivalent circuit diagram, which consists of an inductance L in series with an Ohmic resistance R and connected in parallel with a capacitance C. The voltages around the circuit are summed up equaling zero according to Kirchhoff's circuit laws:

$$\ddot{U} + \frac{R}{L}\dot{U} + \frac{1}{LC}U = 0 \tag{3.4}$$

The solution of this differential equation is a damped oscillation:

$$U(t) = U_0 \cdot \exp\left(-t/\tau + i\omega t\right) \tag{3.5}$$

The real part of the exponent describes the oscillation while the imaginary part contains the damping. The resonance angular eigenfrequency ω becomes:

$$\omega = \sqrt{\frac{1}{LC} - \frac{R^2}{4L^2}} \approx \sqrt{\frac{1}{LC}} \tag{3.6}$$

For typical accelerator cavities the Ohmic resistance R can be neglected compared to L. Therefore, the resonance can be calculated by the Thompson equation $\omega = 1/\sqrt{LC}$.

The time constant $\tau = \frac{2L}{R}$ equals the time needed for the voltage to decay to $1/e$ of its initial value U_0. The time constant for the decay of the stored energy E, which is proportional to the envelope of the voltage squared $E \sim U^2$, is $\tau = L/R$. A number, qualifying the slope and rate of the damped oscillation, is the quality factor, defined below.

3.3.2 The Quality Factor

As described in the previous section, the quality factor Q_0 can be defined by the number of oscillations in the time of one decay period τ and further expressed via the conductance and resistance:

$$Q_0 = \omega_0 \cdot \tau = \omega_0 \cdot \frac{L}{R} = \frac{1}{\omega_0 C R} \tag{3.7}$$

The energy W, stored in the resonator, is being dissipated due to Ohmic losses of the current flow on the surfaces of the resonator. The unloaded quality factor is defined by the amount of power P, which is dissipated within one RF period T, in relation to the total stored energy W in the resonator, respectively the number of RF periods N until the stored energy has decayed to $1/e$ of its initial value W:

$$Q_0 = \omega_0 \cdot \frac{W}{P} = 2\pi \frac{W}{TP} = 2\pi N \tag{3.8}$$

As derived in the previous section, the power of an excited cavity decays exponentially in the time domain. The Fourier transformation from the time into the frequency domain of an exponentially decaying sinusoidal signal becomes the Lorentzian function (also known as the Cauchy-Lorentz distribution):

$$A(\omega) = A_0 \cdot \frac{1}{1 + Q_0^2 \frac{4(\omega - \omega_0)^2}{\omega_0^2}} \tag{3.9}$$

The function describes the frequency distribution of the resonance. A_0 is the height of the resonance peak and w_0 its angular frequency at the peak. The quality factor is now the quotient from ω_0 and the frequency width at FWHM[7]. This is called $3\,\text{dB}$-method. In the power spectra, $-3\,\text{dB}$ is the point of half the power. The Q-value can now be experimentally measured by the width of the resonance peak:

$$Q_0 = \frac{\omega_0}{\Delta\omega_{-3\,\text{dB}}} \tag{3.10}$$

In summary, the quality factor is higher for a narrow resonance peak giving low losses P. Typical Q-values are $10^3 - 10^5$ for normal conducting and $10^8 - 10^{11}$ for superconducting cavities. Because of the frequency dependent skin depth δ, explained in the next sub-chapter, the surface resistance R_S is proportional to $f^{1/2}$. Accordingly, $P \sim R_S \sim \delta^{-1}$ and the quality factor scales with $f^{-1/2}$.

3.3.3 Power Dissipation

The losses of a resonator P_C occur due to surface current densities given by the magnetic field $\left|\vec{H}\right|$. Thus, the magnetic field has to be integrated over the inner surface of the resonator to obtain the overall losses:

$$P_C = \frac{1}{2} R_S \iint_{\mathcal{F}} \left|\vec{H}_0\right|^2 \mathrm{d}A \tag{3.11}$$

R_S is the surface resistance of the normal conducting resonator. It depends on the inverse product of the electrical conductivity σ and thickness of the charge carrying layer δ:

$$R_S = \frac{1}{\sigma\delta} \tag{3.12}$$

Oxygen-free high conductivity phosphorous grade copper alloy (Cu-HCP[8]), which is state of the art for the construction of accelerators, has a conductivity of at least $57 \cdot 10^3 \, (\Omega\text{mm})^{-1}$ at room temperature. The high conductivity is contained

---

[7]**F**ull **W**idth **H**alf **M**aximum

[8]Material designation CW021A and former SE-Cu according to DIN-EN, for more details cf. [Deutsches Kupferinstitut, 2005]

by only adding a limited amount of phosphor for the deoxidation during the heat treatment (the remaining alloyed phosphor mass fraction is 0.002% to 0.007%). Cu-HCP is characterized by an excellent cold and warm formability and machinability. Furthermore, it is suitable for welding and brazing. All those properties make it the perfect choice for accelerators.

The surface layer within the material, which is significantly accountable for the transportation of charges and the current flow, is defined by the skin depth δ in the presence of RF or alternating currents. In comparison, direct currents flow through the entire volume of a conductor by charge carriers. In the case of alternating currents, the change of the magnetic fields, generated by the currents, oppose electric fields. The induced counter-electromotive forces reduce the current density with the depth of the conductor. As a result, the electrons are pushed towards the surface. The current density j in metallic materials decays in dependence of the material depth y and is given by [Jackson, 1975]:

$$j(y) = j_{surface} \cdot \exp^{-y/\delta} \cos\left(y/\delta\right) \tag{3.13}$$

In the case of homogenous currents, the skin depth δ specifies the depth in which the current density has reduced to $1/e$ of its value on the surface:

$$\delta = \sqrt{\frac{2\rho}{\omega\mu_0\mu_r}} = \sqrt{\frac{1}{\sigma\pi f\mu_0\mu_r}} \tag{3.14}$$

The magnetic permeability of vacuum is $\mu_0 = 4\pi10^{-7}$, while μ_r is the relative permeability for the used material. In case of copper, μ_r can be neglected ($\mu_{r,Cu} = 0,9999936$). In conclusion the surface resistance is proportional to $f^{1/2}$ and $\sigma^{-1/2}$:

$$R_S = \sqrt{\frac{\pi\mu_0\mu_r f}{\sigma}} \tag{3.15}$$

3.3.4 Shunt Impedance

The shunt impedance R_p is the preferred unit of measurement for the efficiency of a cavity. It is a direct reference for the amount of the field, which can be used

for accelerating, compared to the losses. The reference for the accelerating field is indicated by the potential difference of the electrodes U and the shunt impedance is given by the squared voltage amplitude divided by the losses P of the cavity:

$$R_p = \frac{U^2}{P} \tag{3.16}$$

With the definition of the quality factor (eq. 3.7) and the energy stored in the cavity $W = \frac{1}{2}CU^2$, the shunt impedance yields:

$$R_p = \frac{U_{max}^2 \cdot Q}{\omega_0 W} = \frac{2Q}{\omega_0 C} = 2Q\sqrt{\frac{L}{C}} \tag{3.17}$$

The capacitance increases with the length of the electrodes (cf. eq. 4.16). To compare RFQ's differing in their length it is useful to define an effective shunt impedance R_{eff}, which is the shunt impedance R_p multiplied by the length l of the electrodes:

$$R_{eff} = R_p \cdot l = \frac{U^2}{P} \cdot l = \frac{U^2 \cdot Q_0}{\omega \cdot W} \cdot l \tag{3.18}$$

Respectively, the power loss for an RFQ with length l is then given by:

$$P = \frac{U^2}{R_{eff}} \cdot l \tag{3.19}$$

3.4 Beam Dynamics of RFQ's

As anticipated in the introduction, the purposes of RFQ's are to bunch, to accelerate and to focus the particle beam. Kapchinskiy and Tepliakov have already proposed in their first publication the principles of RFQ's [Kapchinsky and Teplyakov, 1970], on how to modify the shape of the electrodes in order to obtain an appropriate electric field, which can be used for acceleration and focusing. Fig. 3.6 demonstrates the most common design of sinusoidally shaped electrodes. The minimum distance to the beam axis is called aperture a while the maximum distance is the modulation parameter m multiplied with the aperture. The unit cell length L, which is the
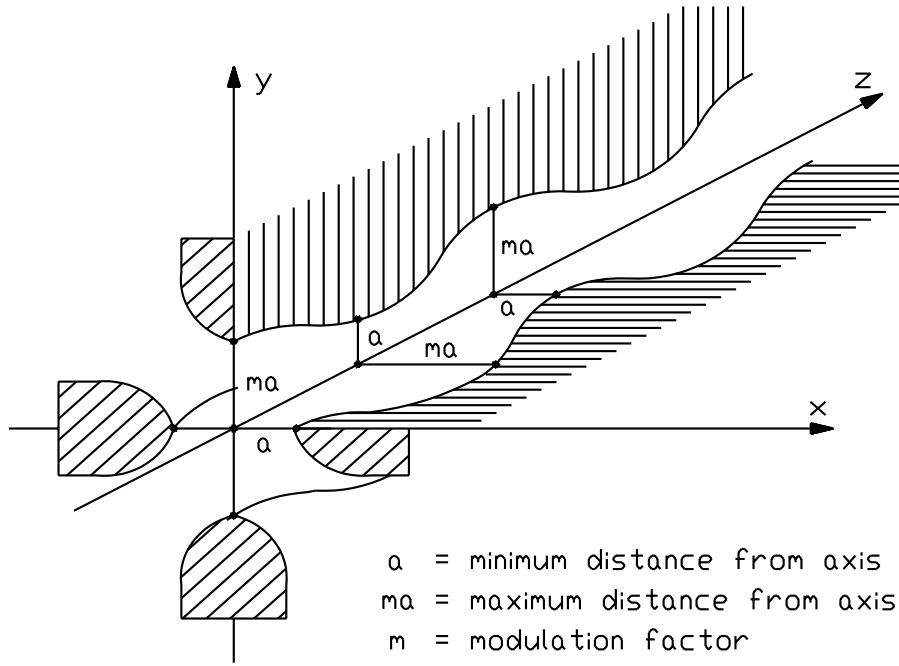
Figure 3.6: Schematic depiction of the electrodes; adapted from [Lombardi, 2005].

longitudinal distance from the minimum aperture a to the maximum aperture $m \cdot a$, depends on the particle velocity $\beta = v/c$ and the frequency f of the RF:

$$L = v \cdot T/2 = \beta \frac{c}{2f} = \frac{\beta \lambda}{2} \tag{3.20}$$

A voltage of $U(t) = \pm U_0/2 \cos(\omega t)$ is applied to the electrodes. In cylindrical coordinates the scalar potential can be expressed as [Wangler, 2008]

$$U(r, \Theta, z, t) = U(r, \Theta, z) \sin(\omega t + \varphi) \tag{3.21}$$

The phase of the potential $U(r,\Theta,z)$ is denoted by φ. The potential is obtained by the solution of Laplace's equation for electrostatics in absence of charges:

$$\Delta U(r, \Theta, z) = \frac{1}{r} \frac{\partial}{\partial r} \left(r \frac{\partial U}{\partial r} \right) + \frac{1}{r^2} \frac{\partial^2 U}{\partial \Theta^2} + \frac{\partial^2 U}{\partial z^2} = 0 \tag{3.22}$$

By separating the variables, the solution is the general potential function:

$$U(r, \Theta, z) = \sum_{s=0}^{\infty} A_s r^{2(2s+1)} \cos\left(2(2s+1)\Theta\right) + \sum_{n=1}^{\infty} \sum_{s=0}^{\infty} A_{ns} I_{2s}(knr) \cos\left(2s\Theta\right) \sin\left(knz\right)$$
(3.23)

To obtain an analytical model, one can introduce a simplified model reducing the infinite number of terms in eq. 3.23. Generally, the solution gets more accurate by including higher order terms. One approach would be to select only the lowest-order terms, which was done by M. Kapchinsky and V. Tepliakov. The two-term potential makes use of the quadrupole term ($s = 0$ in the first sum of eq. 3.23) and the monopole term ($n = 1$ and $s = 0$ in the second sum of eq. 3.23:

$$U(r, \Theta, z) = A_0 r^2 \cos\left(2\Theta\right) + A_{10} I_0(kr) \sin\left(kz\right)$$
(3.24)

One RF period $k = 2\pi/l$ is defined by twice a unit cell $k = 2\pi/(\beta\lambda)$. I_0 is the modified Bessel function of the first kind, which can be approximated with two terms:

$$I_0(kr) = 1 + \frac{(kr)^2}{4}$$
(3.25)

A_0 and A_{10} are constants, defined by the electrode geometry. As shown in fig. 3.6 for $z = 0$, the horizontal electrodes ($\Theta = 0$) have no modulation ($m = 1$), i.e. $r = a$, resulting in the relation:

$$U(r, \Theta = 0, z = 0) = U_0/2 = A_0 a^2 + A_{10} I_0(ka)$$
(3.26)

For the vertical electrodes, the vane displacement is $r = ma$:

$$U(r, \Theta = \pi/2, z = 0) = -U_0/2 = A_0 a^2 + A_{10} I_0(ka)$$
(3.27)

From both eqs. 3.26 and 3.27 the geometry constants A_0 and A_{10} yield

$$A_0 = \frac{U_0}{2a^2} \cdot \frac{I_0(ka) + I_0(kma)}{m^2 I_0(ka) + I_0(kma)} := \frac{U_0}{2a^2} X$$
(3.28)

and

$$A_{10} = \frac{U_0}{2} \cdot \frac{m^2 - 1}{m^2 I_0(ka) + I_0(kma)} := \frac{U_0}{2} A \qquad (3.29)$$

The time dependent potential is completely determined:

$$U(r, \Theta, z, t) = \frac{U_0}{2} \cdot \left[X \left[\frac{r}{a} \right]^2 \cos(2\Theta) + A I_0(kr) \cos(kz) \right] \cdot \sin(\omega t + \phi) \qquad (3.30)$$

The corresponding electric fields are calculated via the gradient of the potential $\vec{E} = \vec{\Delta} U$. In Cartesian coordinates the electric field yields:

$$E_x = -\frac{X U_0}{a^2} x - \frac{k A U_0}{2} I_1(kr) \frac{x}{r} \cos(kz) \qquad (3.31)$$

$$E_y = \frac{X U_0}{a^2} y - \frac{k A U_0}{2} I_1(kr) \frac{y}{r} \cos(kz) \qquad (3.32)$$

$$E_z = \frac{k A U_0}{2} I_0(kr) \sin(kz) \qquad (3.33)$$

The corresponding time dependent field has to be multiplied by $\sin(\omega t + \theta)$. E_z is the field corresponding to an acceleration of the particles. For a present modulation only, i.e. $m > 1$, A and E_z become larger than zero, which means the particles are accelerated. For $m = 1$, the RFQ can be seen as a quadrupole focusing channel. The x and y component provide a focusing and defocusing on the beam. The total energy gain per RF cell ΔW is obtained by the integration over the length of one cell $l = \lambda\beta$:

$$\Delta W = q \int_0^l E_z(r, z, \varphi) \mathrm{d}z = \frac{q k A U_0 I_0(kr)}{2} \int_0^{\lambda\beta/2} \sin(kz) \sin(\omega t + \varphi) \mathrm{d}z \qquad (3.34)$$

Assuming, that the energy gain per gap is small compared to the total energy, the velocity β is approximated as constant within one gap. Accordingly, the argument of

the sine becomes $\omega t \approx \omega z/v = 2\pi f \frac{z}{\beta c} = \frac{2\pi}{\beta\lambda}$.

$$\Delta W = \frac{qkAU_0I_0(kr)}{2} \int\limits_0^{\lambda\beta/2} \sin\frac{2\pi}{\beta\lambda} \sin\left(\frac{2\pi}{\beta\lambda} + \varphi\right) \mathrm{d}z \qquad (3.35)$$

The phase φ can be separated by the angle sum identity $\sin(x+y) = \sin x \cos y + \cos x \sin y$:

$$\Delta W = \frac{q\pi AU_0I_0(kr)}{\beta\lambda} \cos(\varphi) \int\limits_0^{\lambda\beta/2} \sin\frac{2\pi}{\beta\lambda}\left(\sin\frac{2\pi}{\beta\lambda} + \cos\frac{2\pi}{\beta\lambda}\tan\varphi\right)\mathrm{d}z \qquad (3.36)$$

The integral over the cosine, which is a symmetric function, gets zero and can be neglected. With the solution of the integration, the transient time factor yields $\pi/4$:

$$\Delta W = \frac{q\pi AU_0I_0(kr)}{\beta\lambda} \cos(\varphi) \int\limits_0^{\lambda\beta/2} \sin^2\left(\frac{2\pi}{\beta\lambda}\right)\mathrm{d}z = \frac{q\pi AU_0I_0(kr)}{4}\cos(\varphi) \qquad (3.37)$$
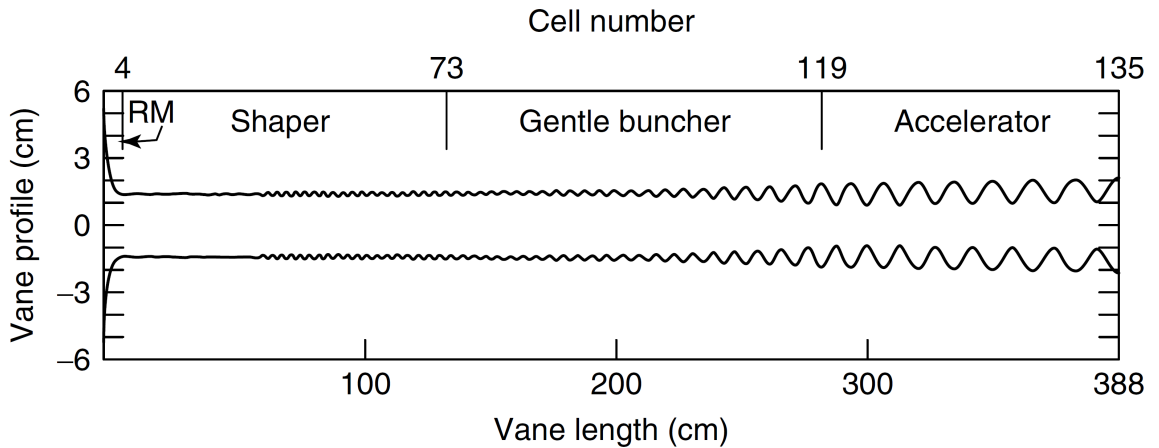
Figure 3.7: Longitudinal schematic section of the electrode modulation, according to the LANL four section procedure (FSP) [Wangler, 2008].

For a numerical computation of the electrode geometry the eight-term potential is much more accurate through the consideration of higher order multipole terms. The established beam dynamics code PARMTEQ-M[9] benefits by using the eight-term

---

[9]**P**hase **A**nd **R**adial **M**otion in **T**ransverse **E**lectric **Q**uadrupoles **M**ultipole

potential. The software was introduced in 1987 by K.R. Crandall and T.P.Wangler at LANL [Crandall and Wangler, 1987]. The program code divides the RFQ into four sections, which is called the LANL Four Section Procedure (FSP, s. fig. 3.7) [Crandall et al., 1979]:

- At the entrance of the electrodes, the **Radial-Matcher (RM)** adopts the incoming time-independent dc beam into the transverse time-dependent RF field of the RFQ. It usually has a length in the range of $2 - 5\,\beta\lambda$, starting with a large aperture. The spatial location and rotation of the input beam ellipse varies with time. The aperture decreases from $5 - 10\,a$ to a. The focusing strength B is increased linearly from zero to its nominal value [Tokuda and Yamada, 1981].

- In the **Shaper (SH)** section the particle beam is smoothly getting pre-bunched in the longitudinal direction, which prepares the bunch for an acceleration. To include the whole separatrix of the beam, the cell lengths obey the Wideroe condition, demanding cell lengths, which are equal to the distance the synchronous particle travels during half an RF period. The modulation and synchronous phase steadily and slowly - in order to maintain a high capture efficiency - begin to increase from $m = 1$ and $\phi_S = -90°$, which adds a longitudinal component to the purely transverse quadrupole field of the RM.

- The **Gentle-Buncher (GB)** initiates an adiabatic bunching of the prebunched beam. At the end of the GB the aperture reaches its minimum. The acceptable minimum aperture is defined by the beam current. The upper current limit of a design is given at this position due to very high space charge effects. B is further on kept constant. At the end of the GB bunching is completed and the final synchronous phase is reached.

- Most of the energy is gained in the last section, the **Accelerator Section (ACC)**. The aperture and synchronous phase are mostly held constant. The modulation and phase have now reached their maximum value, which are typically around two and between $-20°$ and $-40°$ for the phase.

Fig. 3.8 illustrates the typical progress of the electrode parameters along the beam axis (resp. denoted by the cell number) calculated by PARMTEQ. These calculations
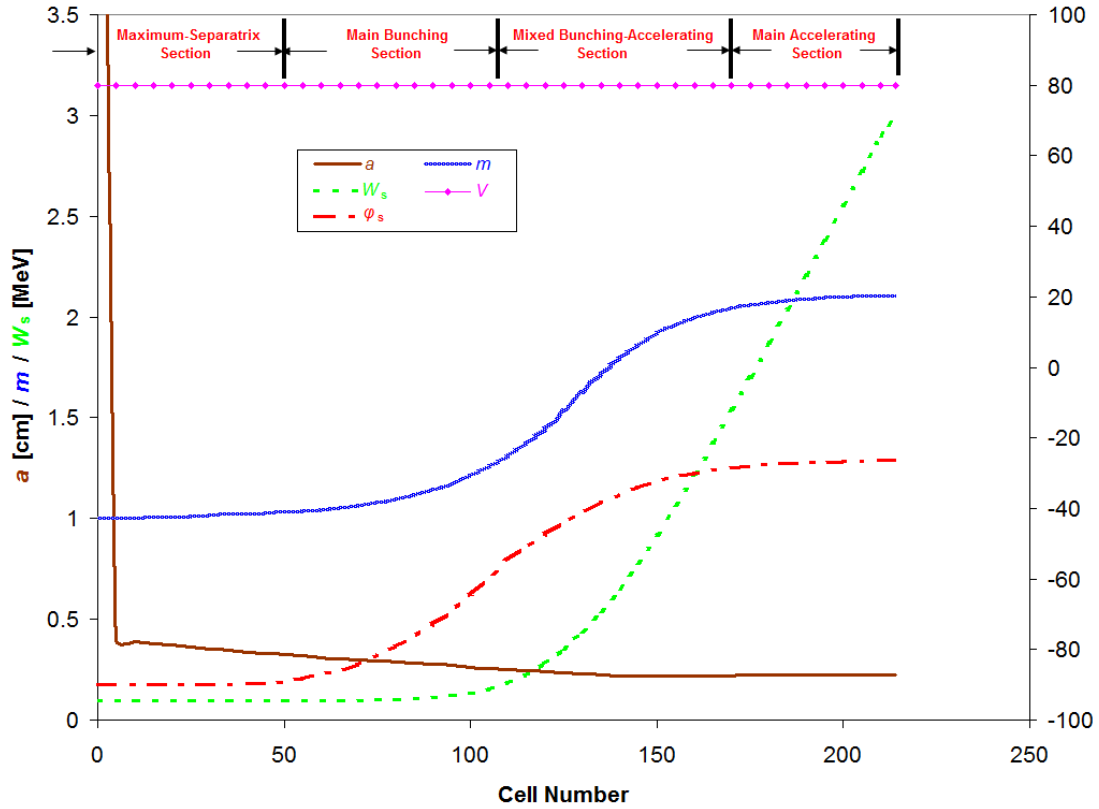
Figure 3.8: Design parameter of the electrodes used for the unmodulated Ladder RFQ. The so-called NSFP concept is a modification of the classical LANL-design procedure. It helps to shorten the RFQ length [Zhang and Schempp, 2009].

[Zhang and Schempp, 2009] served as a basis for the unmodulated prototype of the Ladder RFQ. The aperture of the prototype is kept constant at the mean aperture which is $3.42\,\mathrm{mm}$.

At the beginning of the radial matcher the aperture a is $> 35\,\mathrm{mm}$ and then rapidly decreases from $3.5\,\mathrm{mm}$ to its minimum value of $2.56\,\mathrm{mm}$ at the end of the gentle buncher. At that point, the modulation m noticeably starts increasing to its maximum value of 2 in the accelerating section. The particle energy W_S linearly increases to $3\,\mathrm{MeV}$. The synchronous phase φ_s at the entrance is $-90°$ to accept the full phase width of the beam. During the bunching progress it raises up to $-30°$ at which the beam can be efficiently accelerated and at the same time getting bunched longitudinally and focused transversely. The electrode voltage V is held at a constant level of $80\,\mathrm{kV}$.

The measurements with the unmodulated prototype, especially the results of the power test, as well as the simulations with the modulated electrode geometry gave an impact to further develop and improve the beam dynamics [Syha et al., 2017] at higher vane-vane voltages. The vane radius ρ should be kept constant to allow parametrized simulations including the simulation (s. chap. 8.1). To simplify the tuning process the ratio ρ/r_0 and the rod capacitance should be kept constant, too.

Chapter 4

The Ladder RFQ

> "Physics is like sex. Sure, it may
> give some practical results, but
> that's not why we do it."
>
> *Richard Feynman*

Before starting with the detailed design of the Ladder RFQ, this chapter outlines the historic development and actual state of "ladder-like"-structures. Following this, an analytical model to find the resonance frequency depending on the basic ladder geometry is deducted.
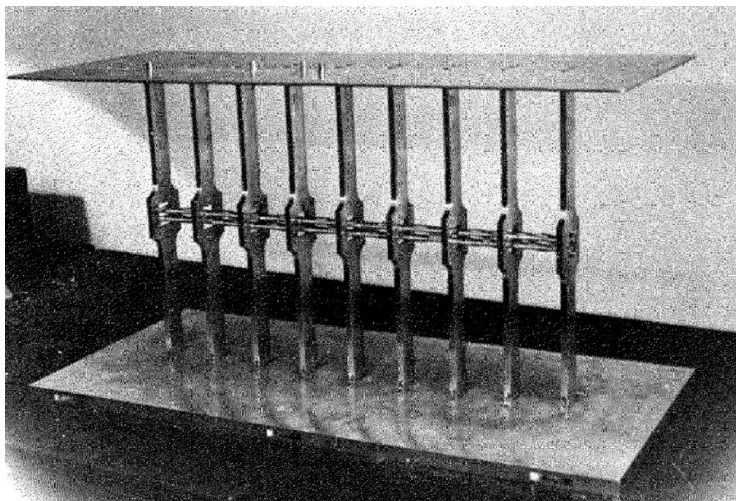
Figure 4.1: First proposal of a 4-Rod-like RFQ with a symmetric mounting of the rods [Fabris et al., 1987].

4.1 Historic Development

The first idea towards a Ladder RFQ was proposed by Fabris, Massarotti and Vretenar at INFN[1] in 1986 (s. fig. 4.1). Based on the 4-Rod RFQ from Frankfurt, they supplied equal current paths to the rods as well as a longitudinal symmetry by equally spacing the electrodes at a distance where the potential is uniform. With those changes, they were able to eliminate the following two drawbacks: Different mounting heights of the rods impose an asymmetry of the quadruple configuration, resulting in the creation of dipole components. Secondly, the potential difference between the electrodes along the beam axis was not constant. By maintaining equal current paths as well as a longitudinal symmetry by equally spaced electrodes, Fabris et al. eliminated those issues.
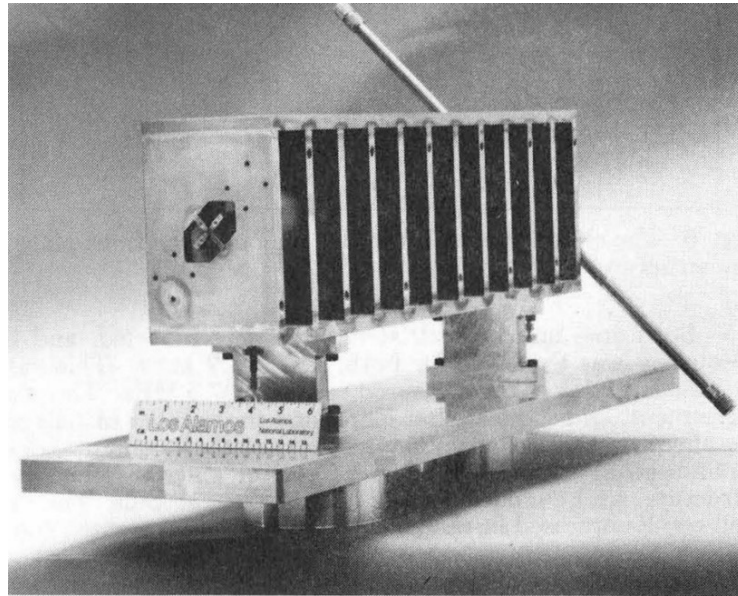
Figure 4.2: Second proposal of a 4-Rod like RFQ with a symmetric mounting of the rods [Browman et al., 1988].

The second approach towards a Ladder RFQ was adressed by Bowman et al. in the 1980s at LANL[2] (s. fig. 4.2). The layout was optimized for 389.9 MHz. The motivation for the development of such a design was to reduce the high capacitance

---

[1]**I**nstituto **N**azionale di **F**isica **N**ucleare
[2]**L**os **A**lamos **N**ational **L**aboratory

of a 4-Rod RFQ at high frequencies, as dimensions and distances between the plates get very small, which leads to high losses. Above all for an operation with cw, a reduction of the losses is very important.
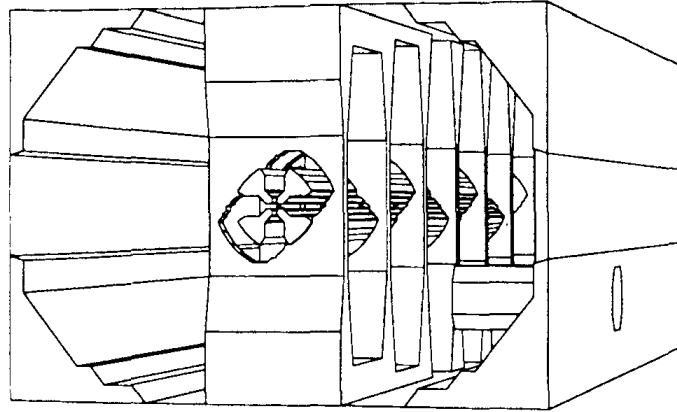
Figure 4.3: MAFIA plot of the Lead Ion RFQ at CERN's Linac3 [Bezzon et al., 1994].

The first RFQ in operation with a ladder structure was developed by Lombardi et al. supervised at LNL[3] for the CERN Lead Ion Linac3 [Bezzon et al., 1994, Lombardi et al., 1992, Cervellera et al., 1992] (s. fig. 4.3). It accelerates $80\,\mu$A of $^{208}Pb^{25+}$ from 2.5 to $250\,$keV/u at a repetition rate of $10\,$Hz and a at duty cycle of 0.4%. The main advantage of this structure is its rigidity and precisely adjustable positioning of the electrodes. The electrical field distribution is adjusted by the volume in the end cells and the frequency is tuned by two inductive plungers. The specifications were confirmed during the measurement and beam commissioning at CERN in 1994. The beam transmission is $90\,\%$.

To reach higher beam currents, A. Schempp et al. investigated a two beam RFQ by funneling without an increase of the emittance. The possible scope of applications might be spallation sources and heavy ion inertial fusion injectors, both demanding high beam currents [Schempp, 1996]. The successful feasibility was shown with a prototype running at $54\,$MHz [Zimmermann et al., 2004].

---

[3]**L**aboratori **N**azionali di **L**egnaro
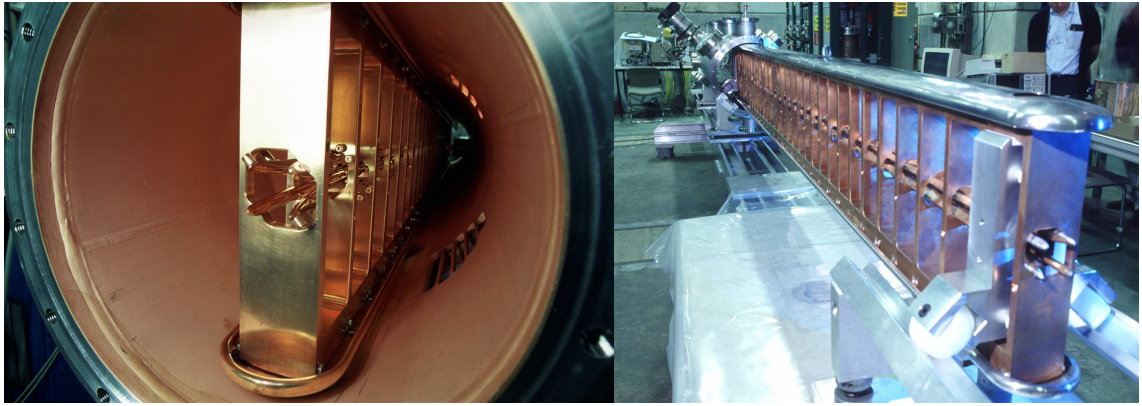
Figure 4.4: Antiproton Decelerator (AD) RFQ at CERN (Photos by L. Guiraud, CERN Document Server, CERN-AC-9911006; Courtesy of A. Lombardi).

At CERN, W. Pirkl and his team [Bylinsky et al., 2000, Lombardi et al., 2001] designed a 3.555 m decelerating RFQ (AD) for the CERN antiproton facility, which was installed in 2000 (s. fig. 4.4). The ladder structure with 34 RF cells is milled out of two, longitudinally connected, copper blocks. The electrodes are directly screwed to the ladder structure. The AD decelerates antiprotons from 5.33 MeV to a variable range of 10 to 120 keV, which is required by the ASACUSA[4] experiment. Operated at 202.5 MHz, it dissipates 1.1 MW of power. The quality factor is 5100, which is about 50% of the theoretical value.

The 36 MHz IH-RFQ, a novel combination of a IH-DTL and a 4-Rod RFQ, was successfully commissioned at the GSI High Current Linac [Ratzinger, 2001] (s. fig. 4.5). Together with two IH-DTL's it replaced the 34 MV prestripper linac, in 1998, to extend the capabilities of the UNILAC [Ratzinger, 1996]. The RFQ has validated and approved the efficient concept of mounting and aligning the electrodes by copper rings. The IH-RFQ accepts ions up to $A/q = 60$ with a beam current of $0.25 \, \text{mA} \cdot A/q$. The operation started in 1999 with a transmission of $> 90\%$ at low currents and with an energy profile from 2.4 keV/u up to 120 keV/u. The adjustment of the field was realized by changing the thickness of the rings. This affects the capacitance of each cell and the field, respectively.

From 2010 onwards, another 104 MHz Ladder IH RFQ was built at the Institute of Heavy Ion Physics (IHIP) of Peking University (PKU) for an RFQ based ^{14}C

---

[4]**A**tomic **S**pectroscopy **A**nd **C**ollisions **U**sing **S**low **A**ntiprotons
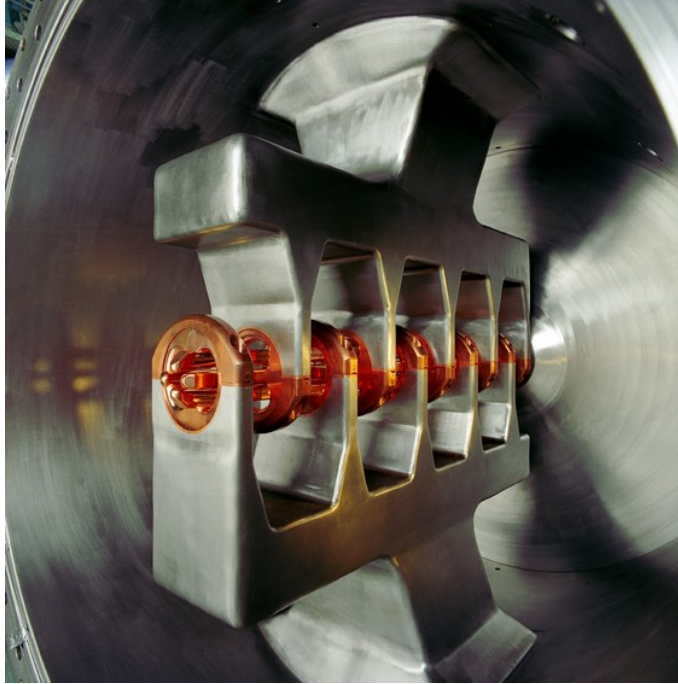
Figure 4.5: View into the 11-Cell Super Lens of the
IH-RFQ before it was copper plated
(Courtesy of U. Ratzinger).

Accelerator **M**ass **S**pectrometry (AMS) [Nie et al., 2014, Lu et al., 2011, Nie et al., 2010a, Nie et al., 2010b]. The 1.1 m RFQ accelerated light ions with an A/q up to 14 from 2.9 keV/u to 35.7 keV/u. Depending on the ion species the electrode voltage is varied between 17.1 kV and 60 kV. The design is very similar to the model of Browman. The electrodes are directly attached to the stems, which are made of copper and water cooled by embedded pipes.

4.2 Analytical Model and Determination of the Basic Parameters

The purpose of the analytical model is to be able to estimate the geometric parameters of the Ladder RFQ for a certain frequency. The Ladder RFQ is a chain of coupled oscillators, composed of *LC*-circuits and connected in parallel. As a first step, the equations for the inductivities and capacities in dependence of the geometry will be derived. Subsequently, the eigenfrequency of coupled oscillators will be calculated.
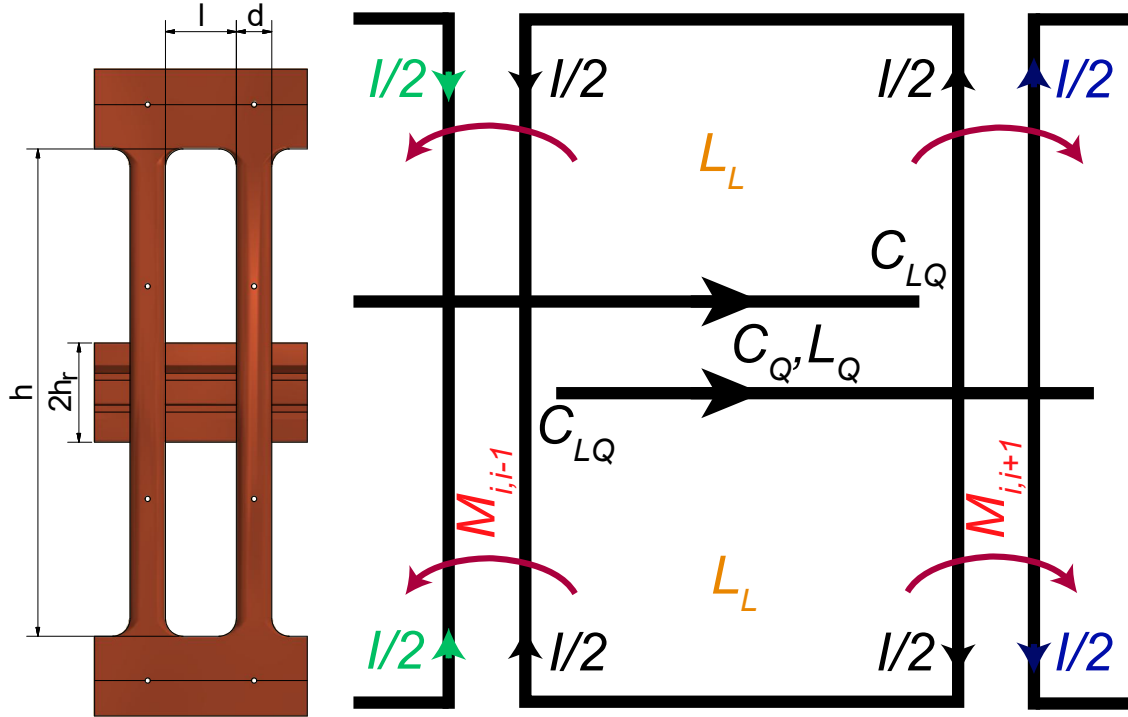
Figure 4.6: Geometric labeling (left) and current flow I (right) of the ladder-electrode structure; adapted from [Ratzinger, 2013]. The magnetic field direction generated by the currents is outlined in red. The main parameters of the ladder structure are its height h, stem distance l and stem thickness d. The length of one RF-cell is $l + d$. The inductance can be separated into the inductance from the stems L_L and from the electrodes L_Q. The capacitance is composed of the capacitance between adjacent electrodes C_Q and the electrodes and the rings C_{LQ}.

The notation of the individual geometrical parameters of the Ladder RFQ is shown in fig. 4.6. The clear distance between the ladder spokes, which is equal to the length of a ladder cell is denoted by l , its height by h and thickness by d. In addition, the height h of the ladder spokes is equivalent to the clear distance between the side rails of the ladder structure. The width of the ladder structure is b. The distance from the beam axis to the backside of the electrodes is labeled as h_r. Further geometric details and figures of the mechanical construction are explicitly described in chapter 6.

Every spoke of the ladder structure contributes with half of its current to the

magnetic field through one ladder cell (s. fig. 4.6). The corresponding inductance of the ladder structure is called L_L. It is calculated by the inductance of two strip lines with a length of $h/2 - 2h_r$, operated in parallel. The magnetic energy $W_{m,cell}$ within the ladder cell on one side of the electrodes is given by:

$$W_{m,cell} = \frac{1}{2}\mu_0 \cdot \iiint_V \vec{H}^2(x,y,z)\mathrm{d}V \tag{4.1}$$

Assuming that the magnetic field (which is verified by the simulations) is constant the magnetic energy yields:

$$W_{m,cell} = \frac{1}{4}\mu_0 \cdot H_0^2 \cdot b \cdot (l - 2h_r) \cdot h \tag{4.2}$$

Alternatively, the magnetic field can be denoted by the inductance L_L and the current flow I_0 through both ladder spokes bounding the ladder cell.

$$W_{m,cell} = L_L \cdot (I_0)^2 \tag{4.3}$$

From Ampère's law, the current I_0 is given by the magnetic flow around the spoke with a circumference U, width b, thickness d and a curvature with a radius of $d/2$:

$$\oint_C \vec{H}\mathrm{d}l = I_0 \quad \Rightarrow \quad I_0 = H_0 \cdot U = H_0 \cdot (2b - 4 \cdot d/2 + \pi \cdot d) \tag{4.4}$$

Combining equations 4.2-4.4 and regarding twice the magnetic energy for each cell on both sides of the electrodes yields the inductance L_L of the ladder cell:

$$L_L = \mu_0 \cdot \frac{l \cdot (h - 2h_r) \cdot b}{4\left(b_{eff} + (\pi - 2) \cdot d\right)^2} \tag{4.5}$$

The effective width b_{eff} of the spokes can be considered as the outer ring diameter (100 mm) plus a fraction of the difference to the actual width b_{real} as the current flow is not constantly spread over the whole width of the spokes. Thus, the effective current conducting width b_{eff} increases more slowly than the actual width and has to be corrected by a reduction factor β examined by the simulations. As a consequence,

the effective width is substituted by:

$$b_{eff} \rightarrow r_{ring} + (b_{real} - r_{ring})/\beta \qquad (4.6)$$

The adaption of the LRC model to the simulations revealed a reduction factor of $\beta = 1.5$.

The current flow of the electrodes can be considered as a linear conductor with radius h_r. With $0.5 < \varepsilon < 1.0$ being a fit parameter, the inductance L_Q of the electrodes is given by:

$$L_Q = \mu_0 \cdot \frac{l}{2\pi} \left(\ln \left(\frac{2l}{\varepsilon \cdot h_r} \right) - \frac{3}{4} \right) \cdot \eta \qquad (4.7)$$

where η represents a current reduction factor, which is the ratio between the capacitance C_Q of the electrodes and the ring-electrode capacitance C_{LQ}:

$$\eta = \frac{C_Q}{C_{LQ} + C_Q} \qquad (4.8)$$

The effective inductance L_{eff} is the sum of each inductance L_L and L_Q:

$$L_{eff} = L_L + L_Q \qquad (4.9)$$

For the derivation of the rod-rod capacitance, the electrodes (s. fig. 4.7) are divided into four parts: The electrode tip and two body extensions with a transition in between. The vane tip with radius ρ has a distance of r_0 to the beam axis. The tip is carried by the first body extension with height h_1. The base body with a height h_2 has a broadened width V due to a greater mechanical rigidity. The broadened base allows a neat screw joint to the mounting of the electrodes in a distance of h_r to the beam axis. Moreover, it stabilizes the mechanical solidity against vibrations. The transition zone between both extension bodies reduces the width to twice the tip radius. The capacitance per unit length C'_{Q1} between the vane tip and the first
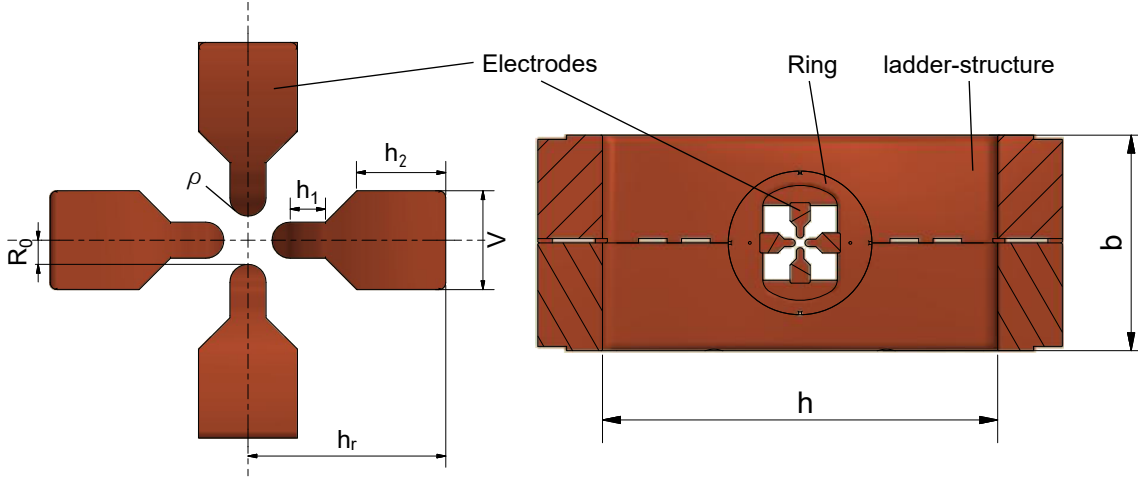
Figure 4.7: Transversal cross section and geometric parameters of the electrodes (left) and of the ladder structure (right) with its width b and height h. Further structural details can be seen in chap. 6.

extension body (h_1) was experimentally defined by Ben-Zvi [Ben-Zvi et al., 1990]:

$$C'_{Q,1}[\text{pF/m}] = \frac{39.37}{\cosh\left(1 + R_0/\rho\right)/\sqrt{2}} + \frac{31.05}{R_0/\rho - 0.414} + 25.28 \cdot \ln\left(1 + \frac{l_1 + l_2}{R_0 + \rho}\right) \quad (4.10)$$

Because of the electrode geometry, an additional term for the capacitance between the opposing faces A of the transition zone in a distance d between the base body and the body carrying the electrode tip has to be added. The capacitance per unit length is calculated by:

$$C_{Q,2} = \varepsilon_0 \cdot \frac{A}{d} = \varepsilon_0 \cdot \frac{(l + d)\sqrt{2(V/2 - \rho)^2}}{\sqrt{2(R_0 + h_1)^2}} = \varepsilon_0(l + d) \cdot \frac{V/2 - \rho}{R_0 + h_1} \quad (4.11)$$

In units of pF/m $C'_{Q,2}$ yields:

$$C'_{Q,2}[\text{pF/m}] = 8.85 \cdot \frac{V/2 - \rho}{R_0 + h_1} \quad (4.12)$$

The capacitance of the orthogonal faces of the electrode bases C_{base} with height h_2 can be considered as the sum of infinitesimal plate capacitors with an area $dA(x)$ in

a distance $d(x)$ integrated over the area:

$$\mathrm{d}C_{base} = \varepsilon_0 \frac{\mathrm{d}A(x)}{\mathrm{d}(x)} \tag{4.13}$$

The evaluation of the integration leads to C_{base}.

$$C_{base} = \frac{\varepsilon_0}{\sqrt{2}}(l+d) \int_0^{h_2} \frac{1}{h_r - h_2 - V/2 + x} \mathrm{d}x = \frac{\varepsilon_0}{\sqrt{2}}(l+d) \cdot \log\left(\frac{h_r - V/2}{h_r - h_2 - V/2}\right) \tag{4.14}$$

$$C'_{base}[\mathrm{pF/m}] = 6.28 \cdot \log\left(\frac{h_r - V/2}{h_r - h_2 - V/2}\right) \tag{4.15}$$

The total electrode capacitance C_Q is the sum of the capacities per unit length $C_{Q,1}$, $C_{Q,2}$ and C_{base} multiplied by the length of one cell $l + d$:

$$C_Q[\mathrm{pF}] = (l+d)\left[\frac{39.37}{\cosh(1 + R_0/\rho)/\sqrt{2}} + \frac{31.05}{R_0/\rho - 0.414} + \right.$$

$$+ 25.28 \cdot \ln\left(1 + \frac{l_1 + l_2}{R_0 + \rho}\right) + \tag{4.16}$$

$$\left. + 8.85 \cdot \frac{V/2 - \rho}{R_0 + h_1}\right]$$

The ring-electrode capacitance C_{LQ} is calculated via the current reduction factor η:

$$C_{LQ} = \frac{1 - \eta}{\eta} \cdot C_Q \tag{4.17}$$

The effective capacitance C_{eff} is given by the sum of the individual capacitance between the electrodes itself C_Q and between the electrodes and the ring C_{LQ}:

$$C_{eff} = C_Q + C_{LQ} \tag{4.18}$$

By Thompson's equation, the resonance angular frequency yields:

$$\omega_0 = \frac{1}{\sqrt{L_{eff}C_{eff}}} \tag{4.19}$$
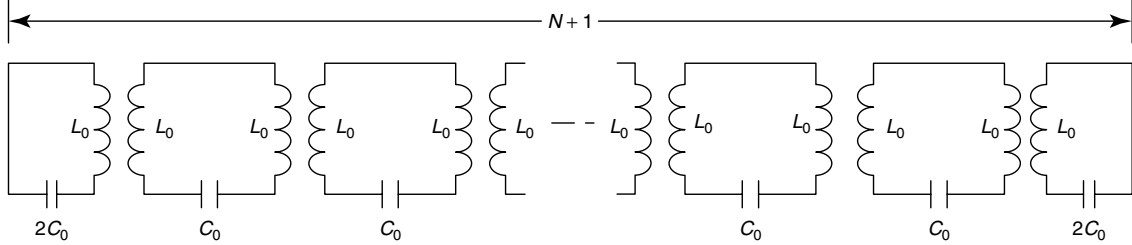
Figure 4.8: $N+1$ coupled oscillators [Wangler, 2008]. The first cell $n = 1$ and last cell $n = N+1$ are considered as "half cells". By having only one adjacent oscillator, they contain half the inductance of mid-cells $1 > n < N+1$, but have double the capacitance to achieve the same resonant frequency ω_0.

To find the eigenfrequency of $N+1$ coupled oscillators (s. fig. 4.8) the circuit equations are obtained by the sum of each voltages around a single circuit n of the oscillator according to Kirchhoff's laws:

$$\left(-L_n\Omega^2 + \frac{1}{C_n}\right)I_n = kL_0\Omega^2\left(I_{n-1} + I_{n+1}\right) \tag{4.20}$$

After dividing the formula by $-L_n\Omega^2$ and introducing the normalized currents $x_{n,q} = I_n\sqrt{(2L_0)}\cos\frac{\pi q}{N}\exp(i\Omega_q t)$, the circuit equations yields a linear system of equations in matrix form, where the currents x_n are the eigenvectors and $\frac{1}{\Omega^2}$ their eigenvalue:

$$\left(1 - \frac{\omega_0^2}{\Omega^2}\right)x_{n,q} - k\frac{L_0}{L_n}\left(x_{q,n-1} + x_{q,n+1}\right) = 0 \tag{4.21}$$

respectively with the matrix operator M:

$$M \cdot x_{n,q} = \frac{1}{\Omega^2} \cdot x_{n,q} \tag{4.22}$$

As $\omega_0 = 1/\sqrt{2L_0C_0}$ is the eigenfrequency of an uncoupled cell, the $(N+1) \cdot (N+1)$

matrix operator M is found to be:

$$
M = \begin{pmatrix}
1/\omega_0^2 & k/\omega_0^2 & 0 & 0 & \cdots & 0 \\
k/2\omega_0^2 & 1/\omega_0^2 & k/2\omega_0^2 & 0 & \cdots & 0 \\
0 & \ddots & \ddots & \ddots & \ddots & 0 \\
0 & \cdots & 0 & k/2\omega_0^2 & 1/\omega_0^2 & k/2\omega_0^2 \\
0 & \cdots & 0 & 0 & k/\omega_0^2 & 1/\omega_0^2
\end{pmatrix}
\tag{4.23}
$$

The eigenfrequencies Ω_i of $N+1$ coupled oscillators can be described by the dispersion relation, which is the solution of the determinant:

$$
\Omega_q = \frac{\omega_0}{\sqrt{1 + k \cos\left(\pi q/N\right)}}
\tag{4.24}
$$

The coupling factor k characterizes the strength of the coupling between adjacent resonators N and $N + 1$. The argument of the cosine $\pi q/N$ represents the phase advance per oscillator n. It can be expressed as the quotient of the ladder and effective inductance $k = \frac{L_L}{2L_{eff}}$. With a constant current distribution along the cells, the zero mode resonance Ω_0 with $q = 0$ becomes:

$$
\Omega_0 = \frac{\omega_0}{\sqrt{1+k}} = \frac{1}{\sqrt{1+k}\sqrt{L_{eff}C_{eff}}}
\tag{4.25}
$$

Based on the calculation of the zero mode frequency, which is desired to be $325\,\mathrm{MHz}$, the geometric parameters can be determined. The formula is only valid for a coupling between directly adjacent cells, or if the coupling between cells N and $N \pm 2$ approaches zero. An ansatz for eigenvalues considering a coupling to the second neighbor cell can be found in [Yan et al., 2014].

The set of parameters can be divided into the ones which are predetermined by the beam dynamics and those which are defined down by the RF. The former parameters, which define the electrodes, are calculated by a beam dynamics code (PARMTEQ, cf. chap. 3.4) resulting in a mean aperture of $r_0 = 3.42\,\mathrm{mm}$ and a vane radius of $\rho = 2.56\,\mathrm{mm}$ [Zhang and Schempp, 2009]. Regarding to a maximization of the quality

Table 4.1: Results for the geometric parameters of the Ladder RFQ based on the theoretical model.

Ladder Parameters	Result [mm]
Cell Length l	40
Spoke Height h	265
Spoke Width b	150
Spoke Thickness d	20
Electrode Parameters	
Mean Aperture r_0	3.42
Radius ρ	2.56
Tip Height h_1	5.0
Base Height h_2	12.59
Base Width V	14
Mounting Height h_r	28.0

Table 4.2: Results of the theoretical model for the RF parameters. A complete list of physical parameters can be found in appendix A. The inductances and capacitances are related to one cell of the ladder structure.

Parameter	Value
ε	0.85
η	0.7
L_L	24.5 nH
L_Q	2.2 nH
L_{eff}	26.8 nH
C_Q	5.2 pF
C_{LQ}	0.92 pF
C_{eff}	6.12 pF
k	0.46
ω_0	2042 MHz
f	325 MHz

factor (s. eq. 3.7) as well as the shunt impedance, the capacitance should be kept as small as possible. At the same time the electrodes should be mechanically stable to withstand vibrations and thermal deformations. The final parameters, chosen according to that maxim, are shown in tab. 4.1. A graphical comparison between the simulation and LRC model is visualized in the next chapter. With the specified parameters of the beam dynamics and the electrodes, the values of the capacitances and inductances are completely determined by the LRC model (s. tab. 4.2). The

parameters found by theory serve as a rough basis for building a 3-dimensional model for the electrodynamical simulations. Based on the optimization of the detailed design in terms of the physical properties in the next chapter, the exact dimensions and geometric parameters are subject to the results of the simulations.

Chapter 5

Simulations and RF-Design of a Prototype Cavity

> "Acceleration is finite, I think
> according to some laws of physics."
>
> *Terry Riley*

Before the mechanical model of the RFQ can be designed and manufactured, the parameters, found by the theoretical model in the previous chapter, have to be verified in simulations regarding a correct behavior of the RF and further physical studies. First of all, the dimensions of the ladder structure will be adjusted to fit to the right frequency. The outer tank, which is a boundary of the electromagnetic field has to be defined. The first and last cell of the resonator are "half cells" comprising only half the inductance compared to cells in between (s. chap. 4.2). At the same time, the longitudinal electric field between the electrodes and the flanges at the entrance and exit of the beam has to be minimized. Therefore, the geometry of the end cells has to be adjusted appropriately to limit effects on the kinetic energy of the particles. Another important issue is the constancy of the voltage difference between the electrodes along the beam axis of the RFQ. Such a flat field distribution is substantial to fulfill the requirements of the beam dynamics. The next step is to investigate the size and position of the coupling loop. The coupling has to be sufficient in order to be able to deliver enough energy into the cavity, yet not too large to fit into the structure. During operation, the RFQ is exposed to temperature fluctuations, which result in a change of the dimensions and consequently the frequency. To

stabilize the frequency, movable frequency tuners as well as a cooling concept have to be designed and proven. The simulations are based on a parametrized model. In the last section of this chapter this model will be compared to an as-built CAD model considering details such as exact curvatures, blended or chamfered edges as well as screw holes. One has to mention that every physical study, being subject of the following simulations, is dependent on almost all geometric parameters. As a result of this circular reference all simulations may not be performed independently. Every change and result of a single investigation has to be verified in all other simulations. In the end, each amendment of the RFQ model has to be reviewed with respect to an optimization, or at least to no diminution, of the quality factor and shunt impedance, respectively.

All simulations are computed by the proprietary software CST Microwave Studio (MWS)[1]. CST MWS is a commercial software and simulation code, which can solve 3-dimensional electrodynamic fields for arbitrary volumes and bodies. Initially, the RFQ is built as a 3D model with parametrized geometrical sizes (s. fig. 5.1 at top). The model has to be as realistic as possible, to obtain most accurate results, yet not too complicated to gain merits from the parameters and minimize computation time. The parameters can be swept between different simulations quickly and automatically, in order to investigate the influence of geometrical modifications on the RF.

To be able to compute 3-dimensional fields, the model has to be converted into a meshed version, which is machine-readable (s. fig. 5.1 at bottom). The geometry is partitioned into cells, in which the partial differential Maxwell equations, taking the boundary conditions into account, are solved. CST offers two different types of meshes - the hexahedral and the tetrahedral mesh. The former divides the model into hexahedrons. The susceptibility to errors is very low for a hexahedral mesh, making it the preferred choice for CAD imported models. Nevertheless, an alignment to circular shapes requires very small cell sizes to accomplish a high precision, resulting in a higher computation time. Tetrahedrons have only four vertices and their sizes may vary. They therefore adapt better to circular structures compared to hexahedrons, which have eight vertices and are even. Disadvantages of the tetrahedral mesh are

---

[1]**C**omputer **S**imulation **T**echnology; for further information cf. www.cst.com
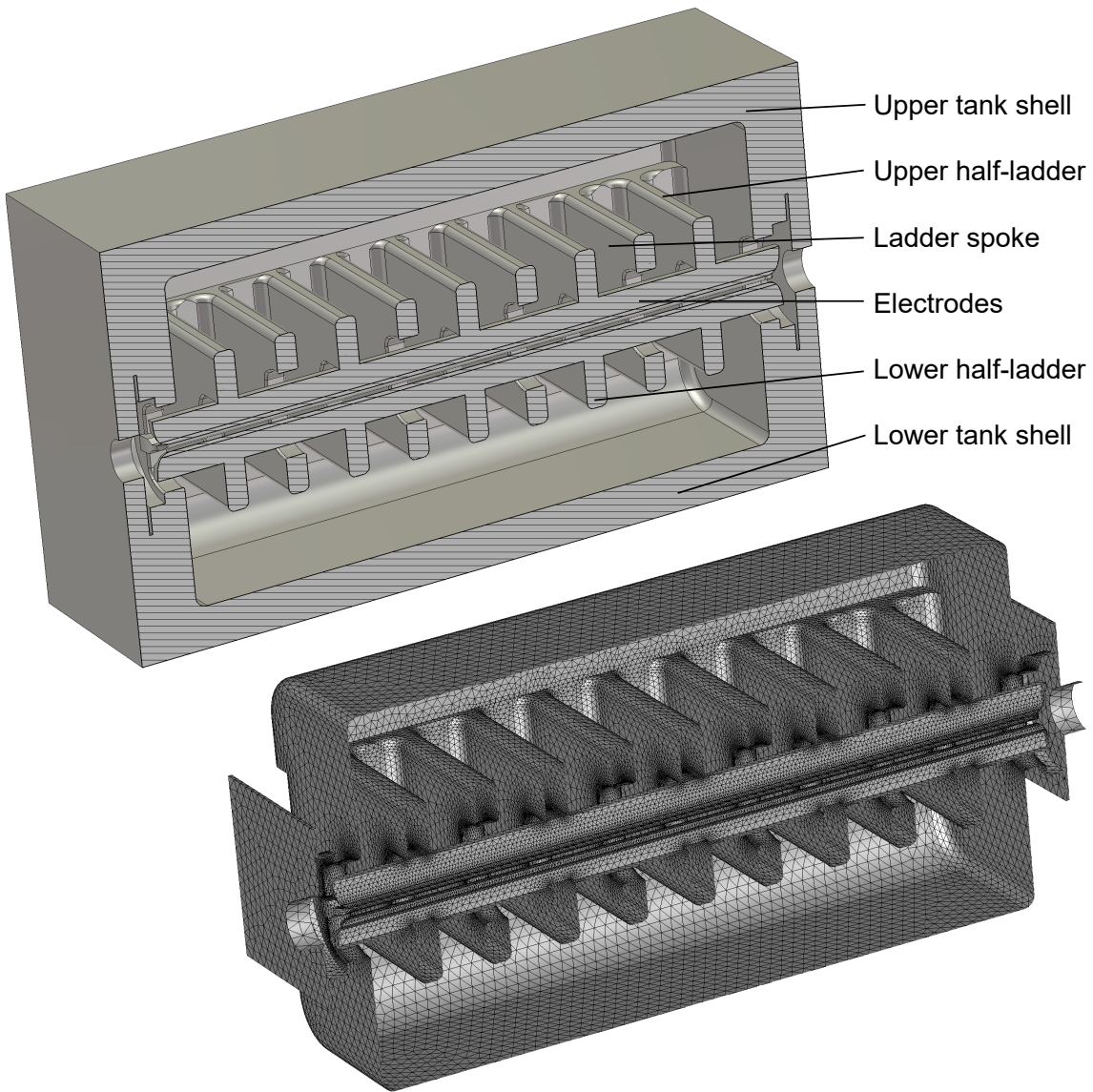
Figure 5.1: Sectional isometric view of the simplified and parametrized CST model (left) and its meshed version with tetrahedrons (right; the background volume meshing is hidden for a better perspective.). The beam axis is represented by the z-axis. The vertical y-axis points in the direction of the ladder width and the transversal x-axis to the ladder height. For details of the mechanical design, naming and assembly of each component please refer to chap. 6.

a longer processing time needed for meshing the model and a higher consumption of memory. If not stated otherwise, the average number of mesh cells used for all simulations in the scope of this work are between 2.5-3 million tetrahedrons, which

is the maximum that can be solved with 256 GB of internal memory in a reasonable time of 20 to 30 minutes by 20 logical state-of-the-art server processors. The used solver is the eigenmode solver. Its primary results are the electromagnetic field distributions, based on the solution of Maxwell's equations as well as eigenfrequencies of closed resonant structures[2]. Based on the Maxwell-Faraday equation and the field phasors[3] $\vec{E}(t) = \vec{E}_0 \cdot \exp\left(-\mathrm{i}\boldsymbol{\omega} t\right)$ and $\vec{B}(t) = \vec{B}_0 \cdot \exp\left(-\mathrm{i}\boldsymbol{\omega} t\right) = \boldsymbol{\mu} \vec{H}(t)$ the field equation becomes

$$\nabla \times \vec{E}(t) = -\frac{\partial \vec{B}(t)}{\partial t} = \mathrm{i}\boldsymbol{\omega}\boldsymbol{\mu}\vec{H}(t) \tag{5.1}$$

where $\boldsymbol{\omega}$ is the complex angular frequency and $\boldsymbol{\mu}$ the complex permeability. The reciprocal of the permeability is the complex reluctivity $\boldsymbol{\nu}$. Applying the curl on both sides yields:

$$\boldsymbol{\nu}\nabla \times \nabla \times \vec{E}(t) = \mathrm{i}\boldsymbol{\omega}\nabla \times \vec{H}(t) \tag{5.2}$$

By using Ampère's law, the equation becomes an eigenvalue problem, which can be solved numerically according to method of finite integration [Krietenstein, 1999].

$$\boldsymbol{\nu}\nabla \times \nabla \times \vec{E}(t) = \boldsymbol{\omega^2}\boldsymbol{\varepsilon}\vec{E}(t) \tag{5.3}$$

The discrete space will then be divided into a lattice in which the eigenvalue problem is solved by an algorithm called simultaneous iteration as the eigensolutions are determined simultaneously [Bauer, 1957, Rutishauser, 1969]. The quality factor can be expressed as the speed of the phase shift [CST, 2017] and therefore is obtained by the complex eigenfrequency:

$$\boldsymbol{\omega} = \omega + \mathrm{i}\frac{\omega}{2Q} \tag{5.4}$$

The quality factor for a certain eigenfrequency ω_0 is then calculated by the phase

---

[2]For more information on the details of the meshing calculus and simulation methods refer to the CST Studio help documentation.

[3]Complex variables are marked in bold.

steepness [Zinke and Brunswig, 1999]:

$$Q = \left(\omega_0 \left| \frac{\mathrm{d}\varphi}{\mathrm{d}\omega} \right| \right) \tag{5.5}$$

By default, the eigenmode solver of CST calculates with an energy of 1 J, stored in the cavity. In the case of the unmodulated Ladder RFQ, that leads to an electrode voltage of $U_{CST} = 140\,\mathrm{kV}$. As the design electrode voltage is $U_0 = 80\,\mathrm{kV}$ the scales of the following field, voltage and current simulations have to be divided by $U_{CST}/U_0 = 1.75$ and power spectra by $U_{CST}^2/U_0^2 = 3.06$.

5.1 Determining the Resonance Frequency
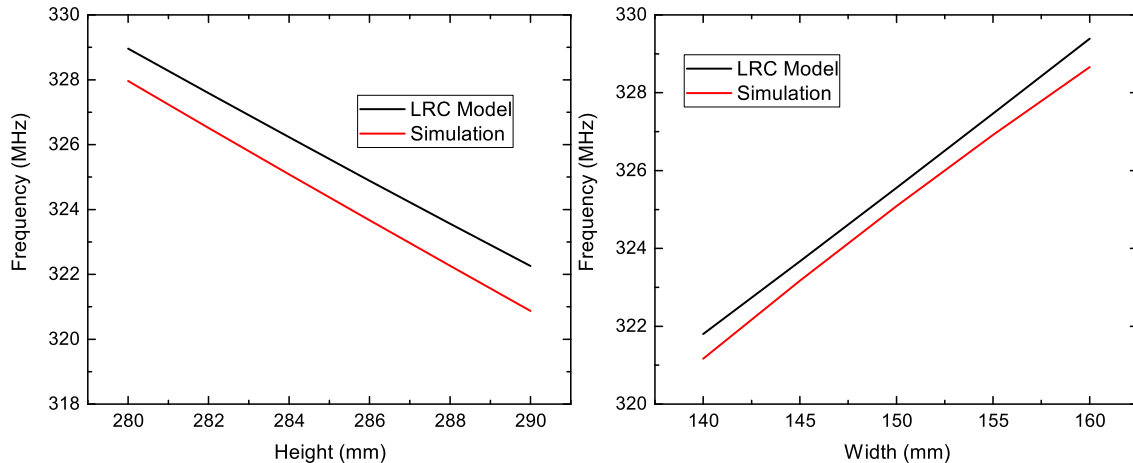
Figure 5.2: Dependence of the frequency from the height (left) and width (right) of the ladder structure. The data from simulations is colored in red and from LRC model (s. chap. 4.2) in black.

The frequency of the RFQ can be adjusted over a wide range from 200 to 400 MHz via the width and clear height of the ladder structure. The formula for the resonance frequency of the analytical model, derived in the previous chapter (s. eq. 4.25), is linearly proportional to the width and inversely proportional to the height. Increasing the width and height decreases, respectively increases the effective inductance. Fig. 5.2 illustrates the results of the simulations, compared to the calculated frequency according to the analytical model.

As expected from eq. 4.5, the inductance of the ladder increases with its height and decreases with its width. Accordingly, the frequency decreases with the height by an increment of $-700\,\text{kHz/mm}$ and increases with the width of the ladder structure by $380\,\text{kHz/mm}$. Both measures serve as a perfect adjustment option for the coarse frequency. The theory does not match the simulations perfectly, because the exact details of the mechanical layout, like the tank with its flanges, are not considered in the analytical model. Especially the layout of the end cells, i.e. the distance between the electrodes and both beam flanges, contributes to a change of the frequency. As the unmodulated Ladder RFQ prototype is designed with an arbitrary electrode length, this effect does not have to be considered. For the modulated Ladder RFQ, the corresponding simulations are shown in chap. 8.3. Based on the simulations, the width has been chosen to be $150\,\text{mm}$ and the height $285\,\text{mm}$. The final tuning to the operating frequency is performed by plungers (s. chap. 5.4).

5.2 Field Distribution

The probability for field emission and RF breakdowns in room temperature copper resonators accumulates with the surface field level. Consequently, the study of the electric fields within the resonator is important. The Kilpatrick criterion correlates the maximum recommended field level E_k implicitly with the frequency f:

$$f[MHz] = 1.64 \cdot E_k^2[MV/m] \cdot \text{e}^{-8.5/E_k[MV/m]} \tag{5.6}$$

This relation is the result of the experimental work by W. D. Kilpatrick in the 1950's [Kilpatrick, 1957] regarding limited pumping capabilities at that time. The ratio between the actual applied surface field E_S and the surface field E_k from the Kilpatrick criteria is expressed as the Kilpatrick factor, respectively bravery factor b. Studies have shown, that after successful RF conditioning on well-prepared surfaces the field level can be raised well beyond the Kilpatrick limit [Williams, 1979, Wang, 1986, Gerhard, 1989]. During operation at frequencies above $300\,\text{MHz}$, it should not exceed a value of $2-3$, yet for pulsed accelerators it may be larger. At $325\,\text{MHz}$ the
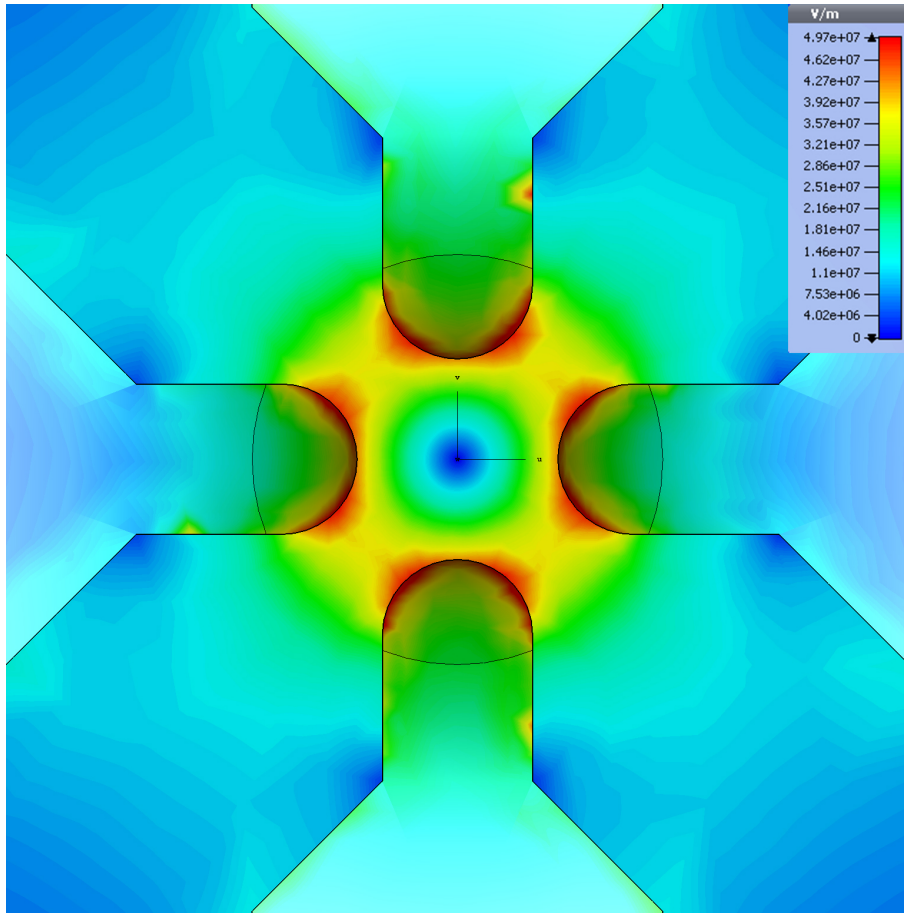
Figure 5.3: Contour plot of the absolute electric field in the x-y-plane perpendicular to the beam axis in the area of the electrodes. The scale is based on a stored field energy of 1 J. Therefore, the real field values have to be reduced by a factor of 0.58.

"Kilpatrick" field for $b = 1$ results in:

$$E_S = 17.85\,\text{MV/m} \tag{5.7}$$

Fig. 5.3 illustrates the absolute electric field around the cross-sectional tip profile of the electrodes, which is the region of the RFQ where most of the electric energy is stored and the highest field values occur. As usual for quadrupole fields, the field is linearly proportional to the distance from the beam axis within the aperture. This field direction, alternating between focusing and defocusing cells in both the x- and
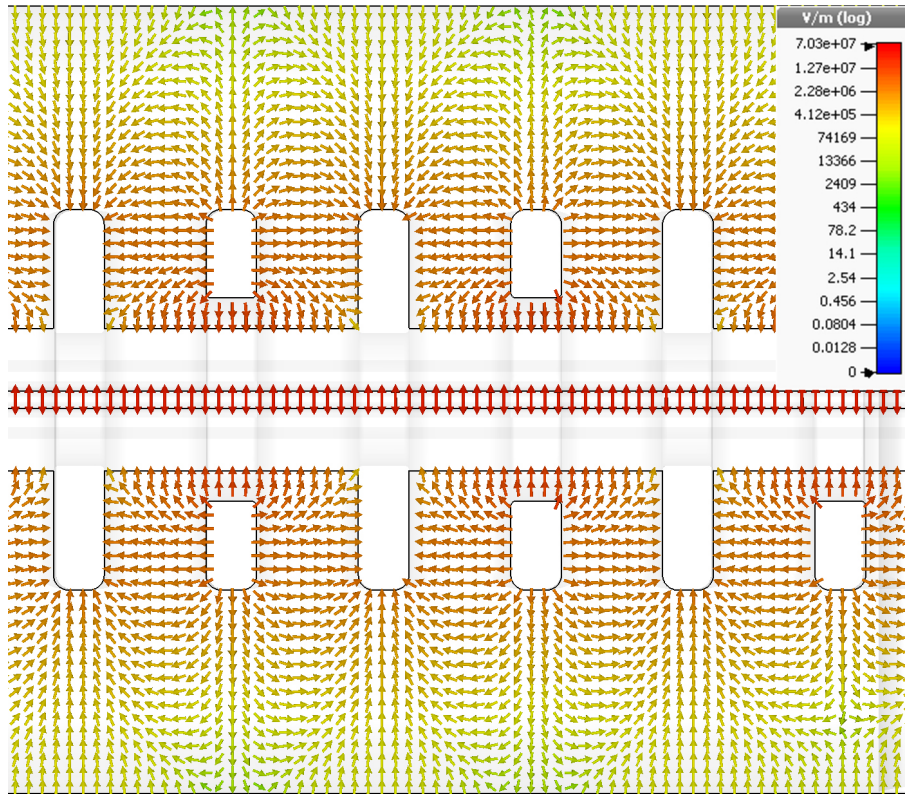
Figure 5.4: Vector plot of the absolute electric field in the y-z-plane
at $x = 0\,\text{mm}$. The scale is based on a stored field energy
of $1\,\text{J}$. Therefore, the real field values have to be reduced
by a factor of 0.58.

y-plane, is the basic principle of the transverse strong-focusing[4]. The maximum electric surface field in the simulations is $28\,\text{MV/m}$ at a vane-vane voltage of $80\,\text{kV}$. That corresponds to a Kilpatrick factor of 1.57, which is in accordance with the beam dynamic calculation [Zhang and Schempp, 2009].

Figs. 5.4 and 5.5 illustrate the electric and magnetic field distributions within the Ladder RFQ. The electric field is concentrated on the beam axis and is perpendicularly oriented between the ladder spokes. The RFQ oscillates in 0-mode, i.e. the direction of the fields alters in every RFQ cell, but its absolute value is constant along the beam axis, leading to a constant vane-vane voltage along the RFQ. The magnetic field

---

[4]The principle of strong-focusing, i.e. focusing by alternating gradients, was discovered theoretically by E. Courant, M. S. Livingston and H. S. Snyder at the Brookhaven National Laboratory in 1952 [Courant et al., 1952].
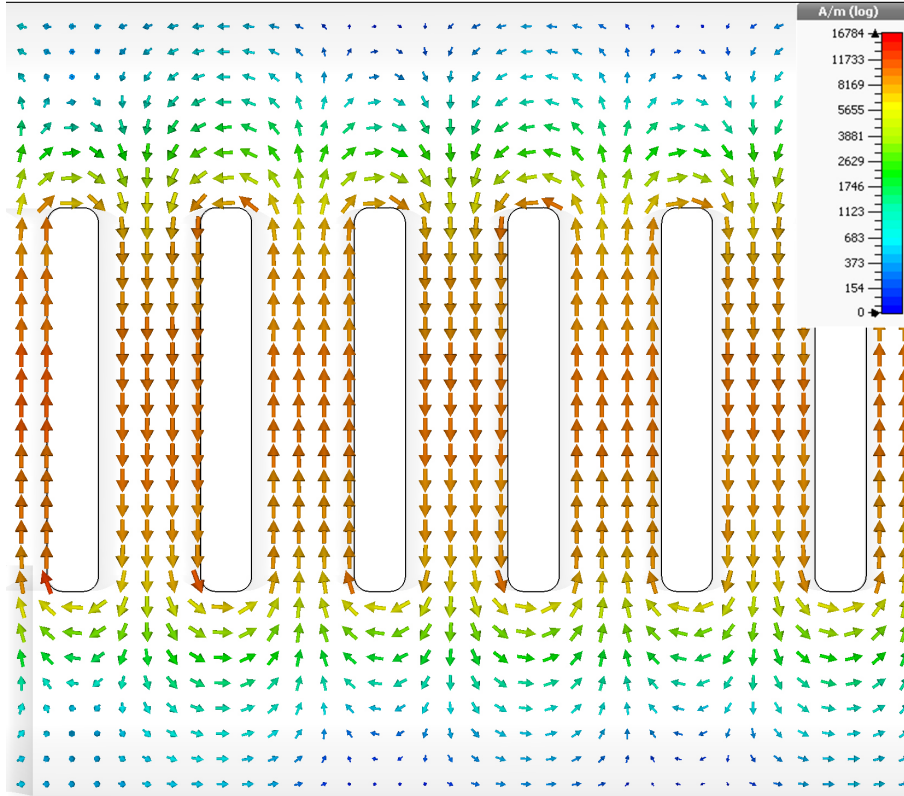
Figure 5.5: Vector plot of the absolute magnetic field in the y-z-plane at $x = 70\,\text{mm}$. The scale is based on a stored field energy of $1\,\text{J}$. Therefore, the real field values have to be reduced by a factor of 0.58.

wraps around the ladder spokes and increases from the beam axis towards the side rails of the ladder structure. The field plots clearly show that the ladder structure is a line-type resonator. The field is dominated by and concentrated around the inner structure. Beyond the copper structure, towards the tank, the field vanishes within several centimeters.

The absolute surface current is shown in fig. 5.6. On the walls of the tank the current tends towards zero (less than 1% as the current of the highest current levels occurs there), whereas no peak fields are expected on the ladder spokes. As a consequence, flange do not significantly disturb the current flow and fields. At the transition from the stems to the rings, the local currents at the surface are raised up to a factor of two. During manufacturing, the milling of a neat and perfect fit,

meeting the closest tolerances, is very important, in order to guarantee a flawless current flow and to minimize risks of sparking or Ohmic losses due to imperfect joints.
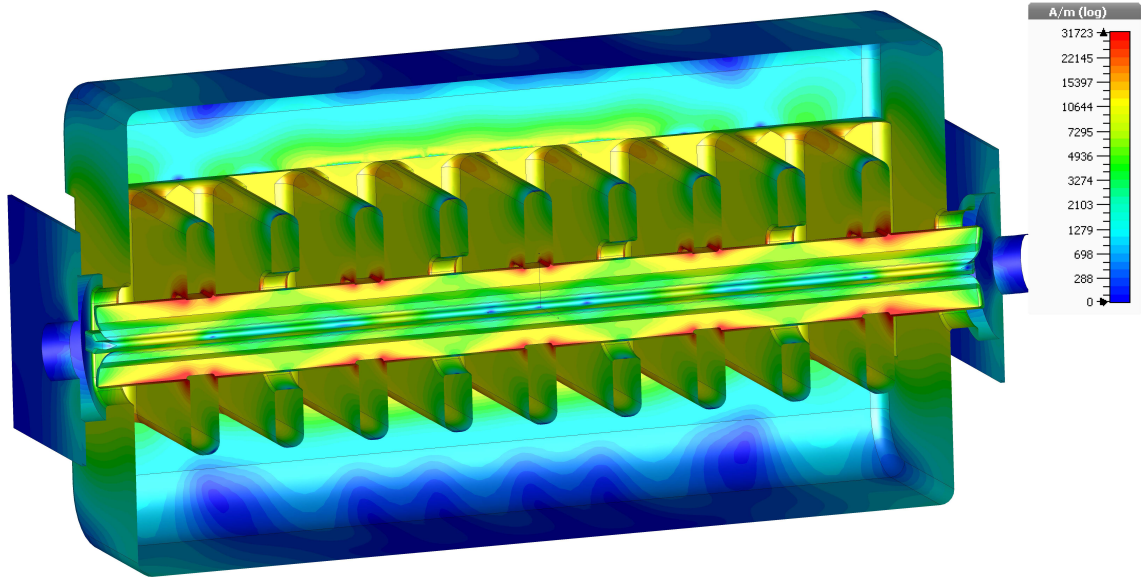
Figure 5.6: Contour plot of the specific surface current. The scale is based on a stored field energy of 1 J. This would correspond to a very high vane-vane voltage of 140 kV. Therefore, to obtain the real current the values have to be reduced by a factor of 0.58.

5.3 Field Flatness

The calculation of the beam dynamics assumes a constant vane-vane voltage along the beam axis. The RFQ will fulfill this basic requirement, if every cell of the ladder structure was tuned to the same eigenfrequency. The eigenfrequency is determined by its inductance and capacitance, which, in turn, are specified by the dimensions of every cell. If the cells are not perfectly equal, the operating eigenmode of the whole RFQ is different from the eigenfrequency of a single cell leading to a local deviation of the voltage distribution.

Due to imperfections in production and in simulation the RFQ as built varies from a perfect symmetrical RFQ and the voltage distribution is not completely flat. Additionally, the eigenfrequency of the first and last cell, which technically are half
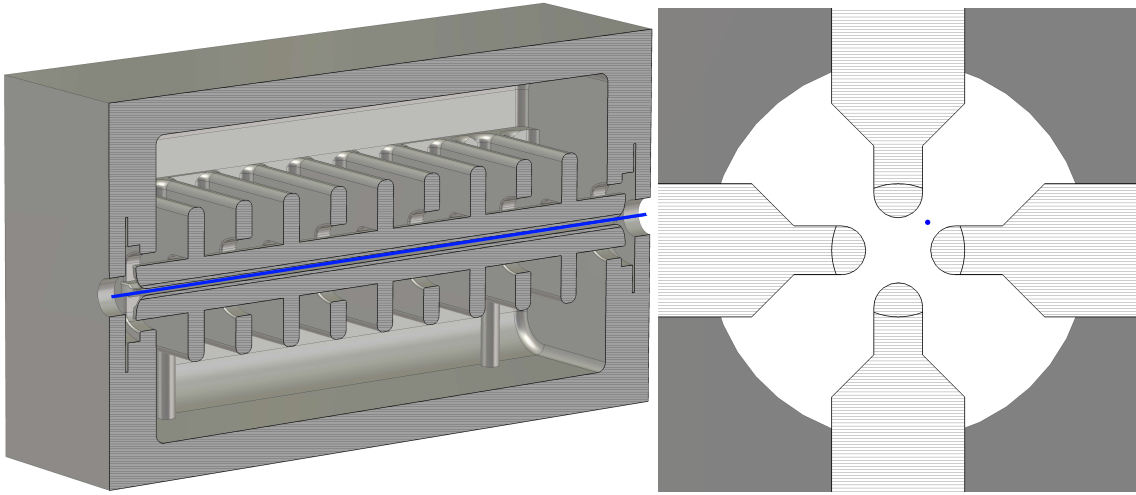
Figure 5.7: Simulation method for the determination of the relative electric field distribution. The absolute electric field, which equals the transversal field for unmodulated electrodes, is measured along a path (colored in blue), located at the high field region in between two adjacent electrodes. The transversal offsets of the curve to the beam axis are $3\,\text{mm}$ in x and y direction.

cells with half the inductance compared to mid-cells, is raised and the local vane-vane voltage at that position of the electrodes are lifted. Furthermore, the capacitance of the electrodes in the end cells varies, depending on their overlap, which is the electrode surplus before (after) the first (last) ring. The electrode overlap refers to the length between the beginning (end) of the electrodes to the lateral area of the first (last) ring. Nevertheless, adjusting the height of single ladder cells changes the length of the current path. Accordingly, the inductance can be corrected to match the desired frequency and voltage difference of this cell, respectively.

In simulations involving an unmodulated RFQ, the longitudinal as well as transversal electric fields on the beam axis are zero. Therefore, the relative transversal electric field distribution between the electrodes has to be measured off-axis. The simulation method is visualized in fig. 5.7. The blue curve parallel to the beam axis is located between two adjacent electrodes at a high field region with $x = y = 3\,\text{mm}$. The transversal electric field along this curve represents the relative transversal electric field between the electrodes and the electrode voltage difference, respectively. The simulation results of the transversal electric field along a path according to fig. 5.7 are shown in fig. 5.8. The basic flatness distribution without any tuning (black curve)
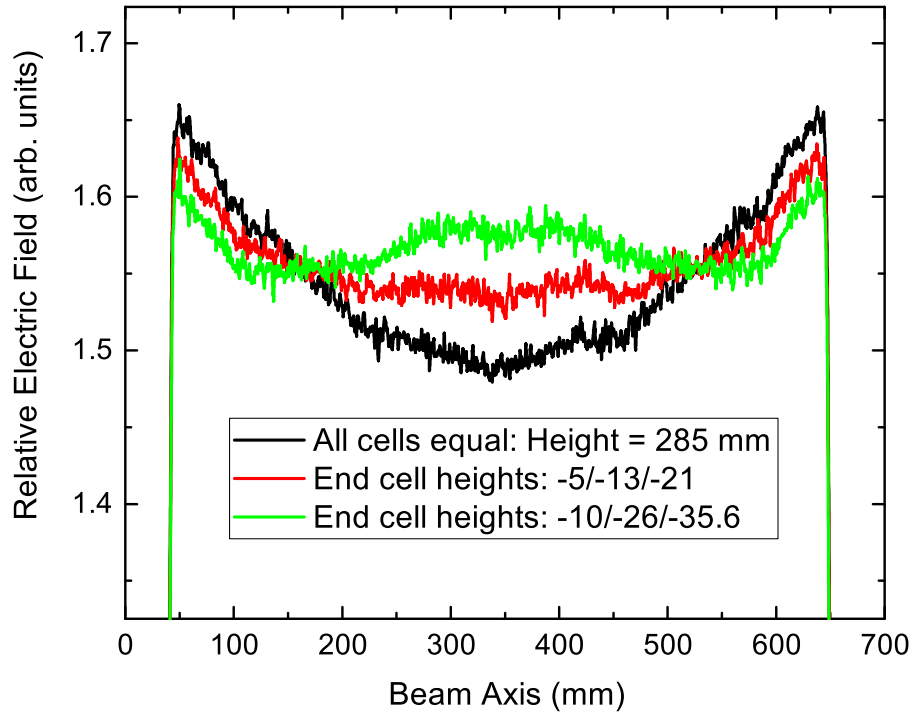
Figure 5.8: Simulation of the relative electric field distribution on the beam axis. The distribution without an adjustment of the cell heights is shown in black with a stepwise reduction of the first and last three ladder cell in red and green, respectively.

has a symmetric, parabolic form with its minimum in the center of the RFQ. To lower the fields at the end and obtain a flat distribution, the local inductance as well as the shunt impedance, which is proportional to $\sqrt{L}$, and voltage have to be decreased (cf. eq. 3.17). The inductance depends on the height of the ladder cells. In consequence, the field flatness can be adapted according to a variation of the height of the ladder cells. Simulations have shown that an adjustment of the first and last three cell heights of the ladder structure, i.e. cells 1-3 and 7-10 in case of the unmodulated prototype, is enough to achieve a flat voltage distribution.

The cell height is adequate to the inner clear distance between the side rails of the ladder structure within one ladder cell. By incrementally decreasing the individual cell heights at both ends of the RFQ, the optimum distribution is found for a decrease of $-33.6\,$mm of cells 1 and 10, $-26\,$mm of cells 2 and 9 and $-10\,$mm of cells 3 and 8 in relation to the height of cells 4-7 (s. green curve of fig. 5.8). In total, the relative
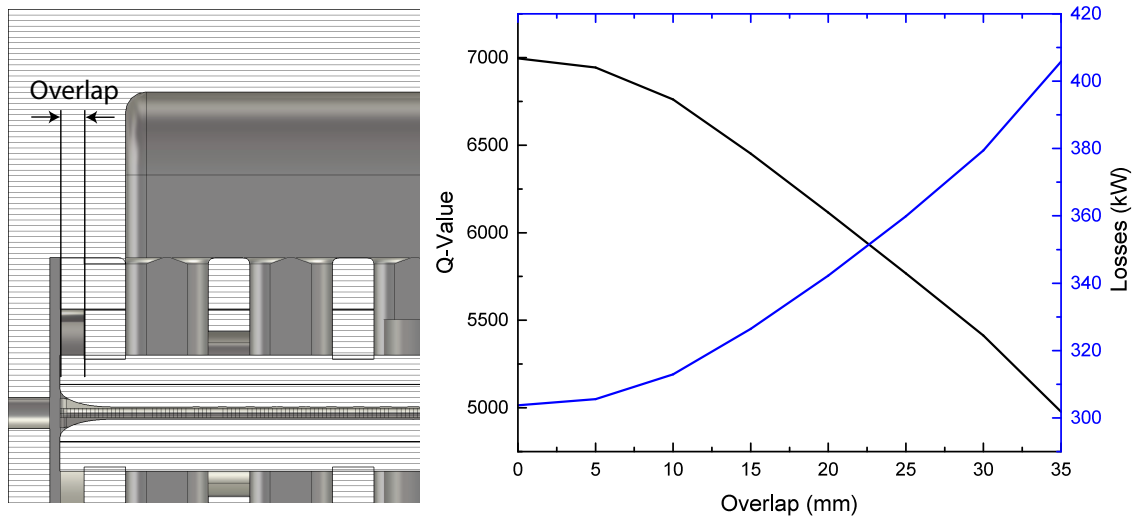
Figure 5.9: Visualization of the overlap of the electrodes (left) and the impact of the overlap on the Q-value and total losses (right).

difference of the electric field could be improved from $\pm 5\%$ to approximately $\pm 1.5\%$.

Another impact on the course of the field flatness and also on the overall performance of the RFQ is the overlap of the electrodes at its tails. The overlap is the length which the electrodes protrude beyond the first and the last ring (s. fig. 5.9 left). For the sake of a symmetric field flatness, this overlap should be the same at the beginning and at the end of the RFQ, if the electrodes provided a constant capacity loading along the beam axis. If the capacity was not constant, an unsymmetrical field distribution could be corrected by shifting the mounting position of the electrodes longitudinally resulting in different overlap lengths on both tails of the electrodes. Since the hollow space between the flanges and the first (resp. last) ring is not an oscillating RF-cell, the potential of the electrodes collapses at a certain length of the overlap, which leads to a reduction of the quality factor as well as the shunt impedance. The maximum overlap is determined by the evaluation of the quality factor as well as total losses (s. fig. 5.9 right). For an overlap larger than 10 mm on every side of RFQ, the Q-value is reduced by more than 3%. From an RF point of view aligning the electrodes with the surface of the outer rings (zero overlap) would be the perfect choice. Due to the mechanical mounting into the ring, a better conductivity and a precise longitudinal positioning, the prototype has an overlap of 5 mm on both ends. If the total length of the electrodes resulted in an overlap greater

than 10 mm, one should consider increasing the number of ladder cells. Another aspect in this context is the total drift length between the entrance flange and the radial matcher, which should be as short as possible to keep an emittance growth as low as possible. The length of the electrodes for the unmodulated prototype was chosen at own discretion (total length 630 mm), whereas the design of the entrance drift for the modulated prototype, as the exact length of the electrodes is given by the results of the beam dynamic calculation, is discussed in chap. 8.3.

5.4 Frequency Plunger

Once a flat field distribution has been found and the frequency has been coarsely adapted to the specifications, the RFQ still has to be tuned to suit the very exact frequency of 325.224 MHz. Even though the simulation methods have reached a very reliable exactness by having higher computational power, more efficient and accurate codes as well as a more detailed meshing, the frequency cannot be predicted with the preciseness, which is needed for operation. For spherical curvatures in the model the number of mesh cells converges to infinity, in case the model perfectly represents the reality. Mechanical tolerances during the manufacturing process are not being regarded by the simulation code. Additionally, the cavity is heated during operations due to Ohmic power losses. A deviation of the temperature implicates a thermal expansion of the cavity. Copper, for example, has a linear thermal expansion of $16.5 \frac{\mu m}{m \cdot K}$. As a consequence, the frequency decreases with increasing temperature.

For the final adjustment of the frequency according to the specification and to keep the frequency stable within the kHz range, a static and a movable frequency plunger are used. The plungers, which are mostly made of solid copper cylinders, are inserted into the cavity and penetrate the RF field of the cavity (s. fig. 5.10). There are two different methods for a frequency tuning - the plunger can either displace the magnetic or electric field and change the energy density. According to the perturbation theory by J. C. Slater [Slater, 1946, Maier and Slater, 1952], the frequency shift Δf is calculated by the change of the magnetic W_m and electric W_e field energy stored in the cavity. The relation is based on the Boltzmann-Ehrenfest Theorem [Boltzmann, 1904, Ehrenfest, 1914, Ehrenfest, 1911] stating that "in a
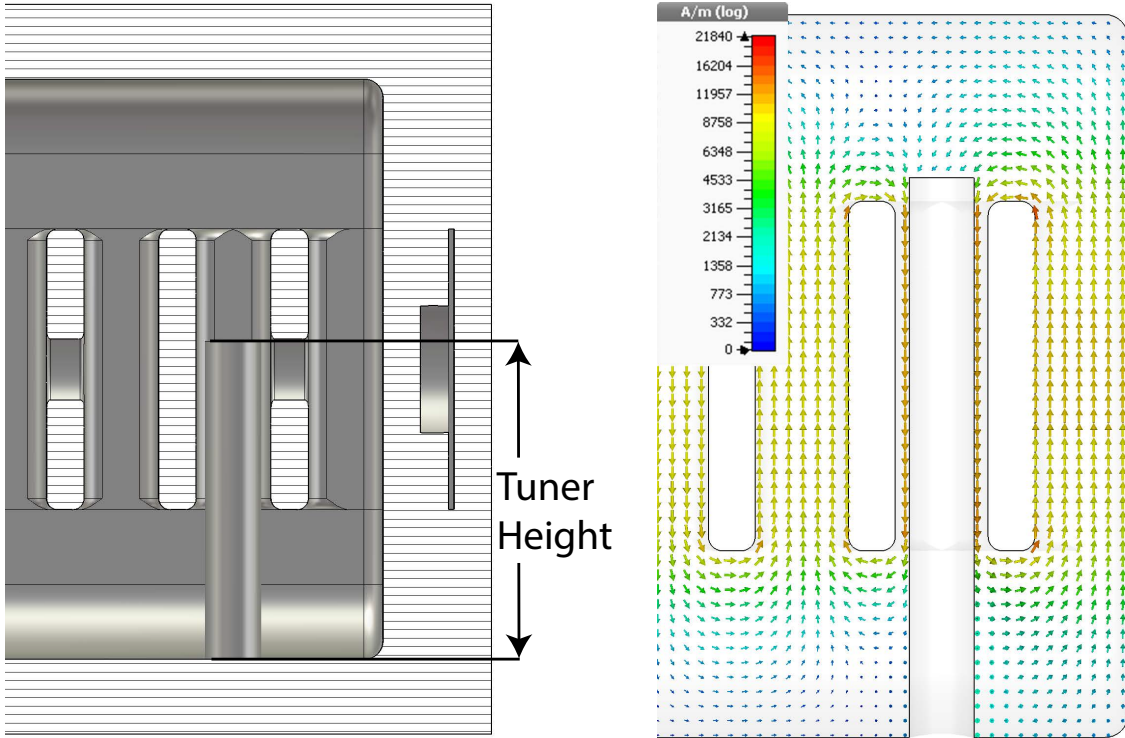
Figure 5.10: Visualization of the mechanical plunger, penetrating the magnetic field. The simulations are calculated with two tuners - one on each side of the cavity, in the second and ninth cell. The clear height of the tuner inside the cavity is also referred to as the penetration depth. The scale is based on a stored field energy of 1 J. Therefore, the real field values have to be reduced by a factor of 0.58.

frictionless machine having a periodic motion, the kinetic action , i.e. the product of mean kinetic energy and period, is invariant against an adiabatic deformation" [Maclean, 1930]. For resonators and relatively small perturbations, that theorem can be restated as:

$$\frac{\Delta f}{f} \approx \frac{\Delta W_m - \Delta W_e}{W_{tot}} \tag{5.8}$$

A capacitive plunger causing a change of the electric energy leads to a decrease of the frequency. For the Ladder RFQ inductive tuners are used which can influence the frequency upwards. The choice for the frequency tuners has two important reasons: On the one hand, the ladder cell heights can easily be milled out. Increasing the cell heights leads to an increase of the inductance of the ladder L_L and accordingly to

a decrease of the frequency. By using inductive frequency tuners, the frequency of the Ladder RFQ can still be adjusted upwards. On the other hand, the efficiency of the plungers is proportional to the square of the absolute field value. Ergo, the favorable positions, for an optimized efficiency of the plungers, are in regions with the highest field values. In case of the Ladder RFQ that position is between the ladder spokes, within the cell and as near as possible at the side rails. In contrast, to gain a significant influence on the electric field energy the plungers need to be directly above the spokes. The distance between capacitive plungers and the upper side of the ladder spokes would have to be in the millimeter range. Therefore, the narrow gap bears the risk of sparking and field emission effects. In case of a purely inductive plunger, the frequency shift Δf becomes:

$$\Delta f = \frac{1}{2W_{tot}} f \int\limits_{\Delta V} \mu \left| \vec{H}(x,y,z) \right|^2 \mathrm{d}V_{Plunger} \qquad (5.9)$$
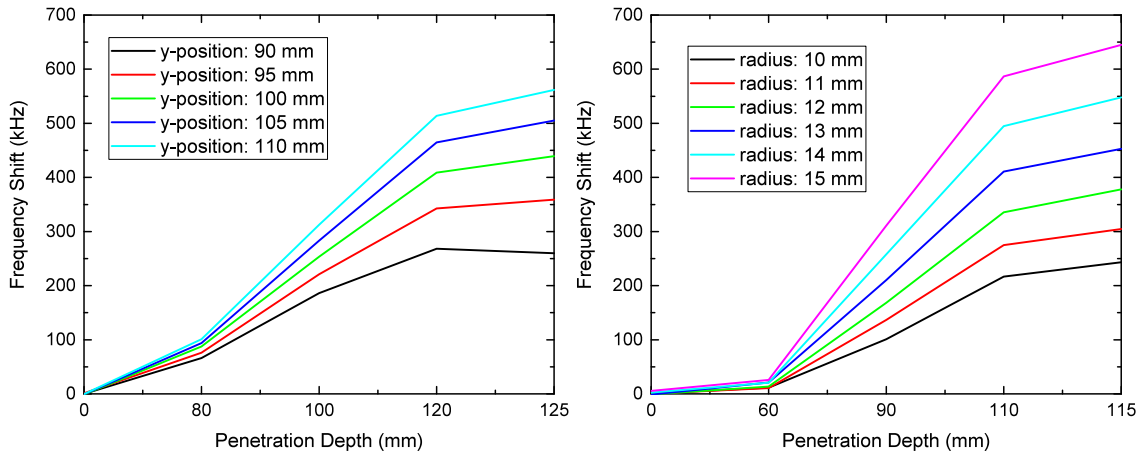
Figure 5.11: Simulation of the frequency shift of two symmetrically moved tuners in dependence of the penetration depth for different y-positions (left) at a fixed radius of 12 mm. The y-position is the transversal distance to the beam axis. The dependence of different radii of the tuner is depicted on the right side at a fixed y-position of 100 mm.

As clearly indicated from the equation, the total frequency shift can be raised by either moving the plunger into a region with a higher field $\vec{H}(x,y,z)$ or by increasing the volume of the plunger. Fig. 5.11 (left) illustrates the frequency dependence on the y-position. The plungers have to be positioned in the outer half of the ladder

cell to minimize its influence on the field flatness as well as on the dipole moment. The magnetic field in the outer area of the cell is constant within 1%. By moving the plunger further into the outer region of the ladder cell towards the side rails, i.e. increasing its distance from the beam axis (y-position), the counterproductive influence from the E-field is reduced (cf. eq. 5.8). In total, the maximum frequency shift can be raised from 360 kHz to 560 kHz by displacing the plunger 20 mm in y-direction. As the frequency shift is proportional to the Volume and the plunger radius squared, $\Delta f \sim dV \sim r^2$, the maximum stroke can be further optimized by increasing the radius and volume of the plunger. The effect can be seen in fig. 5.11 (right). The total frequency shift is extended from 240 kHz to 645 kHz by increasing the radius from 10 to 15 mm for a fixed y-position of 107.5 mm.
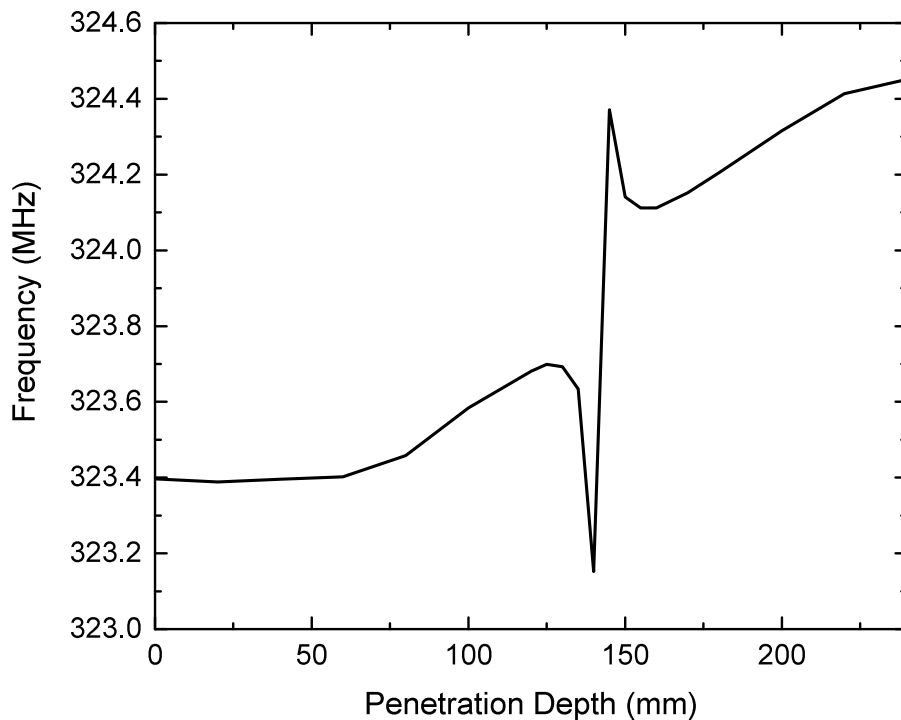
Figure 5.12: Simulation of the frequency shift for the final tuners as built with a radius of 14 mm. The static plunger has a height of 90 mm within the cavity, whereas the second plunger is varied from 0 to 230 mm. The y-position is 107.5 mm.

The simulations have shown that two movable tuners supply a sufficient tuning range of at least 650 kHz. The final tuners of the prototype have a radius of 14 mm at

a y-position of 107.5 mm. The reason for this choice is a maximum possible frequency shift at reasonable distances to the ladder structure. Furthermore, the tuners, both installed on one side of the RFQ, neither generate a significant influence on the field flatness, nor on the dipole component. In the prototype RFQ, one tuner is built as a static plunger at a certain height. The other one will be motor driven limited to a maximum stroke of 100 mm. Fig. 5.12 shows that a frequency shift greater than 350 kHz can be provided by just one moveable tuner, while the other one is kept at a constant height of 90 mm. The motor plunger may only be operated up to a maximum depth within the field and a certain length of the plunger. At a length of $140 - 160$ mm, the plunger is excited at a resonant eigenmode, interfering with the cavity resonance. The eigenresonance leads to a drop of the quality factor and consequently the voltage of the electrodes decreases. For the RFQ as built the eigenresonance is expected to be shifted towards lower penetrations depths, as the total plunger length is extended into the flange and the motor tuner. For a reliable operation, the frequency tuner may only be driven in the linear area, which has a maximum range of at least 350 kHz. It can be assumed to achieve a higher frequency shift, as the tuner resonance is shifted towards lower penetration depths.

5.5 Dipole Fields

For an efficient acceleration a most accurate quadrupole field generated by the electrodes, is essential. A perfect quadrupole can only be realized by infinite precise hyperbolic shaped electrodes. Because of the limited sizes and asymmetric mounting of the electrodes, the field comprises dipole and higher multipole components. A dipole component deflects the beam, resulting in a deterioration of the beam dynamics. Considering the power efficiency, a maximization of the quadrupole component, i.e. by concentrating all the energy into the acceleration field, can be deemed valuable. Consequently, it is necessary to ensure a very low dipole component. Because of its symmetry the ladder structure has an inherent small dipole component. Possible impacts on the dipole component by any asymmetric geometric modifications have to be analyzed.

The dipole component results from unequal potentials of the electrodes. From the
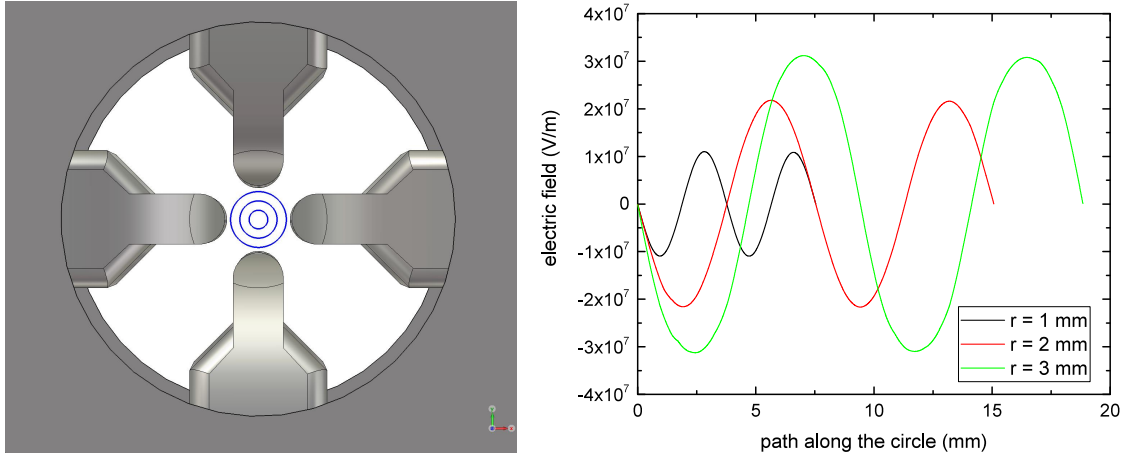
Figure 5.13: Visualization of the simulation of the dipole modes: Circles in the quadrupole plane with a radius of 1, 2 and 3 mm (left). Longitudinal electric field distribution along the path of the circles (right).

conservation of the magnetic flux B_i in every quadrant i of the electrodes, the sum has to be zero: $\sum_{i=1}^{4} B_i = 0$ [Wangler, 2008]. The amplitude of the magnetic flux in opposing quadrants is equal in case of an ideal quadrupole field. In the presence of dipole fields, the difference is greater than zero and the dipole modes are proportional to:

$$D_1 = |B_1 - B_3| / 2$$
$$D_2 = |B_2 - B_4| / 2$$

(5.10)

The quadrupole component is the average of the field of every quadrant:

$$Q = (|B_1| + |B_2| + |B_3| + |B_4|) / 4$$

(5.11)

To study and simulate the dipole fields of the prototype, the electric field was evaluated along a circle, which is concentric to the beam vector (s. fig. 5.13). The dipole mode can be calculated by the integration along the path in every quadrant (B_i) and its differences according to eqs. 5.10. The results were evaluated for various radii and positions along the beam axis. All investigations for different field tuner heights, frequency plunger positions as well as penetration depths have a relative dipole to quadrupole moment of less than 1%. Simulated numbers for the unmodulated Ladder

Table 5.1: Results of the relative dipole moment compared to the quadrupole moment in arbitrary units.

Simulation	D_1	D_2	$D_1 + D_2$	Q	D/Q
Without frequency plunger	1.3E+05	1.7E+04	1.5E+05	1.0E+08	0.15%
Full depth of one frequency plunger	7.7E+01	7.2E+01	1.5E+02	1.0E+05	0.15%
Final tuner height	5.4E+04	4.3E+05	4.7E+05	1.0E+08	0.47%

RFQ are exemplary shown in tab. 5.1.

5.6 Coupling

To feed the cavity with RF-power a coupler is needed. It can be either realized inductively, by a magnetic loop which couples to the magnetic field, or capacitively, by coupling to the electric field. Alternatively, the coupler can be attached galvanically, i.e. by a fixed connection between the conductor and the current carrying part in the cavity. For the unmodulated prototype, an inductive coupling was chosen. Due to its small dimensions, a galvanic coupling would be mechanically hard to realize. A capacitive coupler has to be positioned appropriately to high electric field regions, directly above the ladder structure. Small distances critically increase the risks of field emission and sparking. The inductive coupler short-circuits the inner conductor of the coupler via a water cooled coupling loop to the ground. For a critical coupling without reflection, the power flux P_i through the coupler with an impedance $Z_L = 50\,\Omega$ has to be equal to the power dissipated in the cavity P_C. In case of a beam load the beam power has to be added as well.

$$P_i = \frac{U_{eff}^2}{Z_L} = \frac{U_0^2}{2 \cdot 50\Omega} \overset{!}{=} P_C \tag{5.12}$$

The voltage, that has to be induced to the coupling loop, is given by:

$$U_0 = \sqrt{P_C \cdot 100\,\Omega} \tag{5.13}$$
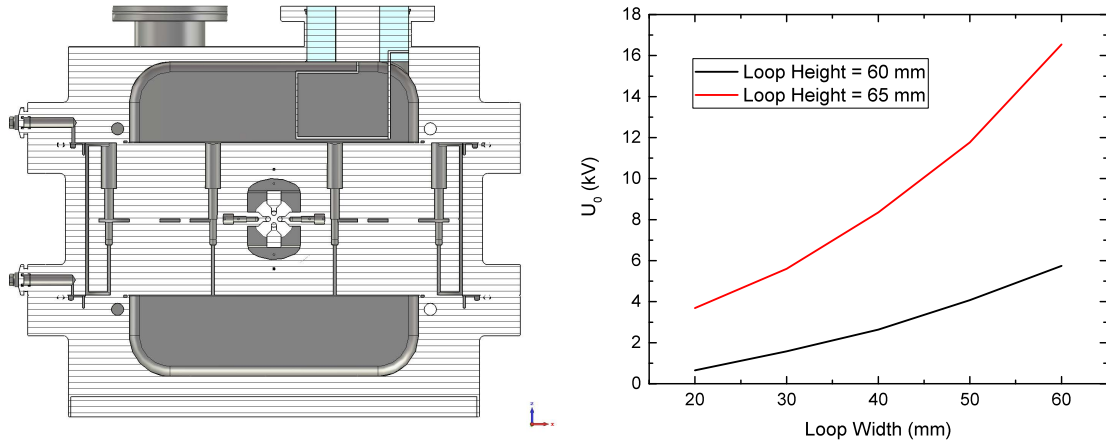
Figure 5.14: CST model including the coupling loop (left). The induced voltage
is given in dependence of different coupling loop heights and widths
(right).

For the prototype with a power loss of approximately 135 kW, the voltage is
calculated to 3.67 kV. In case of a lower quality factor as well as to have the
opportunity for overcoupling, the coupling loop should be designed with a safety
margin of at least 30%, resulting in a minimum design value for the induced voltage
of 4.8 kV. According to Faraday's law of induction, the voltage is as follows:

$$U_0 = -\frac{\mathrm{d}\Phi}{\mathrm{d}t} = -\frac{\mathrm{d}}{\mathrm{d}t}\int \vec{B} \cdot \mathrm{d}\vec{A} \tag{5.14}$$

In the case of the Ladder RFQ, the integral cannot be solved precisely analytically,
because the magnetic field is a nonlinear, spatial dependent function, which strongly
depends on the geometry of the RFQ. For a reliable mechanical design and evaluation
of its size, different loop dimensions were studied in simulations (s. fig. 5.14). The
induced voltage was calculated by the integration of the tangential electric field
along a path with a height of $55 - 65$ mm and is equal to the time derivative of the
magnetic flux (s. eq. 5.14). The highest magnetic flux is concentrated slightly above
the spokes. To capture as much flux as possible, the coupling loop is moved as close
as needed above the spokes yet as far as possible to prevent sparking. The results
of the simulation (s. fig. 5.14 right) show that a coupling height of 55 mm is not
sufficient to induce at least 4.8 kV. Otherwise, a loop height of 65 mm reduces the

clear distance to the spoke to 5 mm. The perfect compromise between the maximum induced voltage and distance to the ladder stem is a height and width of 60 mm. The width could also be extended, since it is only limited by the diameter of the flange, which is a CF100[5].

5.7 Temperature Distributions
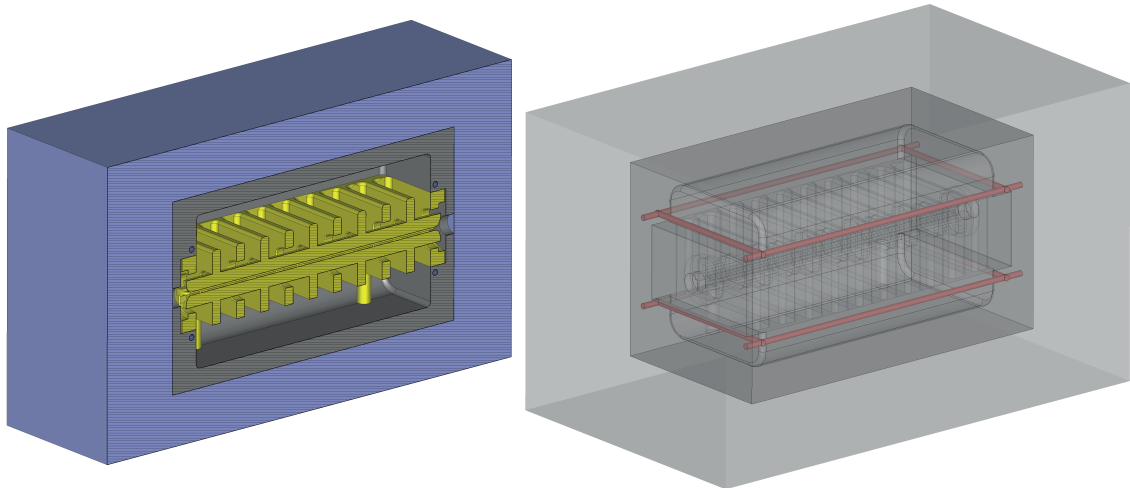
Figure 5.15: The temperature distributions were simulated for air cooling (left) and with a water cooling implemented by two closed pipes within the upper and lower steel tank (right). The details and features of the mechanical cooling construction are described in chap. 6.3. Color-codes: Blue - air, dark grey - stainless steel (copper-plated), yellow - copper, red - water pipes.

During operation, the Ohmic losses of the Ladder RFQ are converted into heat. The heat has to be dissipated to prevent a thermal expansion of the material and guarantee a safe and stable operation. A bending of the electrodes due to thermal expansion even on a small scale can compromise the beam dynamics. Moreover, it may lead to a destruction of the materials or even vacuum leaks. According to the simulations, the total peak losses for the prototype are 100 kW. At a repetition rate of 4 Hz and at a pulse length of 200 μs, the duty factor is 0.08 %. Consequently, the average thermal losses yield 80 W at an ideal conduction of the copper surface. If

---

[5]**C**on**F**lat Flanges; ref. to ISO/TS 3669-2/2007.

the theoretical Q-Value cannot be achieved in the measurements, the losses will be accordingly higher.
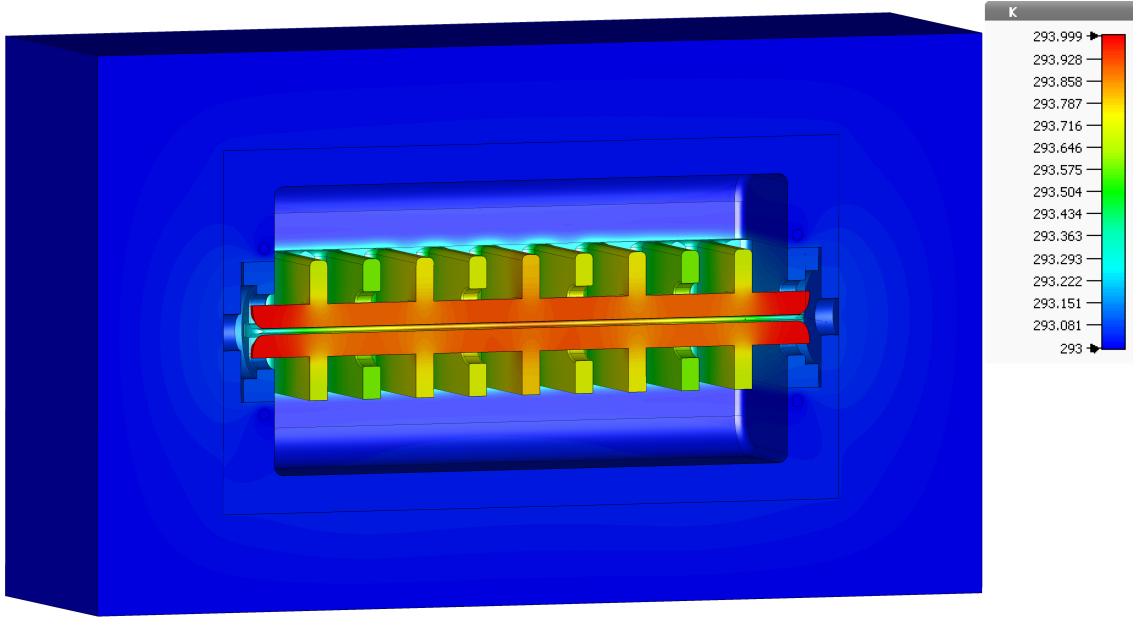
Figure 5.16: Temperature distribution with air and water cooling for the unmodulated prototype at an average power of 100 W corresponding to a duty factor of 0.1%. With water cooling channels within the tank the overall increase of temperature is less than 1 K.

For a more realistic simulation of the temperature distributions, the RFQ was embedded into a larger background filled with air (s. fig. 5.15 left). The results are compared with a more efficient water cooling. The simulation does not consider a change of the water temperature. Its temperature is kept at a constant level of the ambient temperature of 293 K. Overall, two closed cooling channels were evenly distributed beside the ladder structure within the steel tank (s. fig. 5.15 right). At moderate average power losses of 100 W the maximum temperature hypothetically rises up to 550 K according to the simulation regarding air cooling only without heat convection. By contrast, an increase of the temperature including also an additional water cooling is negligible ($\Delta T < 1$ K, s. fig. 5.16). According to the heat transfer Q from the cavity to the water, the minimum water flow $\dot{V}$ can be calculated by the heat flow $\dot{Q}$, which is equivalent to the average losses P:

$$\dot{Q} = \dot{m} \cdot c_{H2O} \cdot \Delta T = \dot{V} \rho \cdot c_{H2O} \cdot \Delta T = P \qquad (5.15)$$
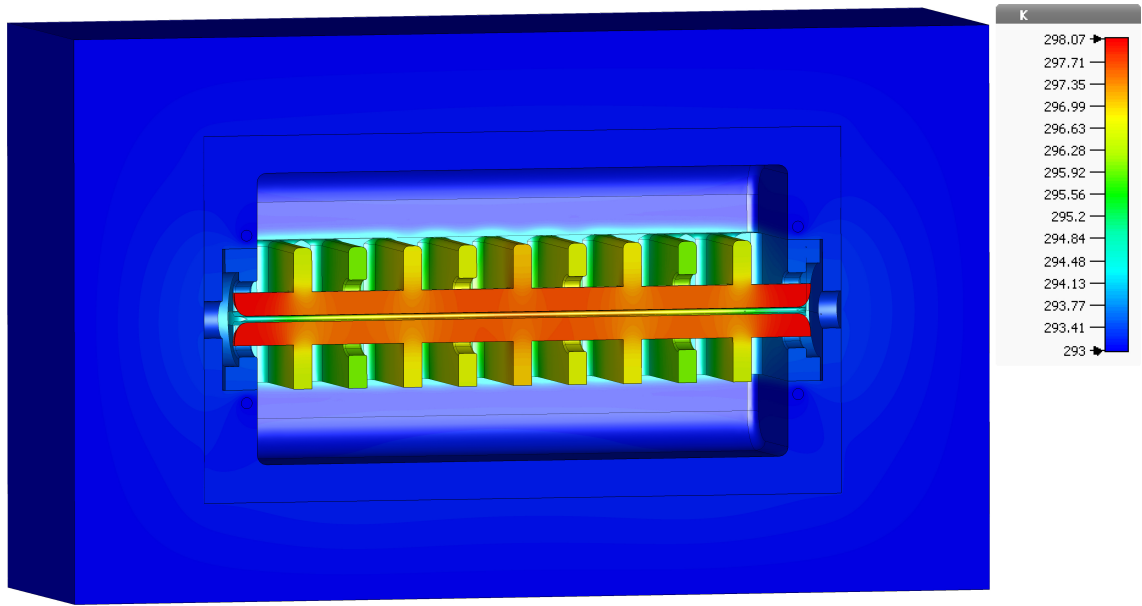
Figure 5.17: For a higher average power loss of 500 W (duty factor 0.5%) the maximum temperature rise is approx. 10 K.

The specific heat capacitance of water equals $c_{H2O} \approx 4.13 \, \text{kJ} \cdot \text{kg}^{-1} \cdot \text{K}^{-1}$. Assuming an increase of the cooling water temperature of 1 K at average losses of 200 W[6] , the minimum water flow needed for cooling is 2.85 l/min, which can be easily achieved by the cooling circuit. To test the limits of that cooling mechanism, the simulations were additionally performed at a higher power levels of 500 W (s. fig. 5.17). In the first case, the growth of 1 K is still acceptable, while more than $\Delta T = 20 \, \text{K}$ is the upper limit for a safe operation, at which the thermal expansion of all components is well below 1/10 mm. In that case, the average temperature increase of the copper block is still less than 5 K and for the tank even below 2 K. The simulations clearly show that the maximum temperatures reached only at the end of the electrode pair which are not mounted to the first and last ring. At this point, the heat cannot be dissipated like the heat of the mounted pair of electrodes which is directly transferred to the copper structure. Furthermore, at the electrode end the heat flow is only possible in one direction. Otherwise, the rise of the temperature at this point is limited because the surface currents (s. fig. 5.6) on the electrodes are minimal in the center plane between two mounting point at which the surface current reaches its

---

[6]according to the simulation the average power is 80 W, for safety reasons a factor of 2.5 was taken into account.

maximum. The thermal expansion of the electrode for $\Delta T = 10\,\text{K}$ at this position is approx. $7\,\mu\text{m}$ and therefore does not influence the beam dynamics remarkably. The RFQ was also studied at an average power loss of $4000\,\text{W}$ which refers to a duty factor of 4%. The temperature theoretically rises over $600\,\text{K}$. As the surface resistance increases with the temperature ($R_S \propto \sqrt{1/\sigma(T)}$), the simulations are not reliable anymore. In conclusion, the water cooling should be improved for power losses exceeding $500\,\text{kW}$.

The consequences of high temperatures are the expansion and bending of the material. This could cause damages to the cavity. In the case of the Ladder RFQ, the total extension of the electrodes Δl is linear proportional to its length l and to the temperature difference ΔT. The proportional factor is the coefficient of thermal expansion $\alpha_{Cu} = 16.5 \cdot 10^{-6}\,\text{K}^{-1}$.

$$\Delta l = \alpha_{Cu} \cdot l \cdot \Delta T \tag{5.16}$$

The maximum length of the electrodes is between two subsequent mounting points of the rings, which is $120\,\text{mm}$, leading to a total extension of $\approx 20\,\mu\text{m}$ for an increase in the temperature of $10\,\text{K}$. The next step is the calculation of the temperature, at which a buckling of the electrode may occur. According to Euler's critical load, the critical force F_K, that a column fixed on both ends can bear, is given by:

$$F_K = 4\pi^2 \cdot \frac{E \cdot I}{l^2} \tag{5.17}$$

E is the modulus of elasticity defining the materials resistance to being mechanically deformed. I denotes the minimum area moment of inertia, depending on the cross section of the column. For the electrode geometry used for the prototype the moment of inertia can be approximated by a cylinder for the electrodes within the unsupported length l between two mounting points:

$$I \approx \frac{\pi d^4}{64} \tag{5.18}$$

The diameter d can be approximated by the electrode base width of $14\,\text{mm}$. The

axial compressive force F_T is caused by the thermal expansion of a cylinder with a cross-sectional area A:

$$F_T = A \cdot E \cdot \Delta l / l = A \cdot E \cdot \alpha_{Cu} \cdot \Delta T \qquad (5.19)$$

By equating eqs. 5.17 and 5.19 the temperature ΔT, at which a transversal buckling starts and subsequently a fraction of the electrode occurs, is calculated by:

$$\Delta T = \frac{4\pi^2 \cdot I}{A \cdot \alpha_{Cu} \cdot l^2} \approx \frac{4\pi^3 \cdot d^4}{A \cdot \alpha_{Cu} \cdot l^2 \cdot 64} \qquad (5.20)$$

For the prototype with $l = 120\,\text{mm}$ and $A = 254\,\text{mm}^2$ the buckling temperature theoretically becomes $1.2 \cdot 10^3\,\text{K}$. Therefore, at a duty cycle of 0.08% no issues due to any bending or demolition of the ladder structure have to be expected as the maximum increase of $10\,\text{K}$ is far below the buckling temperature.

5.8 CAD Model Comparison Study

The parametrized CST model is very useful for automatically sweeping through different geometrical dimensions and also physical parameters. Flanges, curvatures, sealings and screw holes are not included in the model, which makes its meshing easier and reduces the computing time by having less mesh cells compared to a very detailed model. Nevertheless, a review and validation of the preliminary detail design model is inevitable to reexamine the correct frequency and to check the model for an unexpected behavior or interfering modes prior to a production release. CST is capable of importing any type of 3D-models, such as step files. The RF simulations with an imported as built CAD model confirm that the simulations for the field distributions, the dipole component and the behavior of the frequency plungers are equal to the CST model within negligible errors of less than 5%. The frequency is about $0.7\,\text{MHz}$ higher, which can be explained by the actual curvatures of the RFQ as build. The level of details, especially the implementation of smooth transitions between different curvatures of the ladder structure, is very restricted by the software. To maintain its ability of sweeping parameters and to keep its parametrization,

curvatures and blendings have been omitted as much as possible. Otherwise a parametric update of the model fails. Nevertheless, the simulated frequency of the CAD model gives a more realistic estimation of the final measured frequency (cf. chap. 7). Furthermore, the quality factor is 6800 compared to $7000 - 7200$ with the CST model. The latter is a very idealized model, which concentrates on the main physical components and does not take detailed structural elements as machined and manufactured into account. By adding flanges and screw holes, the current flow will

Table 5.2: Comparison of the basic physical properties of the unmodulated prototype according to the simulations with the parametrized CST model and the imported CAD model.

Parameter	CST Model	CAD Model
Frequency (prior to tuning)	331.3 MHz	332 MHz
Quality factor	6900-7000	6800-6900
Losses peak/avg.	95 kW / 76 W	100 kW / 80 W
Shunt Impedance	$42\,\mathrm{k\Omega m}$	$40\,\mathrm{k\Omega m}$

be disturbed, resulting in a lower Q-value and higher losses, respectively. The RF behavior and frequency spectrum of both models are identical, i.e. no excitations of RF modes in hollow spaces of the cavity have to be excepted. Finally, the simulation revealed a total loss of approx. $100\,\mathrm{kW}$ for the prototype. That yields a shunt impedance of $31 \pm 1\,\mathrm{k\Omega m}$, if the simulated ideal quality factor was reached in the measurements. The most important physical properties from the simulations are highlighted in table 5.2. A complete list of all physical and geometrical properties and features are gathered in annex A.

Chapter 6

Mechanical Design of the Prototype

"Symmetry calms me down, lack of
symmetry makes me crazy."

Yves Saint Laurent
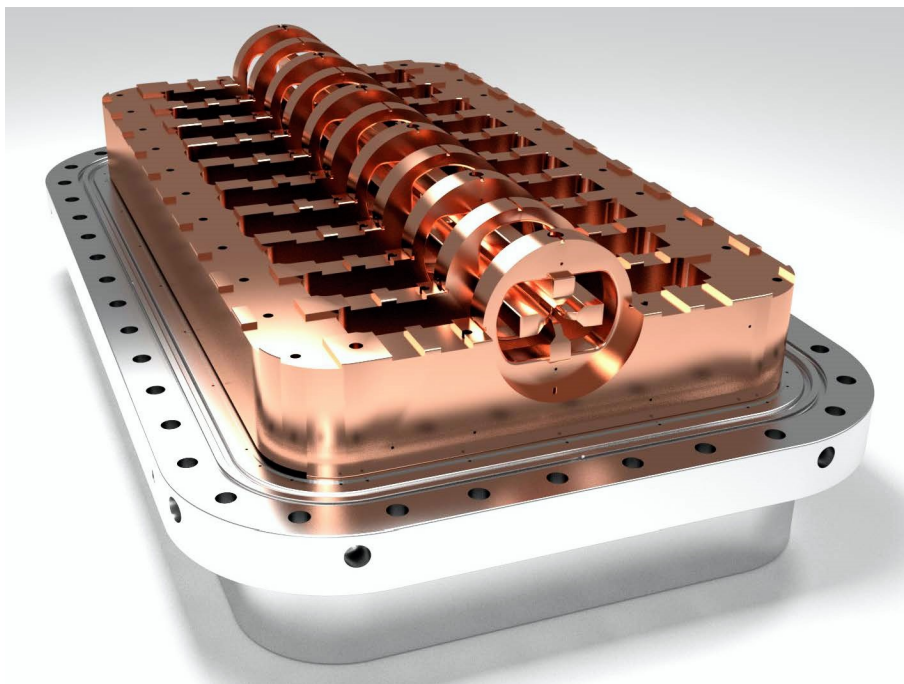
Figure 6.1: Isometric rendering of the Ladder RFQ prototype model.

Based on the simulations a mechanical detail design and mock-up of the Ladder RFQ was created (s. fig. 6.1). The focus of the construction of single components is the feasibility of manufacturing in compliance to the tolerances of the dimensions. Simultaneously, the costs should be kept to a minimum. Another important issue

is the ability of exchanging components and maintenance, i.e. having a fast and easy access to all components of the RFQ. The water cooling system as well as the vacuum system have to be laid out adequately. The final requirement for operation is the construction of the frequency plungers and of the coupling loop.

6.1 General Layout
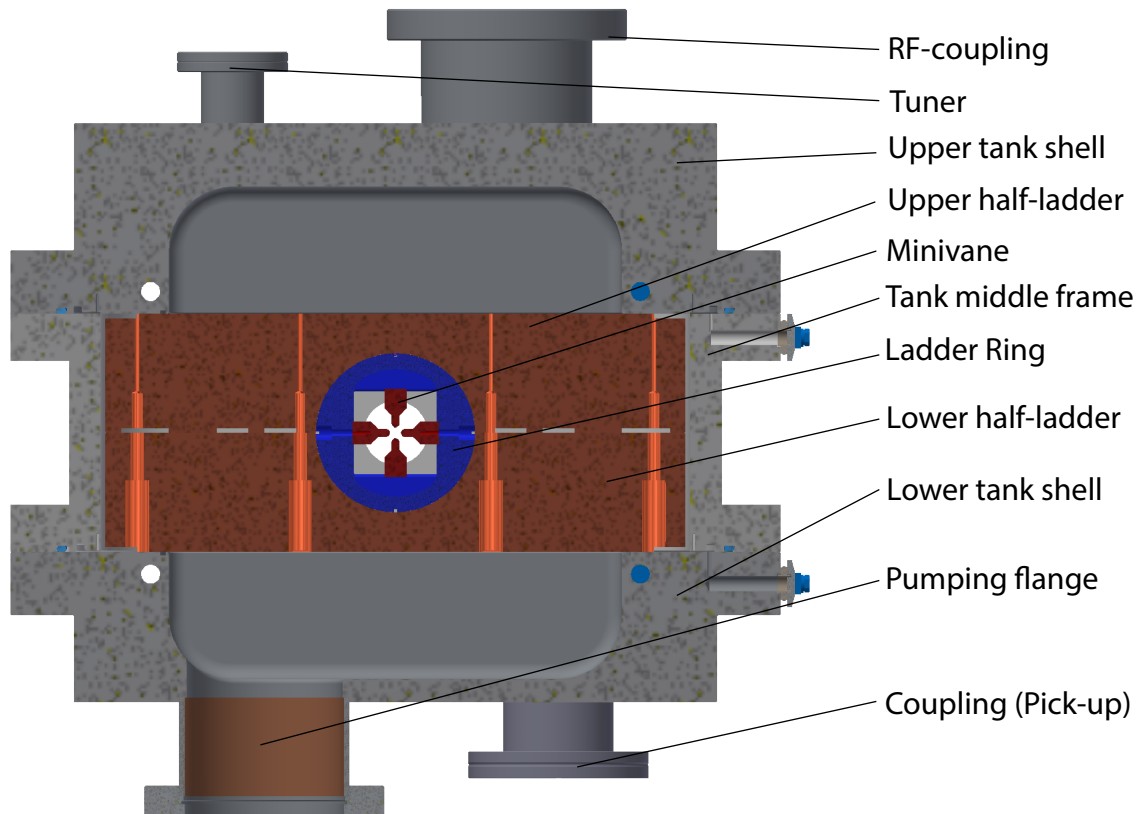
Figure 6.2: Transverse section view of the RFQ with its components. For a better visualization, the rings are colored in blue. A complete list of the dimensions can be found in appendix A and further overview drawings in appendix C.

The basic layout of the Ladder RFQ is shown in fig. 6.2. The structure can be divided into two main parts - the vacuum tank and the ladder structure:

- The vacuum tank comes in three parts, which are vertically divided over the full length of the RFQ. It consists of a lower shell, a middle frame and an upper

shell. Supported by dowel pins, the lower shell carries and adjusts the exact position of the resonating ladder structure. The pumping as well as pick-up flanges are located on the lower side. Tuner and coupler flanges are on top of the cavity. The main task of the tank is to provide a vacuum at the level of 10^{-8} mbar. The inner dimensions of the tank have no significant influence on the RF and the frequency. To minimize RF losses in the walls, the lower and upper shells are copper-plated. The components are bolted together and double vacuum sealed.

- The ladder structure, constituting the resonating structure, consists of two symmetric half-ladders (see fig. 6.3 right), each made from a single piece of bulk copper. The half-ladders press and grout the carrier-rings in between. The diameter of the precisely thrilled hole is slightly smaller than the carrier-rings, ensuring an optimal RF contact. Both half-ladders have significantly reduced contact surface areas between each other to improve the pumping speed and the operating pumping pressure. Indium sealings between the tank and the copper structure provide a good heat and RF contact.
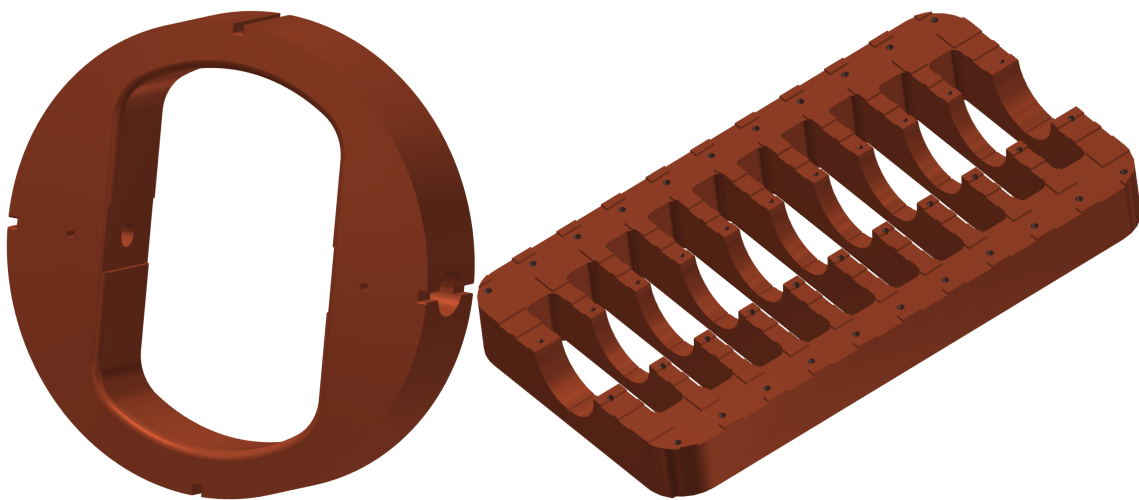
Figure 6.3: Isometric view of the ring (left) and the lower half-ladder (right). The outer diameter of the ring is 100 mm and the dimension of a half-ladder is 650x365x75 mm.

All components of the Ladder RFQ are screwed. Relinquishing any welding and brazing procedures guarantee a simple and precise assembling, as well as access to

all parts for maintenance. The rings are pressed in between the half-ladders and fixed via guide pins to prevent a rotation or displacement. The diameter of the rings (s. fig. 6.3 left) have a tolerance of $100^{+0.02}_{+0.00}$ mm. Yet, the absolute vertical and horizontal diameter of the ring is locally reduced by four slits of 2x2 mm each (s. fig. 6.3 left and fig. 6.4 right), which prevent the rings from any rotations within the ladder structure. The effective diameter at these points is $99.98^{+0.02}_{+0.00}$ mm. The cylindrical counterpart of the rings milled into each of the half-ladder has a lower allowance of $100^{-0.02}_{-0.04}$ mm. Accordingly, the absolute excess of the rings, which are pressed between the half-ladders, is between 0 and 4/100 mm. This value seems to be appropriate for two reasons. Firstly, the ring and the ladder have to fit perfectly without gaps to ensure an optimal electrical connection and to prevent sparking. Secondly, the ring must not be too large to still fit into the ladder structure and to avoid a gap between the upper and lower half-ladder. Similarly, the total width of the ladder structure is machined with a lower deviation of $150^{-0.10}_{-0.15}$ mm, which is slightly smaller than the middle frame, to be able to seal the tank neatly between the tank parts.
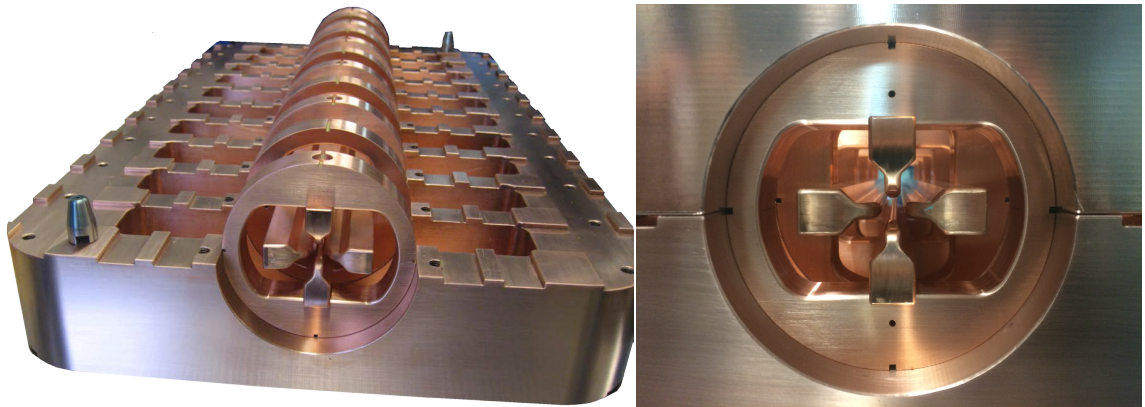
Figure 6.4: Isometric view of the ladder-ring system with the upper half-ladder removed (left) and the transversal view along the beam axis (right).

The contacting vis-á-vis surfaces between the half-ladders has been reduced by partly milling off the surface of the upper side of the lower half-ladder (s. fig. 6.3-6.5). Likewise, the surfaces between the bottom side rails of the lower half-ladder and the lower tank shell, respectively the top side rails of the upper ladder and the upper tank shell, are reduced. The idea of reducing contacting surfaces is based on

the risk minimization of virtual vacuum leaks as well as on reducing the pumping time. Additionally, the profile roughness parameter R_a needs to be kept within certain values. The roughness parameter is an indication for the smoothness of surfaces. It is calculated as the arithmetic average of the absolute amplitudes in the height profile on a two-dimensional surface. On sealing surfaces the surface roughness should not exceed $R_a = 1.6$ on sealing surfaces and 3.2 on surfaces within the vacuum, to minimize the total surface and pumping time. All surfaces intended to be copper-plated require a maximum roughness of $R_a = 3.2$.
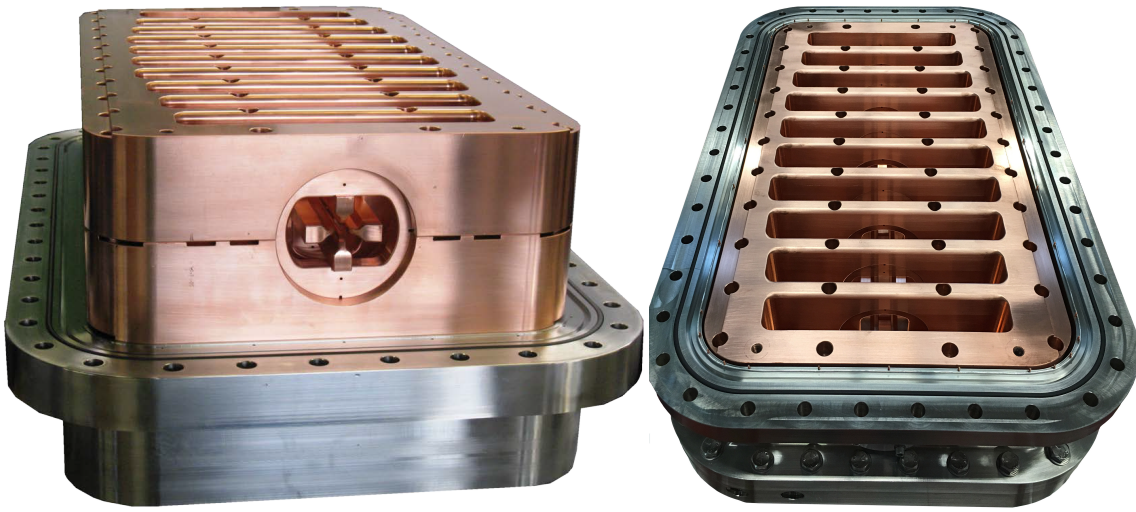
Figure 6.5: Isometric view of the Ladder RFQ before (left) and after (right) the assembly of the middle frame.

Present CNC milling techniques are able to provide the precision and accuracy, which is needed to fulfill the requirements of the beam dynamics calculations and simulations. The most important tolerance is the position of the electrode tip relative to the beam axis. Over the full length of the RFQ the absolute deviation may not exceed $5/100$ mm. Accordingly, the maximum transversal shift of the rings, respectively the cylindricity of the milled radii within the half-ladders, needs to be smaller than $5/100$ mm in relation to the theoretical beam axis. The distance of the opposing surfaces for the electrode mounting in the rings has a tolerance of $54^{+0.02}_{+0.01}$ mm. The error of the modulation profile in relation to the beam axis should be kept less than $3/100$ mm (s. fig. 6.6). For an improvement of the RF contact between the ladder structure and the tank indium sealings are used.
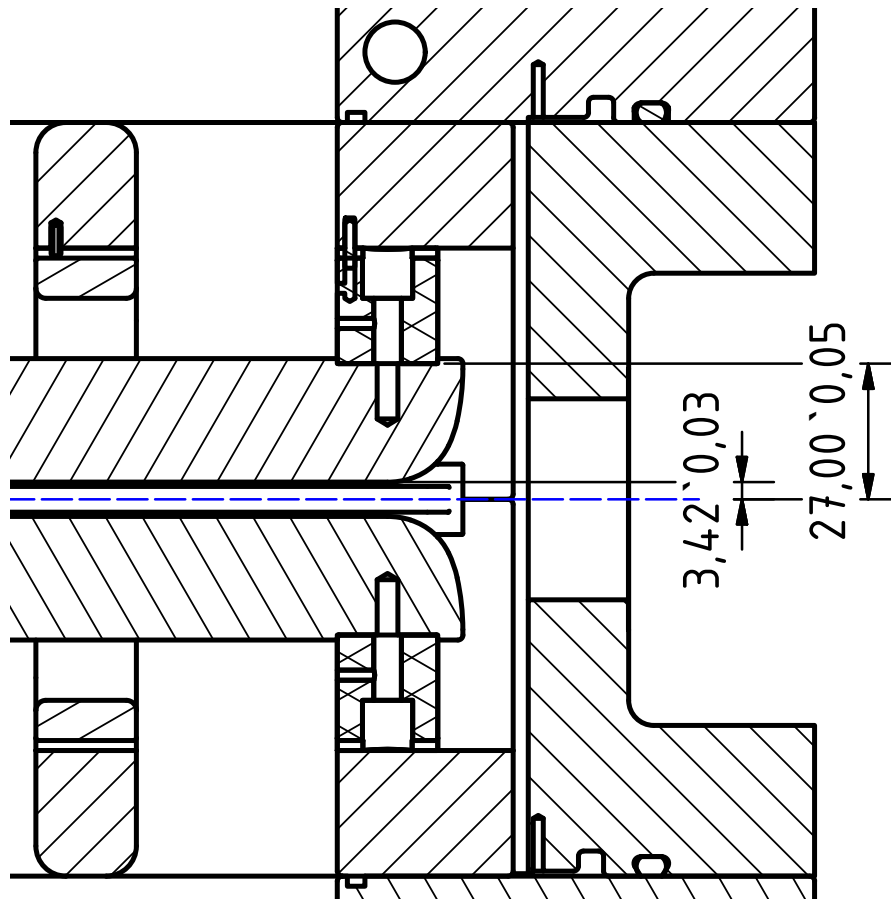
Figure 6.6: Detail drawing of crucial tolerances between the ideal
beam axis (blue dotted line) and the rings / aperture.

6.2 Vacuum System

The vacuum sealings of the tank consist of a two-stage differential pumping system
to reduce the relative pressure gradients (s. fig. 6.7). The outer sealing is a viton
o-ring within a dovetail nut. The prevacuum channel is pumped by two vertical bore
holes. To improve the pumping efficiency, the height of the prevacuum channel in the
tank is increased to a height of 4 mm compared to the UHV sealing surface, which is
milled off by 1 mm. The prevacuum and UHV is separated by an aluminum wire
with a diameter of 2 mm. The screw connection between the upper/lower tank shells
and the middle frame presses the wire down to a diameter of 1 mm. The aluminum
sealing is made out of a single wire, which is cold welded at its ends. It is held in
position by guide springs and pins. The schematic pumping diagram is shown in
fig. 6.8.
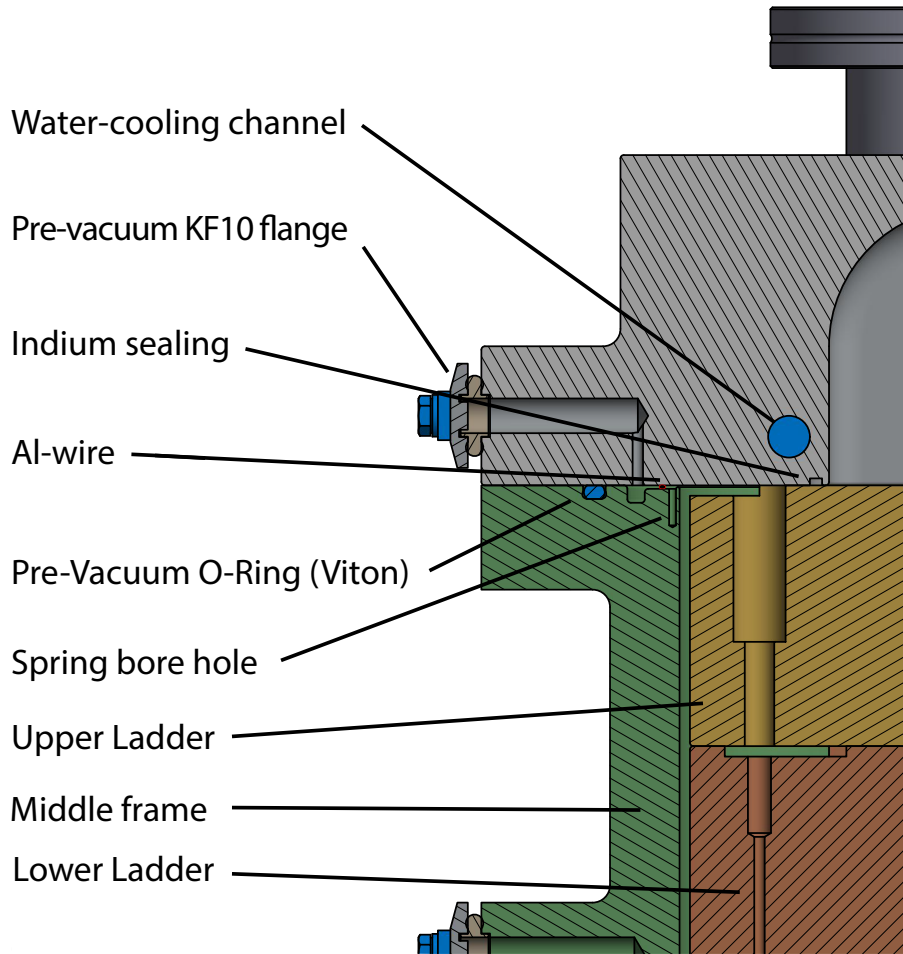
Figure 6.7: Schematic overview of the differential vacuum system.

The next step is to estimate the number and pumping speed of the turbomolecular pumps (TMP), which have to be used. The final end pressure p_{end}, which is reached after the pumping time t, times the effective pumping rate S_{eff} of the pump, equals to the sum of leakage rates $Q_i(t)$ [Pfeiffer-Vacuum, 2013]:

$$\sum_i Q_i(t) = p_{end}(t) \cdot S_{eff} \tag{6.1}$$

In comparison to the specific pumping rate of the pump, the effective pumping rate S_{eff} is reduced, due to a limited flange diameter and a certain length of the flange. The pumping flange is not completely milled out to optimize the current flow on the RF side. The most significant contribution to the leak rate of a perfect cavity without shrinkage cavitation is mostly dependent and given by the outgassing rate
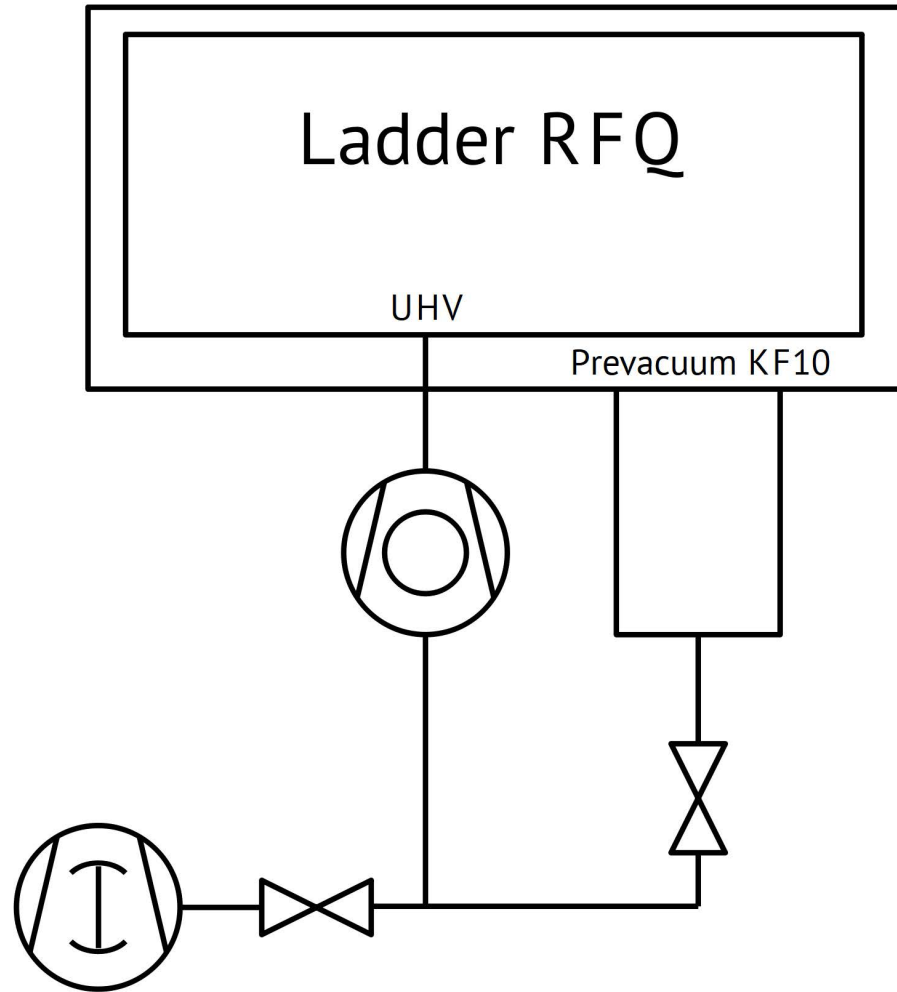
Figure 6.8: The schematic piping and instrumentation diagram of the prevacuum system.

of the surfaces. In case of the Ladder RFQ, the inner surfaces are large due to the ladder structure. The total area A is approx. $18{,}000\,\mathrm{cm}^2$. The leakage rate Q_{Des} from desorption of molecules on the metallic surfaces is linearly dependent from the actual pumping time t and the specific leakage rate q_{Des} after a certain time t_0, which is $3.5 \cdot 10^{-9}\,\mathrm{mbar} \cdot \mathrm{l/s/cm}^2$ for $t_0 = 5\,\mathrm{h}$ [Umrath, 1997]:

$$Q_{Des}(t) = q_{Des} \cdot A \cdot \frac{t_0}{t} \tag{6.2}$$

Whereas the rate for plastic materials depends from the square root of the pumping

time:

$$Q_{Diff}(t) = q_{Diff} \cdot A \cdot \sqrt{\frac{t_0}{t}} \tag{6.3}$$

Another contribution to the leakage rate, is the permeation of molecules through the walls of the cavity by diffusion:

$$Q_{perm} = k_{perm} \cdot A \cdot \frac{\Delta p}{d} \approx k_{perm} \cdot A \cdot \frac{p_{outer}}{d} \tag{6.4}$$

The process is not time dependent and can only be reduced by increasing the wall thickness d. The permeation rate k_{perm} varies for different molecules, temperatures and materials of the wall. The highest contribution to the permeation rate is caused by the diffusion of H_2 through viton sealings. The permeation rate is $k_{perm} = 3.5 \cdot 10^{-12}\,\mathrm{m^2/s}$ at room temperature. Permeation through metallic walls can be neglected. Another contributor is the leakage rate Q_L which is given by the change of the pressure $\dot{p}$ in a certain volume V, through leaks in the tank or virtual blow holes within the cavity. By using metal gaskets for the sealing of the CF flanges, appropriate manufacturing processes (e.g. low surface roughness, blow hole free materials) and a cleaning procedure suitable for UHV (i.e. high pressure water cleaning, ultrasonic cleaning with appropriate detergents and rinsing with deionized water at 50°C), a leakage rate Q_L of at least $10^{-8}\,\mathrm{mbar \cdot l/s}$ is achievable (cf. [Pfeiffer-Vacuum, 2013]). Thus, the leakage rate Q_L can be neglected hereafter.

In case of the prototype RFQ, which does not have viton sealings the total outgassing rate is $q_{Des} \approx 10^{-4}\,\mathrm{mbar \cdot l/s}$. The total time needed for pumping, until the desired end pressure of $10^{-8}\,\mathrm{mbar \cdot l/s}$ is reached, is calculated by the sum of the time needed for the backing pump with a pumping speed S_{BP} to reach the starting point of the turbo pump and the time to reach the working pressure according to eq. 6.1:

$$t_{tot} = \frac{V}{S_{BP}} \cdot \ln \frac{p_{atm}}{p_1} + q_{Des} \cdot A \cdot \frac{t_0}{p_{end} \cdot S_{eff,TMP}} \tag{6.5}$$

For the prototype, the interior Volume is $V = 35\,\mathrm{l}$ and the dry multi-stage roots pump, used as a backing pump, has a pumping rate of $37\,\mathrm{m^3/h}$. The TMP starts at

a pressure of $p_1 = 1 \cdot 10^{-3}$ mbar and has a specific pumping rate of $700 \, \text{l/s}$, mounted on a reducing flange from CF160 to CF100 at the tank. Moreover, the feed-trough of the pumping flange at the cavity is reduced by having bore holes instead of a single transfixion of the flange. On the one hand, the current flow and RF on the tank surface are thereby disturbed less and the RF is prevented from penetrating into the pump. On the other hand, the effective pumping rate of the TMP is reduced to approximately $260 \, \text{l/s}$. The effective pumping speed is calculated by the number n of TMPs, multiplied with their individual pumping speed S_{TMP}, divided by one plus the product of S_{TMP} and the conductance L of the gas through the pump line:

$$S_{eff,TMP} = \frac{n \cdot S_{TMP}}{1 + S_{TMP}/L} \tag{6.6}$$

Reaching an end pressure of 10^{-7} mbar takes a total pumping time of approximately one day. An end pressure of 10^{-8} mbar leads to a total pumping time of almost ten days. However, RF conditioning supports and shortens the pumping process, as the surface is cleaned due to the electric fields and local heating by electric currents favoring desorption. One turbo pump with $700 \, \text{l/s}$ will be sufficient for operation in any case. The gain in a reduction of the total pumping time by using a pump with a higher performance is negligible, as the effective pumping rate is limited due to the size of the flange.

6.3 Cooling System

The cooling system has to be capable of cooling the heat produced by Ohmic losses. The peak power losses (equivalent to total loss in case of a cw operation) of the prototype are $130 \, \text{kW}$ at an electrode voltage of $80 \, \text{kV}$. The average losses at a duty factor of 0.08% ($4 \, \text{Hz}$ repetition rate and $200 \, \mu\text{s}$ pulse length) are $100 \, \text{W}$. Besides a cooling by radiation and a heat transfer to the surrounding air, the RFQ will be cooled by a water cooling circuit in the tank. Both the lower and upper tank shells have cooling channels with a diameter of $12 \, \text{mm}$ (s. fig. 6.9). At a water pressure of $6 \, \text{bar}$ from the water circulation system, the volume flow is at least $3 \, \text{l/min}$ and therefore exceeds the minimum required water flow of $2.85 \, \text{l/min}$, as calculated in
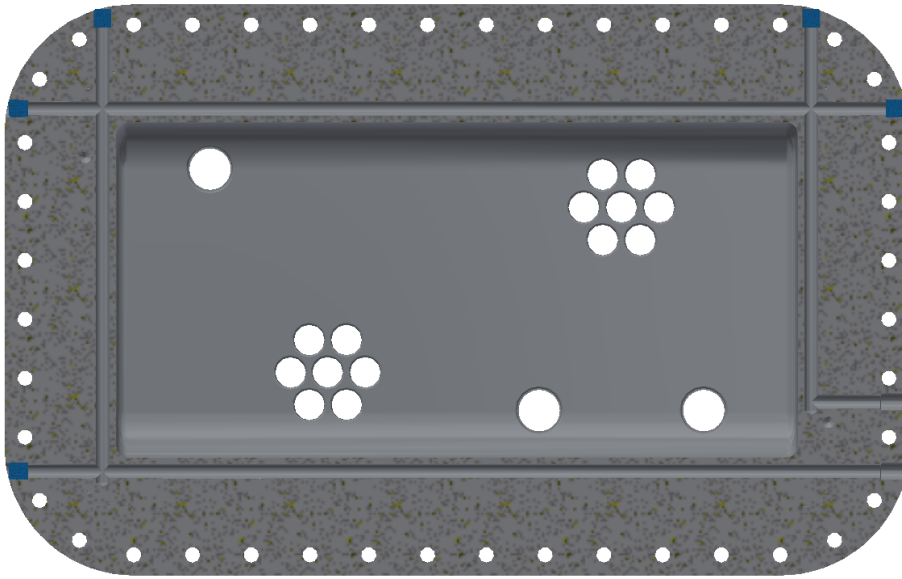
Figure 6.9: Visualization of the cooling channels in the lower shell of the tank. The plugs are colored in blue. The upper tank shell has identical cooling channels. The flanges for the pump (2 in total, one as spare) are not entirely drilled through to improve the current flow on the tank surface.

chap. 5.7. The channels are made by four deep-hole borings, which are led as near as possible to the inner surface and the cooper structure, to optimize the heat transfer. The water supply is connected via two 3/8" thread holes. The openings of the deep-hole bores are closed by stainless steel plugs welded into the tank.

6.4 Assembly

The lower shell of the tank serves as the basic alignment of the ladder structure. The supporting surface of the lower tank shell has a parallel tolerance of its upper surface of $\pm 5/100\,\text{mm}$. The relative horizontal position of the ladder structure is fixed by two guide pins between the lower tank shell and the lower half-ladder. Before lowering the lower half-ladder, the indium RF sealing has to be inserted. The half-ladders are also fixed by guide pins against each another and bolted together by four M6 screws per spoke, in order to ensure a seamless connection and ideal conduction between the rings and the ladder structure. The ring-electrode system can be assembled
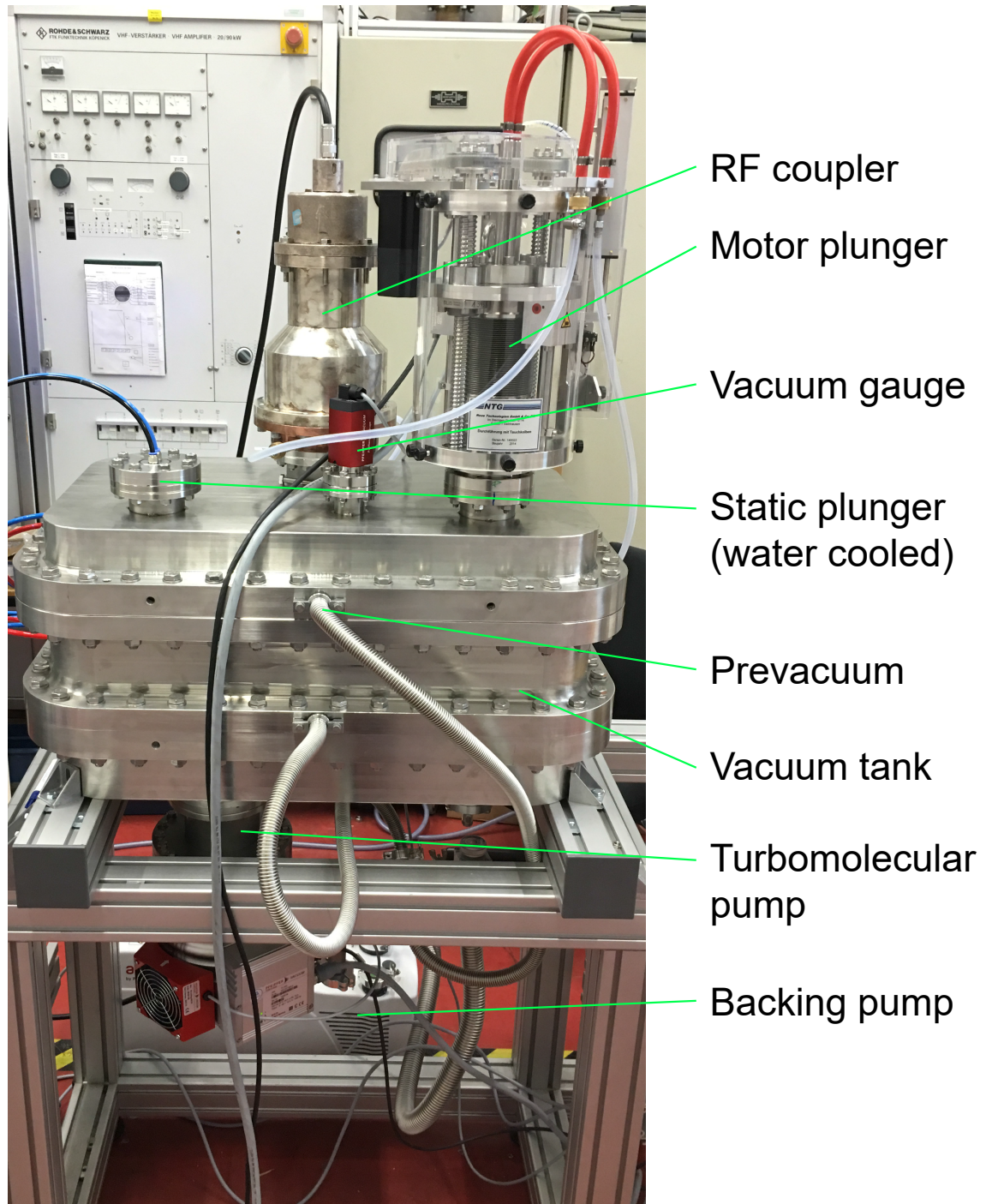
Figure 6.10: Fully assembled RFQ. On the upper tank shell: frequency plungers (static plunger on the left CF63 flange and motor tuner on the right side), coupling loop and vacuum gauge. On the lower side of the RFQ: Turbopump and multi-stage roots pump. The KF10 connection for the pre-vacuum is at the middle front.

separately and inserted as a single piece. To simplify the assembly all grooves for the vacuum sealings are on top of the components.

Once manufacturing of the cavity is finalized, the vacuum, tuner and water cooling support are installed. The following list gives an overview of all installed components:

- The permanent frequency tuner flange is made from a custom made water-cooled CF63 blank flange. The vacuum side is copper plated and includes a socket for mounting the solid permanent copper plunger (for the design and measurement of the plungers cf. chap. 7.3).

- The motor driven tuner with a structurally identical copper plunger is installed on the opposite side of the RFQ. The plunger depth is manually driven by means of a control electronics with a maximum stroke of 100 mm.

- A water-cooled inductive power coupler is installed on the upper CF100 flange. It connects the waveguide with the coupling loop. The mechanical design and measurements of the coupling loop are described in chap. 7.4. The power coupler is equipped with a 100 mm connection flange to a circular waveguide. For the low level RF tests, a transition to an N-connector[1] was assembled.

- For the UHV a HiPace 700 turbopump[2] with hybrid bearing is connected via a reducing flange from CF160 to CF100 on the lower side of the RFQ.

- A Pfeiffer ACP 40 backing pump, which is a multi-stage roots pump, generates the prevacuum. It is connected with KF 25 to the TMP and via KF 10 to the prevacuum flanges of the tank.

Fig. 6.10 depicts the RFQ assembled with all supports as explained above. The water cooling supply is provided by Festo[3] clutches for the circulation loop of both tank shells, the coupler, the motor plunger and the flange of the static plunger.

---

[1] Invented by Paul Neill in the 1940s at Bell Labs [Lee, 2004].

[2] for more informations cf. https://www.pfeiffer-vacuum.com/en/products/turbopumps/hybrid-bearing/hipace-700/

[3] cf. http://www.festo.com

Chapter 7

Measurements

> "That which is not measurable is not science."
>
> *Ernest Rutherford*

After the manufacturing had started in August 2014, the RFQ was delivered to IAP in February 2015. Among the first low-level RF measurements, performed at the non copper-plated Ladder RFQ, were the frequency and the quality factor, the frequency spectrum and the field flatness. Afterwards, the measurements were compared with the simulations, in order to find the appropriate ladder cell heights to match the exact operating frequency as well as to reach the desired field flatness. After the examination of the final tuning geometry, the next steps were reworks of the ladder structure, i.e. the final milling of the individual ladder cell heights and the copper-plating of the lower and upper tank shell from July to October 2015. After completing further corrections regarding the addition of pumping holes and dowel pins, the site acceptance test has been passed in December 2016. During the following two months the RF measurements were repeated and the RFQ was completely mounted and finalized for the conditioning and power tests, which took place from March to May 2016.

7.1 Frequency and Spectra

The frequency of the ground mode of the Ladder RFQ, used for operation, in the first manufacturing step was designed to be slightly higher than the final frequency by

purpose. In order to flatten the field flatness (s. chap. 7.2 for the flatness tuning) the cell heights have been increased in a second milling step, which leads to a decrease of the frequency. The frequency changes by approx. $-0.75\,\mathrm{MHz}$ per additional millimeter of the average cell height. Changing all cell heights by equal values modifies the resonance frequency without influencing the flatness, which, however, is solely adapted via the outer cells heights. A total additional layer of $5\,\mathrm{mm}$ per side in all cells allows a mechanical feasibility and a margin for the flatness tuning without risking to end up at a frequency, which is significantly lower than the design value.The frequency after the second machining step has to be slightly below the operating frequency, where it can still be adjusted by the inductive plungers.

Table 7.1: Development of the simulated designed frequency and its measured value for the different manufacturing stages. *) By default the background in CST provides vacuum properties. If the structure is embedded and filled by air at standard pressure, the simulation results will exactly be $100\,\mathrm{kHz}$ lower than the results shown here.

Measurement Stage	Frequency (sim.)	Frequency (meas.)
First delivery	$331.3\,\mathrm{MHz}$	$332.85\,\mathrm{MHz}$
After flatness tuning and copper plating	$323.4\,\mathrm{MHz}$	$324.96\,\mathrm{MHz}$
With mounted frequency plungers (initial position)	$323.5\,\mathrm{MHz}$	$325.06\,\mathrm{MHz}$
Evacuated	*)	$325.14\,\mathrm{MHz}$

Tab. 7.1 compares all measured frequencies with the simulated frequencies. For all kind of manufacturing steps and geometrical changes after adding the frequency plungers, the simulated frequency is $1.5\,\mathrm{MHz}$ below the measured value, which is $0.46\,\%$. The constant discrepancy of $1.5\,\mathrm{MHz}$ between simulations and the measurement was regarded in the simulations and favored the design of the final tuners as well as the flatness tuning. Therefore, the ladder cell heights were adjusted to obtain a frequency of $323.5\,\mathrm{MHz}$, which corresponds to $325\,\mathrm{MHz}$ in the measurements and is slightly below the design value of $325.224\,\mathrm{MHz}$. After evacuating, the frequency is expected to increase by approx. $100\,\mathrm{kHz}$, which was confirmed in the measurements. By using inductive frequency plungers, the frequency can only be raised. The final frequency - after evacuating the cavity and installing the frequency plungers in their

basic position - is 325.14 MHz, which is an ideal initial situation for operation, as the maximum frequency stroke is expected to be at least 300 kHz.

Model	Lorentz
Equation	y = y0 + (2*A/PI)*(w/(4*(x-xc)^2 + w^2))
Plot	D
y0	2.41907E-10 ± 6.96847E-11
xc	3.24963E8 ± 9.16163
w	64130.61958 ± 34.21865
A	0.05773 ± 2.80522E-5
Reduced Chi-Sqr	1.68726E-17
R-Square(COD)	0.99931
Adj. R-Square	0.99931
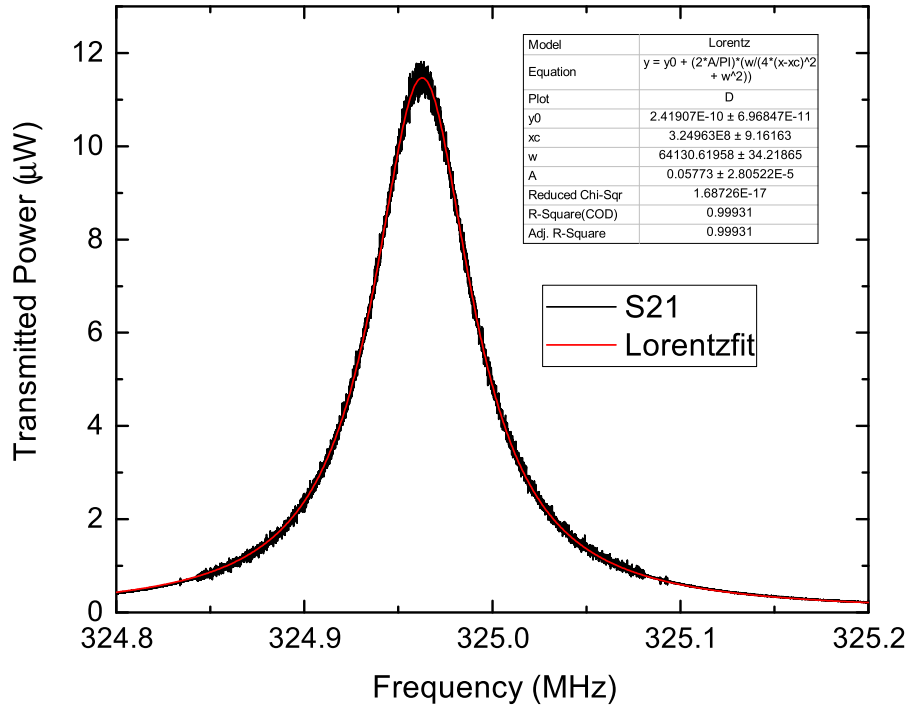
Figure 7.1: Resonance curve of the 0-mode after copper-plating and the power tests (atmospheric pressure and without frequency plungers). The FWHM is 64.13 ± 0.034 kHz according to the Lorentz fit.

Fig. 7.1 depicts the resonance curve for the RFQ after the conditioning and the high power measurements. The frequency plungers were removed and the cavity was aerated during the measurements. The S_{21} signal, measured with a minimum coupling, i.e. the coupling factor tends to approach zero ($\beta_e \to 0$) and can be neglected, is converted into the transmitted power P_t by:

$$P_t = P_{NWA} \cdot 10^{S_{21}[\text{dB}]/10} \tag{7.1}$$

The maximum output power of the network analyzer, which was used in the measurements, is $P_{NWA} = 13\,\text{dBm} = 20\,\text{mW}$. By fitting the measurement data with the Cauchy-Lorentz distribution, the resonance frequency f_0 as well as the FWHM Δf

can be determined. Hence, the quality factor is calculated by:

$$Q_0 = \frac{f_0}{\Delta f_{FWHM}} \tag{7.2}$$

Tab. 7.2 lists an overview of all measurements of the quality factor for different manufacturing steps and setups. In the first measurement with a stainless steel tank, a quality factor of 3000 was measured. The largest gain could be reached by copper plating the upper and lower tank shells, which led to an increase of the Q-value to 4600. Despite relatively low losses of 3% in the tank (cf. tab. 7.3), the relative permeability of stainless steel as well as the reduced conductivity $\sigma_{Cu}/\sigma_{SS} \approx 40$ reason the growth of the quality factor after the tank was copper-plated. After the power measurements the Q-value was determined by at least 5080, which is 75% of the simulated value. The most likely explanation is a cleaning of surfaces contaminated by oil and residuals from the manufacturing process during the high power RF conditioning.

Table 7.2: Development of the quality factor for different measurement stages. The errors are less than 1%.

Measurement Stage	Q_0
before copper plating	3000
after copper plating	4600
after power meas.	5080
with copper plates	5080
with AL RF sealings	5080
increased torque	5080

Finally, several measures were taken to investigate a possible growth of the quality factor. At first, the indium sealings have been replaced by aluminum, which has a better conductivity. Next, copper plates with a diameter of 10 cm have been implemented at the beam entrance and exit flange on the inner side of the tank. Due to the simulations, the middle frame of the tank only contributes with 0.03% to the losses (cf. tab. 7.3). Therefore the middle frame has not been copper-plated to save expenses of the prototype. By adding copper plates, losses that might occur

Table 7.3: Power losses itemized by the mechanical components of the Ladder RFQ according to the simulations with the CAD model.

Part	Losses (peak)	rel. Losses
Ladder structure	60.3 kW	57.1%
Rings (11 pcs.)	20.6 kW	19.5%
Electrode tip	0.3 kW	0.3%
Electrode body	21.3 kW	20.2%
Tank middle frame	0.03 kW	0.03%
Tank upper shell	1.5 kW	1.4%
Tank lower shell	1.5 kW	1.4%
Total	**105.5 kW**	**100%**
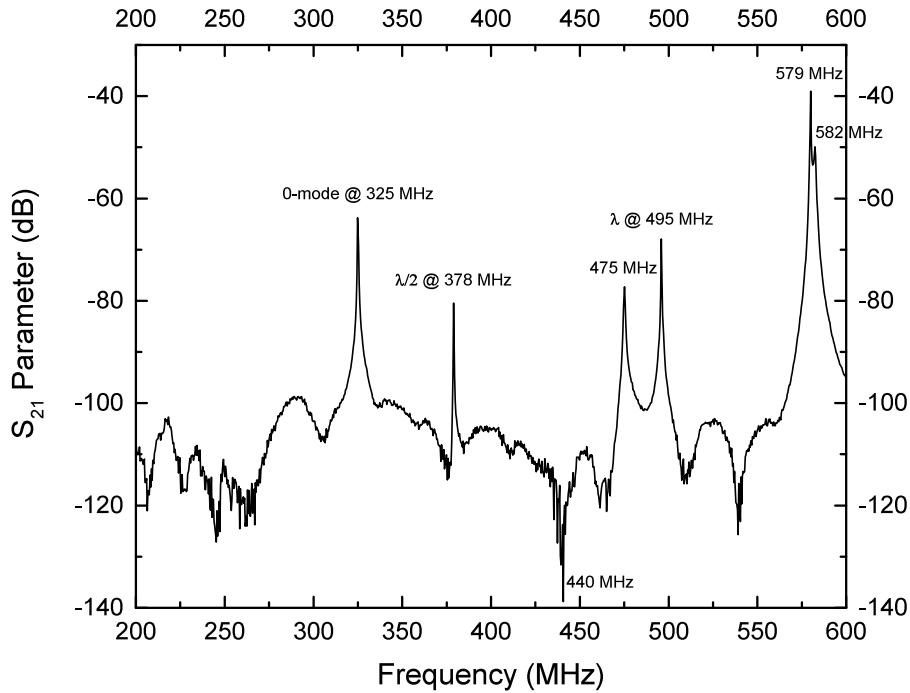
Figure 7.2: Frequency spectrum of the Ladder RFQ from 200 MHz to 600 MHz.

by induced currents due to the electrode potential on the facing steel tank surface can be excluded. Finally, the torque of the screwing between the electrodes and the rings has been raised by approx. 50% to uniformly 10 Nm and between the upper

and lower half-ladder to 35 Nm, respectively. Nevertheless, the measurements have shown that the quality factor was not influenced (cf. tab. 7.2).

The frequency spectrum was measured within a range from 200 MHz to 600 MHz (s. fig. 7.2). As expected, the 0-mode, which has a flat longitudinal field distribution, is located at 325 MHz. The first higher order mode (HOM), which is the $\lambda/2$-mode, i.e. the longitudinal field distribution has a maximum in the middle of the beam axis, is more than 50 MHz apart at 378 MHz. The 0-mode as well as the $\lambda/2$- and λ-mode were correctly predicted by the simulations. In the case of the relatively short prototype RFQ with an electrode length of 630 mm, interferences with higher order modes can be excluded.

7.2 Field Flatness
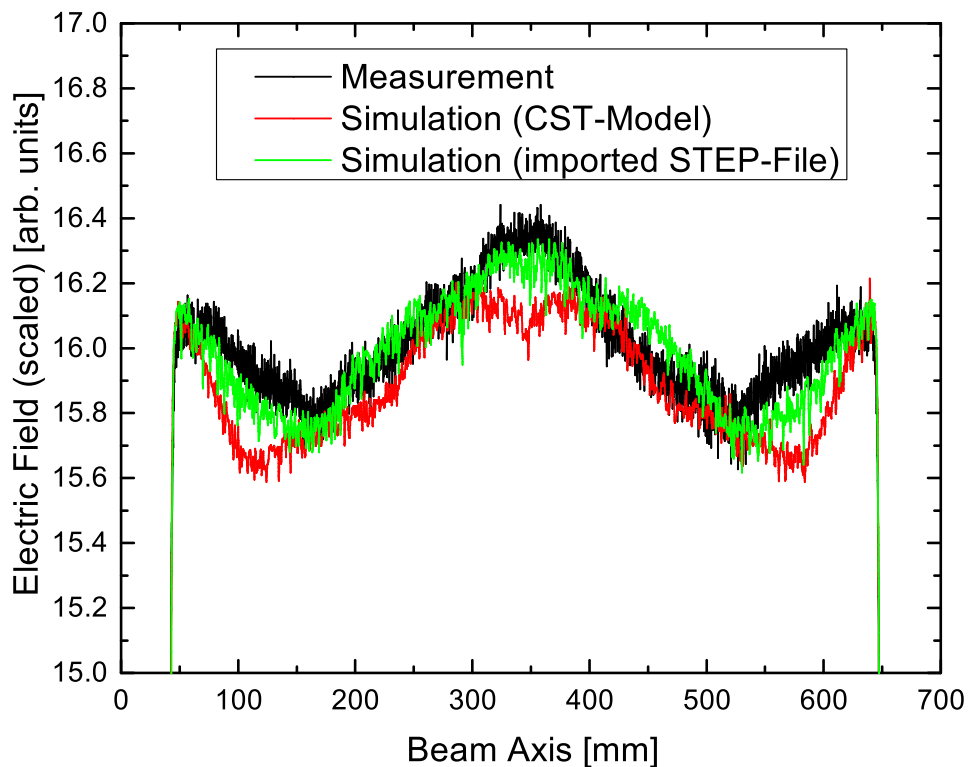
Figure 7.3: Comparison of the field flatness measurement between the first revision (black curve) with the simulations of the CST model (red) and the imported step file model (green).

The field flatness was measured before and after the tuning reworks by the second machining step - remilling the cell heights. The measurement results of the first revision of the RFQ, before it was copper-plated and finally flatness tuned, were compared with the simulations (s. fig. 7.3). The course as well as the relative difference of the field flatness simulations, both from the parametrized CST model and the imported step model, are in a good agreement with the measurement data within an error of less than 5%. The relative difference is determined by the averaged maximum field value, subtracted by the minimum field value and divided by the average field value. This results in a relative field flatness of $\pm 1.9\%$ after the first revision. With the confirmation of the consistency between the simulations and the measurements, the final tuner parameters, which are the individual cell heights of each ladder cell, were examined in simulations with different tuning configuration. As explained in the simulations chapter (chap. 5.3), only the first and last three ladder cells need to be adjusted to flatten the field. In a second machining step and contemporaneous copper plating of the tank, all cell heights were milled to their

±0,4% overall Flatness
±0,1‰ on 70% of Beam Axis
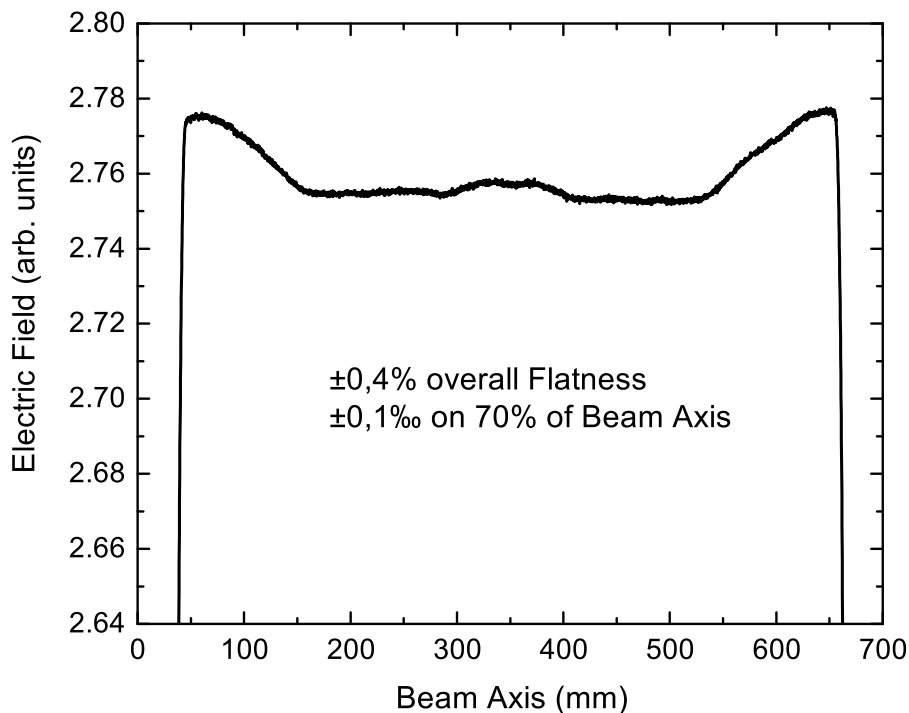
Figure 7.4: Bead pull measurement of the final field flatness of the second revision along the beam axis with adjusted tuner heights.

105

final height to match both the field flatness and the frequency. The result of the measured field flatness after the second revision is shown in fig. 7.4. The relative field flatness has dropped to less than $\pm 0.4\%$ and $\pm 0.01\%$ along 70% of the beam axis. In contrast, the simulations predicted a relative field flatness of approx. $\pm 1.4\%$ (s. fig. 7.5 left). This configuration of the cell heights seemed to be the optimum distribution according to the simulations (rel. Flatness: $\pm 1.3\%$). However, the errors of the simulation are larger than the measured field flatness. A possible explanation for those errors could be the limited number of tetrahedrons of the mesh. As a consequence, the surface is not smooth and generates errors like this. The noise can be reduced by smoothening the simulation results with a percentile median filter (cf. green curve). The direct comparison between the first and second revision is shown in fig. 7.5 (right), which clearly visualizes the influence and profit of the tuning process.
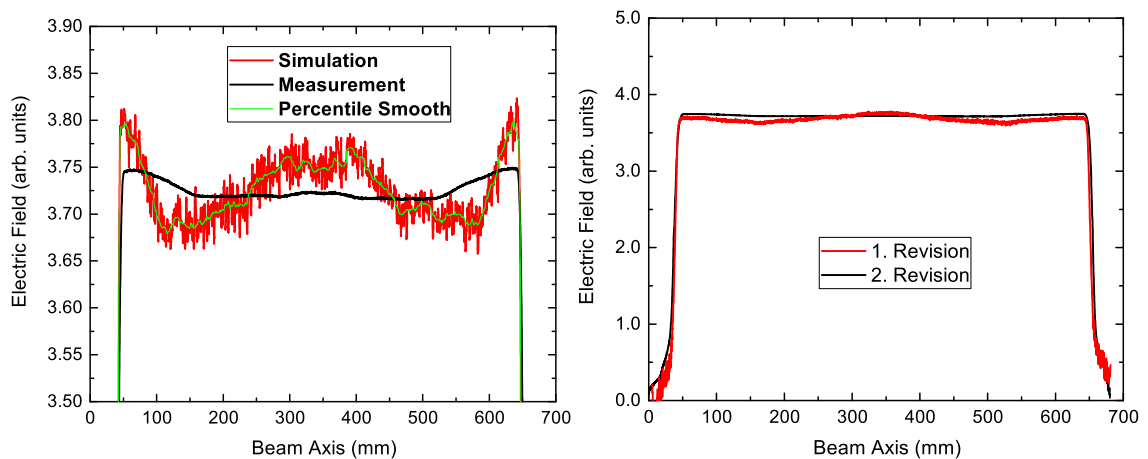
Figure 7.5: Left: Comparison between the field flatness measurement of the second revision and the simulations. Right: Comparison of the measurements of the field flatness between the first (red) and second revision (black) after the final tuning process.

The field flatness is measured by the bead pull method. A small bead is pulled through the cavity on the beam-axis[1]. The unmodulated electrodes simplify the measurement and allow for an on-axis measurement technique. The bead is made of a Teflon cylinder with a length of 10 mm and a radius, which is equal to the mean

---

[1]Even in the unmodulated RFQ, which actually has no electric field component on-axis, the dimensions of the bead are sufficient to influence non field free regions.
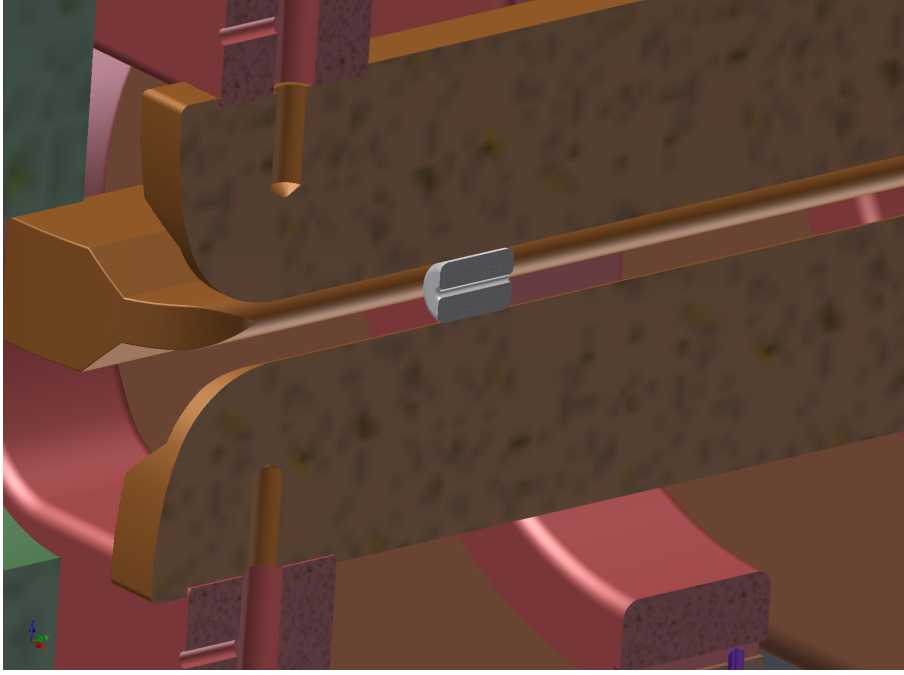
Figure 7.6: Visualization of the bead pull measurement. The radius of the cylindrical Teflon bead (grey cylinder) equals the aperture and is guided by the unmodulated electrodes.

aperture (s. fig. 7.6). The electrodes therefore serve as a guide for the bead. The bead leads to a local variation of the field energy and, according to the Slater theorem [Slater, 1946, Slater, 1950, Maier and Slater, 1952], to a change of the resonance frequency (cf. eq. 5.8). The total change of the frequency, which is the difference between the disturbed ω and the undisturbed ω_0 frequency, can be expressed by the actual field the bead displaces [Wang, 2015]:

$$\frac{\omega - \omega_0}{\omega_0} = -\frac{\oint_{\partial V} \left((\mu_r - 1)\mu_0 H^2(x,y,z) + (\varepsilon_r - 1)\varepsilon_0 E^2(x,y,z) \right) \mathrm{d}V_{bead}}{\oint_V \left(\mu_0 H^2(x,y,z) + \varepsilon_0 E^2(x,y,z) \right) \mathrm{d}V_{Cavity}} \qquad (7.3)$$

The denominator equals the undisturbed field energy within the volume of cavity, whereas the numerator represents the field energy change due to the disturbance within the volume of the bead. For the cylindrical Teflon bead used in these measurements the volume is $V = \pi r^2 l$, the relative permittivity $\varepsilon_r \approx 2.1$ and the magnetic permeability equals $\mu_r = 1$. Consequently, the equation can be reduced to

the mean electric component along the beam axis z:

$$\Delta\omega(z)/\omega_0 \propto -\frac{\pi r^2 l}{W}\varepsilon_0 \bar{E^2}(z) \tag{7.4}$$

Due to the relatively small size of the bead, the influence on the frequency is very small, compromising a measurement. Instead, a higher precision is be achieved by the measurement of the phase difference. The phase difference of the forced oscillation of the RFQ is measured by the S_{21} signal, which indicates the phase difference between the forward and transmitted wave. For small angles, the phase is related by $\tan\Delta\varphi = 2Q\Delta\omega/\omega_0{}^2$ to the linear range of the resonance frequency ω_0. Thus, the root mean square of the electric field $E(z)$ is proportional to the square root of the phase difference, while pulling the bead along the beam axis z:

$$\sqrt{\bar{E^2}(z)} \propto -\sqrt{\tan\varphi(z)} \tag{7.5}$$

Another important aspect is the influence of the frequency plungers on the field flatness. The displacement of the magnetic field of the plunger, on the one hand, has to be large enough to generate a sufficient range of the tuning shift. On the other hand, the influence on the local voltage difference of the electrodes has to be kept as small as possible. The overall influence of the effective penetration depths of both plungers, which is the length of the frequency plunger within the RFQ, can be seen in fig. 7.7. The black curve represents the field flatness without any plungers (plunger height $= 0\,\mathrm{mm}$)[3]. For a single penetration depth of one tuner up to $150\,\mathrm{mm}$, the relative course of the electric field along the beam axis as well as the absolute field strength is not affected significantly. The absolute field begins to decrease as both tuners become larger than $145\,\mathrm{mm}$. The reason is a growth of losses as the plungers are excited by an eigenmode and the stored energy of the RFQ and the voltage of the electrodes, respectively, decreases (for tuner eigenmodes cf. chap. 5.4). For even larger tuner depths beyond $160\,\mathrm{mm}$, an operation of the RFQ is not possible any more.

---

[2]A derivation of that relation can be found in [Klein, 1992].

[3]The plunger height or penetration depth refers to the clear length of the plunger within the cavity, i.e. from the inner shell surface to the top of the tuner (cf. fig. 5.10).
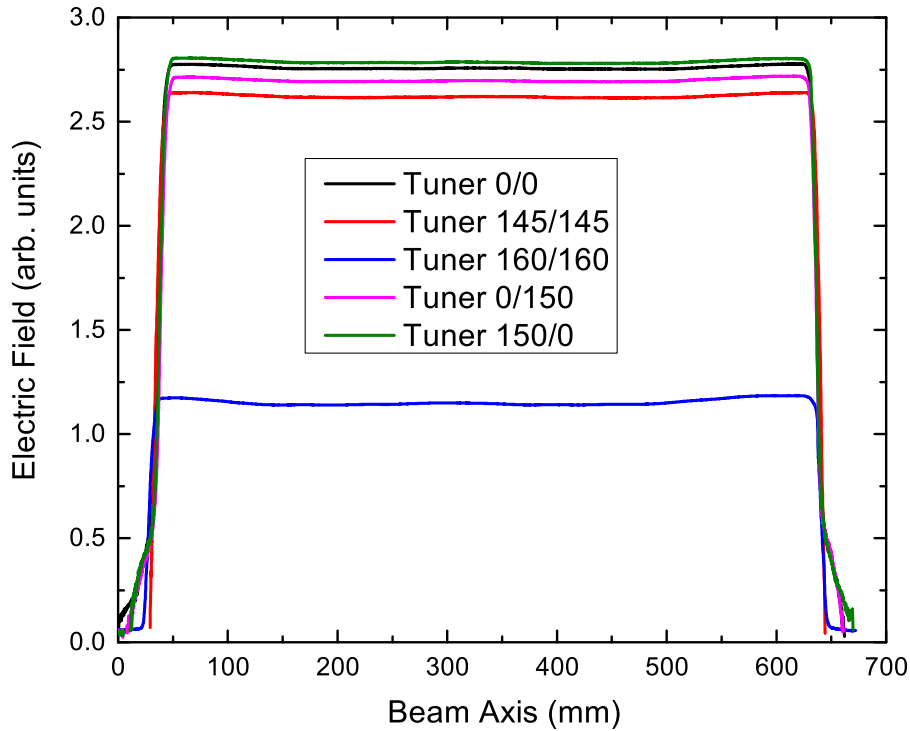
Figure 7.7: Measurement of the field flatness for various penetration depths of the static and motor driven frequency plunger. The field flatness will not be affected from both plungers, if a total penetration depth of 150 mm is not exceeded. The difference in the relative electric field for tuner heights up to 150 mm is less than 5%. These errors are owed to different independent measurements and measurement inaccuracies above all in finding a base line for the phase difference. Therefore, a physical relevance is only given for large tuner heights above 145 mm.

7.3 Frequency Plunger

During operation, two frequency plungers are used for the fine tuning of the frequency and fast frequency corrections due to detuning as the cavity heats up due to the power dissipation. The plungers are machined from a solid cylindrical copper block. The diameter of 28 mm and the transversal offset from the beam-axis of 107.5 mm are designed to maximize the displacement of the magnetic field and to enhance the overall frequency shift, respectively (cf. simulations in chap. 5.4). As a consequence, the penetration depth can be kept small to prevent a perturbation of the accelerating mode and the field course on the beam axis. One plunger is a static plunger with a
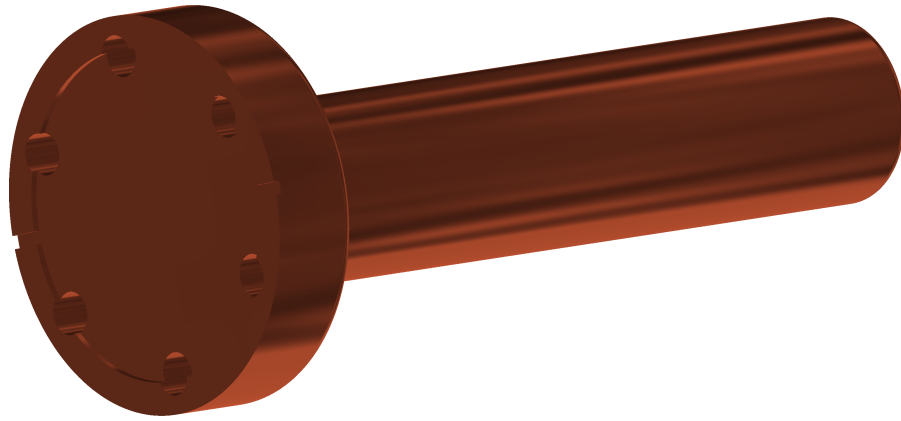
Figure 7.8: Isometric view of the static frequency plunger with a diameter of 28 mm and a length of 145 mm.

fixed length of 145 mm, which equals to an effective tuner height of 98 mm within the cavity (s. fig. 7.9). The plunger is mounted on a copper-plated CF63 flange which is water-cooled. The second plunger is motor-driven with a maximum stroke of 90 mm. The design resembles the static tuner, but it has a reduced length of 121 mm. The lengths of both plungers are designed to achieve equal penetration depths at the operating frequency without power. When the motor plunger is in an
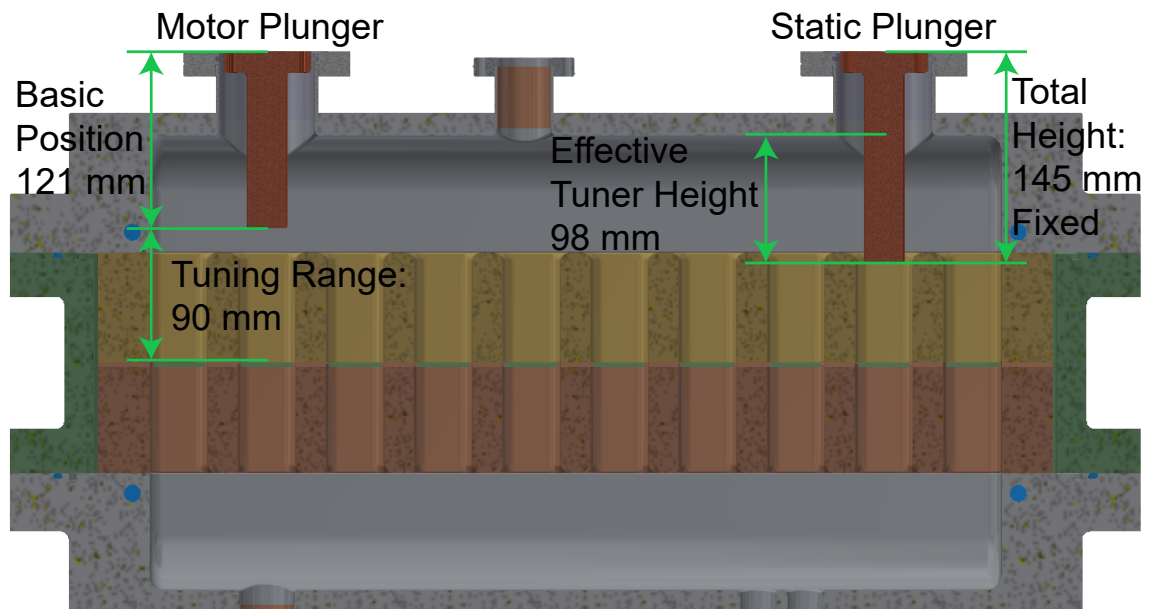
Figure 7.9: Longitudinal transverse section at the tuner plane $y = 107.5$ mm for the visualization of the final tuners in the RFQ as built.

extended position, the resonance frequency is 325.14 MHz, which is 84 kHz below the operating frequency.
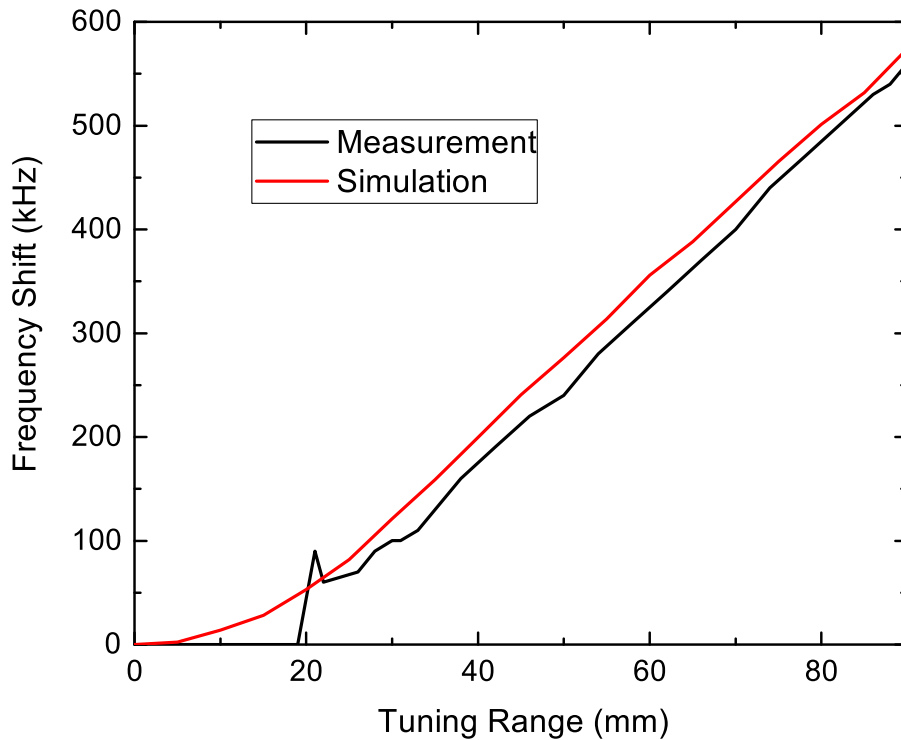
Figure 7.10: Frequency shift in dependence of the motor tuning range and the static plunger fixed at 145 mm. The tuners as built have a diameter of 28 mm and a transversal offset from the beam axis of 107.5 mm.

The frequency shift is plotted in fig. 7.10 in dependence of the tuning range of the motor-driven plunger. The basic position of the motor plunger without power and beam load at room temperature is 27 mm to match the frequency of 325.224 MHz. During operation, the frequency will decrease as the cavity heats up due to the RF power resulting in a thermal expansion of the materials. Accordingly, the working area of the tuner ranges from a penetration depth of 27 mm to 90 mm, leading to an effective maximum tuning range of 470 kHz. The basic operation point is slightly above a tuner eigenresonance located at a tuner depth of 20 mm, at which an operation of the cavity is not possible. Yet, that tuning range can be neglected as the working area is above that point. The eigenresonance occurs, when the plunger is driven into the field at a certain length of approx. $\lambda/8$. However, with regard to a

future design of a Ladder RFQ, the shape of the plungers may be constructed with a different shape than a homogenous cylinder, for which an eigenresonance of the tuner is further shifted to lower frequencies and penetration depths, respectively, or completely suppressed.

7.4 Power Coupling
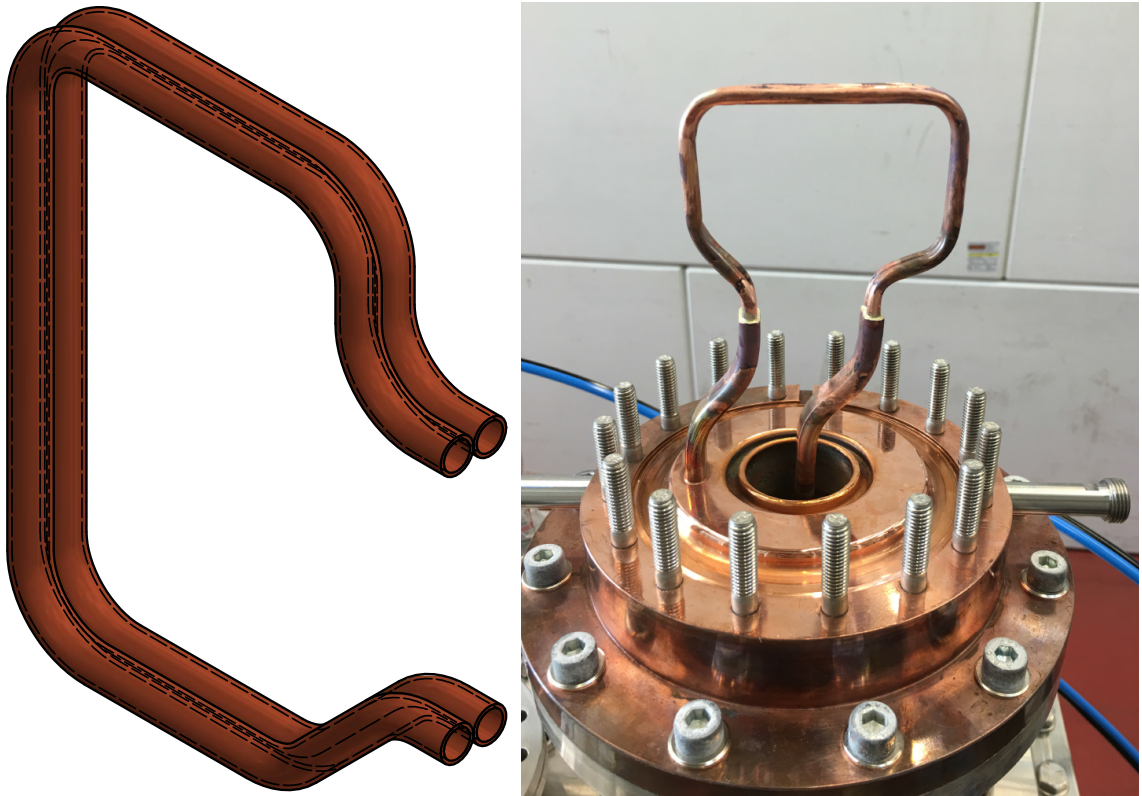
Figure 7.11: Isometric drawing (left) and photograph of the brazed coupling loop.

The dimensions of the power loop coupler (s. fig. 7.11) have been designed according to the simulations. The following chapter describes the measurements of the external quality factor and the coupling strength of the power coupler. The loop is made of a water-cooled 5x0.5 mm copper double pipe. With an offset of 10 mm is slightly asymmetrically shaped in relation to the rotation axis of the flange, to gain different coupling strengths by rotating the coupler by 180°. Thus, the overall scope of different configurable coupling strengths is enhanced, compared to a symmetric coupling loop. Beside the power coupler, three pickups are installed on the lower

side of the cavity to survey the resonance frequency and phase for controlling the motor plunger as well as for monitoring the field energy stored in the RFQ. Once a couplers are attached to the cavity, they dissipate and conduct power throughout the coupler P_e and the pickups P_t. The total loss P of the RFQ accordingly is:

$$P = P_c + P_e + P_t \tag{7.6}$$

The intrinsic quality factor is defined by the Ohmic losses of the cavity itself:

$$Q_0 = \omega \cdot \frac{W}{P_c} \tag{7.7}$$

Analogous to that definition, the external Q_e refers to the losses of the energy flow through the coupler:

$$Q_e = \omega \cdot \frac{W}{P_e} \tag{7.8}$$

The loaded Q is associated with the total losses:

$$Q_L = \omega \cdot \frac{W}{P} \tag{7.9}$$

The individual Q-values are connected by the following relation:

$$\frac{1}{Q_L} = \frac{1}{Q_0} + \frac{1}{Q_e} + \frac{1}{Q_t} \tag{7.10}$$

The introduction of the coupling parameter β gives an expression for the strength and interaction of the coupling between the waveguide and the cavity.

$$\beta_e = \frac{Q_0}{Q_e} = \frac{P_e}{P_c} \tag{7.11}$$

Likewise, a β_t for the pickup can be defined. Together with eq. 7.10 the intrinsic quality factor Q_0 yields:

$$Q_0 = Q_L \cdot (1 + \beta_e + \beta_t) \tag{7.12}$$

If $\beta < 1$ ("undercoupled resonator"), the losses through the coupler will be lower than the intrinsic losses. Hence, the loaded Q_L equals the intrinsic Q_0, in case the coupling of the pickups is very low ($\beta_t \ll 1$). As a pick up only serves as a detector of the phase and for an amplitude measurement of the stored field energy, its loop is kept very small. The resonator will be "critically" coupled, if $\beta_e = 1$, i.e. the power, flowing through the coupler, equals the resonator losses $P_e = P_c$ and $Q_e = Q_0$, respectively. Thus, the intrinsic Q_0 is then twice the loaded quality factor Q_L. If $\beta > 1$, the cavity is said to be "overcoupled" adequately. In order to compensate beam power in operation, the RFQ has to be overcoupled adequately for the given beam power. In case of the p-linac, the total beam power is $P_b = 210\,\text{kW}$ for a beam current of $70\,\text{mA}$ accelerated by the RFQ to $3\,\text{MeV}$. The beam load lowers the loaded quality factor and more power has to be coupled into the cavity to reach the design voltage of the cavity. The loaded quality factor thus yields:

$$Q_L = \frac{\omega \cdot W}{P_c + P_b + P_e + P_t} \tag{7.13}$$

Accordingly, during assembly the power coupler has to be adjusted, so that the resonator is critically coupled without beam, i.e. the external coupling strength β_e becomes at least one plus the proportion for the beam power. In other words, the overall coupling factor β then corresponds to the combined losses of the coupler and the beam load:

$$\beta = \frac{P_e + P_t + P_b}{P_c} \approx 1 + \frac{P_b}{P_c} \tag{7.14}$$

From the equivalent circuit of a transmission line coupled to a resonator, the reflection coefficient can be obtained by:

$$\Gamma = \frac{\beta - 1}{\beta + 1} \tag{7.15}$$

Additionally, the reflection coefficient is given by the ratio of the reflected and forward amplitudes and voltages, respectively, of the RF wave:

$$\Gamma = \pm\sqrt{\frac{P_r}{P_f}} = \pm\frac{U_r}{U_f} \tag{7.16}$$

Combining eq. 7.15 and eq. 7.16 β_e yields:

$$\beta_e = \frac{1 \pm \sqrt{\frac{P_r}{P_f}}}{1 \mp \sqrt{\frac{P_r}{P_f}}} \tag{7.17}$$

The ratio of P_r/P_f is determined by a network analyzer (alternatively by a power meter). The RFQ can be seen as a two-port network with the coupler as port 1 and the pickup as port 2. The S_{11} parameter is the input voltage reflection coefficient [Zinke and Brunswig, 1999], respectively the ratio of reflected power to input power in decibel. Thus, the coupling strength can be easily calculated by:

$$\beta_e = \frac{1 \pm \sqrt{10^{S_{11}[\text{dB}]/10}}}{1 \mp \sqrt{10^{S_{11}[\text{dB}]/10}}} \tag{7.18}$$

The sign depends on whether the cavity is over- or undercoupled. By calculating β and inserting into eq. 7.12 the intrinsic quality factor is determined reliably. If Q_0 is measured directly with a very small coupling strength, i.e. $\beta_e \to 0$ and errors become very high, due to a low transmission of the transmitted power $S_{21} < -80\,\text{dB}$, the quality factor can be corrected via the S_{11}-Parameter. Furthermore, the position of the coupling loop, which refers the magnetic flux and coupling strength, respectively, does not have to be regarded. The coupling strength of the pickup, in general, can be neglected for small loop sizes. In case of the prototype, the forward power gain is $S_{21} \approx -50\,\text{dB}$, i.e. $\beta_t \to 0$. During the assembly, the power coupler was positioned to be overcoupled with a reflection of $S_{11} \approx -31.2\,\text{dB}$. After tightening the coupler screws, the reflection increased to $S_{11} \approx -24.6\,\text{dB}$ and to $S_{11} \approx -9.55\,\text{dB}$ in vacuum, which corresponds to a coupling strength of $\beta_e \approx 2$, matching the simulations, where the induced voltage for the coupling loop is approx. $\sqrt{2}$ times the voltage which is needed to compensate P_c:

$$\beta_{e,sim.} = \frac{P_e}{P_c} = \frac{U_{ind}^2/2Z_0}{U_0^2/2Z_0} = \frac{U_{ind}^2}{U_0^2} \approx 2 \tag{7.19}$$

If the power dissipation of the pickup may not be neglected, the quality factor is be

calculated by:

$$Q_t = Q_0 \cdot \frac{P_c}{P_t} = Q_0 \cdot \frac{P_f - P_r - P_t}{P_t} = Q_0 \cdot \frac{1 - P_r/P_f - P_t/Pf}{P_t/P_f} \qquad (7.20)$$

in terms of the scattering parameters it can be expressed by:

$$Q_t = Q_0 \cdot \frac{1 - 10^{S_{11}[\text{dB}]/10} - 10^{S_{21}[\text{dB}]/10}}{10^{S_{21}[\text{dB}]/10}} \qquad (7.21)$$

The external quality factor of the pickup, used for the Ladder RFQ prototype, becomes $Q_t \approx 4.5 \cdot 10^7$ and, accordingly, the coupling factor $\beta_t \approx 1.1 \cdot 10^{-4}$ can be neglected.

7.5 Power Measurements

The final measurements included the conditioning and high power tests to proof functioning and the electric strength. In March 2016, the conditioning took place in-house at IAP Frankfurt up to 440 W cw and also pulsed. Immediately following from April to Mai 2016, the high power tests were performed in the test bunker of GSI at the 325 MHz klystron test stand.

7.5.1 Low Level RF Pre-Conditioning

The cavity is not able to accept high power signals ab initio. Impurities on the surfaces, dust particles and absorbed gas molecules on the vacuum walls lower the withstanding capability for electric surface fields and produce sparking and electrical breakdown due to discharges and multipacting. As a consequence, almost all forward power is reflected due to a collapsing coupling factor, leading to a deterioration of the vacuum and to power interlocks. During the conditioning procedure, i.e. by maintaining low intensities and slowly raising the power, which is coupled into the cavity, the rate of breakdowns decreases during conditioning by burning off dust particles in a plasma on the surfaces of the resonator components. Thus, multipacting and sparking can be reduced by improving the purity of the surface.

Figure 7.12: Schematic setup of the RF components for low level RF tests and conditioning of the RFQ.

For the low power test and conditioning, the in-house test stand for superconducting cryomodules at IAP was used[4]. The RFQ was driven with up to approx. 440 W at 100% duty cycle, which corresponds to almost four times the thermal design power and also pulsed with various duty factors. The experimental setup is shown in fig. 7.12. A function generator creates a low level sine voltage at 325.224 MHz and drives the input of the amplifier. The amplified RF signal is connected with a circulator, a three-port device which transmits every incoming RF signal at one port within a small bandwidth of approx. 2 MHz to the next port in rotation and protects the amplifier from reflected power signals. With intrinsic losses of approx. 0.1-0.3 dB, it transmits the forward power to the cavity and, at the same time, it redirects reflected signals from the cavity into a water-cooled load at port three. Besides sending the input power from port one to port two, the bi directional coupler branches the forward and also the reflected signals to ports three and four with an attenuation of −44 dB. These signals are split to be measured simultaneously with a

---

[4]Special thanks to H. Podlech et al. for the support and provision of the equipment, used for conditioning.

Figure 7.13: Forward (yellow), reflected (blue) and transmitted (purple) voltage signals during the pre-conditioning of the RFQ up to 500 W.

power meter and to survey their time-resolved behavior with an oscilloscope. The output port of the bi directional coupler is connected to the power loop coupler of the RFQ. The losses of all cables, couplers and RF-components were measured in advance to gain reliable data from the power meters. No frequency, amplitude and phase control units were used for these measurements. Instead the frequency were manually adjusted within the range of 100 kHz.

The time-dependent voltage signals are shown in fig. 7.13. The rectangular shaped forward power signal, colored in yellow, has a length of 140 µs. The reflected signal, colored in blue, clearly indicates that the RFQ is over-coupled. According to the

relation of the peaks P_1, when the RF is switched on, and P_2, when the RF is switched off, the coupling strength can be estimated in case of a theoretically[5] rectangular shaped forward signal:

$$\beta_e = \frac{1}{2\sqrt{\dfrac{P_1}{P_2}} - 1} = \frac{1}{2\dfrac{U_1}{U_2} - 1} \approx 1.5 \tag{7.22}$$

The accuracy of this method is, in contrast to the measurement of the reflection coefficient S_{11}, more inaccurate, because the resolution of absolute height of the voltage signals with the digital oscilloscope is limited. Nevertheless, it can be verified that the RFQ is over-coupled, which is in accordance with the results calculated and simulated in the previous chapter.
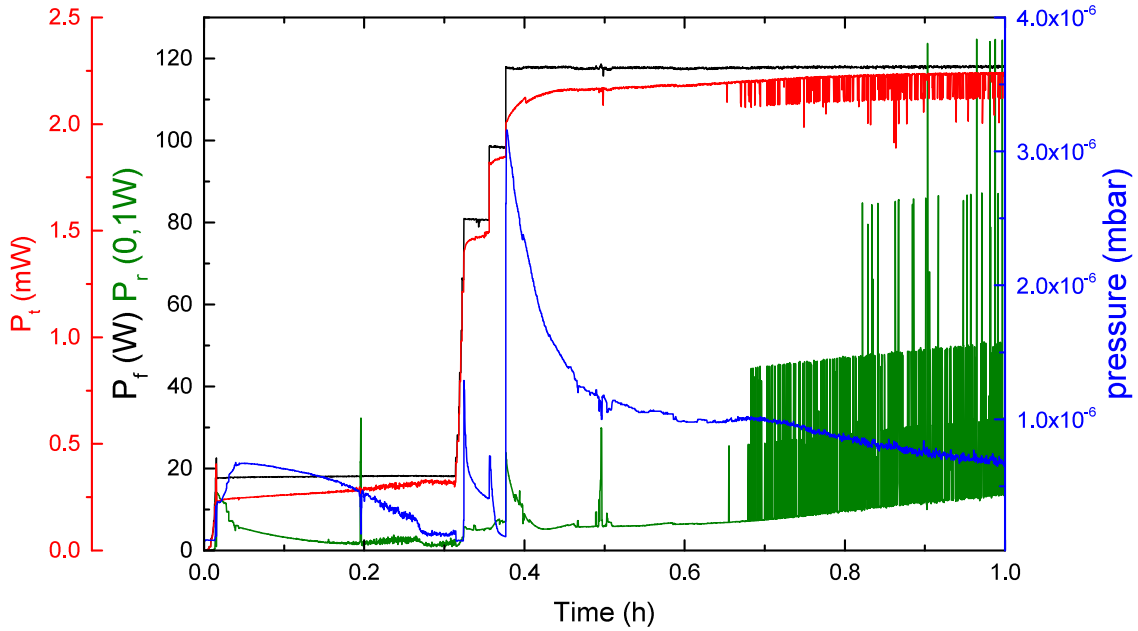
Figure 7.14: Progress of the forward power P_f (black), the reflected power P_r (green), the transmitted power P_t (red) and the pressure (blue) during conditioning up to 120 W.

The progress of the conditioning process up to 120 W forward power is plotted in fig. 7.14. The RFQ had already been conditioned up to 20 W in advance, where

---

[5]As the devices and the RF are limited within a small frequency band, a perfectly rectangular shaped curve is not possible and always features an overshoot.

most of the multipacting thresholds occur. The forward power (plotted in black) is slowly raised further until a new threshold emerges, e.g. for $P_f \approx 80\,\text{W}$. The pressure rises, as the reflection P_r increases and the transmitted power P_t decreases. The power is kept at that level until arcing effects have diminished, all of the forward power is accepted and the transmitted power has reached the flat-top. The low level conditioning took seven days in total at different power levels and pulse lengths (between $10\,\mu\text{s}$ and $200\,\mu\text{s}$). The duty factor was varied between 10% and 100%. The maximum energy, used for conditioning, was $440\,\text{W}$ cw. The low-level RF pre-conditioning is inevitable for subsequent high power tests, as the GSI test stand starts at a minimum operating power of approx. $1\,\text{kW}$ due to a reasonable limited dynamic range of the measurement instruments. Once the pre-conditioning had been completed in March 2016, the high power measurements could be started.

7.5.2 High Power Test
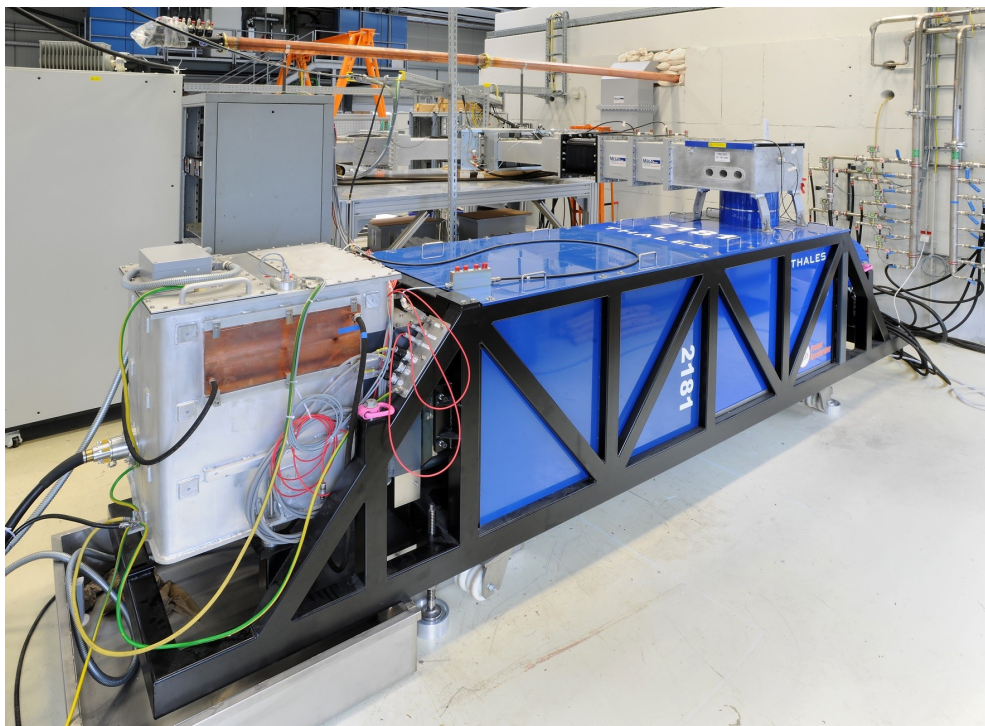
Figure 7.15: Thales klystron at the GSI test stand. In the background one sees the waveguides through the circulator to the test bunker. Courtesy of A. Schnase, GSI.

After the successful and necessary low level pre-conditioning, the Ladder RFQ was installed at the test bunker at GSI. The dedicated RF test stand, operating at 325 MHz, was completed in 2015 for the test of RF components and cavities for the FAIR Proton Linac [Schnase et al., 2015]. A Thales TH2181 klystron (s. fig. 7.15) delivers up to 2.8 MW peak power [Joly et al., 2014]. The maximum applied cathode voltage is 115 kV at a cathode current of 53 A, resulting in a perveance of $1.39\,\mu A/V^{3/2}$. The klystron was fed by a modulator temporarily provided from Linac 4 at CERN [Lombardi, 2016, Lombardi, 2017].
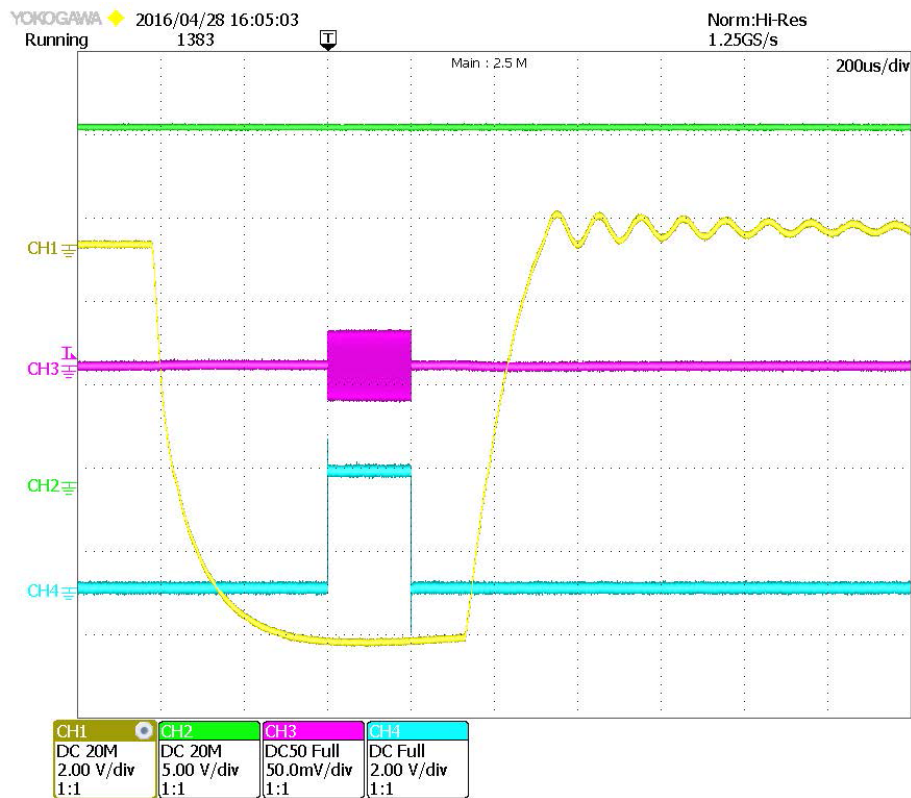
Figure 7.16: Voltage signals of the RF switch command (cyan), cathode voltage (yellow), interlock signal (green) and output signal of the 300 W driver (purple).

The course of the modulator voltages, generating the cathode voltage for the klystron, is shown in fig. 7.16. As the cathode voltage reaches its flattop, the driver amplifier is switched on by the RF switch feeding the input coupler of the klystron for 200 µs. Both the modulator voltage and the driver amplifier are triggered by an external pulse generator. Accordingly, the klystron is supplied by a constant
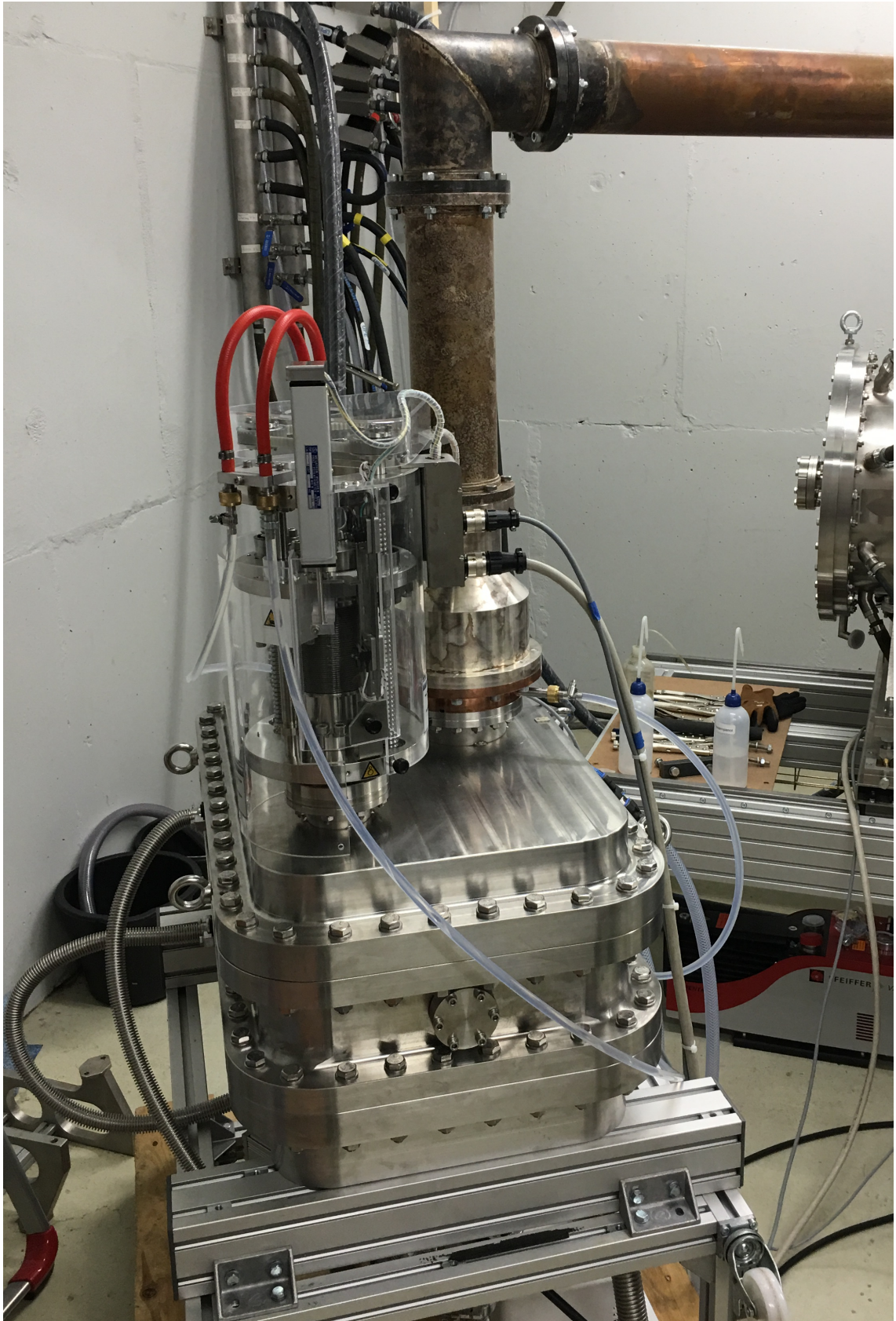
Figure 7.17: RFQ built up for the high power tests at the GSI bunker.
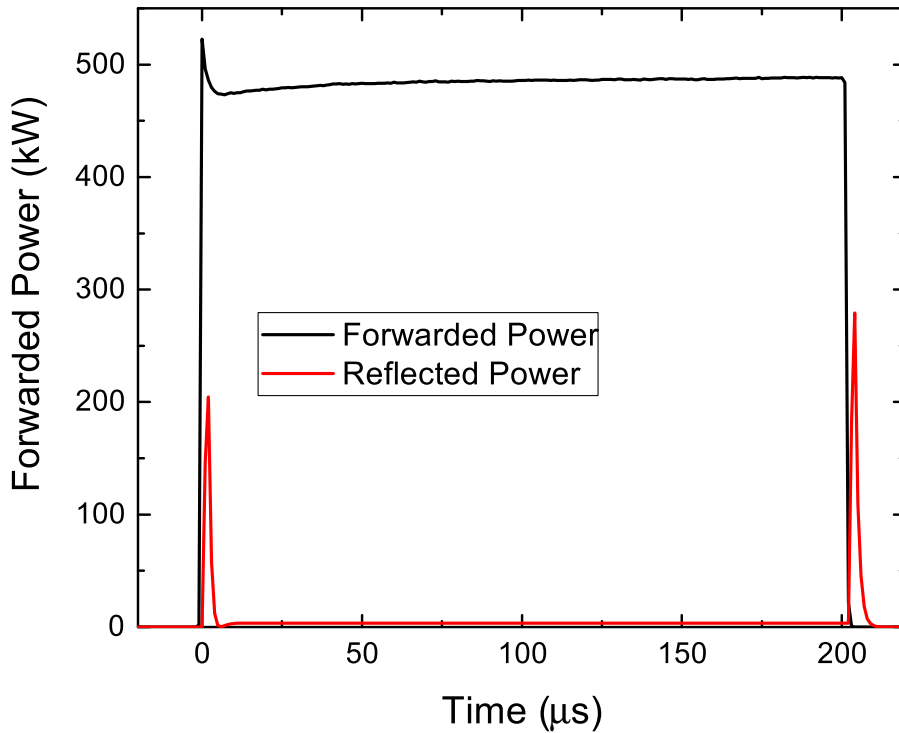
Figure 7.18: Time-resolved reflected and forward power within one pulse of 200 µs.

signal with a variation of max. 1%, when the 300 W driver amplifier is active. The total output power is controlled by the output gain of a frequency generator, feeding the driver amplifier. The repetition rate of the Linac4 modulator is 2 Hz instead of 5 Hz, which is the design value, specified for the FAIR modulator[6]. The RF is delivered by WR2300s[7] rectangular waveguide into the bunker. After a transition to a coaxial waveguide with a diameter of $6^1/_8$ inch, the diameter is further reduced to a coaxial line with a diameter of 100 mm, which is connected to the loop coupler at the RFQ. Furthermore, the test stand is equipped with calibrated directional couplers, a circulator and a water load. The pre-conditioning of the RFQ in advance saved time as the test stand had no more free capabilities [Schreiber et al., 2016] and the modulator had to be decommissioned and returned to CERN in Mai 2016.[8]

The overall setup of the RFQ is shown in fig. 7.17. During April and Mai 2016,

---

[6]Even though the design repetition rate is 5 Hz, the p-Linac will be operated at 4 Hz.

[7]Waveguide standardization according to the Electronic Industries Alliance.

[8]Particular thanks to A. Schnase, G. Schreiber and B. Schlitt from GSI for the efforts and the realization of the high power tests.

the Ladder RFQ was tested for nine days up to a klystron power of 513 kW. The power signals are shown in fig. 7.18 corresponding to the highest peak power of $P_f = 487$ kW, which were reached during the tests. The forward power signal in front of the RFQ (plotted in black) has a length of 200 µs, as specified for the FAIR project. The flattop of the forward power reached 487 kW, which is equivalent to a klystron power of 513 kW. The reflected power is 3.34 kW and the reflection accordingly is $S_{11} = -21.64$ dB. Thus, the maximum power, which was accepted from the cavity, reached 483.66 kW.
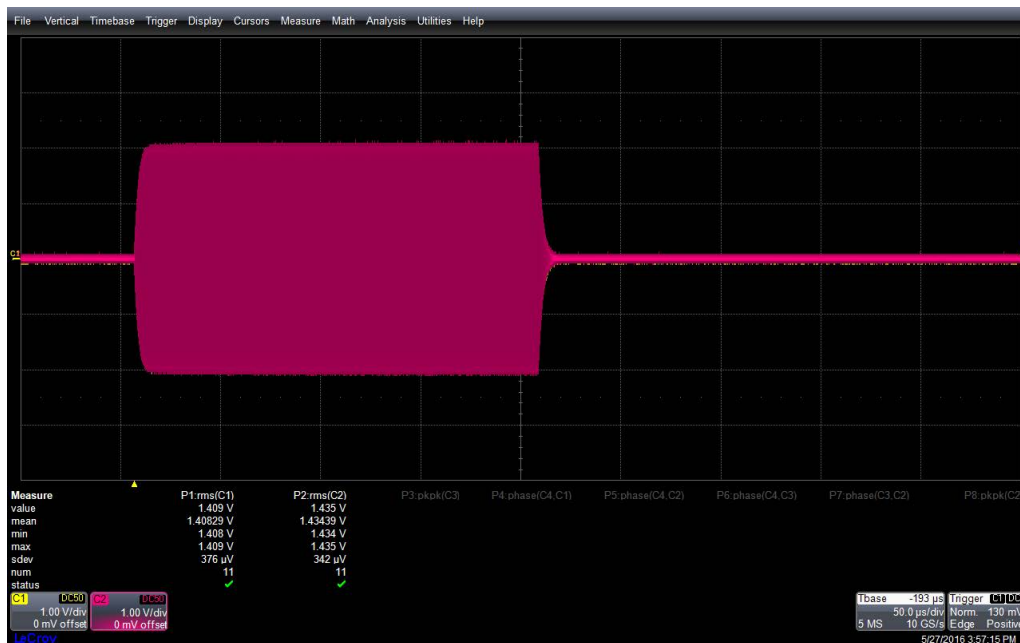
Figure 7.19: Time-resolved transmitted voltage of the pick up probe. The signal corresponds to the square root of the transmitted power $\sqrt{P_t}$.

As long as the whole power, which is coupled into the RFQ, is converted into the RF field and not dissipated by sparking or multipacting, the level of the stored energy P_c should increase linearly with the forward power P_f. It is therefore of particular interest to monitor the stored field energy, which is measured by a pickup probe. The pickup consists of a small inductive loop with a very low coupling of approx. -50 dB. The pickup voltage can be directly measured, which is proportional to the square root of the stored field energy. The time-resolved pickup power, corresponding to the power stored in the cavity P_c, is plotted in fig. 7.19.
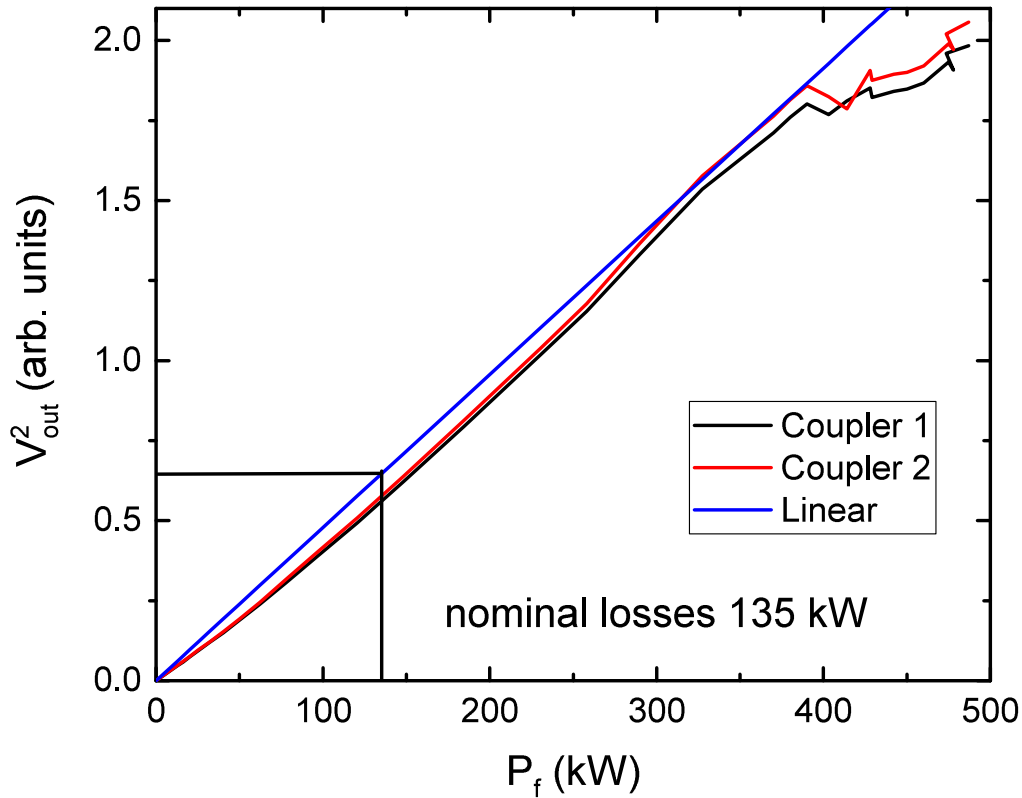
Figure 7.20: Transmitted power as a function of the forwarded power P_f up to 487 kW. The data were recorded within one run at the end of the high power tests. In this case they were taken from the ninth day of the high power measurements.

As the transmitted power, which is the pick up (transmitted) voltage squared, is related to the forward power ($P_t = \beta_t \cdot P_c$), it is linear dependent on the forward power, as long as all the power is only converted into the RF field of the RFQ. The forward power, which is coupled into the cavity, minus the reflected power equals the power stored in the field, assuming that sparking or field emission effects do not occur. The measurements have shown, that the linearity holds up to approx. 400 kW (cf. fig. 7.20). For reasons of better statistics and reliable data two pickup signals at different positions on the cavity have been used (Coupler 1 and 2). The second pickup could also be used for a phase-dependent and automatically driven frequency plunger. On a closer look, the transmitted power is not perfectly linear. During the measurements, the motor driven plunger was not operated automatically, for example by a phase detector and an automatic controller device, but manually. With increasing power, the resonance frequency decreases due to an extension of the

resonator, as the temperature rises. If the resonance frequency ω_0 is not corrected by the frequency plunger, it will not match the klystron frequency ω and the stored field energy, which is indicated by the stored power P_c, will decrease according to [Podlech, 2008]:

$$P_c = \frac{4P_f/(Q_e Q_0)}{\left(1/Q_e + 1/Q_0\right)^2 + \left(\omega/\omega_0 - \omega_0/\omega\right)^2} \tag{7.23}$$

The stored power will reach its maximum, if the RFQ is operated at its resonance frequency. Additionally, during the measurements the plunger was adjusted manually several times. Both facts explain minor deviations of the transmitted power from the linear curve. From 400 kW upwards, the transmitted power noticeably differs from the linearity, which is only explainable by field emission. However, the rate of field emission at this power level was still decreasing. It seems very probable to have reached even higher power levels $P_c > 500$ kW of power within the cavity, if the cavity had been conditioned for more than nine days, especially without interruption. Nonetheless, the measurements have successfully proven that the Ladder RFQ is suitable to stand more than 3.6 times the nominal operating power, which is 135 kW. The electrode voltage accordingly reached values of at least 150 kV (the design voltage is 80 kV). The Kilpatrick value at that level is 3.1. The nominal Kilpatrick factor (bravery factor) is calculated by the voltage difference ΔU between the electrodes, divided by their distance and the Kilpatrick electric field level for $b = 1$ at $f = 325$ MHz:

$$b = \frac{\Delta U}{E_k(f = 325\,\text{MHz})\left(\sqrt{2}(\rho + R_0) - 2\rho\right)} \cdot 1.2 \approx 1.6 \tag{7.24}$$

The correction factor of 1.2 is necessary for the used electrode geometry, compared to an infinite plate capacitor. Hence, the nominal Kilpatrick factor calculates to $b = 1.6$. The value is in accordance with the simulations (cf. chap. 5.2). A visual inspection of the inner surfaces of the RFQ after the high power test clearly showed discolorations on the tank as well as on the electrodes. Yet, the surface was not adversely affected by any damage or scratches.

The time variation of the reflection coefficient S_{11} is shown in fig. 7.21. It was not

126
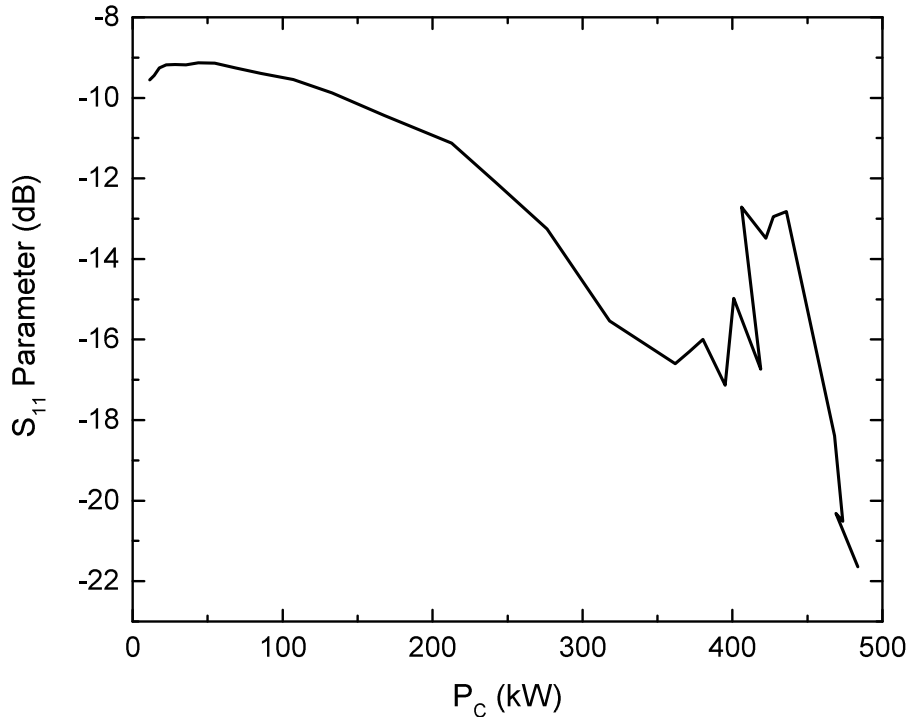
Figure 7.21: S_{11} parameter in dependence of the wall power loss P_c up to 483 kW. The optimum coupling was reached at approx. $P_c = 400$ kW. The double measurement values at $P_c = 406$ kW occurred, as the forward power was increased from 452 to 453 kW, but increased due to sparking the reflection, leading to a decrease of the stored power.

measured directly during the power tests, but can be calculated by the fraction of the reflected power to the forward power in front of the RFQ:

$$S_{11}\,[dB] = 10 \cdot \log \frac{P_r}{P_f} \tag{7.25}$$

At low power, the reflection is -9.55 dB as already measured prior to the pre-conditioning. As the measurement continues to higher power levels, the resonance frequency is shifted and the reflection coefficient changes. At $P_C = 473$ kW the frequency plunger was manually corrected. Nevertheless, for power levels > 400 kW the calculation of the reflection parameter is not reliable anymore. Due to fast fluctuations of the resonance frequency, the reflection power also varies. If sparking

occurs and the interlock of the klystron is activated, the temperature and resonance frequency, respectively, changes within only a few RF pulses.
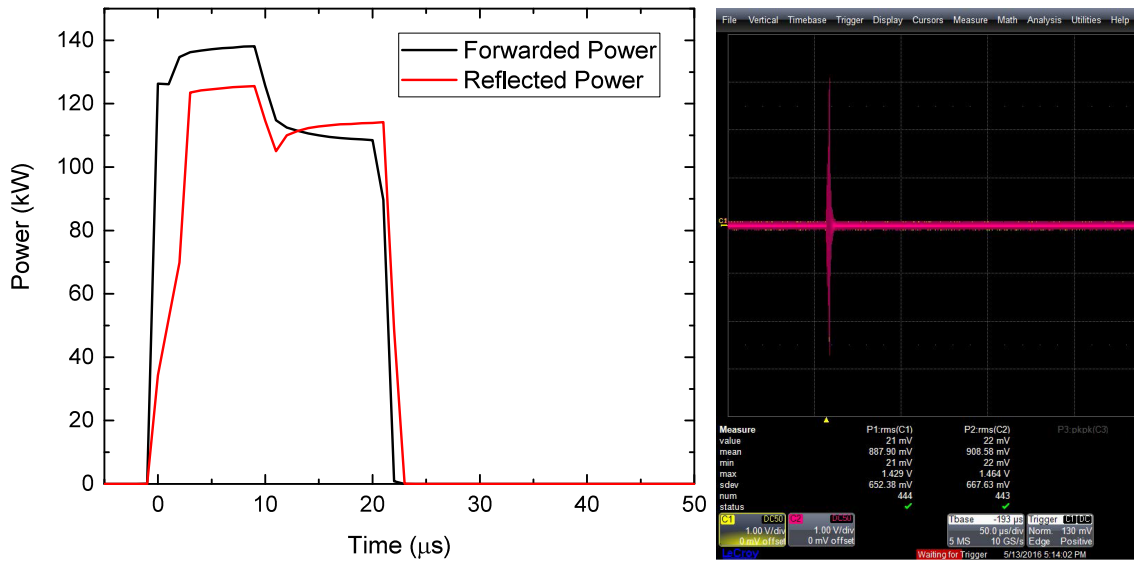
Figure 7.22: Reflected and forward (left) power in the case of a failure in the signal generator. In case of a sparking within the cavity, the transmitted power instantly drops to zero (right).

The event of a power interlock can be seen in fig. 7.22 left. Due to a malfunction of the signal generator the forward power reached $> 1.2\,\mathrm{MW}$. After approx. $20\,\mu s$, the interlock system, which was probably triggered by a diode recognizing sparking in the waveguides, switched off the modulator voltage and the driver amplifier, respectively. The transmitted and reflected power drops to zero within less than $5\,\mu s$. In addition, the interlock system can be triggered by outreaching a certain vacuum level, which can be seen in fig. 7.23.

The time trace of the pressure is visualized in fig. 7.23. Every peak belongs to a single RF macro pulse. The vacuum threshold is indicated by the upper dashed line. The power level of $P_C = 453\,\mathrm{kW}$ could be kept stable in the first $30\,s$. After raising the forward power to $465\,\mathrm{kW}$, arcing effects can be seen by the increase of the vacuum level. Arcing in the cavity can be noticed by the transmitted power signal, which is not stable any more during the full nominal pulse length (s. fig. 7.22 right). After an additional 20 seconds, the interlock system shuts off the driver amplifier. No more RF pulses can be seen in the vacuum level, which exponentially drops to its

nominal value of $7 \cdot 10^{-8}$ mbar. Once the pressure is stabilized to its nominal value, operation can be continued.
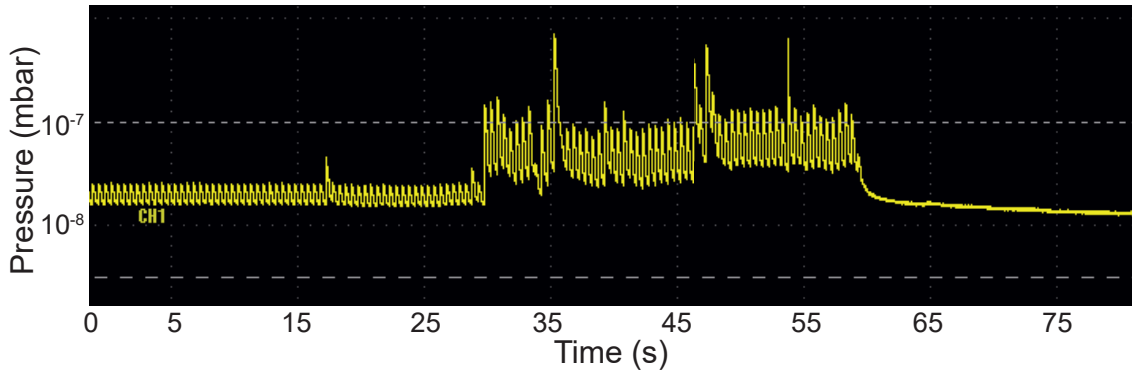
Figure 7.23: Temporal progress of the vacuum level during the high power measurement. The voltage signal of the vacuum gauge is shown on the ordinate with $0.5\,\text{V/div}$. The sampling rate is 500 signals/s with $10\,\text{s/div}$ on the abscissa.

The time behavior of the circulator losses is visualized in fig. 7.24 (black curve), in dependence of the power P_C, coupled into the RFQ. The circulator loss can be considered as constant, but may slightly change with the temperature. Accordingly, the forward power gain S_{21} for both pickups are plotted in red and blue, which is the relation between the transmitted and forward power:

$$S_{21}\,[dB] = 10 \cdot \log \frac{P_t}{P_f} \tag{7.26}$$

Pursuant to the preset, the nominal transmission of the pickups is approx. $-47\,\text{dB}$. All signals feature a similar slope to the reflection coefficient, with a local extremum around $P_C \approx 350\,\text{kW}$. Up to that value the transmitted power increases with the cavity losses. It is reasonable to assume that the frequency at this point perfectly matched the resonance.
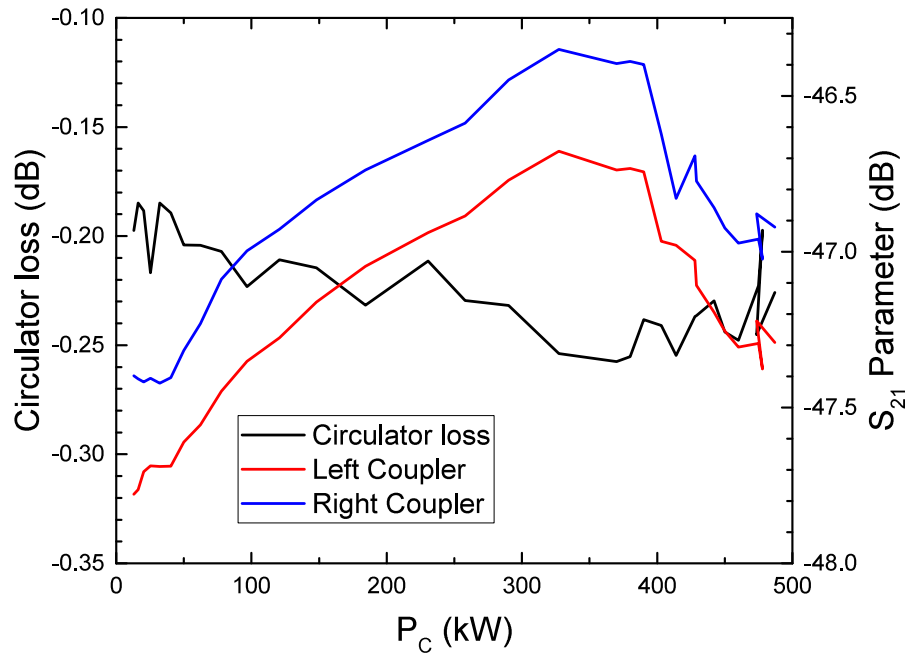
Figure 7.24: Circulator loss and S_{21}-parameter in dependence of the power, coupled into the cavity, up to 483 kW.

Chapter 8

Simulation and Design of the Modulated Full-Length Prototype RFQ

> "Every important machine's got to have a big red button."
>
> *Joseph DeRisi*

The successful manufacturing and measurements of the unmodulated 10 cell prototype Ladder RFQ - above all the high power measurements - proved that the Ladder RFQ works as expected and can be deemed as a serious alternative design for RFQ's. The next and last step towards an entire proof of principle is to design and to build a full size modulated Ladder RFQ in order to perform beam tests at 3 MeV, 70 mA. Beforehand, the ability of tuning the flatness and the RF behavior, in general, is validated by simulations in the next chapter, which have been studied since 2016. In particular, the influence of the modulation of the electrodes has to be regarded (cf. chap. 8.1). Moreover, when considering an operation with beam, the entrance and exit drifts in the fringe fields have to be checked and optimized, both from the RF as well as from a beam dynamical point of view (cf. chap. 8.3). Finally, in chap. 8.4 and 8.5, the final mechanical design of the 55 cell Ladder RFQ [Schuett et al., 2017b, Schuett et al., 2017a] as well as the changes and improvements, compared to the unmodulated prototype, are outlined and explained.

8.1 Simulation of a complete modulated RFQ-Model

The first calculation of a beam dynamics for the parameters of the Proton Linac RFQ was accomplished by C. Zhang, resulting in an electrode length of 3170 mm and an electrode voltage of 80 kV in 2009 [Zhang and Schempp, 2009]. These parameters, like the electrode tip radius and mean aperture, were taken as a basis for the simulation and construction of the short unmodulated Ladder RFQ prototype. The measured electric strength with a Kilpatrick factor > 3 during the power tests allows a raise of the electrode voltage between 80 kV and 100 kV, in order to be more flexible in the beam dynamics design and to improve the transmission as well as the overall output beam quality. For a given length of the RFQ the acceleration section is shorter at higher voltages gaining more space for the bunching section. During the mechanical design phase, the number of ladder cells was set to 55 and accordingly, the total length of the electrodes has to be at least 3320 mm (56 rings á 20 mm and 55 ladder cells á 40 mm), requiring a redesign of the electrodes. Besides, a new design with a constant electrode tip radius along the beam axis as well as a
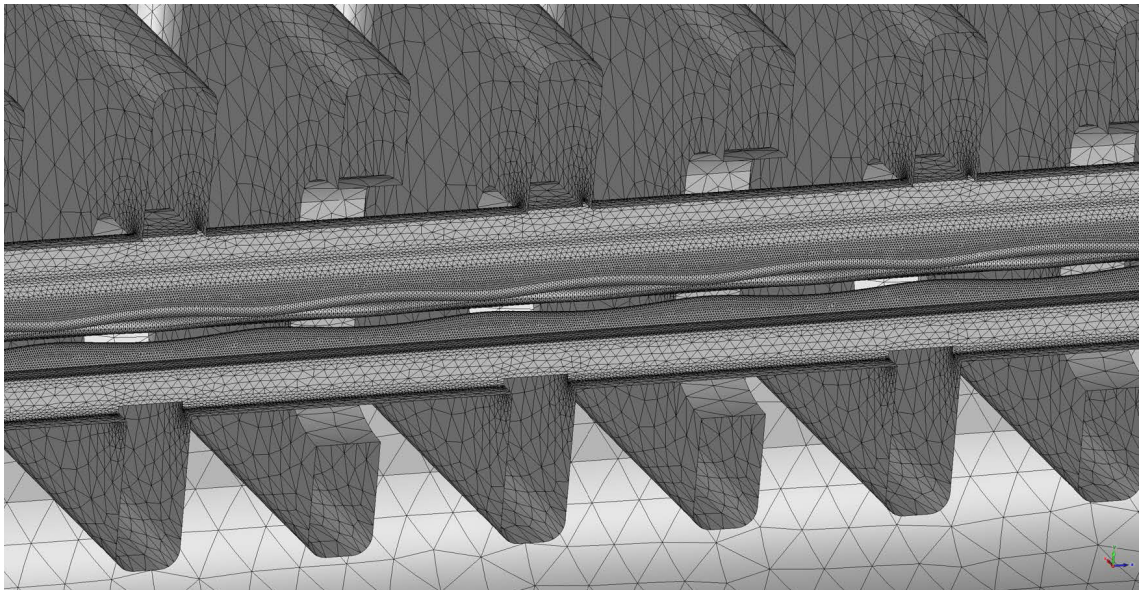
Figure 8.1: Parametrized meshed simulation model including the modulation of the electrodes. The mesh is sufficient to resolve the modulation even on the low energy end. In total number of mesh cells is approx. 3.3 million. To reduce the number of mesh cells it is valid to apply two symmetry planes for the simulation (xz and yz).
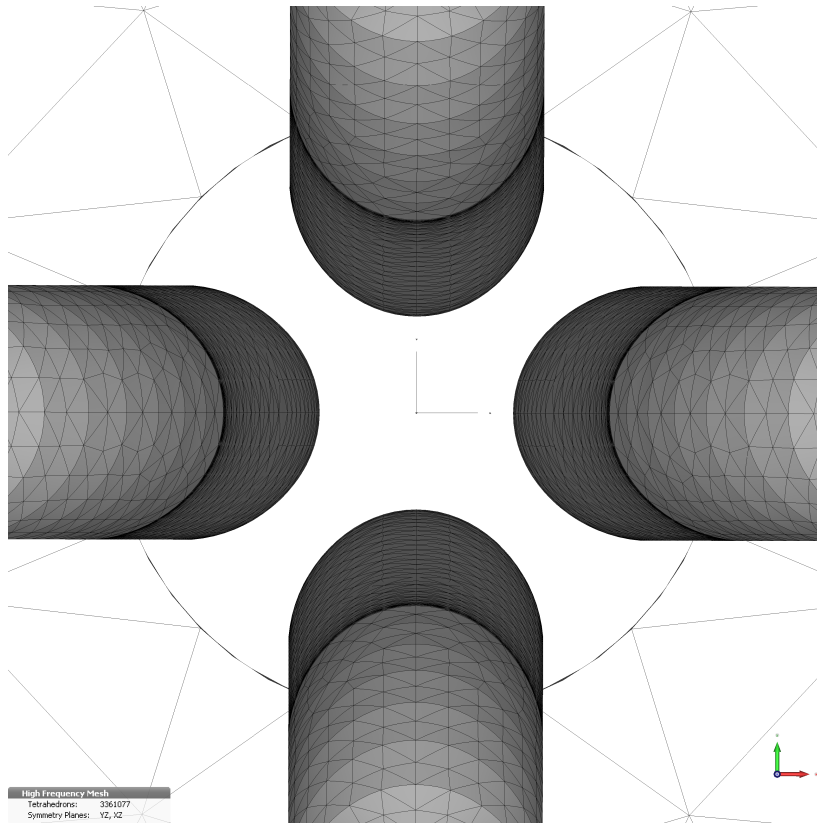
Figure 8.2: Transverse sectional view of the parametrized meshed simulation model including the modulation of the electrodes within the aperture.

homogenous ρ/r_0 ratio, entailing a constant electrode capacity, seems to be a more encouraging approach, above all with respect to a flat field distribution as well as to a simplification of manufacturing. Therefore, a new beam dynamics has to be developed. The final results have been calculated by M. Syha since 2017 [Syha et al., 2017]. Further impacts for working on a new beam dynamics are the consideration of real particle distributions from the LEBT and a better beam matching to the following CH structures by adding adequate matching out cells at the high energy end. Additionally, the electrodes are designed with respect to an optimization of the beam parameters, especially a decrease of the capacitance and losses, respectively, while maximizing the transmission. The overall beam dynamics and RF parameters are now oriented on that from the Linac4 4-Vane RFQ at CERN [Lombardi, 2017, Rossi et al., 2008].

In the following chapter, the modulated Ladder RFQ, including its entire modulation, is investigated in respect to the impact on the RF and especially to tuning possibilities of the field flatness. The electrode modulation of the parametrized model can be seen in fig. 8.1. Within a radius of $a \cdot m$ around the beam axis, the mesh density is locally enhanced to achieve a resolution, which allows to consider even small modulations at the low energy end of the RFQ. The maximum step width of the mesh cells is less than one millimeter compared to the cell length of 6.6 mm in the first cell (s. fig. 8.2). In contrast to former approaches regarding a modulation of the electrodes [Kurennoy et al., 2014], the modulation is not imported from a step model. The modulation parameters for every cell, generated by PARI[1], are integrated into the parametrized model by importing tuples, which contain the *xyz*-coordinates of the electrode tips. The individual points are connected to a linear curve, which is lofted along the electrode tip radius, resulting in a 3D body. The benefit further on is the preservation of full flexibility of the parametrized model, as the geometry may be adapted without constraints during the tuning process. In addition, the field maps generated by the 3-dimensional electrodynamical solver can be used as the basis for a particle tracking simulation, using a PIC[2] solver.

8.2 RF Simulations

Due to the length of the modulated RFQ, the spoke height of the Ladder RFQ has to be decreased from 285 mm to 280 mm, to achieve the same frequency as the short unmodulated prototype. The frequency increments for a deviation of the average height and width of the ladder spokes are equivalent to the unmodulated prototype (-690 kHz/mm for the spoke height and $+400$ kHz/mm for the width, s. fig. 8.3). Higher order modes are shifted closer to the zero mode. Yet, the first HOM ($\lambda/2$-mode) is still 10 MHz apart.

Similar to the unmodulated model, the modulated prototype is frequency tuned by inductive plungers. The RFQ contains twelve tuner flanges in total. Six tuner flanges are equally aligned in a distance of ten ladder cells ($\triangleq 60$ cm) on each side

---

[1]Part of PARMTEQ; the PARI code generates a set of modulation parameters based on the 8-term potential.

[2]**P**article **i**n **C**ell
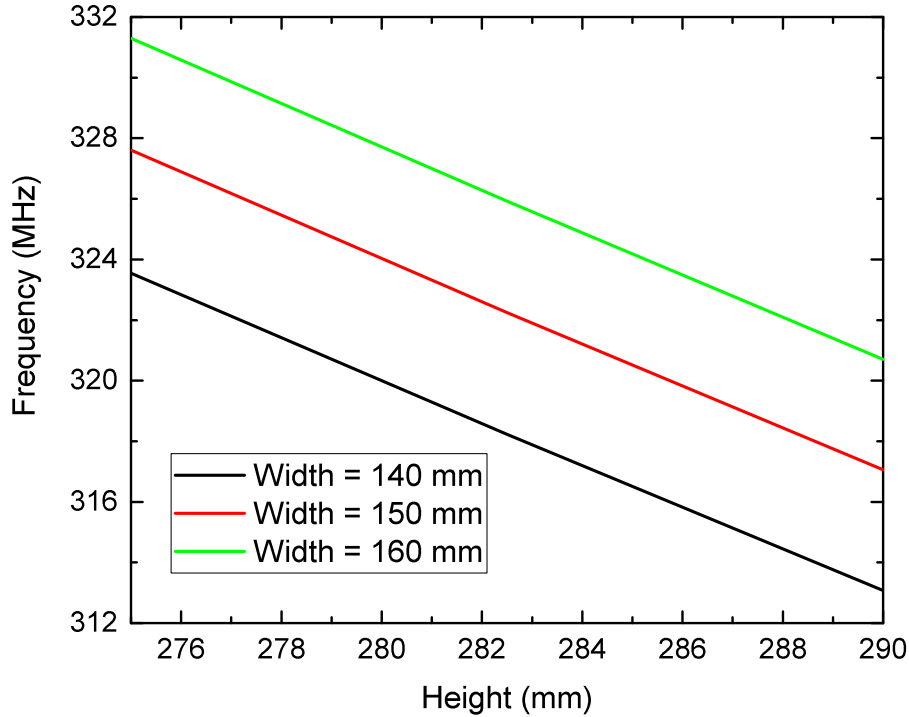
Figure 8.3: Frequency dependence on the ladder height and width
for the modulated Ladder RFQ.

of the beam axis along the RFQ. For reasons of maintaining a high symmetry, the flanges are located on both sides, 110 mm transversely shifted from the beam axis. According to the simulations, using half of the tuners may be sufficient for tuning during operation. Nonetheless, the other half could be either used as a backup to increase the frequency shift or even to perform minor corrections on the flatness. The total frequency shift with six plungers reaches up to 2.3 MHz (cf. fig. 8.4). As explained above for the unmodulated Ladder RFQ, the coarse frequency adjustment is performed by milling out the overall ladder cells to a certain spoke height (referred to as the permanent tuner height, which is a safety margin as an additional layer on the side rails of every cell, reducing the height of every cell). In a first machining step, the frequency is designed to be above the final operating frequency. After comparing the measurement with the simulations, the flatness will be tuned by adjusting the outer cell heights. As the simulations in fig. 8.4 show, the procedure does not influence the functionality of the frequency plungers. The individual final spoke height is not only subject to reach the final frequency, but also to obtain an
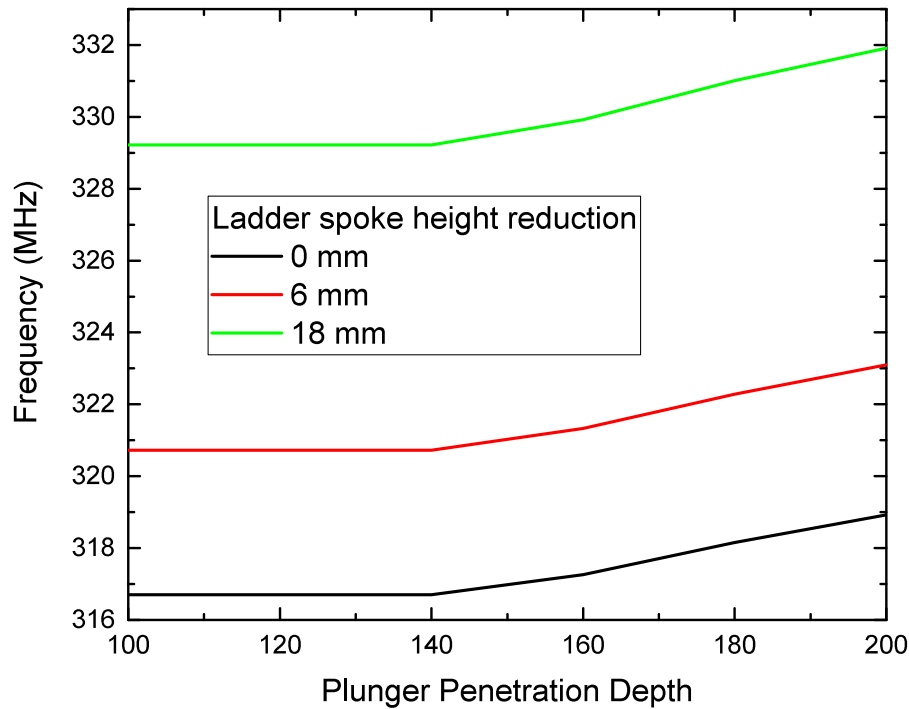
Figure 8.4: Simulation of the frequency shift in dependence of the penetration depth of six frequency plungers for the modulated Ladder RFQ prototype. The effect of the plungers was simulated for different spoke heights but a fixed total height of the ladder structure.

appropriate field flatness. The flatness is tuned by adjusting the individual spoke height of the first and last four cells (Cells 1-4 and 52-55). An additional overall cell height offset of 9 mm per side, covers a total frequency range of 12 MHz. After obtaining the final frequency, the spoke heights are approx. 10 mm shorter than the width of the tank. In contrast to the unmodulated prototype, where the final spoke height equals the width of the tank, the high magnetic fields, at the outer region of the ladder spokes are not spread above the transition between the half-ladder and the tank, in order to avoid losses at that region.

The modulated model reveals the longitudinal electric field distribution on the beam axis, which is the accelerating field component of an RFQ (cf. fig. 8.5). For the unmodulated RFQ's this component is always zero. Every unit cell length $L = \lambda\beta/2$ of the electrode is denoted by a sine-shaped field distribution. The integration of the time independent electric field within a cell yields the gross acceleration voltage gain
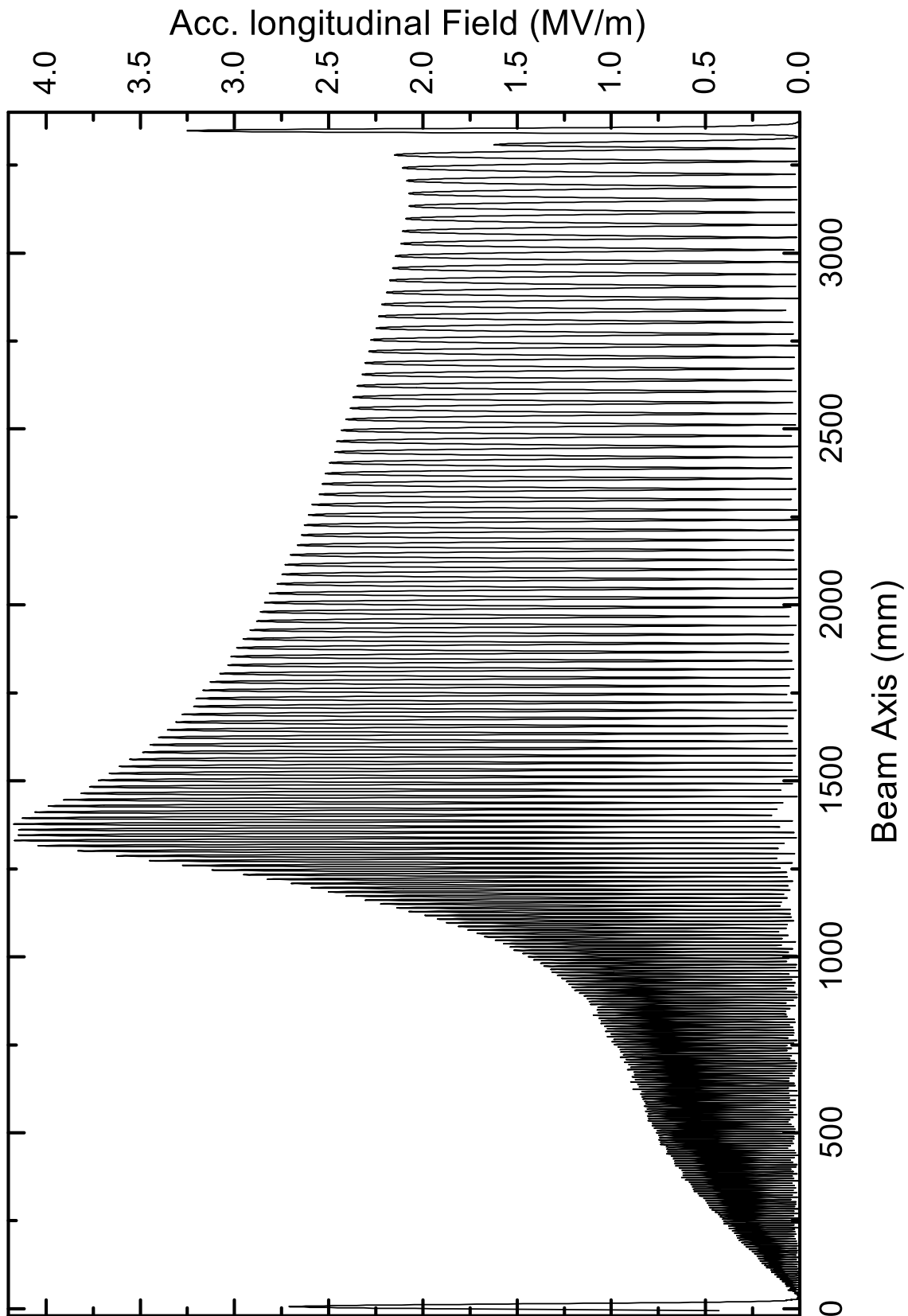
Figure 8.5: 3D electrodynamic simulation of the longitudinal accelerating electric field component of the modulated Ladder RFQ along the beam axis.

U_0 of that cell along the beam axis:

$$U_0 = \int\limits_{-L/2}^{-L/2} E_{0,z} \cdot \cos(kz) \cdot \mathrm{d}z \qquad (8.1)$$

With the correction of the relative RF synchronous phase φ, which is defined as the phase difference of the particle to the RF at the cell center, and the transient time factor T, the simulation matches the net energy gain W, acquired from the beam dynamics calculation. The transient time factor for every cell is constant and calculated by the proportion of the integration of the time and spatial dependent electric field $\vec{E}(t) = E_{0,z} \cdot \cos(kz) \cdot \cos(\omega t + \varphi)$ to the constant maximum potential difference U_0 (cf. [Wangler, 2008]). The center of the cell is $z = 0$ per definition. By applying the angle sum identity for the cosine the net energy gain can be expressed as:

$$W = eU_o T \cos\varphi = e \int\limits_{-\lambda\beta/4}^{\lambda\beta/2} E_{0,z} \cos(kz)\left(\cos(\omega t)\cos(\varphi) - \sin(\omega t)\sin(\varphi)\right) \cdot \mathrm{d}z \quad (8.2)$$

The angular wave number of the oscillation is denoted by $k = \frac{2\pi}{2L} = \frac{2\pi}{\lambda\beta}$. Assuming a constant velocity within a cell, the time dependent argument ωt can be substituted by the spatial coordinate z:

$$\omega t \approx 2\pi f \cdot \frac{z}{\beta c} = \frac{2\pi}{\beta\lambda} \cdot z \qquad (8.3)$$

By factorizing $\cos\varphi$ and neglecting the symmetric integration over sine, the transient time factor T becomes:

$$T = \frac{\displaystyle\int\limits_{-\lambda\beta/4}^{\lambda\beta/4} E_{0,z} \cdot \cos^2\left(\frac{2\pi}{\beta\lambda}z\right) \cdot \mathrm{d}z}{\displaystyle\int\limits_{-\lambda\beta/4}^{\lambda\beta/4} E_{0,z} \cdot \cos\left(\frac{2\pi}{\beta\lambda}z\right) \cdot \mathrm{d}z} \qquad (8.4)$$

The solution of the integral yields:

$$T = \frac{\pi}{4} \approx 0.785 \tag{8.5}$$

Regarding that factor, the net accelerating field of the simulation matches the beam dynamics calculation for every cell. Besides, the modulation allows a particle in cell simulation of a real particle distribution that is transported through the RFQ. A scope of major interest is the validation, if the simulation model with unmodulated electrodes and an averaged mean aperture is also able to generate valuable results. The benefit of such a simplified model is either saving a lot of simulation time or by increasing the amount, detailedness and, respectively accuracy of the simulations as the total number of mesh cells is limited (cf. chap. 5). According to the two-term potential the mean aperture is given by [Wangler, 2008]:

$$r_0 = a \left(\frac{I_0(ka) + I_0(kma)}{m^2 I_0(ka) + I_0(kma)} \right)^{-1/2} \tag{8.6}$$

For small arguments the Bessel functions I_0 remain 1 and the mean aperture can be approximated by the following expression:

$$r_0 \approx a \left(\frac{m^2 + 1}{2} \right)^{1/2} \tag{8.7}$$

The comparison between the modulated and unmodulated field flatness is shown in fig. 8.6[3]. Both field distributions have the same course. Slight artifacts from the modulations can be seen. For even better results, the aperture can be adjusted to an individual mean value for a length of approx. ten RF cells. In summary, an approximation with an averaged constant aperture is valid. An a priori smooth field flatness is based on a constant ρ/r_0 ratio and a constant electrode capacitance along the beam axis, which is not given for every beam dynamics but facilitates the tuning process. A review of the beamdynamics by simulations in consideration of the actual

---

[3]The curves presented in the figure refer to the flatness of the first revision prior to the second machining step of the spoke heights adjusting the final flatness. The latter is simulated after including the final beam dynamic design as well as regarding the bead pull measurements.
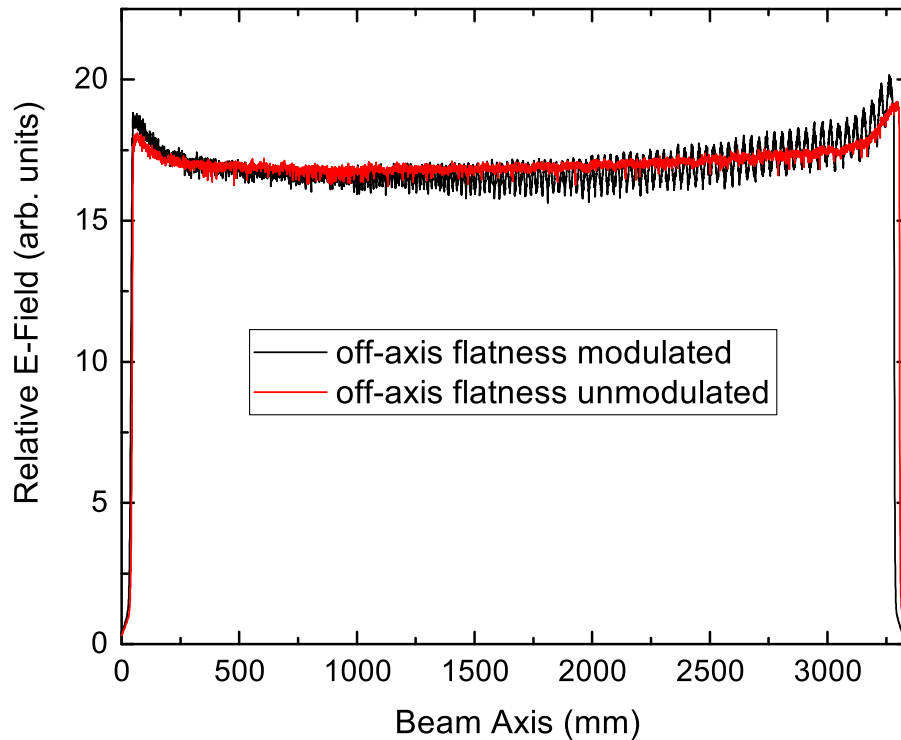
Figure 8.6: Comparison of the field flatness simulations with modulated (black) and unmodulated electrodes, having a constant mean aperture (red). The flatness was determined on a path parallel to the beam axis between the electrodes, evaluating the transversal electric field (cf. chap. 5.3).

modulation is therefore essential, especially when the tuning process is mostly worked out by simulations as in the case of the Ladder RFQ. In addition, the inclusion of a modulation in RF simulations is necessarily required for the compensation of fringe fields, which is described in the next chapter.

8.3 Entrance Beam Dynamics and Fringe Field Compensation

To reduce any RF radiation throughout the beam entrance and exit flange, its diameter should be kept as small as possible. Yet, the aperture should be considerably larger than the maximum beam envelope. For validation, the beam dynamics were simulated backwards from the electrodes to the entrance flange considering space

charge effects. The input emittance of the RFQ beam dynamics simulation with $\varepsilon_{rms,norm} = 0.3\,\pi \cdot \text{mm}\,\text{mrad}$ is a 4D waterbag distribution with Twiss parameters $\alpha = 0.4$ and $\beta = 0.04\,\text{mm/mrad}$ (also known as Courant-Snyder parameters).
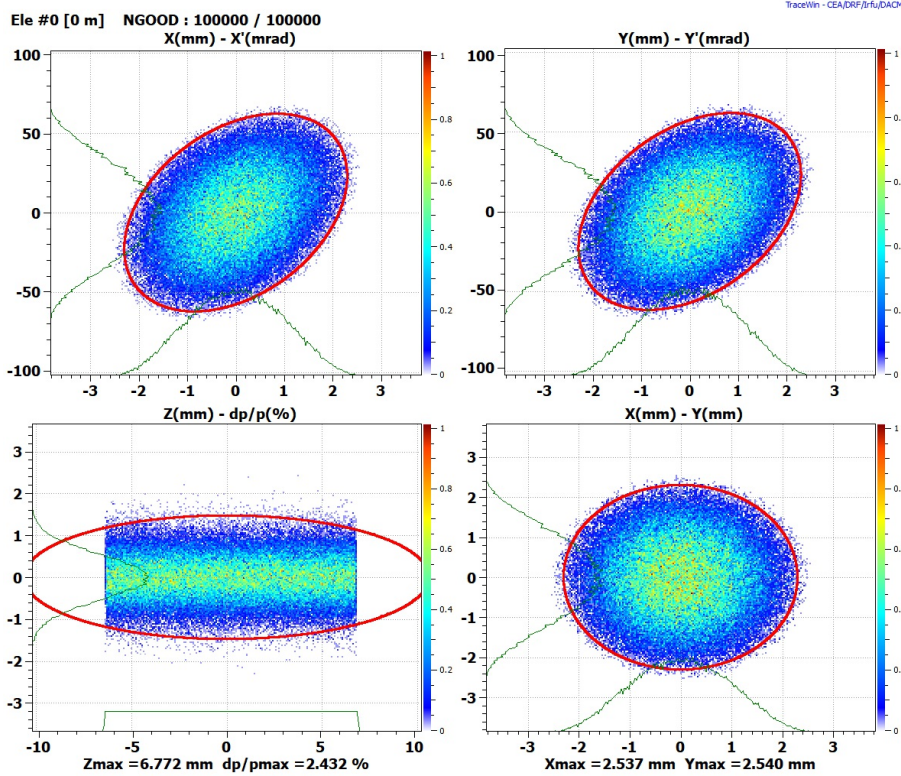
Figure 8.7: Input emittances at the beginning of the electrodes (at the radial matcher) including the 99%-ellipse (red). The input emittances at the electrodes serve as a basis for the beam dynamics simulation with PARMTEQ/RFQGEN as well as a basis for a back-calculation of the emittance at the entrance flange.

The parameters with a positive α serve as the input beam parameters to simulate the beam envelopes at the entrance flange (s. fig. 8.7). The beam transport in this drift section was calculated by TraceWin[4]. For a diameter at the entrance flange of 28 mm at the interior side of the cavity and 18 mm on the outer side (s. fig. 8.8), the five sigma rms envelope remains well below the aperture of the entrance flange.

---

[4]For more information cf. http://irfu.cea.fr/Sacm/logiciels/index3.php
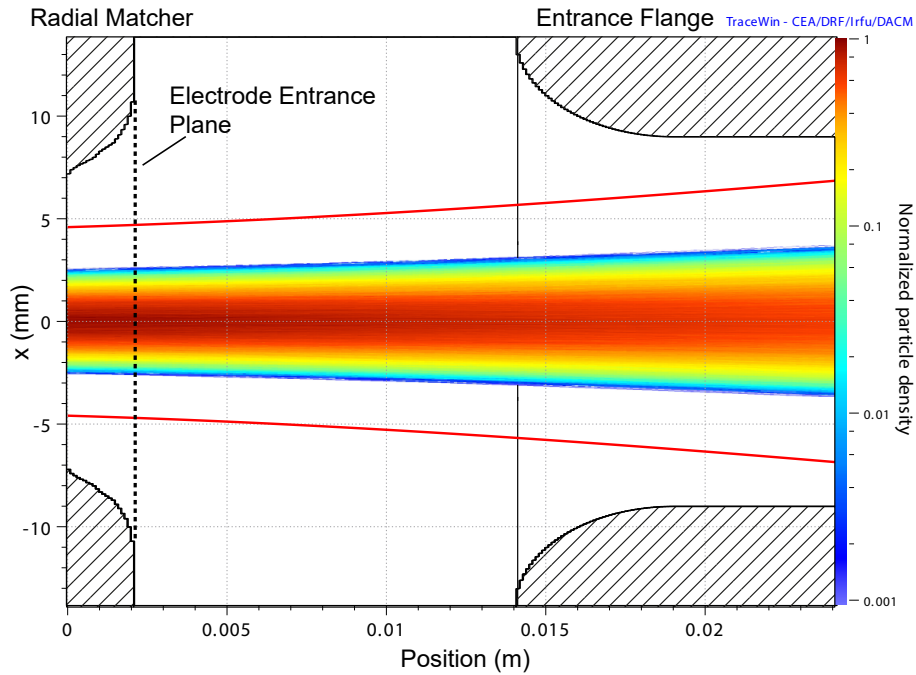
Figure 8.8: Result of the beam dynamics simulation at the RFQ entrance. The density plot illustrates the normalized particle density for the drift between radial matcher and the entrance flange. The left side refers to the beginning of the electrodes (Radial Matcher) and the right side to the entrance flange of the RFQ tank (black line). A total drift of 25 mm and an aperture of 18 mm at the entrance flange is sufficient to avoid any particle losses. The $5\,\sigma$ rms beam envelope is plotted in red.

Apart from an appropriate beam matching, the beam is exposed to longitudinal fringe fields. Due to the different mounting points of adjacent electrodes, their absolute "RF potential" is neither equal nor simultaneously zero. As a consequence, the longitudinal on axis field integral between the grounded entrance flange and the electrode entrance plane (s. fig. 8.8) is not zero. These peaks in the longitudinal on-axis field distribution, both at the entrance and exit of the RF electrodes are not considered in the beam dynamics calculation. Therefore, the beam is already getting "pre-bunched" at the entrance plane by an energy modulation, which may be disadvantageous for the beam dynamics of the RFQ especially at the low-energy end. In contrast, the electrodes of 4-Vane RFQ's have a symmetric potential $\pm V_0$ and do not generate a longitudinal fringe field. Based on the simulations, the net

energy gain of the fringe field becomes larger for a smaller beam flange, which was designed to be as small as possible in the previous step, in order to avoid radiation losses. The compensation of the fringe field is divided in two approaches - one for the entrance and one for the exit gap.

The first solution for the cells of ending vane tips at the high energy end was proposed by Crandall [Crandall, 1984]. By calculating the electric exit field, the ending electrode shapes were adjusted according to the equipotential lines of a certain radial matching potential function, satisfying Laplace's equation. The method had two drawbacks. Firstly, adjacent electrodes differed in length and secondly, the transition to the field free region outside the RFQ wasn't smooth at all. Another approach was made by Iwashita and Fujisawa in 1992, who introduced half cells [Iwashita and Fujisawa, 1992]. The electrodes should end near to the quadrupole symmetry position in the middle of a unit cell, where the aperture is r_0. In 1994, the final solution was achieved, again by Crandall [Crandall, 1994]. He established a transition cell at the end of the electrodes. Instead of terminating the electrodes at mid-cell aperture, a smooth transition is performed from full to zero modulation. The on-axis field at the end of the transition cell, given by a three-term potential, becomes zero. The transition cell can be seen as a quadrupole focusing transport channel. By adjusting the length of zero modulation at the high energy end of the electrodes, the exit phase of the particles can be determined. Accordingly, the influence of the fringe field can be reduced to a minimum. The energy gain will be zero, if the synchronous particle has a phase around $-90°$, at which it exits the electrodes and enters the fringe field. Alternatively, the phase can be adjusted appropriately to match succeeding structures.

On the low energy side of the RFQ, the cw beam is not bunched yet. Consequently, the entrance phase between the particles and the RF cannot be set to the same phase, since the phase width of the incoming beam is 2π. Still, the influence of the fringe field can be suppressed by the following strategy. First of all, the integral of the longitudinal electric fringe field is minimized by an optimization of the distance between the tank wall and first modulated RFQ cell, which follows directly behind the radial matcher. Actually, the sum of the distances between the tank and the ladder structure as well as the surplus of the width of the first ladder spoke, which is
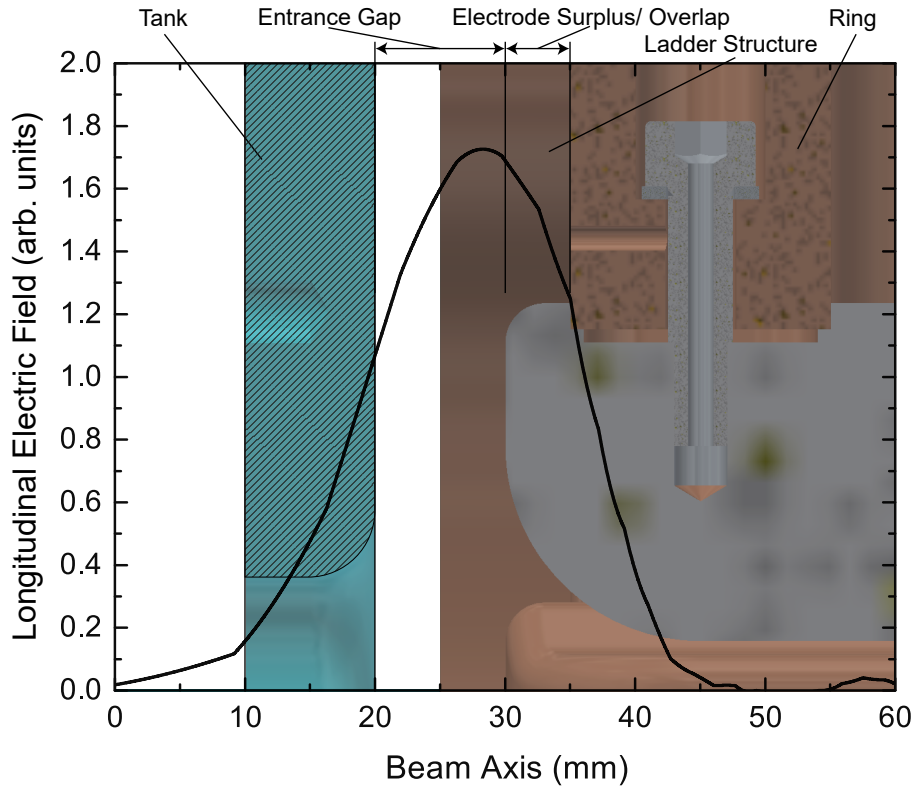
Figure 8.9: Course of the fringe field (longitudinal electric field component E_z on the beam-axis) from the entrance flange in the tank (colored in blue) to the first cell of the electrodes at 55 mm.

thicker than the rings (cf. fig. 8.9), is varied to reduce the gross acceleration voltage caused by the longitudinal fringe field. The longitudinal electric field distribution along the beam axis is plotted in fig. 8.9. The integral of the fringe field $\int E_z(r = 0)\mathrm{d}z$ is shown in fig. 8.10 in dependence on the total distance between the entrance flange and the first ladder spoke, which is the distance from the entrance flange to the radial matcher plus the overlap of the electrodes. A total gap length greater than 20 mm does not effectively reduce the voltage by more than 5%. For a successful beam matching between the LEBT and RFQ, the preceding focusing optics (e.g. a solenoid) in front of the RFQ have to be capable of focusing the beam into the radial matcher. Regarding also the emittance growth by space charge effects, the drift for the spacecharge decompensated beam should be as short as possible. A total distance of approx. 15 mm seems to be a reasonable compromise between a reduced fringe field and an acceptable beam dynamics.
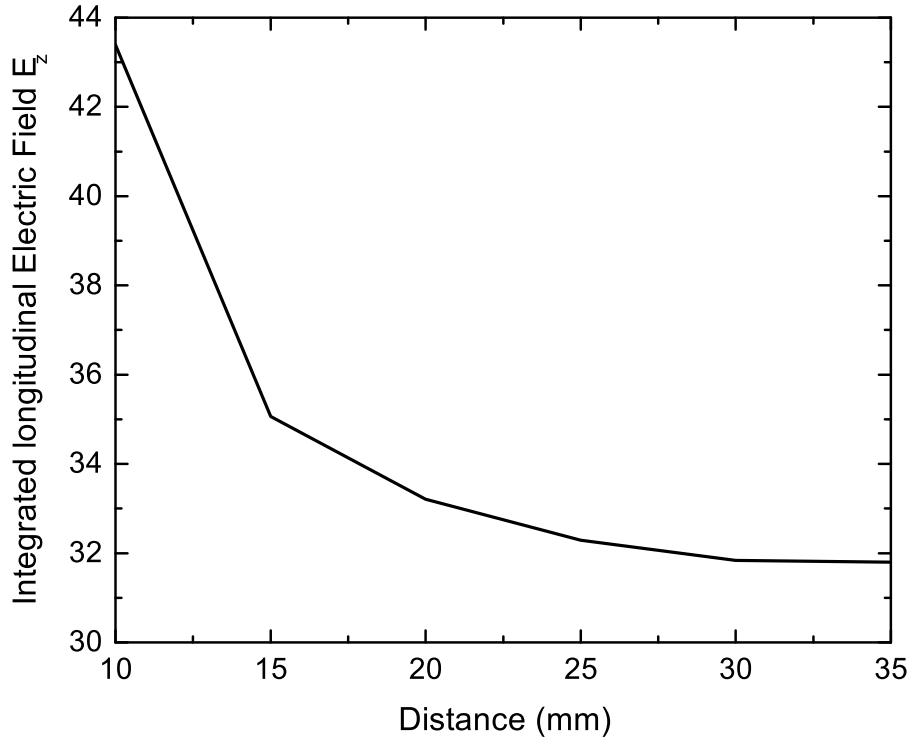
Figure 8.10: Absolute longitudinal voltage difference from the entrance gap to the center of the first cell on the beam-axis in dependence of the gap distance between the entrance flange and beginning of the electrodes.

The next step is to calculate the net energy gain E_{tot}, which is obtained by the integration of the gross longitudinal electric field along the length L of the entrance gap, depending on the entrance phase φ_0. Since the electric field of the gap is shaped like a so-called asymmetric double sigmoidal function, it is not possible to find an analytical expression for the energy gain. The numerical integration of the field in the entrance gap with a length $l = i \cdot \delta x_i$ is given by:

$$E_{tot}(\varphi_0) = \int_0^L E(x,t) \cdot dx = \sum_i E_i(x) \cdot \delta x_i \cdot \cos\left(\varphi(z) + \varphi_0\right) \tag{8.8}$$

For $i = 10{,}000$ steps the energy gain is plotted in fig. 8.11 as a function of the incoming phase φ_0. The numerical calculation of the energy gain of approx. $\pm 1.1\,\text{keV}$ due to the fringe field for particles matches the result of the CST simulation using a constant synchronous phase of $-30°$. The incoming phase width of a "dc beam

bunch" is 360°, which refers to a spatial width of $\beta\lambda \approx 12.92\,\text{mm}$. As the incoming beam is cw, the plot shows the energy modulation of the beam segment with a length of $\beta\lambda$. The distance between entering the longitudinal entrance fringe field and the mid of the first cell is 55 mm. The passed phase difference accordingly is:

$$\Delta\varphi(z) = \omega \cdot \frac{\Delta z}{\beta c} \tag{8.9}$$

The effective spatial phase shift from the entrance gap to the end of the radial matcher at $\Delta z = 55\,\text{mm}$ is $\Delta\varphi = 72°$, which implies that a particle, entering the entrance gap at a phase of $\varphi_0 = -90°$, will have a phase of $\varphi_0 = -18°$ at the center of the first modulated cell of the electrodes. The prebunching effect of the fringe field will be profitably used, if the particles passing the fringe field without an energy gain on the rising edge of the energy modulation arrived at center of the first cell with a phase of $\varphi_0 = -90°$. In this case that refers to particles entering the RFQ
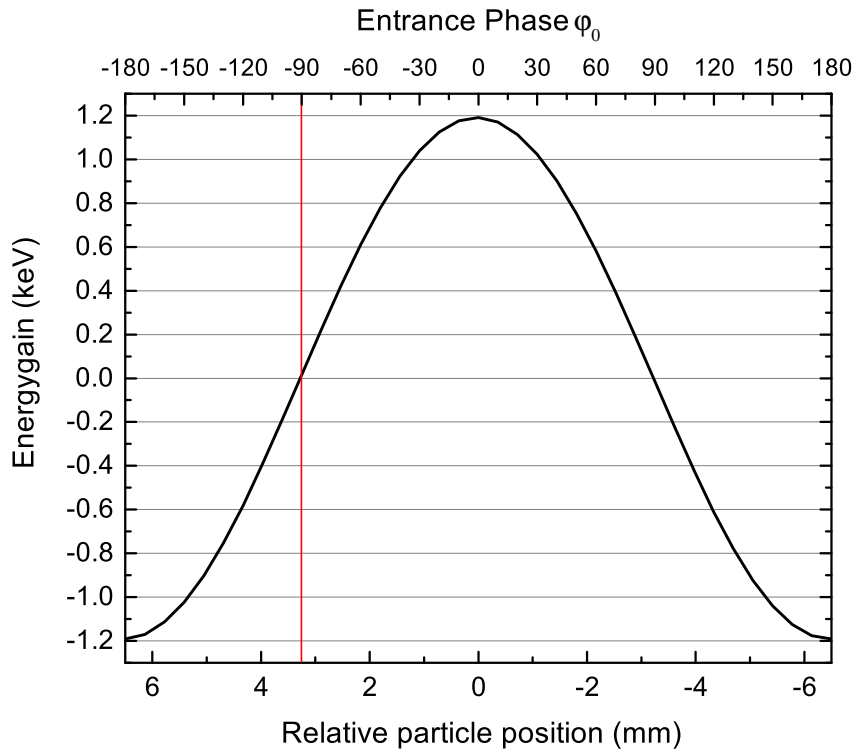
Figure 8.11: Energy gain along the fringe field in dependence of the entrance phase and particle position, respectively.

at a synchronous phase of $\varphi_0 = -90°$ (cf. fig. 8.11). If the particles, having a synchronous phase of $\varphi_0 = -18°$ at the center of the first cell, were supposed to pass the cell center at a phase of $\varphi_0 = -90°$, a drift cell will have to be inserted between the radial matcher and the first modulated cell in order to attain a phase delay of $\Delta\varphi_{delay} = 288° \pm n \cdot 180° = 108°$. The additional length l_{delay} of that very transition cell accordingly becomes:

$$l_{delay} = \varphi_{delay} \cdot \frac{\beta c}{\omega} \approx 3.93 \, \text{mm} \qquad (8.10)$$

Alternatively, the electrodes can be shortened resulting in an phase shift of $-72°$, which refers to a reduction of the electrode length by $2.62 \, \text{mm}$. The maximum energy modulation, caused by the fringe field, for particles within a full phase width of 2π, is up to $\pm 1.1 \, \text{keV}$ (s. fig. 8.11). That effect is equivalent to the bunching process within the first five RF cells of the shaper section.

After calculating the length adjustment l_{delay}, an appropriate mounting of the electrode pairs has to be determined. The longitudinal fringe field is mainly generated by the potential of the pair of electrodes which are not mounted within the first but in the second ring. Consequently, if the beam is bunched at the entrance gap the potential of the "unmounted electrodes" is effectively on the falling edge of the RF $(+ \rightarrow -)$. To then further bunch the beam within the first RFW cell, the polarity of the electrodes has to be appropriately. As a consequence the mounting of the horizontal and vertical electrodes has to be adequately chosen according to the actual phase difference between the effective RFQ entrance gap mid and the mid of the first cell. By inter-exchanging the horizontal and vertical electrode pairs, the RF phase of the first RFQ cell can be shifted by $180°$. The condition for the phase difference between the entrance gap mid plane of the RFQ and the mid of the first cell is plotted in fig. 8.12. For $n = 1$ the depicted electrode mounting is correct. For $n = 0$, the electrode mountings would have to be mutually changed between the electrode pairs, which is equivalent to an exchange of the horizontal and vertical electrode modulation $(a \Leftrightarrow a \cdot m)$.

If an adjustment of the electrode length will lead to a change of the entrance

Figure 8.12: Schematic illustration of the phase difference between the effective mid plane of the entrance gap and the first cell. The outlined electrodes each represent a vertical and horizontal adjacent electrode. The upper one is mounted to the first ring and the lower one is mounted to the second ring ("unmounted electrode"), respectively. For a better visualization the modulation and distances are not to scale.

gap distance, as the electrodes are longitudinally symmetrically mounted with an overlap of equal length on both sides, the transition cell length has to be determined iteratively. Another solution is to shift the electrodes a bit longitudinally against the cavity midplane, which also varies the distance between the entrance flange and the first cell to match an appropriate phase. For that case, the field flatness has to be reviewed. If the capacity per unit length differed between the low and high energy end, an asymmetrical mounting of the electrodes will either be advantageous or disadvantageous and has to be examined for the particular beam dynamics.

8.4 Mechanical Layout

The mechanical concept is similar to the unmodulated prototype and consists of the inner copper ladder structure, which is mounted into an outer stainless steel

Figure 8.13: Perspective view of the full-length modulated Ladder RFQ. A complete
list of the dimensions can be found in appendix A and further overview
drawings in appendix C.

tank. The tank is vertically divided into three parts: A lower shell carrying the inner
resonating structure, a middle frame and the upper shell (s. fig. 8.13). The lower shell
carries and fixes the position of the resonating ladder structure. The ladder structure
is machined from solid copper blocks. As a total length of 3.34 m is too long for most
CNC milling machines and bears a higher risk of distortions and damages during
handling of such bulky components, the resonating ladder structure is made from
two lower and two upper half-ladder elements, which are precisely aligned via guide
pins. Because of machining reasons and for an easier handling, the ladder structure
is longitudinally divided in the center of cell number 28, resulting in 1670 mm half-
ladders of equal length. For the same reasons each electrode is divided into three
pieces at adequate positions between the carrier rings, where the longitudinal current
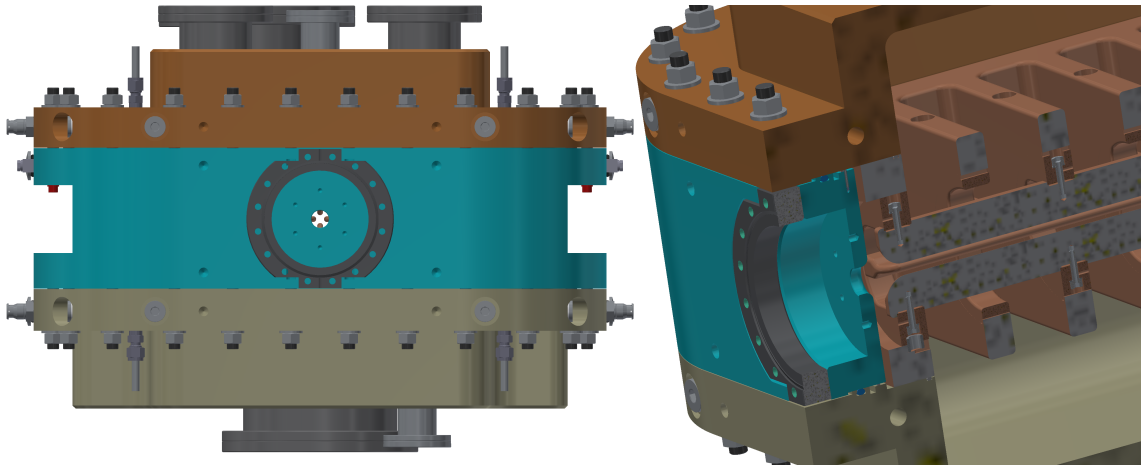
Figure 8.14: Entrance flange of the modulated Ladder RFQ. The flange size is CF100. The aperture of the beam entrance and exit holes in the tank is 18 mm.

approaches zero level. According to the simulations, the RF features are mainly determined by the resonating structure, while the dimensions of the tank have no significant influence on the frequency. Three TMP700 turbomolecular pumps at the lower tank shell of the RFQ provide a vacuum in the 10^{-8} mbar range. The tank wall of the middle frame is cut out at the entrance and exit flange to acquire the option for direct integration of an "entrance cone" and of a steerer (s. fig. 8.14). The nominal wall thickness of the middle frame is 60 mm. Within the diameter of the flange (CF100) the effective wall thickness is reduced to 10 mm. The gained space within the middle frame decreases the total distance between connecting parts and the electrodes to approximately 35 mm. Shortening the drift lengths, especially at the RFQ entrance, dramatically reduces the emittance growth. For a total drift up to 50 mm between the repeller at the end of the cone and the entrance of the RFQ electrode (radial matcher entrance), the normalized rms emittance can be kept below than 0.3 mm mrad. If the cone is not shifted into the RFQ, which results in a total drift of approx. 100 mm, the emittance will increase by at least 50% considering a charge compensation of 80% [Chauvin, 2013]. Bearing in mind that the space charge compensation drops to zero after the end of the repeller, the total emittance growth is expected to be even higher. In this context and to achieve a high flexibility, the beam flanges are CF100. As their outer diameter (152 mm) is slightly larger than the height of the middle frame of the tank (146 mm), the custom-made flanges are

reduced in height to fit into the middle frame and to gain space for the thread holes of the tank screw connection.

8.5 Improvements and Enhancements of the modulated Ladder RFQ compared to the unmodulated Prototype

As explained in the previous chapter, the influence on the beam by the fringe field is reduced to a minimum by adjusting spaces, phases and the RF cells of the electrodes. Beyond, to further improve the conductivity between different components of the RFQ and to increase the quality factor, several measures were taken, which include the following: The tank middle frame will be copper-plated now too, additionally to the lower and upper tank shells. The middle frame of the unmodulated Ladder RFQ was not copper-plated. However, in the area of the beam entrance and exit the electrodes may induce currents on the facing part of the middle frame, which would cause higher losses on a stainless steel surface. Therefore, the middle frame will now also be copper-plated. The contacting surfaces of the mounting area of the electrodes are reduced around the screw connection, to shift the contact pressure between the electrodes and the ring to the rims, where the main current is flowing. The electrodes as well as the whole ladder structure come with thread inserts (Helicoil[5]), to raise the torque from 30 to 45 Nm, to ensure an ideal conductivity and to prevent damages on the thread holes in the copper. Besides, the screws between the lower and upper half-ladders were exchanged from M6 to M8. All bolts in vacuum are silver-plated. Instead of indium, the RF sealings will be made from aluminum. The hardness of aluminum is more than twice (2.75 compared to 1.2 on the Mohs scale) and the conductivity threefold ($37 \cdot 10^6 \, \mathrm{AV^{-1}m^{-1}}$ compared to $12 \cdot 10^6 \, \mathrm{AV^{-1}m^{-1}}$) against indium, resulting in a higher contact pressure and conductivity, respectively.

Based on the experience gained from the unmodulated Ladder RFQ, further amendments of the modulated Ladder RFQ are listed below:

---

[5]Originally invented in 1938 for aircraft engines and distributed since 1954; cf. http://www.boellhoff.com

- The head of frequency plungers are shaped spherically to prevent field peaks. For safety and conservation of a high symmetry, the total number of flanges for frequency plungers is increased to six on both sides of the beam axis. In addition, minor corrections of the flatness will be mandatory.

- Pump slits are inserted to the groove for the RF sealing to improve pumping and to avoid virtual blow holes.

- To reduce an emittance growth at the input and exit drifts, the distances between the beam flanges and the electrodes are shortened as much as possible. The flange sizes are CF100 leaving enough space in the walls, which guarantees the best flexibility for assembling the LEBT as well as following components, like a steerer (for details cf. the previous chapter). To avoid RF radiation losses, the aperture for the beam entrance and exit hole in the tank is reduced to 9 mm.

- Guide pins are used for the alignment between the middle frame and the lower and upper shells of the tank.

- The tank is screwed by threaded bolts within threaded holes instead of screws and nuts, to simplify an assembly and to safe space at the middle frame.

- Integration of calibrated surfaces for the clamping of fiducial target seats, in order to align the RFQ by laser tracking.

Advanced Cooling Concept

By analogy with the unmodulated prototype (cf. chap. 6.3), the modulated Ladder RFQ is equipped with water-cooling channels drilled into the upper and lower tank shells. Both loops in the upper and lower tank shell are separated in the middle of the RFQ for two reasons. First, a deep-hole drilling of half the depth is more convenient for manufacturing and secondly, the number of circulation loops are doubled to gain cooling capability. Besides the cooling of the tank, the ladder side rails of the lower- and upper half-ladders are directly cooled within the copper structure. Along the side rails of all half-ladders a groove is milled (eight channels in total; two on each half-ladder element). The groove will be closed by a cover bar from copper
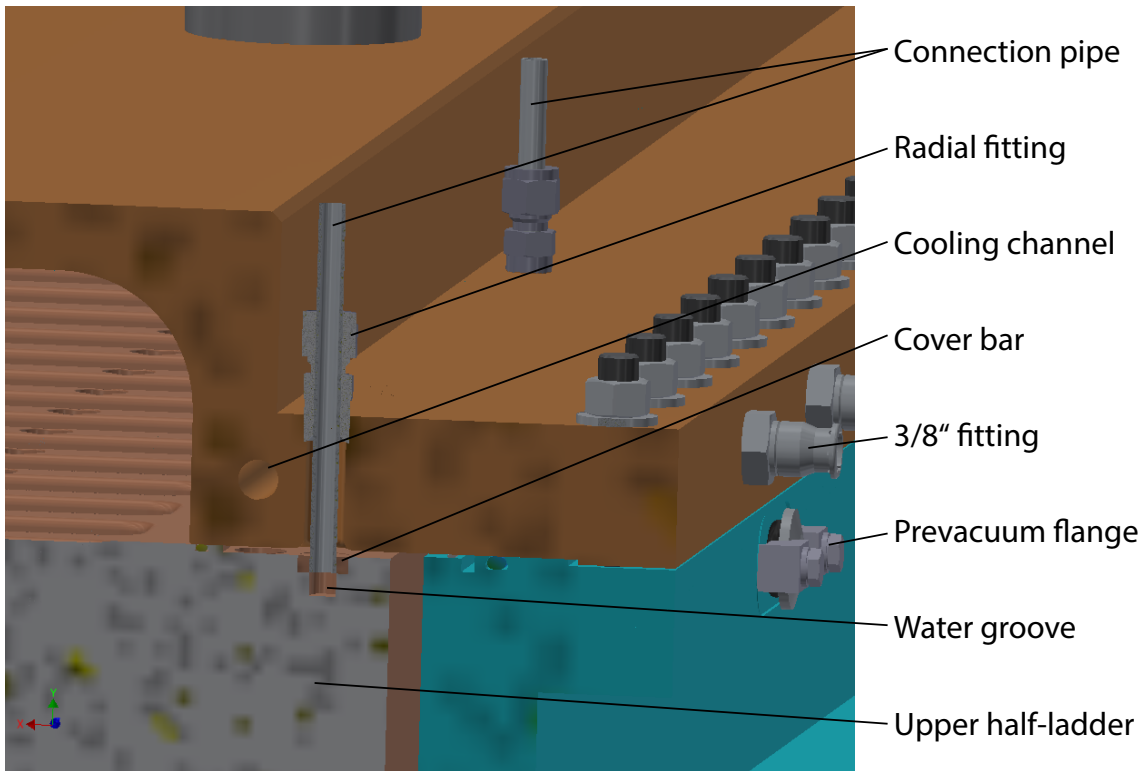
Figure 8.15: Cooling mechanisms in the transverse sectional view of the modulated Ladder RFQ prototype. The bore hole in the tank shell is the same cooling pipe as used for the unmodulated prototype. It circularly leads around the tank. The connection pipe supplies the ladder structure with water.

with connection pipes at both ends. All weldings on the ladder structure apply electron beam technology to reduce heat and deformation during manufacturing. The mechanical mock up can be seen in fig. 8.15.

Pursuant to temperature simulations, the RFQ can be operated with the advanced cooling system up to a duty factor of at least 5% (s. fig. 8.16). The longitudinal displacement of the ladder-structure, which is caused by thermal expansion, extends from 0 to approx. 150 µm at the outer spokes carrying the electrodes (s. fig. 8.17). The maximum transversal displacement of 407 µm occurs at the end of unmounted electrodes, where the heat can only be dissipated over the mounting at the nearest ring in one direction. The simulated displacements are in line with the theoretical
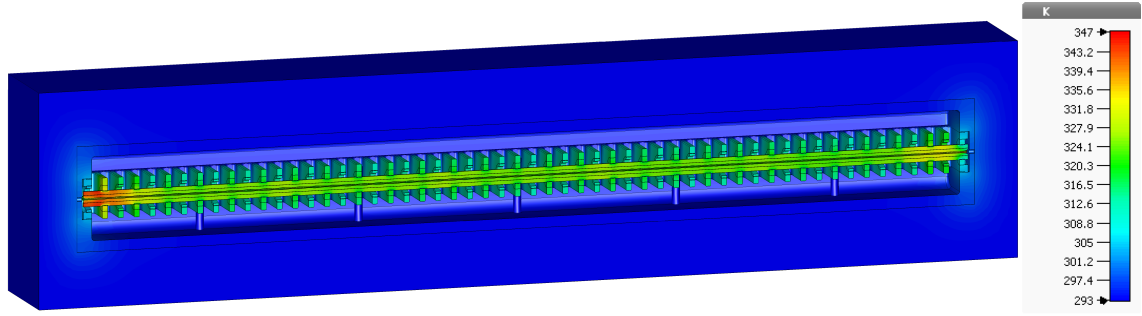
Figure 8.16: Temperature distribution for the modulated prototype with a duty factor of 5%, which refers to a time average power of 33.8 kW. The structure is embedded by air at room temperature and cooled by water pipes within the copper structure as well as in the tank. The maximum temperature rise of approx. 55°K is found at the end of the electrodes. The temperature of the ladder spokes increases by approx. $5 - 20$°K.
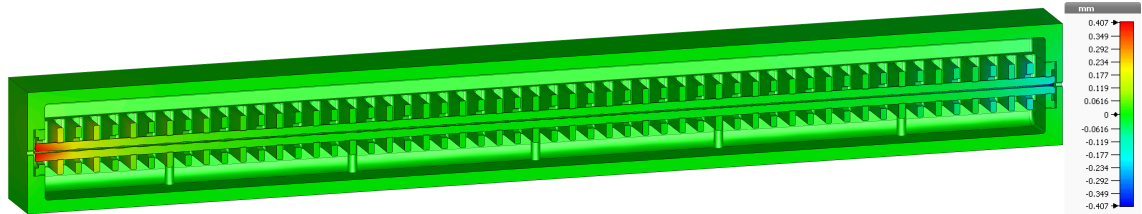
Figure 8.17: Mechanical longitudinal displacement (z-direction) of the modulated prototype due to thermal expansion at a duty factor of 5%. The lower base of the RFQ is held fixed. The main displacement occurs at the electrodes in accordance with the increase of the temperature.

thermal expansion assuming an average temperature increase of 15 K of the electrodes:

$$\Delta l = \alpha_{Cu} \cdot l \cdot \Delta T \approx 1.6\,\mathrm{m} \cdot 16.5 \cdot 10^{-6}\,\mathrm{K^{-1}} \cdot 15\,\mathrm{K} \approx 0{,}4\,\mathrm{mm} \qquad (8.11)$$

The real expansion can be expected to be less due to the following reasons: On the one hand, the electrodes are rigidly fixed in their mounting position within the rings and the expansion of the ladder, which only increases by 10 K, is negligible. On the other hand, each electrode is divided into three parts by expansion joints of approx. 1 mm each. At higher duty cycles the cooling channels have to be extended closer to the electrodes.

Chapter 9

Summary and Outlook

> "Eternity is a long time, especially towards the end."
>
> *Woody Allen*

In its first part, the thesis describes the development, the physical and mechanical design, the manufacturing as well as subsequent RF-measurements of an unmodulated Ladder-RFQ prototype with an electrode length of 630 mm. The historical development of ladder-like structures was presented and a detailed analytical model was derived. It provides a basis for understanding the main geometric cavity parameters. In 3-dimensional RF-simulations the physical and geometrical parameters were validated and the parameters for the first Ladder-RFQ at such a high frequency of 325 MHz were investigated. An unmodulated prototype has been designed at IAP and was fabricated in industry in close collaboration[1]. The flatness was measured and compared with the simulation directly after manufacturing. In further simulations the flatness had been optimized by adjusting the cell heights, before the final geometry was adapted in a second machining step. The final result revealed a very good flatness with a maximum relative difference of $\pm 0.4\%$. The resonating frequency was measured at 325.14 MHz, which is just below the operating frequency of 325.224 MHz. The quality factor of 5080 reached 85% of the theoretical value. That value is equivalent to a shunt impedance of 31 kΩm, which is well above the FAIR p-Linac requirement defined at 16.6 kΩm. The motor driven frequency plunger covers a tuning range of 470 kHz. After the complete assembly of the vacuum support,

---

[1]Fa. Kress Sondermaschinenbau GmbH.

coupling loop and cooling circuits, the low-level RF-conditioning took place in-house at IAP up to 440 W cw. Soft multipacting barriers, mainly below 10 W, could be exceeded after seven days with a typical active conditioning time of eight hours per day. The high power RF-test at the GSI test bunker achieved promising results up to 483 kW of power in the cavity within nine days of measurements, which corresponds to 3.6 times the nominal losses. Accordingly, the Kilpatrick value at that point reached up to 3.1 compared to 1.6 at design level. A stable operation at high power levels - well above the nominal power of 135 kW was clearly demonstrated by that experiment for short RF pulses (200 µs @ 1 Hz).

The successful RF-tests motivated the pursuing development of a modulated Ladder RFQ at its full length of 3.5 m. Furthermore, the electrode design voltage has been be raised from 80 kV to $85 - 90$ kV in beam dynamics layout. The RF field simulations were successfully performed on a fully modulated and parametrized model. The flatness and frequency tuning possibilities were proven and discussed in this work. On this basis and by including the experience from the short prototype, a mechanical model was designed and presented. The cooling system has been enhanced for a theoretical duty factor up to 5%. Further improvements, taken from the experience feedback from the unmodulated prototype have been applied to the modulated RFQ, in order to increase the quality factor and its overall performance. In addition, the beam dynamics at the RFQ entrance has been studied in detail, to reduce drifts and emittance growth at the entrance gap.

The current time schedule anticipates the manufacturing to be finished at the beginning of 2018. The copper-plating of the tank should also be completed until the end of 2017. The first low level RF-measurements are expected as of early 2018. The flatness measurement will be compared with the simulations and the second revision, i.e. the flatness tuning by adjusting the cell heights, will be done until mid 2018. The RFQ will be conditioned up to 12 kW at IAP. The high power measurements are envisaged for the end of 2018, once the modulator for the klystron at the GSI test stand has been commissioned [Pütz, 2017]. Another important step is to fully integrate the cone into the RFQ and to optimize the matching between the LEBT and the RFQ. Once the p-Linac building will be finished with installation and commissioning at the end of 2020 [Knie, 2017, Kleffner et al., 2017] the source

and LEBT can be installed. That configuration involving the source and LEBT will be used as a test site to perform the final and last measurements, above all the acceleration of a 70 mA proton beam from 95 keV to 3 MeV and hereby to fully proof the complete feasibility and functionality of the Ladder RFQ. The beam emittance measurement at different beam currents accompanied by beam dynamics simulations will be a major result after the assembly of the whole test setup. Furthermore, the influence of the plungers on the beam energy as well as the flatness will be studied in detail.

The successful measurements offer space for future studies. An improved cooling mechanism could raise the duty factor for applications above 5%. To achieve smaller and more efficient structures - regarding RF losses as well as expenses per length - an investigation of higher frequencies is valuable. Nevertheless, the existing structure offers a serious alternative to state of the art 4-Vane RFQ's at high frequencies above 250 MHz. Suitable applications for the Ladder RFQ are first of all synchrotron injector linacs, but also pulsed spallation neutron sources like ESS and SNS, Furthermore, an interesting application is for medical use. To reduce costs high frequencies are required to achieve small facilities. In particular, the production of radioactive isotopes for diagnostics, Brachytherapy as well as for a direct proton tumor therapy. The Ladder RFQ is completely maintainable and repairable, the electrodes are interchangeable. Neighboring RF modes are distant to each other simplifying the tuning process. In contrast, 4-Vane RFQ's require a very high manufacturing precision to suppress neighbored dipole modes. The tuning process is very time-consuming due to the symmetric alignment of coupled tuners. The tuning process of the Ladder RFQ consist of the adaption of just four end cells based on simulations and a measurement. 4-Vane RFQ's can be operated cw, as the electrodes and the tank is "brazed into" a single peace favoring an integration of cooling channels. Both RFQ's offer a very flat field distribution and low dipole components. The manufacturing costs and duration of the Ladder RFQ is on a similar level with 4-ROD structures, but significantly less compared to a 4-Vane.

Bibliography

[Abderrahim et al., 2010] Abderrahim, H. A., Baeten, P., Bruyn, D. D., Heyse, J., Schuurmans, P., and Wagemans, J. (2010). *MYRRHA, a Multipurpose hYbrid Research Reactor for High-end Applications.* Nuclear Physics News, 20(1):24–28.

[Almalki et al., 2014] Almalki, M., Brodhage, R., Fork, P., Kaufmann, W., Kester, O., Kowina, P., Sieber, T., Balaguer, J., Girardot, P., and Simon, C. (2014). *The Mechanical Design of the BPM Inter-tank Section for p-linac at FAIR.* Proceedings of IPAC, Dresden, Germany, pages 3474–3476.

[Baschke et al., 2016] Baschke, M., Podlech, H., Groening, L., Mickat, S., and Zhang, C. (2016). *The new RF-Design of the 36 MHz-HSI-RFQ at GSI.* Proceedings of IPAC, Busan, Korea, pages 883–885.

[Bauer, 1957] Bauer, F. L. (1957). *Das Verfahren der Treppeniteration und verwandte Verfahren zur Lösung algebraischer Eigenwertprobleme.* Zeitschrift für angewandte Mathematik und Physik ZAMP, 8(3):214–235.

[Bayle et al., 2014] Bayle, H., Delferriére, O., Gobin, R., Harrault, F., Marroncle, J., Senée, F., Simon, C., and Tuske, O. (2014). *Effective shielding to measure beam current from an ion source.* Rev. Sci. Instrum., 85(2):02A713.

[Bechtold, 2003] Bechtold, A. (2003). *Eine integrierte RFQ-Driftröhrenkombination für ein Medizin-Synchrotron.* Dissertation, Johann Wolfgang Goethe-Universität, Frankfurt am Main.

[Bechtold et al., 2006] Bechtold, A., Habs, D., Fischbach, J., Ratzinger, U., Rehberg, J., Reichwein, M., Schempp, A., Kester, O., and Häuser, J. (2006). *The MAFF IH-RFQ Test Stand at the IAP Frankfurt.* Proceedings of EPAC, Edinburgh, Scotland, pages 1557–1579.

[Ben-Zvi et al., 1990] Ben-Zvi, I., Jain, A., and Wang, H. (1990). *Electrical Characteristics of a short RFQ Resonator.* Proceedings of LINAC, Albuquerque, NM, USA, pages 73–75.

[Bezzon et al., 1994] Bezzon, G., Lombardi, A., Parisi, G., Pisent, A., and Weiss, M. (1994). *Construction and Commissioning of the RFQ for the CERN Lead-Ion Facility.* Proceedings of LINAC, Tsukuba, Japan, pages 557–559.

[Blanchard, 1941] Blanchard, J. (1941). *The History of Electrical Resonance.* Bell Labs Tech. J., 20(4):415–433.

[Blewett, 1952] Blewett, J. P. (1952). *Radial Focussing in the Linear Accelerator.* Phys. Rev., 88:1197–1199.

[Boltzmann, 1904] Boltzmann, L. (1904). *Vorlesungen über Mechanik, II.* J.A. Barth, Leipzig.

[Brodhage et al., 2013] Brodhage, R., Ratzinger, U., and Almomani, A. (2013). *Design Study of a high Frequency Proton Ladder RFQ.* Proceedings of IPAC, Shanghai, China, pages 3788–3790.

[Brodhage et al., 2015] Brodhage, R., Vinzenz, W., Vossberg, M., Kaiser, M., and Ratzinger, U. (2015). *Status of the FAIR Proton Linac.* Proceedings of IPAC, Richmond, VA, USA, pages 3702–3704.

[Browman et al., 1988] Browman, M. J. ., Spalek, G., Friedrichs, P. B., and Barts, T. C. (1988). *Studies of the Four-Rod RFQ using the MAFIA Codes.* Proceedings of LINAC, Williamsburg, VA, USA, pages 119–121.

[Busch, 2015] Busch, M. (2015). *Auslegung und Messungen einer supraleitenden 325 MHz CH-Struktur für Strahlbetrieb.* Dissertation, Johann Wolfgang Goethe-Universität, Frankfurt am Main.

[Bylinsky et al., 2000] Bylinsky, Y., Lombardi, A., and Pirkl, W. (2000). *RFQD - A Decelaration Radio Frequency Quadrupole for the CERN Antiproton Facility.* Proceedings of LINAC, Monterey, CA, USA, pages 554–556.

Bibliography

[Cervellera et al., 1992] Cervellera, F., Fortuna, G., Lombardi, A., Parisi, G., Pisent, A., Amendola, G., Vretenar, M., and Weiss, M. (1992). *Design Study of the Low Energy Part of the CERN Pb Ion Injector.* Proceedings of EPAC, Berlin, Germany, pages 545–547.

[Chauvin, 2013] Chauvin, N. (2013). *Beam dynamics studies for the FAIR p-linac LEBT.* Internal Report from CEA.

[Clemente et al., 2010] Clemente, G., Barth, W., Groening, L., Yaramishev, S., Brodhage, R., Ratzinger, U., and Tiede, R. (2010). *The FAIR Proton Linac: The First Linac Based on a Room Temperature CH-DTL.* Proceedings of Advanced Beam Dynamics Workshop on High-Intensity and High-Brightness Hadron Beams, pages 115–119.

[Cockcroft and Walton, 1932a] Cockcroft, J. D. and Walton, E. (1932a). *Experiments with High Velocity Positive Ions. (I) Further Developments in the Method of Obtaining High Velocity Positive Ions.* Proc. Roy. Soc., A136(830):619–630.

[Cockcroft and Walton, 1932b] Cockcroft, J. D. and Walton, E. (1932b). *Experiments with High Velocity Positive Ions. II. The Disintegration of Elements by High Velocity Protons.* Proc. Roy. Soc., A136(831):229–242.

[Courant et al., 1952] Courant, E. D., Livingston, M. S., and Snyder, H. S. (1952). *The Strong-Focusing Synchroton: A New High Energy Accelerator.* Phys. Rev., 88:1190–1196.

[Crandall, 1994] Crandall, K. (1994). *Ending RFQ Vanetips with Quadrupole Symmetry.* Proceedings of LINAC, Tsukuba, Japan, pages 227–229.

[Crandall et al., 1979] Crandall, K., Stokes, R., and Wangler, T. (1979). *RF Quadupole Beam Dynamics Design Studies.* Proceedings of LINAC, Montauk, NY, USA, pages 205–216.

[Crandall and Wangler, 1987] Crandall, K. and Wangler, T. (1987). *PARMTEQ - A Beam Dynamics Code for the RFQ Linear Accelerator.* Proceedings of Workshop on Linear Accelerator and Beam Optics Codes, San Diego, CA, USA.

[Crandall, 1984] Crandall, K. R. (1984). *RFQ Radial Matching Sections and Fringe Fields.* Proceedings of LINAC, Seeheim, Germany, pages 109–111.

[CST, 2017] CST (2017). *CST Studio Suite help documentation.*

[Deutsches Kupferinstitut, 2005] Deutsches Kupferinstitut (2005). DKI Werkstoff Datenblatt Cu-HCP. Online resource http://www.kupferinstitut.de; accessed on 04/20/2017.

[Ehrenfest, 1911] Ehrenfest, P. (1911). *Welche Züge der Lichtquantenhypothese spielen in der Theorie der Wärmestrahlung eine wesentliche Rolle?* Annalen der Physik, 341(11):91–118.

[Ehrenfest, 1914] Ehrenfest, P. (1914). *A mechanical theorem of Boltzmann and its relation to the theory of energy quanta.* Proceedings of the Amsterdam Academy, 16:591–597.

[Fabris et al., 1987] Fabris, A., Massarotti, A., and Vretenar, M. (1987). *A model of Four Rods R.F.Q.* New Techniques for Future Accelerators, 29:265–269.

[Fischer, 2006] Fischer, P. (2006). *Ein Hochleistungs-RFQ-Beschleuniger für Deuteronen.* Dissertation, Johann Wolfgang Goethe-Universität, Frankfurt am Main.

[Gerhard, 1989] Gerhard, A. (1989). *Felddurchschlag in elektrischen Hochfrequenzfeldern (Sparking).* Dissertation, Johann Wolfgang Goethe-Universität, Frankfurt am Main.

[Greinacher, 1921] Greinacher, H. (1921). *Über eine Methode, Wechselstrom mittels elektrischer Ventile und Kondensatoren in hochgespannten Gleichstrom umzuwandeln.* H. Z. Physik, 4:195–205.

[Groening et al., 2004] Groening, L., Barth, W., Dahl, L., Hollinger, R., Spädtke, P., Vinzenz, W., Yaramishev, S., Hofmann, B., Li, Z., Ratzinger, U., Schempp, A., and Tiede, R. (2004). *A dedicated 70 MeV Proton LINAC for the Antiproton physics program of the future Facility for Antiproton and Ion Research (FAIR) at Darmstadt.* Proceedings of LINAC, Lübeck, Germany.

[Heilmann et al., 2015] Heilmann, M., Adonin, A., Appel, S., Barth, W., Gerhard, P., Heymach, F., Hollinger, R., Vinzenz, W., Vormann, H., and Yaramyshev, S. (2015). *Unilac Proton Injector Operation for FAIR*. Proceedings of IPAC, Richmond, VA, USA, pages 3709–3711.

[Hinterberger, 2008] Hinterberger, F. (2008). *Physik der Teilchenbeschleuniger und Ionenoptik*. Springer Verlag, Berlin Heidelberg, 2. edition.

[Iwashita and Fujisawa, 1992] Iwashita, Y. and Fujisawa, H. (1992). *Half End-Cell Geometry of RFQ*. Proceedings of LINAC, Ottawa, Ontario, Canada, pages 698–700.

[Jackson, 1975] Jackson, J. D. (1975). *Classical Electrodynamics, 2nd Edition*. Wiley.

[Joly et al., 2014] Joly, C., Lesrel, J., Plechov, E., Schnase, A., and Schreiber, G. (2014). *RF Power Systems for the FAIR Proton Linac*. Proceedings of LINAC, Geneva, Switzerland, pages 236–238.

[Kapchinsky and Teplyakov, 1970] Kapchinsky, M. and Teplyakov, V. (1970). *Linear Ion Accelerator with Spatially Homogenous Focusing (English Translation)*. Prib. Tekh. Eksp., 2:19–22.

[Kester, 2013] Kester, O. (2013). *The FAIR Proton Linac*. Technology and Components of Accelerator-driven Systems. Second International Workshop Proceedings, pages 325–328.

[Kester et al., 2014] Kester, O., Barth, W., Dolinskyy, O., Hagenbuck, F., Knie, K., Reich-Sprenger, H., Simo, H., Spiller, P., Weinrich, U., Winkler, M., Maier, R., and Rrasuhn, D. (2014). *Status of the FAIR Accelerator Facility*. Proceedings of IPAC, Dresden, Germany, pages 2084–2087.

[Kester et al., 2015] Kester, O., Spiller, P., Becker, F., Dolinskyy, O., Groening, L., Knie, K., Reich-Sprenger, H., Vinzenz, W., Winkler, M., and Prasuhn, D. (2015). *The Accelerator Facility of the Facility for Antiproton and Ion Research*. Proceedings of IPAC, Richmond, VA, USA, pages 1343–1345.

[Kilpatrick, 1957] Kilpatrick, W. (1957). *Criterion for Vacuum Sparking Designed to Include Both rf and dc*. Rev. Sci. Instrum., 28(10):824–826.

[Kleffner et al., 2017] Kleffner, C. M., Berezov, R., Daehn, D., Fils, J., Forck, P., Groening, L., Kaiser, M., Knie, K., Muehle, C., Puetz, S., Schnase, A., Schreiber, G., Sieber, T., Trueller, J., Vinzenz, W., Will, C., and Ratzinger, U. (2017). *Status of the FAIR pLINAC.* Proceedings of IPAC, Copenhagen, Denmark, pages 2208–2210.

[Klein, 1992] Klein, H. (1992). *Basic Concepts I.* Proceedings of the CERN Accelerator School on RF Engineering for Particle Accelerators, Oxford, UK, pages 97–122.

[Knie, 2017] Knie, K. (2017). *p-Linac Schedule / Building G020.* p-Linac Kick-Off Meeting, GSI, Darmstadt, 23.01.2017.

[Krietenstein, 1999] Krietenstein, B. (1999). *Zur numerischen Berechnung von IH-Resonatoren.* Dissertation, TU Darmstadt.

[Kurennoy et al., 2014] Kurennoy, S., Batygin, Y., Olivas, E., and Rybarcyk, L. (2014). *Realistic Modeling of 4-Rod RFQs with CST Studio.* Proceedings of IPAC, Dresden, Germany, pages 3119–3121.

[Lee, 2004] Lee, T. H. (2004). *Planar Microwave Engineering.* Cambridge University Press, Cambridge, UK, 1. edition.

[Lombardi, 2016] Lombardi, A. (2016). *The LINAC4 Project.* Proceedings of HB, Malmö, Sweden.

[Lombardi, 2017] Lombardi, A. (2017). *LINAC4: From Initial Design to Final Commissioning.* Proceedings of IPAC, Copenhagen, Denmark, pages 1217–1219.

[Lombardi et al., 1992] Lombardi, A., Parisi, G., and Vretenar, M. (1992). *Comparison Study of RFQ Structures for the Lead Ion Linac at CERN.* Proceedings of EPAC, Berlin, Germany, pages 557–559.

[Lombardi, 2005] Lombardi, A. M. (2005). *The Radio Frequency Quadrupole (RFQ).* Proceedings of CERN Accelerator School - Small Accelerators / Zeegse, The Netherlands, pages 201–207.

[Lombardi et al., 2001] Lombardi, A. M., Pirkl, W., and Bylinsky, Y. (2001). *First Operating Experience with the CERN Decelerating RFQ for Antiprotons.* Proceedings of PAC, Chicago, Il, USA, pages 585–587.

[Lu et al., 2011] Lu, Y.-R., Wei, C., Nie, Y.-C., Liu, G., Gao, S.-L., Zeng, H.-J., Yan, X.-Q., and Chen, J.-E. (2011). *Power Test of the Ladder IH-RFQ Accelerator at Peking University.* Chinese Physics Letters, 28(7):072901.

[Maclean, 1930] Maclean, W. R. (1930). *The Resonator Action Theorem.* Quart. Appl. Math., 2:329–335.

[Mäder, 2014] Mäder, D. (2014). *Die CH-Sektion des 17 MeV Injektors für MYRRHA.* Dissertation, Johann Wolfgang Goethe-Universität, Frankfurt am Main.

[Maier and Slater, 1952] Maier, L. C. and Slater, J. C. (1952). *Field Strength Measurements in Resonant Cavities.* Journal of Applied Physics, 23(1):68–77.

[Mathot et al., 2010] Mathot, S., Bourquin, P., Briswalter, A., Callamand, T., Carosone, J., Favre, N., Geisser, J.-M., Lombardi, A., Maire, V., Malabaila, M., Pugnat, D., Richerot, P., Riffaud, B., Rossi, C., Timmins, M., Vacca, A., Vandoni, G., and Vretenar, M. (2010). *Mechanical Design, Brazing and Assembly Procedures of the LINAC4 RFQ.* Proceedings of IPAC, Kyoto, Japan, pages 807–809.

[Nie et al., 2010a] Nie, Y.-C., Lu, Y.-R., Chen, J.-E., Yan, X.-Q., Gao, S.-L., Zhu, K., Liu, K.-X., and Guo, Z.-Y. (2010a). *Theoretical Design of a* 104 MHz *Ladder Type IH-RFQ Accelerator.* Chinese Physics Letters, 27(11):112901.

[Nie et al., 2014] Nie, Y.-C., Lu, Y.-R., Gao, S.-L., X.-Q.Yan, Guo, Z.-Y., and Chen, J.-E. (2014). *Theoretical and Experimental Studies on* 104 MHz *Ladder IH-RFQ Accelerator.* Nucl. Instrum. Meth. B, 737:229–236.

[Nie et al., 2010b] Nie, Y.-C., Lu, Y.-R., Gao, S.-L., Zhu, K., Yan, X.-Q., Guo, Z.-Y., Fang, J.-X., and Chen, J.-E. (2010b). *Simulation Study on* 104 MHz *Radio Frequency Quadrupole Accelerator.* Preceedings of ICEEE, Henan, China, pages 3411–3414.

[Pasini et al., 2004] Pasini, M., Kester, O., Habs, D., and Sieber, T. (2004). *RF Design of the MAFF IH-RFQ.* Proceedings of EPAC, Lucerne, Switzerland, pages 1216–1218.

[Paul, 1955] Paul, W. (1955). *Das elektrische Massenfilter.* Z. Phys., 140(3):262–273.

[Pfeiffer-Vacuum, 2013] Pfeiffer-Vacuum (2013). *The Vacuum Technology Book Volume II.* Pfeiffer Vacuum GmbH.

[Podlech, 2008] Podlech, H. (2008). *Entwicklung von normal- und supraleitenden CH-Strukturen zur effizienten Beschleunigung von Protonen und Ionen.* Habilitationsschrift, Johann Wolfgang Goethe-Universität Frankfurt am Main.

[Pütz, 2017] Pütz, S. (2017). *A high reliability, cost optimised Klystron Modulator for FAIR@GSI.* p-Linac Kick-Off Meeting, GSI, 23.01.2017.

[Ratzinger, 1996] Ratzinger, U. (1996). *The New GSI Prestripper Linac for High Current Heavy Ion Beams.* Proceedings of LINAC, Geneva, Switzerland, pages 288–290.

[Ratzinger, 1998] Ratzinger, U. (1998). *Effiziente Hochfrequenz-Linearbeschleuniger für leichte und schwere Ionen.* Habilitationsschrift, Johann Wolfgang Goethe-Universität Frankfurt am Main.

[Ratzinger, 2001] Ratzinger, U. (2001). *Commissioning of the new GSI high current linac and HIF related RF linac aspects.* Nucl. Instrum. Meth. A, 464:636–645.

[Ratzinger, 2013] Ratzinger, U. (2013). *Proposal of* 325 MHz *Ladder RFQ.* Presentation (unpublished). Talk at the RFQ Meeting, GSI Darmstadt, 20./21.11.2013.

[Ratzinger et al., 1998] Ratzinger, U., Kaspar, K., Malwitz, E., Minaev, S., and Tiede, R. (1998). *The GSI* 36 MHz *high-current IH-type RFQ and HIIF-relevant extensions.* Nucl. Instrum. Meth. A, 415:281–286.

[Rossi et al., 2008] Rossi, C., Bourquin, P., Lallement, J.-B., Lombardi, A., Mathot, S., Timmins, M., Vandoni, G., Vretenar, M., Cavaux, S., Delferriere, O., Desmons,

M., Duperrier, R., France, A., Leboef, D., and Piquet, O. (2008). *The Radiofrequency Quadrupole Accelerator for the LINAC4.* Proceedings of LINAC, Victoria, BC, Canada, pages 157–159.

[Rossi et al., 2012] Rossi, C., Dallocchio, A., Hansen, J., Lallement, J. B., Lombardi, A. M., Mathot, S., Pugnat, D., Timmins, M., Vandoni, G., Vretenar, M., Desmons, M., France, A., Noa, Y. L., Novo, J., and Piquet, O. (2012). *Assembly and RF Tuning of the LINAC4 RFQ at CERN.* Proceedings of LINAC, Tel-Aviv, Israel.

[Rubbia et al., 2001] Rubbia, C., Abderrahim, H. A., Björnberg, M., Carluec, B., Gheradi, G., Romero, E. G., Gudowski, W., Heusener, G., Leeb, H., von Lensa, W., Locatelli, G., Magill, J., Martínez-Val, J. M., Monti, S., Mueller, A., Napolitano, M., Pérez-Navarro, A., Salvatores, M., Soares, J. C., and Thomas, J. B. (2001). *A European roadmap for developing accelerator driven systems (ADS) for nuclear waste incineration.* ENEA, Rom.

[Rutishauser, 1969] Rutishauser, H. (1969). *Computational Aspects of F.L. Bauer's Simultaneous Iteration Method.* Numerische Mathematik, 13(1):4–13.

[Schempp, 1992a] Schempp, A. (1992a). *RFQ Accelerators for Ion Implantation.* Nucl. Instrum. Meth. B, 62:425–430.

[Schempp, 1992b] Schempp, A. (1992b). *The Application of RFQs.* Proceedings of LINAC, Ottawa, Ontario, Canada, pages 545–549.

[Schempp, 1996] Schempp, A. (1996). *Design of compact RFQs.* Proceedings of LINAC, Geneva, Switzerland.

[Schempp, 2008] Schempp, A. (2008). *An Overview of Recent RFQ Projects.* Talk at LINAC, Victoria, BC, Canada.

[Schempp et al., 1985] Schempp, A., Deitinghoff, H., Ferch, M., Junior, P., and Klein, H. (1985). *Four-rod-$\lambda/2$ -RFQ for light Ion Acceleration.* Nucl. Instrum. Meth. B, 10-11:831–834.

[Schmidt, 2014] Schmidt, J. (2014). *Tuning and Optimization of the Field Distribution for 4-Rod Radio Frequency Quadrupole Linacs.* Dissertation, Johann Wolfgang Goethe-Universität, Frankfurt am Main.

[Schmidt et al., 2014] Schmidt, J. S., Koubek, B., Schempp, A., Tan, C. Y., Bollinger, D. S., Duel, K. L., Karns, P. R., Pellico, W. A., Scarpine, V. E., Schupbach, B. A., and Kurennoy, S. S. (2014). *Investigations of the output Energy Deviation and other Parameters during Commissioning of the Four-ROD Radio Frequency Quadrupole at the Fermi National Accelerator Laboratory.* Phys. Rev. ST Accel. Beams, 17:030102.

[Schnase et al., 2015] Schnase, A., Plechov, E., Salvatore, J., Schreiber, G., Vinzenz, W., Joly, C., and Lesrel, J. (2015). *Progress of the Klystron and Cavity Test Stand for the FAIR Proton Linac.* Proceedings of IPAC, Richmond, VA, USA, pages 2802–2804.

[Schreiber et al., 2016] Schreiber, G., Plechov, E., Salvatore, J., Schlitt, B., Schnase, A., and Vossberg, M. (2016). *First High Power Tests at the* 325 MHz *RF Test Stand at GSI.* Proceedings of LINAC, East Lansing, MI, USA, pages 287–289.

[Schuett et al., 2016a] Schuett, M., Obermayer, M., and Ratzinger, U. (2016a). *Development and Measurements of a* 325 MHz *Ladder-RFQ.* Proceedings of LINAC, East Lansing, MI, USA, pages 578–580.

[Schuett et al., 2014] Schuett, M., Ratzinger, U., and Brodhage, R. (2014). *Proposal of a* 325 MHz *Ladder-RFQ fot the FAIR Proton-Linac.* Proceedings of LINAC, Geneva, Switzerland, pages 1016–1018.

[Schuett et al., 2015] Schuett, M., Ratzinger, U., and Brodhage, R. (2015). *Development of a* 325 MHz *Ladder-RFQ of the 4-ROD-Type.* Proceedings of IPAC, Richmond, VA, USA, pages 3745–3747.

[Schuett et al., 2017a] Schuett, M., Ratzinger, U., Schnase, A., Syha, M., and Obermayer, M. (2017a). *Status of the modulated* 3 MeV 325 MHz *Ladder-RFQ.* Journal of Physics: Conference Series, 874(1):012048.

[Schuett et al., 2016b] Schuett, M., Ratzinger, U., and Zhang, C. (2016b). *Development of a* 325 MHz *Ladder-RFQ of the 4-Rod-Type.* Proceedings of IPAC, Busan, Korea, pages 899–901.

[Schuett et al., 2017b] Schuett, M., Syha, M., and Ratzinger, U. (2017b). *Status of the modulated* 3 MeV 325 MHz *Ladder-RFQ.* Proceedings of IPAC, Copenhagen, Denmark, pages 2249–2251.

[Siebert, 2001] Siebert, T. (2001). *Entwicklung von 4-Rod- und IH- Radio-Frequenz-Quadrupol (RFQ)-Beschleunigern für radioaktive Ionenstrahlen bei REX-ISOLDE und MAFF.* Dissertation, Ludwig-Maximilians-Universität, München.

[Slater, 1946] Slater, J. (1946). *Microwave Electronics.* Rev. Mod. Phys., 18(4):441–512.

[Slater, 1950] Slater, J. C. (1950). *Microwave Electronics.* D. Van Nostran Company, New York.

[Syha et al., 2017] Syha, M., Schuett, M., Obermayer, M., and Ratzinger, U. (2017). *Beam Dynamics for a High Current* 3 MeV*,* 325 MHz *Ladder-RFQ.* Proceedings of IPAC, Copenhagen, Denmark.

[Teng, 1954] Teng, L. C. (1954). *Alternating Gradient Electrostatic Focusing for Linear Accelerators.* Phys. Sci. Instrum., 25(3):264–268.

[Teplyakov, 1992] Teplyakov, V. (1992). *RFQ Focusing in Linacs.* Proceedings of LINAC, Ottawa, Ontario, Canada, pages 21–24.

[Tokuda and Yamada, 1981] Tokuda, N. and Yamada, S. (1981). *New Formulation of the RFQ Radial Matching Section.* Proceedings of LINAC, Santa Fee, NM, USA, pages 313–315.

[Umrath, 1997] Umrath, W. (1997). *Grundlagen der Vakuumtechnik.* Leybold Vakuum.

[Vretenar et al., 2014] Vretenar, M., Dallocchio, A., Dimov, V. A., Garlasché, M., Grudiev, A., Lombardi, A. M., Mathot, S., Montesinos, E., and Timmins, M. (2014). *A compact high-frequency RFQ for medical applications.* Proceedings of LINAC, Geneva, Switzerland, pages 935–938.

[Wang, 2015] Wang, H. (2015). *Bead-pulling Measurement Principle and Technique Used for the SRF Cavities at JLab.* U.S. Particle Accelerator School, Newport News, VA, USA.

[Wang, 1986] Wang, J. W. (1986). *Some Problems on RF Breakdown in Room Temperature Accelerator Structure, a possible Criterion.* SLAC-AP-51.

[Wangler, 2008] Wangler, T. P. (2008). *RF Linear Accelerators.* WILEY-VCH Verlag GmbH & Co. KG, Weinheim, 2. edition.

[Wangler and Stokes, 1980] Wangler, T. P. and Stokes, R. H. (1980). *The Radio-Frequency Quadrupole Linear Accelerator.* Proceedings of the sixth conference on the Application of Accelerators in Research and Industry, North Texas State University, Denton, TX, page 7.

[Williams, 1979] Williams, S. W. (1979). *Voltage Breakdown Testing for the Radio-Frequency Quadrupole Accelerator.* Proceedings of LINAC, Montauk, NY, USA.

[Yan et al., 2014] Yan, C., Schmidt, J., and Schempp, A. (2014). *Simple lumped circuit model applied to field flatness tuning of four-rod radio frequency quadrupoles.* Phys. Rev. ST Accel. Beams, 17(012002).

[Zhang et al., 2016] Zhang, C., Groening, L., Kester, O., Mickat, S., Vormann, H., Baschke, M., Podlech, H., Ratzinger, U., and Tiede, R. (2016). *HSI Upgrade for the UNILAC Injection to FAIR.* Proceedings of IPAC, Busan, Korea, pages 877–879.

[Zhang and Schempp, 2009] Zhang, C. and Schempp, A. (2009). *Design of an upgradeable $45 - 100\,\mathrm{mA}$ RFQ accelerator for FAIR.* Nuclear Instruments and Methods in Physics Research Section A: Accelerators, Spectrometers, Detectors and Associated Equipment, 609(2-3):95–101.

[Zimmermann et al., 2004] Zimmermann, H., Bartz, U., Müller, N., Schempp, A., and Thibus, J. (2004). *The Frankfurt Funneling Experiment.* Proceedings of EPAC, Lucerne, Switzerland, pages 1213–1215.

[Zinke and Brunswig, 1999] Zinke, O. and Brunswig, H. (1999). *Hochfrequenztechnik 1.* Springer-Verlag, Berlin Heidelberg, 6. edition.

Appendices

Appendix A

Physical and Geometric Parameters

The physical and geometrical properties both of the short unmodulated as well as of the modulated prototype is listed below. The data from the unmodulated Ladder RFQ is taken from the RF and High power measurements. In case of the modulated Ladder RFQ all values refer to the simulations as first data from measurements is expected after completion of manufacturing in 2018[1].

Table A.1: Physical parameters of the unmodulated and modulated prototype.

Parameter	unmod. Prototype	mod. Prototype	Unit
RF Parameters			
Operating Frequency	325.224	325.224	MHz
Q-Value (sim)	6800	7000	
Q-Value (meas)	5080	TBA	
Loss peak/av. (sim.)	100 / 80	675 / 360	kW / W
Loss peak/av. (meas.)	135 / 110	tba	kW / W
Shunt impedance (calc.)	31	45	$k\Omega m$
Electrode Voltage	80	91	kV
Beam Power	–	210	kW

---

[1]The exact electrode parameters may still be subject to change as in October 2017 the beam dynamics has not been finalized yet.

Table A.2: Electrode parameters of the unmodulated and modulated prototype.

Parameter	unmod. Prototype	mod. Prototype	Unit
Electrode Dimensions			
Mean aperture r_0	3.42	3.1	mm
Vane tip radius ρ	2.56	3.67	mm
Tip height h_1	5.0	5.0	mm
Base Height h_2	12.59	12.59	mm
Base Width V	14	14	mm
Mounting height h_r	28	28	mm
Electrode length	630	≈ 3330	mm
Electrode Physical Parameters			
ε	0.7	0.7	
η	0.8	0.8	
L_L	24.5	23.46	nH
L_Q	2.2	4.2	nH
L_{eff}	26.8	27.7	nH
C_Q	5.2	5.5	pF
C_{LQ}	0.9	1.4	pF
C_{eff}	6.1	6.4	pF
k	0.46	0.43	
ω_0	2042	2477.84	MHz
Frequency (theory)	325	317	MHz
ρ/r_0	0.75	0.85	

Table A.3: Geometrical dimensions of the unmodulated and modulated prototype.

Parameter	unmod. Prototype	mod. Prototype	Unit
Ladder Dimensions			
Ladder Width b	150	150	mm
Ladder Height h	285	280	mm
Stem Thickness d	20	20	mm
Stem Distance l	40	40	mm
No. of Cells	10	55	
Ring Diameter	100	100	mm
Tank Dimensions			
Length	770	3470	mm
Height	365	370	mm
Width	485	590	mm
Coupling flange	CF100	CF160	
Frequency tuning flanges	2x CF63	12x CF63	
Pumping	1x CF100	3x CF160	

Appendix B

Time Schedule and Milestones of the Ladder RFQ

Table B.1: Time Schedule of the unmodulated Prototype.

since 2013	RF Simulations
05/2014	Tendering successfully completed and contracted
06/2014	Manufacturing Design Documentation started
08/2014	Manufacturing Release
09/2014	Disposition of Materials and commencement of construction
02/2015	First Delivery (scheduled 12/2014)
02-03/2015	First measurements: RF-Spectra and Field-Flatness
04/2015	Kick off of copper-plating and final mechanical treatment
07/2015	Rework due to surface treatment for Copper Plating
08-10/2015	Copper Plating
10/2015	First SAT (failed)
11/2015	Rework at Fa. Kress (Pumping holes & dowel pin corrections)
12/2015	Site Acceptance Test passed
01-02/2016	Final tests and measurements (RF, flatness, frequency-tuning with motor driven plungers, mechanical test, vacuum test)
03/2016	In-House power tests and Conditioning (400 W pulsed & cw)
04-05/2016	High power tests at GSI up to 500 kW @ 2 Hz & 200 µs

Table B.2: Time schedule and outlook of the modulated Prototype.

since 2015	Simulations of the modulated prototype
04-06/2016	Mechanical Design & Specification
06/2016	Tendering
07/2016	Award of Contract
12/2016-05/2017	Preliminary examination documents / review
until 02/2017	Material disposition
06/06/2017	Manufacturing release for the tank
09/2017	Manufacturing release for the ladder structure
end of 2017:	Manufacturing of the first revision
Q4/17 - Q1/18	Copper-plating
05/2018	First RF-measurements of the frequency and flatness accompanied by simulations
Q3/2018	Re-milling of the ladder structure for tuning the flatness and reaching the correct frequency.
Late 2018	**Final FAT**
Q4/2018	Re-verification of RF-measurements.
Q4/2018	Installation of tuners and coupler. Final Assembly (Vacuum System, Gages, Outcoupler)
2019	Conditioning & High power test at the GSI test bunker
>2020	Beam tests including LEBT, Emittance measurements

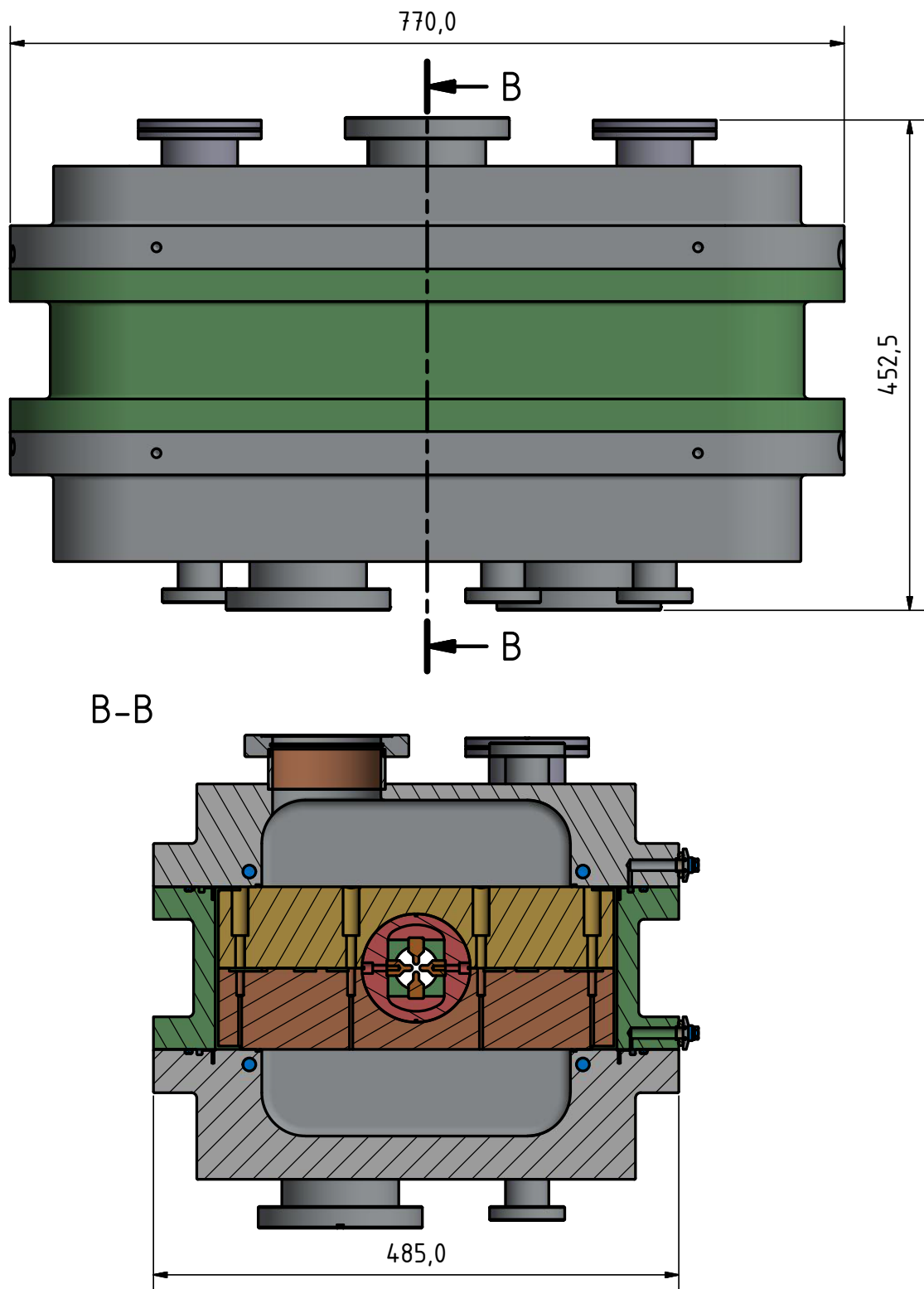# Appendix C

Technical Drawings

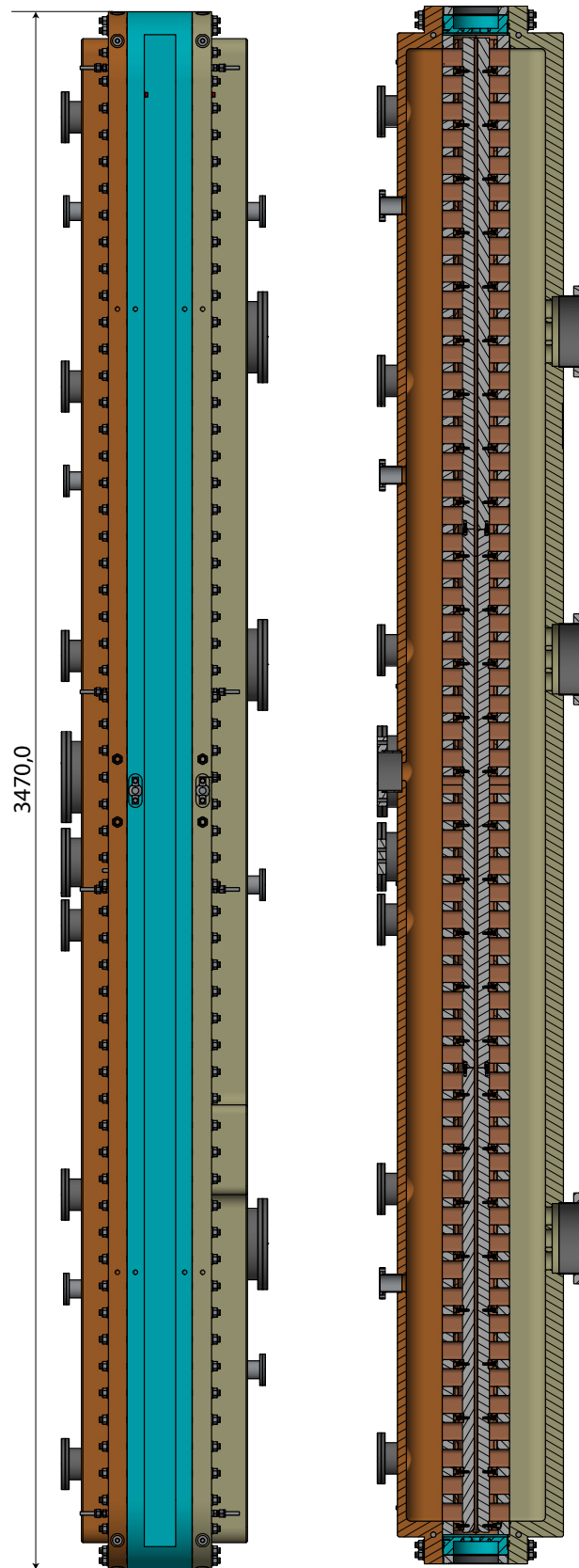Figure C.1: Profile and transversal cut section of the unmodulated Ladder RFQ.

Figure C.2: Profile and longitudinal cut section of the modulated Ladder RFQ.

Appendix D

Units and Variables

Variable	Description
A	Area; Current
A/q	(Atomic) mass to charge ratio
a	Aperture
α	Thermal expansion; Twiss parameter
$\vec{B}$	Magnetic field
β	Velocity relative to the speed of light $\beta = v/c$
	Twiss parameter
	Coupling factor
c	Speed of light
C	Capacitance
D	Dipole moment
δ	Skin depth
$\vec{E}$	Electrical field
E	Modulus of elasticity
ε	Permittivity $\varepsilon = \varepsilon_r \varepsilon_0$ with $\varepsilon_0 = 8.8541 \cdot 10^{-12}\,\mathrm{Vs/m^2}$
f	Frequency
Γ	Reflection coefficient
η	Current reduction factor
$I_n(x)$	n-th order Besselfunction
$\vec{j}$	Current density
$\vec{H}$	Magnetic field

Variable	Description
k_{perm}	Permeation rate
L	Inductance
l	Length
λ	Wavelength
m	Modulation
μ_0	Magnetic permeability of vacuum, $\mu_0 = 4\pi 10^{-7}$
p	Pressure
P_C	Power losses (Ohmic)
P_e	Emitted Power
P_f	Forward Power
P_t	Transmitted Power
Φ	Magnetic Flux
φ	Phase
Q	Quality factor; Pumping rates; Quadrupole moment
Q_0	Intrinsic quality factor
Q_l	Loaded quality factor
q_{Des}	Desorption rate
q_{Diff}	Diffusion rate
R_a	Profile roughness parameter of surfaces
R_{eff}	Effective Shunt Impedance
R_p	Shunt Impedance
R_S	Surface Resistance
r_0	Mean aperture
ρ	Electrode tip curvature
S	Pumping speed
S_{ii}	Scattering parameters
σ	Electrical conductivity
T	Temperature; Transient time factor; Period length
t	Time
U	Potential
V	Voltage; Volume

Variable	Description
W	Energy
ω	Angular frequency
x	X-coordinate perpendicular to the beam-axis
	(spoke width, vertical axis in the 3D-model)
y	Y-coordinate perpendicular to the beam-axis
	(spoke height, horizontal axis in the 3D-model)
z	Z-coordinate along the beam axis
Z	Impedance; Shunt impedance
Z_{eff}	Effective shunt impedance: $Z_{eff} = Z_0 \cdot l$

Acknowledgements

Zunächst danke ich Prof. Dr. Ulrich Ratzinger für die Annahme als Doktorand in seine Arbeitsgruppe und das Vertrauen über die Durchführung dieses spannenden Projektes. Besonders hervorheben möchte ich die Vielzahl an bereichernden und motivierenden fachlichen Gesprächen, wofür Prof. Ratzinger immer ein offenes Ohr und Zeit hatte. Ebenso bedanke ich mich bei meinem Zweitgutachter Prof. Dr. Holger Podlech!

Ein weiterer herzlicher Dank gilt allen Mitgliedern (und Ehemaligen) des IAP für die großartige Zeit in der Arbeitsgruppe. Besonders erwähnt seien hier das Winterseminar und IPAC/Linac Konferenzreisen, die eine große Bereicherung des Erfahrungshorizontes erwirkten. Aber auch die Vielzahl an Grillfeiern dürfen nicht unerwähnt bleiben. Ebenso danke ich Prof. Podlech und Dr. Iberler für die herausragenden, jährlichen Skiurlaube!

Im speziellen möchte ich noch Marco Busch (nicht nur als Trainingspartner) aber auch Malte Schwarz u.a. für die tolle Zeit in Südkorea (und weiteren Teilen der Welt...) herzlich danken! Ebenso auch allen anderen der Arbeitsgruppe für das tolle Arbeitsklima und die außerbetrieblichen Aktivitäten.

I am most grateful for the extraordinary experience, hospitality and fruitful discussions to my friend Garam Hahn and his team at the Korea Institute of Radiological and Medical Sciences! Thank you! Furthermore, I would like to thank Sang-Hoon Nam and Byung-Joon Lee.

Ebenso möchte ich den GSI Mitarbeitern Bernhard Schlitt, Alexander Schnase und Gerald Schreiber für ihre tatkräftige Unterstützung bei den Hochleistungstest am GSI Bunker danken. Allen voran bin ich Alexander Schnase sehr dankbar für seine

schier umfassenden Kenntnisse im Bereich der HF-Technik, sowie seine unermüdliche Hilfs- und Diskussionsbereitschaft!

Für die tolle Zusammenarbeit mit dem p-Linac Team danke ich Carl Kleffner und Klaus Knie.

Fa. Kress, insbesondere Jürgen Häuser, danke ich für die reibungslose und unkomplizierte Zusammenarbeit, sowie die qualitativ hochwertige und pünktliche Herstellung des RFQs.

Ein weiterer Dank gilt Daniel Bänsch, ohne dessen Hilfe die Arbeit in der Experimentierhalle zum Erliegen gekommen wäre. Danke für den immer hilfsbereiten Einsatz bei technischen Belangen und (spontanen) Problemlösungen aller Art. Darüber hinaus danke ich dem Werkstattteam rund um Herrn Reploeg für die zeitnahe Ertüchtigung essentieller Bauteile und die Organisation der Betriebsausflüge. Rudolf Tiede danke ich für die interessanten Gespräche über strahldynamische Themen und die Administration in Sachen Hard- und Software.

Bei Tanja Harji, Astrid Hergt, Karin Brost, Kirstin Schäfer und Laura Quist bedanke ich mich für ihre geduldige Unterstützung in allen administrativen Belangen.

Dem BMBF sei für die durchgehende, finanzielle Unterstützung meiner Arbeit gedankt (05P12RFRB9, 05P15RFRBA)!

Zuletzt richte ich meinen Dank an meine Familie und vor allem an meine Freundin Sabrina, die mich über den gesamten Zeitraum durchgehend unterstützt, motiviert und bereichert hat und dabei so einiges über Beschleunigerphysik lernen musste. So waren auch die anstrengenden Zeiten nicht nur erträglich, sondern großartig. Darüber hinaus danke ich auch allen namentlich ungenannten Freunden, die mich auf diesem Weg begleitet haben. Danke, dass ihr an meiner Seite steht!